The Dissertation Committee for Austin Patrick Lane Certifies that this is the approved version of the following dissertation:

Patternable Materials for Next-Generation Lithography

Committee:

C. Grant Willson, Supervisor

Christopher Ellison

Roger Bonnecaze

Chris Mack

Carlos Baiz

Patternable Materials for Next-Generation Lithography

by

Austin Patrick Lane, B.S.

Dissertation

Presented to the Faculty of the Graduate School of

The University of Texas at Austin

in Partial Fulfillment

of the Requirements

for the Degree of

Doctor of Philosophy

The University of Texas at Austin

May 2017

Dedication

For my family.

Acknowledgements

It is hard to imagine my life in grad school without the people who supported and contributed to my studies. I am very grateful for everyone who made my experience at UT so meaningful.

I would like to specifically thank my advisor, Dr. Willson, for providing me with an exceptional academic home during my five years in Austin. He has created a remarkable research group where students thrive and succeed as young scientists. I am always inspired by his leadership and dedication to teaching, and I feel privileged to be counted among his students. I would also like to thank my unofficial advisor, Dr. Ellison, for his advice and support throughout grad school. I especially appreciate his recommendations which gave me numerous opportunities to be successful. Special thanks go to Donna Martin, Kathleen Sparks, and Mindy Maloney for taking care of the day-to-day logistics and keeping the group running smoothly. I would also like to acknowledge my committee members: Roger Bonnecaze, Chris Mack, and Carlos Baiz. Thank you for your suggestions and encouragement.

To my labmates: thank you for leading by example and teaching me how to be a better scientist, presenter, and writer. When I first joined the group, I was fortunate to learn the basics of phthalaldehyde polymerization from Chris Bates, who was a patient teacher during my first few months in lab. Will Bell and Chris Chen were always fun to be around and made me feel welcome in a new place. My research on block copolymers would not have been possible (or nearly as enjoyable) without contributions from Michael Maher, Gregory Blachut, Will Durand, Colin Hayes, Yusuke Asano, Sunshine Zhou, and Andrew Dick. I always felt that I could come to you with questions or requests and you would not hesitate to help. I will miss the spicy memes we shared playing

Subgroup Bingo. I would like to thank my fellow Aggie, Ben Cassidy, for the many times we broke (crazy)bread in the office. My work on the “unzipping” resist would not have been possible without collaborations from a number of talented chemists: Ryan Mesch, Kensuke Matsuzawa, Wade Wang, Wontae Joo, and Di Liu. Thank you for your help and hard work to make the “unzipping” project a success. I was also very fortunate to work with several talented undergraduate researchers: Anthony Engler, Scott Willis, Benjamin Hausmann, Emily Young, and Stephen Tung. Thank you for your patience and hard work in lab.

I would also like to acknowledge the industry collaborators I have worked with, specifically Steve Sirard and Ratchana Limary at Lam Research for their support and collaborative efforts towards my work. XiaoMin Yang and Kim Lee at Seagate were excellent hosts when we travelled to Fremont and provided me with a memorable summer internship opportunity.

Finally, I would like to acknowledge my friends and family who supported me through the high and low points in grad school. Mom, Dad, Morgan, Abbey, and Hallie: I love you and thank you for giving me a place to call home. Abby, thank you for making these last few years so enjoyable. You are my favorite person to spend time with.

Patternable Materials for Next-Generation Lithography

Austin Patrick Lane, Ph.D.

The University of Texas at Austin, 2017

Supervisor: C. Grant Willson

One of the salient truths facing the microelectronics industry today is that photolithography tools are unable to meet the resolution requirements for manufacturing next-generation devices. In the past, circuit feature sizes have been minimized by reducing the exposure wavelength used for patterning. However, this strategy failed with the worldwide dereliction of 157 nm lithography in 2003. Extreme ultraviolet (EUV) lithography still faces many technical challenges and is not ready for high volume manufacturing. How will the microelectronics industry continue to innovate without regular advances in photopatterning technology? Regardless of which paradigm is adopted, new materials will probably be required to meet the specific challenges of scaling down feature sizes and satisfying the economic ultimatum of Moore's Law.

In the search for higher resolution patterning tools, device manufacturers have identified block copolymer (BCP) lithography as a possible technique for next-generation nanofabrication. BCP self-assembly offers access to sub-5 nm features in thin films, well beyond the resolution limits of photolithography. However, BCP materials must be carefully designed, synthesized, and processed to create lithographically interesting features with good etch resistance for pattern transfer. In this dissertation, we describe a

pattern transfer process for 5 nm BCP lamellae and a directed self-assembly (DSA) process for aligning 5 nm structures in thin films. To achieve defect-free alignment, the interfacial interactions between the BCP and pre-patterned substrate must be precisely controlled. We also discuss a new process for selectively modifying oxidized chromium films using polymer brushes, which could further improve the aforesaid DSA process. To facilitate better pattern transfer of BCP structures, several new BCPs with "self-developing" blocks were synthesized and tested. These materials depolymerize and evaporate in strongly acidic environments, leading to developed BCP features without the need for etching or solvent.

"Self-developing" polymers may also be useful materials for traditional photolithography. Chemically amplified resists used in manufacturing today are fundamentally limited by a trade-off between sensitivity and pattern quality. To overcome this problem, we present a new type of photoresist that relies on depolymerization, rather than catalysis, to achieve amplification without producing significant roughness or bias in the final pattern.

Table of Contents

List of Tables xiii

List of Figures xiv

List of Illustrations xxix

Chapter 1: Introduction to High Resolution Lithography 1

1.1 A Brief History of Microelectronics 1

1.2 Optical Lithography 6

1.3 Minimum Resolution 9

1.4 Optical Lithography Beyond 193 nm Immersion 10

1.5 Other High Resolution Patterning Techniques 15

1.5.1 Electron Beam Lithography (EBL) 15

1.5.2 Nanoimprint Lithography (NIL) 20

1.5.3 Block Copolymer Lithography 23

Chapter 2: Materials for High Resolution Lithography 30

2.1 Photoresist Design 30

2.1.1 Negative-tone Resists 30

2.1.2 DNQ/Novolak 32

2.1.3 Chemically Amplified Resists (CAR)s 35

2.2 Block Copolymer Materials Design 38

2.2.1 Block Copolymer Thermodynamics 38

2.2.2 Self-Assembly in Thin Films 41

2.2.3 Limitations of PS-*b*-PMMA 43

2.3 Silicon-containing Block Copolymers 44

2.3.1 The Path to Smaller Feature Sizes 44

2.3.2 Orientation Control 46

2.3.3 Etch Resistance and Pattern Transfer 47

Chapter 3: Directed Self-Assembly and Pattern Transfer of 5 nm Block Copolymer Lamellae....49
3.1 Introduction....49
3.2 Pattern Transfer of 5 nm BCP Features....52
3.2.1 Reactive Ion Etching (RIE)....52
3.2.2: Pattern Transfer via Molecular Transfer Printing....53
3.3 Directed Self-Assembly....57
3.3.1 Process Flow....57
3.3.2 Initial DSA results....60
3.3.3 Process Optimization....63
3.3.4 Cross-section Analysis Using STEM/EELS....70
3.4 Conclusions....72
3.5 Experimental....73
3.5.1 Materials....73
3.5.2 Guide line preparation....75
3.5.3 BCP and top coat processing....76
3.5.4 Thin film analysis....77
3.6 Acknowledgements....77
Chapter 4: Selective Surface Modification using Polymer Brushes....78
4.1 Introduction and Brush Synthesis....79
4.2. The Limits of Brush Polymers for Directed Self-Assembly....82
4.3 Selective Grafting Chemistry on Chromium Thin Films....88
4.4 Conclusions....107
4.5 Experimental....108
4.5.1 Materials....108
4.5.2 Brush Processing....110
4.5.3 Thin Film Analysis....110
4.6 Acknowledgements....111
Chapter 5: Self-developing Block Copolymers for Lithographic Applications....112
5.1 Introduction....112

5.2 Poly(phthalaldehyde) 115
5.2.1 o-phthalaldehyde 117
5.2.1.1 Monomer and Homopolymer Synthesis 117
5.2.1.2 Block Copolymer Synthesis 119
5.2.2 4,5-dichlorophthalaldehyde 122
5.2.2.1 Monomer and Homopolymer Synthesis 122
5.2.2.2 Block Copolymer Synthesis 125
5.2.2.3 BCP Self-assembly 131
5.3 Poly(methoxy α-methylstyrene) 134
5.3.1 PMAMS Homopolymer Synthesis 137
5.3.2 Thin Film Depolymerization Experiments 141
5.3.3 Block Copolymer Synthesis 146
5.3.4 Thin Film Self-assembly of PMAMS-*b*-PTMSS 153
5.4 Conclusions 159
5.5 Experimental 159
5.5.1 Instrumentation 159
5.5.2 Syntheses 160
5.6 Acknowledgements 170

Chapter 6: A Chemically Amplified Resist without Catalyst 171
6.1 Introduction 171
6.1.1 Chemically Amplified Resist Design 171
6.1.2 Amplification Via Depolymerization 177
6.1.3 Candidates for “Unzipping” Resists 180
6.2 Monomer and Polymer Synthesis 185
6.3 Initial Photopatterning Experiments 188
6.4 Optimization of Resist Performance Using Electron Beam Lithography (EBL) 192
6.4.1 Effect of Post-apply Bake (PAB) Temperature 195
6.4.2 Effect of Post-exposure Bake (PEB) Temperature 198
6.4.3 Effect of the Molecular Weight of Unzipping Polymer 199

6.4.4 Effect of changing the matrix resin....201
6.5 Etch Resistance Study....203
6.6 Line Width Roughness (LWR) Study....205
6.7 Conclusions....209
6.8 Experimental....210
6.8.1 Materials....210
6.8.2 Thin Film Processing....210
6.8.2.1 Resist Preparation:....210
6.8.2.2 Exposure:....212
6.8.2.3 Post-Exposure:....213
6.8.2.4 Development:....214
6.8.3 Thin Film Analysis....214
6.9 Acknowledgements....215
Bibliography....216

List of Tables

Table 5.1: PPHA homopolymer characterization data.....118

Table 5.2: PPHA-Cl_2 homopolymer characterization data 124

Table 5.3: Experimental details and thin film characterization for PMAMS depolymerization experiments.....142

Table 5.4: Characterization data for the polymers presented in Figure 5.18. M_n and Đ values were calculated from GPC using dn/dc values reported at the end of this chapter. Volume fractions were calculated from NMR. L_0 values were calculated using data from island/hole experiments and AFM characterization of island/hole films.....152

Table 6.1: A summary of the experiments that were performed to optimize the unzip/matrix system. Contrast and dose-to-clear (D_0) were chosen to be the response variables for this study. The results for PMMA and ZEP, commonly available e-beam resists, are provided for comparison. All films were developed for 1 minute, unless noted otherwise (PNBHFA). Contrast and D_0 data could not be collected for the third Novolak sample because features were essentially fully developed at the lowest possible exposure dose.....195

Table 6.2: Roughness data calculated from PSD curves, which were generated by averaging data from 20-30 CD-SEM images for each sample. The ArF resist data is marked due to the unusually high dose required to clear the features. This data should be treated skeptically. 207

List of Figures

Figure 1.1: The ENIAC, one of the world's first electronic computers. Technicians worked constantly to find and replace broken vacuum tubes. 2

Figure 1.2: A replica of Bardeen and Brattain's original point-contact transistor.[8]3

Figure 1.3: Jack Kilby's original integrated circuit.[12] 4

Figure 1.4: A NOR gate built from a 2x3 array of integrated transistors (center). Thousands of these chips provided computational power for the Apollo Guidance Computer.[14] 5

Figure 1.5: Cartoon schematic of photolithography process, including pattern transfer. 8

Figure 1.6: An EUV lithography system manufactured by ASML. 13

Figure 1.7: A photograph of a MoSi multilayer mirror used for EUV lithography.14

Figure 1.8: Vertical layout of typical shaped e-beam tool.[35] 17

Figure 1.9: A depiction of forward and backscattering phenomena which occur when high energy electrons interact with the resist and substrate.....19

Figure 1.10: Plot of resolution versus area throughput for various lithography techniques. Reproduced with permission from Sreenivasan, S.V. *et al*. *MRS Bull.* **2008**, *33*, 854–863. Copyright 2008 Materials Research Society.....21

Figure 1.11: The S-FIL process flow for generating nanoscale features. 22

Figure 1.12: Block copolymer fingerprint patterns. (A) Lamellae-forming PS-*b*-PMMA[54] (B) parallel PS-*b*-P2VP cylinders etched into silicon.[55] 25

Figure 1.13: Density multiplication of sparse HSQ guide lines patterned by electron beam lithography.[64] 27

Figure 1.14: SEM images of DSA process where assembling a BCP film on top of a poor pre-pattern can repair defects and improve feature size uniformity.[62] 28

Figure 2.1: "Snaking" that results from polymer features swelling in the development solvent.[71].....31

Figure 2.2: The Meyerhofer plot for DNQ/Novolak. It demonstrates that the photoproducts of DNQ accelerate the development rate of Novolak compared to the development rate of the pure polymer. Unexposed DNQ reduces the development rate of Novolak. Here "bleached" means fully exposed. Reproduced with permission from Meyerhofer, D. *IEEE Trans. Electron Devices* **1980**, *27*, 921–926. 2011 IEEE. 33

Figure 2.3: Developed features in DNQ/Novolak films after imaging at (A) 365 nm and (B) 248 nm. The sloped sidewalls in (B) can be attributed to the opacity of DNQ/Novolak at 248 nm.[75].....35

Figure 2.4: Photoresist features printed in melamine/Novolak/DNQ resist blends.[78] 36

Figure 2.5: (A) Theoretical phase diagram for diblock copolymers. Reproduced with permission from Cochran, E. W. *et al*. *Macromolecules* **2006**, 39, 2449–2451. Copyright 2006 American Chemical Society. (B) Cartoon depiction of different available morphologies for diblock copolymers39

Figure 2.6: Cartoon schematic of ideal BCP lithography process.....42

Figure 2.7: Over-simplified cartoon depicting BCP self-assembly in thin films. Lamellae-forming BCPs can form either parallel or perpendicular features, depending on the surface energy of the underlying substrate. 43

Figure 3.1: Top-down and tilted view SEMs of (A) fully developed 5 nm domains on top of a Cr/SOC-coated silicon wafer and (B) transferred patterns after the Cl_2/O_2 etch process. An oxidizing RIE process was used to completely remove the PVBD block in (A). The full height of the mask in (A) and (B) is approximately 26 nm. Scale bars = 100 nm. 53

Figure 3.2: (A) Materials and (B) MTP process used for replication of DSA films. CL stands for "conformal layer".....55

Figure 3.3: Results from the MTP process depicted in Figure 3.2. The images in the top row demonstrate that the large sub-fields of the original NIL pattern could be copied with good fidelity. However, the DSA obtained from the "daughter" film contained many defects, although some DSA was evident. The distortion seen in the "daughter" film SEM images is due to charging effects from the underlying glass substrate. The scale bars correspond to 100 μm and 100 nm for the top and bottom row of images, respectively. 57

Figure 3.4: Schematic showing the materials (A) and process steps (B) used for producing directed self-assembly of 5 nm features. Arrow 1 and 2 describe the process flow with and without a grafted brush, respectively. 59

Figure 3.5. Tilted and cross-sectional SEM images of unetched NIL lines. Scale bar = 100 nm for both images. 60

Figure 3.6: SEMs of BCP assembly on tall NIL features. The images in (A) were taken from samples in which a layer of brush was grafted to the substrate and rinsed before spin-coating the BCP film. The sample corresponding to the box in the first column was not imaged. The images in (B) were taken from samples prepared without grafting a neutral brush to the substrate. All BCP films were annealed at 190°C for 2 minutes. Scale bar = 50 nm. 62

Figure 3.7: (A) SEM image of BCP DSA after grafting a thin brush layer (3 nm) by annealing at 150°C for 10 mins and then annealing at 250°C for 5 mins. (B) SEM image of BCP DSA using the same process to prepare the sample shown in (A), but without the 10 min bake at 150°C. The improvement in DSA quality seen in (A) could be the result of the polymer brush flowing away from the NIL lines during the soft bake at 150°C, improving the selectivity of the grafting reaction during the 250°C bake. Scale bar = 100 nm.....65

Figure 3.8. SEMs of BCP assembly on substrates patterned by NIL, demonstrating how DSA quality is affected by NIL feature height. “h” is the average height of the NIL lines for both images in a given row, as measured by AFM. All BCP films were 33 nm (3.3 L_0) thick and were annealed at 190°C for 2 minutes. Scale bar = 200 nm.....67

Figure 3.9: (A) A quantitative comparison of DSA quality between samples produced with and without brush. The DSA score (y-axis) is calculated using custom computer software and represents the normalized average percentage of pixels participating in DSA. Error bars correspond to ±1 standard deviation from the mean score. The lines connecting the points are only meant to be visual aids, not to indicate a continuous relationship between individual pitches. The red dotted line represents the average score of a random fingerprint pattern. (B) Representative SEM images that approximately correspond to the normalized score in the colored box. All samples used a BCP film thickness of 33 nm and were annealed at 205°C for 10 min. Scale bar = 50 nm. 69

Figure 3.10. Images of NIL guide lines (top), BCP self-assembly (middle) and cross-sectional STEM in conjunction with EELS mapping (bottom) for three surfaces investigated in this study: (A) SiO_2 with brush, (B) untreated SiO_2, and (C) thin Cr_xO_y (2 nm) on SiO_2. The height of the NIL lines for the samples made on SiO_2 and Cr_xO_y is approximately 12 nm and 8 nm, respectively. BCP features for the samples made on SiO_2 were etched before STEM analysis, while the sample made on Cr_xO_y was not. The starting BCP film thickness for all three samples was approximately 33 nm. The samples on SiO_2 were annealed at 190°C for 2 min, while the sample prepared on Cr_xO_y was annealed at 205°C for 10 min. Scale bar for the top-down SEM images is 100 nm. Scale bar for the cross-section EELS images is 15 nm. 72

Figure 4.1: (A) A CD-SEM image and cartoon depicting the three-tone guiding patterns used for DSA. (B) The process used for creating three-tone patterns. Reproduced with permission from Williamson, L. *et al*. *ACS Appl. Mater. Interfaces* **2016**, 8, 2704–2712. Copyright 2016 American Chemical Society. 83

Figure 4.2: (A) The process for creating sidewall-guided DSA. (B) A cartoon depicting how the oxidized sidewalls interact with the block copolymer domains. (C) Line/space patterns from BCP assembly which have been transferred into a silicon substrate. Reproduced with permission from Cushen, J. *et al*. *ACS Appl. Mater. Interfaces* **2015**, *7*, 13476–13483. Copyright 2015 American Chemical Society. 85

Figure 4.3: Results from an experiment to determine if polymer brushes react with oxidized polymer surfaces. The wetting behavior of the surface was determined by depositing BCP films on top of various surfaces and thermally annealing the samples in air to produce island/hole topography. The resulting films were imaged by AFM. Samples were made using both a (A) PS-XST and (B) PtBuSty-XST polymer surface. BCP films were annealed at 180°C for 10 mins and the brush grafting step was performed at 250°C for 5 mins.....87

Figure 4.4: Water contact angles for Cr_xO_y and NIL surfaces after reacting with various alkene and alkyne functionalized compounds at 100°C. The data colored in orange represents NIL resist samples. 90

Figure 4.5: Water contact angle measurements taken after grafting various P(Sty-*r*-DVB) copolymers to Cr_xO_y films at 20, 60, and 100°C.....93

Figure 4.6: WCAs produced after reacting P(S-*r*-DVB) and various polystyrene homopolymers with Cr_xO_y surfaces at 100°C for 1 min. The two PS homopolymers synthesized by free radical polymerization were made using different free radical initiators.....94

Figure 4.7: Measured WCAs after reacting Cr_xO_y films with various aliphatic and aromatic molecules without obvious functionalities. The films were processed in the same way as the samples from Figure 4.4. Freshly oxidized Cr films were placed in a beaker pre-heated to 100°C containing 5 mL of each compound. After one minute, the films were removed, rinsed with MIBK, and baked at 180°C for 1 min. The WCA was measured in triplicate for each sample. 96

Figure 4.8: WCA results for polystyrene and poly(tert-butylstyrene) made by free radical and nitroxide-mediated polymerization (NMP). Polymer films were spun onto oxidized Cr and NIL films and processed by heating to 100°C for 1 minute, then rinsing with MIBK and baking again at 180°C for 1 minute.....98

Figure 4.9: WCAs and AFM scans showing island/hole results for grafted surfaces using a 25:75 tBuSty:Styrene copolymer synthesized by NMP. The brush was grafted at several temperatures to determine the approximate window for neutrality.....100

Figure 4.10: WCAs and AFM scans showing island/hole results for grafted surfaces using a 50:50 tBuSty:Styrene copolymer synthesized by NMP. 101

Figure 4.11: WCAs and AFM scans showing island/hole results for grafted surfaces using a 75:25 tBuSty:Styrene copolymer synthesized by NMP. 102

Figure 4.12: WCAs and AFM scans showing island/hole results for grafted surfaces using a 100% tBuSty copolymer synthesized by NMP. 103

Figure 4.13: SEMs of BCP films sandwiched between a neutral top coat and a polymer-grafted Cr film. With the exception of the sample in the top right, every polymer composition/grafting temperature combination corresponds to an "inconclusive" result by the islands and holes test. Scale bar = 50 nm. 104

Figure 4.14: SEM micrographs of BCP films annealed between a neutral top coat and a PtBuSty-treated Cr film. The brush films grafted at high temperatures still produce perpendicular BCP lamellae. Scale bar = 50 nm. 105

Figure 4.15: SEM micrographs of BCP assembly on oxidized Cr and NIL films after treatment with the same polymer brush at 100°C. After sequentially spin coating an 18 nm thick film of BCP and neutral top coat, the samples were annealed at 180°C for 5 mins. Scale bar = 50 nm. 106

Figure 5.1: Identical PS-*b*-PMMA films developed using (A) exposure to UV light followed by acetic acid washing and (B) oxygen-based RIE process. Reproduced with permission from Ruiz, R. *et al*. *ACS Nano* **2011**, *5*, 79–84. Copyright 2011 American Chemical Society. 113

Figure 5.2: Representative GPC traces for PS-OH (red), M_n = 2.5 kDa, Đ = 1.02 and the PS-PPHA BCP product (black) from the reaction depicted in Scheme 6.2. The small peak shift towards lower retention volume indicates low conversion for the polymerization. 121

Figure 5.3: Effect of aromatic ring substituents on solution stability of PPHA. Special thanks goes to Dr. Anthony DiLauro for generating the data for this plot.....122

Figure 5.4: Representative GPC traces for PS-OH (red), M_n = 7.0 kDa, Đ = 1.07 and the PS-PPHA BCP product (black) from the reaction depicted in Scheme 6.2. The small peak shift towards lower retention volume indicates low conversion for the polymerization. 126

Figure 5.5: Thermogravimetric analysis (TGA) traces for PPHA(red) and PPHA-Cl_2 (black). The structures corresponding to each trace have been drawn for clarity. 127

Figure 5.6: (A) GPC traces for PS-NH_2 (red, M_n = 10.1 kDa, Đ = 1.1), PPHA-isocyanate (blue, M_n = 5.3 kDa, Đ = 1.26), and the PS-*b*-PPHA-Cl_2 BCP product (black). The PS-NH_2 was modified by reaction with phenyl isocyanate prior to GPC analysis. (B) GPC traces of the BCP product taken at various reaction times. Starting from 1 hr (lightest blue), the plot shows the kinetics of the amine-isothiocyanate coupling reaction until it reaches completion after approximately 24 hrs (darkest blue).129

Figure 5.7: (A) GPC traces of PS-*b*-PPHA-Cl_2 before (black) and after (red) treatment with trifluoroacetic acid. (B) NMR spectra of PS-*b*-PPHA-Cl_2 before (black) and after (red) treatment with trifluoroacetic acid. The presence of peaks corresponding to the PHA-Cl_2 monomer confirmed the clean degradation of the PPHA-Cl_2 block.....130

Figure 5.8: SAXS data for two PS-*b*-PPHA-Cl_2 samples annealed in acetone vapor for 1 hour: $PS_{10.1}$-*b*-PPHA-$Cl_{2,\ 5.3}$ (red), $PS_{10.1}$-*b*-PPHA-$Cl_{2,\ 7.9}$ (black)132

Figure 5.9: GPC traces of $PS_{10.1}$-*b*-PPHA-$Cl_{2,\ 7.9}$ before SAXS measurement (solid) and after (dashed). The peak shift towards higher retention volumes indicates depolymerization may have resulted from exposure to X-ray radiation 133

Figure 5.10: MALDI spectra for PAMS homopolymer before (black) and after (red) reaction with NBS as drawn in Scheme 5.11.....138

Figure 5.11: MALDI spectra of brominated PAMS after reaction with KOtBu.139

Figure 5.12: Synthesis of PMAMS homopolymers by anionic polymerization. PMAMS with (A) hydrogen end groups and (B) phenylallyl end groups could be synthesized with good control over molecular weight and dispersity.....141

Figure 5.13. Optical micrographs of PMAMS films after exposure to UV light and annealing at 100°C for 1 minute. All polymer films were loaded with 5% TPS-nonaflate PAG (A) PMAMS-H exposed to 135 mJ/cm^2 (B)) PMAMS-alkene exposed to 135 mJ/cm^2 (C) PMAMS-H exposed to 270 mJ/cm^2 (D) PMAMS-alkene exposed to 1,135 mJ/cm^2. Scale bars = 50 μm 143

Figure 5.14: Thermogravimetric (TGA) data (A) and differential scanning calorimetry (DSC) data (B) for phenylallyl-PMAMS. The heating curve in (B) was the second run in the DSC experiment.....144

Figure 5.15: Plot showing the effect of ring substitution on the degradability of several poly(α-methylstyrene) derivatives. Although not well understood at the time, it is hypothesized that the PMAMS polymer did not depolymerize fully in this experiment due to the presence of minute quantities of airborne organic base in the lab where the exposure and post-apply bake was performed. 145

Figure 5.16: (A) reaction scheme for anionic polymerization of phenylallyl-functionalized PTMSS-*b*-PMAMS. (B) GPC traces for the PTMSS aliquot (red) and product after sequential addition of methoxy α-methylstyrene and 2-phenylallyl bromide (black). 148

Figure 5.17: MALDI spectra before and after deprotection of the terminal alkyne group. The colors correspond to the polymers in Scheme 5.16.....151

Figure 5.18: GPC traces for PMAMS-alkyne (red), PTMSS/PtBuSty-azide (blue), and BCP products after purification with selective solvent washing (black). The colors of the GPC traces correspond to the colors in Scheme 5.17.....152

Figure 5.19: Optical micrographs showing island/hole terracing for (A) PMAMS-*b*-PtBuSty and (B) PMAMS-*b*-PMAMS on different substrates and at various BCP film thicknesses. 155

Figure 5.20: SEM images of perpendicular structures formed by annealing PMAMS-*b*-PTMSS between neutral surfaces at 200°C for 5 minutes. Scale bar = 50 nm 156

Figure 5.21: Acid exposure chamber used for exposing BCP films to either triflic acid or HBr vapor. BCP films are placed inside the chamber in the middle of the image. This chamber can be heated to promote depolymerization.....157

Figure 5.22: SEM images of PMAMS-*b*-PTMSS films after exposure to triflic acid at different temperatures and pressures. In each experiment, thin films were pumped down in the chamber, exposed to acid vapor at the listed temperature and pressure, and then purged using N_2 for 2 minutes. This constituted a single cycle. 158

Figure 6.1: Spectral power output of high pressure Hg light source. 173

Figure 6.2: Cartoon depicting the bias/blur problem with CARs 175

Figure 6.3: (A) The "triangle of death", depicting the relationship between resist sensitivity, resolution, and line edge roughness. (B) Graph that plots the sensitivity of commercially available CARs against LWR measurements. An "exclusion zone" exists in the lower left corner of the plot, which is a demonstration of how difficult it is to design a CAR that prints patterns quickly and with high fidelity. 176

Figure 6.4: Examples of patterns printed in PPHA/PAG blends using DUV and e-beam exposure.[77] 179

Figure 6.5: Examples of novel unzipping polymers developed for this project .183

Figure 6.6: Multiple NMR spectra taken before and after exposing a solution of aromatizing polyester to UV light. The disappearance of the peaks labelled in green and red and the appearance of peaks labelled in blue indicate the polyester is demopolymerizing to form toluene. Furthermore, no photosensitive end cap is require to achieve degradation.....187

Figure 6.7: Dissolution curves for unzipping polymer/Novolak blend at two different PAB temperatures. Starting film thicknesses were between 60 and 70 nm. Films were developed in 2.38% TMAH for 1 min after the PAB.189

Figure 6.8: (A) Contrast curve data for the unzip/Novolak blend after exposure to 248 nm light. Films were exposed to various doses of UV light and developed in 2.38% TMAH for 1 minute after exposure. (B) an optical micrograph of micron-sized features printed in unzip/Novolak using 248 nm light. 190

Figure 6.9: Contrast curve of 25% blend of unzip polymer in Novolak. Samples were exposed to varying doses of EUV radiation (synchrotron source) and developed in TMAH. Credit goes to Ryan Mesch for generating this data.[233] 191

Figure 6.10: (A) E-beam contrast curves for PMMA and a 15% unzip/Novolak blend. The PMMA film was baked at 180°C for 2 mins prior to exposure and was developed in 1:3 MIBK:IPA for 1 min. The unzip/Novolak blend was baked at 95°C for 1 min prior to exposure and developed in 2.38% TMAH for 1 min. (B) 100 nm line/space patterns printed in the unzip/Novolak resist. 193

Figure 6.11: (A) Contrast curves for 20% unzip/Novolak blends baked at different PAB temperatures for 1 minute. (B) 100 nm line/space patterns imaged in samples that were post-apply baked at 80 and 110°C. 197

Figure 6.12: Thermogravimetric analysis (TGA) data for aromatizing polyester. Heating was performed under nitrogen atmosphere. 198

Figure 6.13: Optical micrograph of developed 1 μm features in unzip/Novolak after a PEB at 120°C for 5 min. In the dark background region, the unzip/Novolak has been completely developed away. The dose matrix increases going from left to right and top to bottom; the features that received the largest dose are crosslinked and retained full film thickness after development. Scale bar = 10 μm. 199

Figure 6.14: (A) Contrast curves for 15% unzip/Novolak blends containing unzip polymers with different molecular weights (B)) 100 nm line/space patterns imaged in samples that contained 7.0 kDa unzip polymer (red) and 2.5 kDa unzip polymer (blue). 200

Figure 6.15: SEM micrographs of 100 nm lines and spaces patterned in 15% unzip/Novolak and unzip/PNBHFA blends. The dose-to-clear under each image represent the amount of dose required to completely develop 2:1 aspect ratio features. 202

Figure 6.16: Contrast curves for two 15% unzip/PNBHFA blends developed using TMAH solutions with different concentrations. The contrast curve for a 15% unzip/Novolak blend is plotted for reference. 203

Figure 6.17: (A) Amount of polymer film etched plotted versus time for thermal oxide, PMMA, i-line resist (15% DNQ in Novolak), 15% unzip/Novolak, and 15% unzip/PNHFA blends. Films were exposed to CF_4/CHF_3 plasma chemistry, a common recipe for etching dielectric materials. Transient etch behavior can be seen in the first few seconds of etching the unzip blends. (B) Selectivity data for each of the resists studied. The selectivity is calculated by normalizing the steady-state etch rate of each resist to the steady-state etch rate of thermal oxide 204

Figure 6.18: CD-SEM images of 1:1, 100 nm (half-pitch) line/space gratings patterned in PMMA, ZEP, 15% unzip/Novolak, and 15% unzip/PNBHFA blends. The D_0 value represents the dose required to completely clear the resist film and achieve symmetric lines and spaces. The image contrast is inverted for the PMMA/ZEP samples because these resists were processed on bare wafer, whereas the unzip blends were processes on a BARC film. For clarity, the “line” feature in each image is marked by a yellow “L”. 206

Figure 6.19: A typical plot of PSD curves for line width roughness (LWR), line edge roughness (LER), and pattern placement roughness (PPR). σ^2 can be estimated by integrating the area under the curve. The unbiased roughness can be calculated by subtracting out the roughness corresponding to high frequency noise. The correlation length (ζ) can be estimated by the formula $f = 1/2\pi\zeta$, where f represents the frequency at the "knee" of the curve. 208

Figure 6.20: Column graph with LWR correlation length and dose-to-clear for each resist tested in the roughness study. Notably, the unzip formulations are approximately as sensitive as (or even more sensitive than) ZEP without having significantly larger correlation length values.....209

Figure 6.21: Typical pattern design for EBL experiments. The large cross makes the exposure field much easier to find after patterning. The region boxed in red corresponds to the 1 μm line/space dose matrix used to generate contrast curves. The region boxed in blue corresponds to the 100 nm line/space dose matrix used for LWR analysis.....213

List of Illustrations

Scheme 4.1: Different synthetic routes for making hydroxyl-terminated polymers. Both anionic and controlled free-radical polymerization can produce polymers with controlled molecular weights and compositions. 81

Scheme 4.2: Synthesis of phenyl allyl ethers. 91

Scheme 4.3: Synthesis of poly(styrene-*r*-divinylbenzene) brushes 92

Scheme 5.1: Typical PPHA polymerization using the benzyl alcohol/NaH initiator system 118

Scheme 5.2: PS-*b*-PPHA synthesis using PS-OH as a macroinitiator. 120

Scheme 5.3: Synthesis of 4,5-dichlorophthalaldehyde 123

Scheme 5.4: Synthesis of PPHA-Cl_2 using the P_2-t-Bu/benzyl alcohol system .. 124

Scheme 5.5: PS-*b*-PPHA-Cl_2 synthesis using PS-OH as a macroinitiator. 125

Scheme 5.6: Possible synthetic route to PS-*b*-PPHA-Cl_2 using PPHA-Cl_2 as a macroinitiator. 127

Scheme 5.7: PS-*b*-PPHA-Cl_2 synthesis using amine-isothiocyanate coupling chemistry. 129

Scheme 5.8: Depolymerization of the PPHA-Cl_2 block using trifluoroacetic acid 130

Scheme 5.9: Ito's observation that only poly(hydroxyl α-methylstyrene) made by cationic polymerization could be degraded using strong acid catalyst.[202] 136

Scheme 5.10: Typical anionic polymerization of methoxy α-methylstyrene. PMAMS terminated with a hydrogen atom behaves as a stable polymer. 137

Scheme 5.11: Synthesis of alkene-terminated poly(α-methylstyrene) by bromine substitution and subsequent elimination. 138

Scheme 5.12: Synthesis of 2-phenylallyl bromide.....140

Scheme 5.13: Attempted synthesis of PTMSS-b-PMAMS by sequential anionic polymerization. Initiating the PMAMS block from a styryl anion largely failed due to the instability of the propagating tertiary anion. 147

Scheme 5.14: Synthesis of azide-terminated blocks for "click" chemistry 149

Scheme 5.15: Synthesis of end cap for PMAMS polymerization than includes both terminal alkyne and phenyl allyl moieties. 149

Scheme 5.16: Deprotection of terminal alkyne group using TBAF.....150

Scheme 5.17: Synthesis of PMAMS BCPs using Cu(I)-catalyzed azide-alkyne click chemistry.....152

Scheme 6.1: Reaction scheme for the conversion of diazonaphthoquinone (DNQ) to indene carboxylic acid 174

Scheme 6.2: Overall synthesis of the (A) monomer and (B) aromatizing polyester185

Chapter 1: Introduction to High Resolution Lithography

1.1 A Brief History of Microelectronics

The first computers were not machines; rather, they were human beings who specialized in mathematics and worked in parallel to perform difficult engineering calculations. Human computers frequently solved problems in the fields of fluid dynamics[1] and space flight[2] before the end of World War II. Naturally, they also built the electronic computers that would ultimately replace them. One of the first was the Electronic Numerical Integrator and Computer (ENIAC),[3,4] a massive machine that consisted of thousands of vacuum tubes, crystal diodes, relays, resistors, and capacitors all soldered together by hand. While it could perform up to 5000 arithmetic operations per second, the near-constant failure of vacuum tubes left the computer inoperative 50% of the time. When it was available for calculations, the ENIAC consumed 150-175 kW of electricity, reportedly dimming the lights in Philadelphia when it was turned on.[5] Reflecting on the shortcomings of the ENIAC, Bell Labs engineer J. R. Pierce declared, "Nature abhors the vacuum tube".[6] Although it was an important demonstration that electronic computers were powerful tools for computation, it was clear that cheaper and more reliable components would be needed to build better machines.

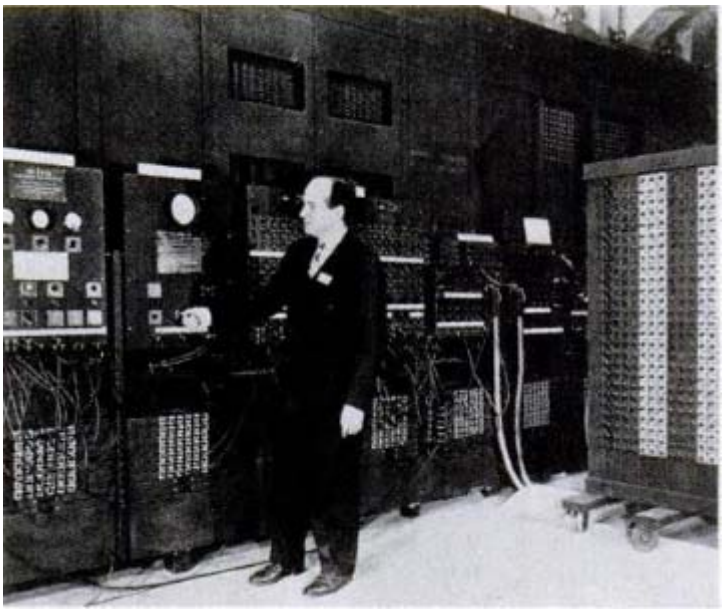

Figure 1.1: The ENIAC, one of the world's first electronic computers. Technicians worked constantly to find and replace broken vacuum tubes.

Vacuum tubes function by "boiling off" electrons from a hot filament to establish current flow; thus, they require constant heating during operation. A much more efficient electronic switch, the transistor, was discovered by John Bardeen and Walter Brattain in 1947 as a result of their experiments with germanium crystals.[7] The first transistor design was bulky and almost unrecognizable by today's standards; nevertheless, their invention was revolutionary, and Bardeen and Brattain shared the 1956 Nobel Prize in Physics with William Shockley "for their researches on semiconductors and their discovery of the transistor effect".

Figure 1.2: A replica of Bardeen and Brattain's original point-contact transistor.[8]

With the invention of the bipolar junction transistor in 1948,[9] electronic computers could be made using smaller, discrete components that consumed far less power and operated more reliably. The first computer built entirely using transistors was the Harwell CADET,[10] constructed in 1955. While it was certainly an improvement over vacuum tube technology, the size of the circuit elements set a limit on how densely circuits could be arranged. Only so many logic structures can be incorporated on the same device before manufacturing became unwieldy.

This paradigm changed in 1958, when Jack Kilby and Robert Noyce independently invented the first integrated circuits.[11] The demonstration of this technology meant that, for the first time, transistors could be patterned directly into semiconducting materials to create monolithic electronic circuits. Not only did this make

devices more mechanically stable, electronic components like resistors, capacitors, and conducting wires could be patterned simultaneously instead of installing discrete components by hand. In addition, manufacturing costs could be decreased dramatically by patterning more and more features at the same time.

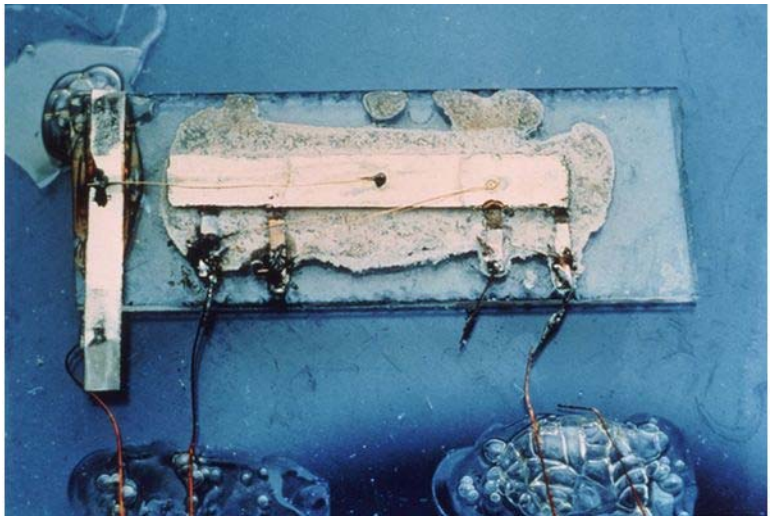

Figure 1.3: Jack Kilby's original integrated circuit.[12]

One of the first computers to rely on integrated circuits was the Apollo Guidance Computer (AGC),[13] designed in 1966 by the MIT Instrumentation Laboratory. Although it had no more computing power than a modern handheld calculator, it provided all of the electronic interfaces for guiding, navigating, and controlling all of the command and lunar modules used for the Apollo program. Figure 1.4 is an image of the NOR gate ICs used in the AGC design, which were supplied by Fairchild Semiconductor. The 2x3 array of components in the middle of the chip are individual transistors.

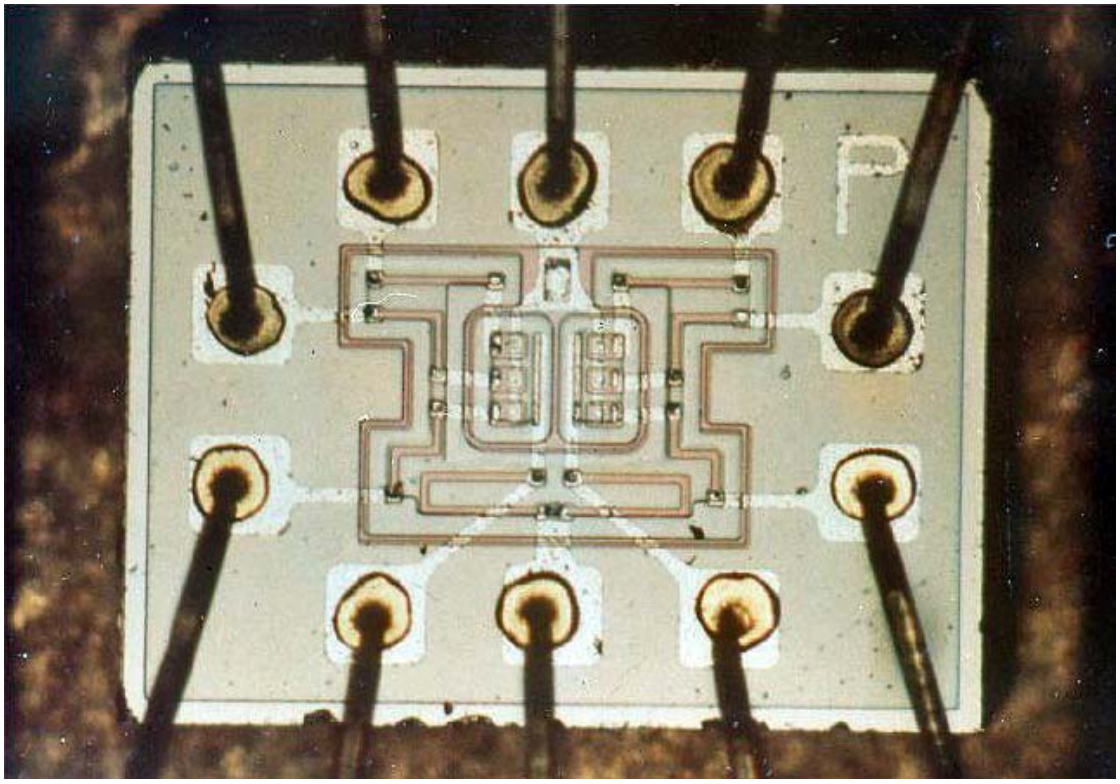

Figure 1.4: A NOR gate built from a 2x3 array of integrated transistors (center). Thousands of these chips provided computational power for the Apollo Guidance Computer.[14]

In 1965, determined to convince the world that integrated circuits were the future of electronics, Gordon Moore wrote a highly influential paper,[15] which made a profound but simple prediction: the number of transistors incorporated in microelectronic devices would double approximately every one-two years. Since that time, "Moore's Law" has become a self-fulfilling prophecy, endlessly driving the microelectronics industry towards smaller circuit features and more densely-packed chip designs. Modern ICs incorporate billions of transistors per die in a complex, three-dimensional architecture.

Each layer of wiring, starting with the transistors at the bottom, must be patterned precisely such that it is aligned and electrically connected to the layers above. For every layer in the device, the information about the location and size of each circuit feature is transferred into the wafer via a process known as photolithography.

1.2 Optical Lithography

Photolithography is the primary technological tool for defining the complex circuit patterns in semiconductor devices.[16] At the most fundamental level, photolithography processes use light to transmit information from a master pattern (called the photomask) into a substrate (called the photoresist) to create a three-dimensional relief image of the mater pattern. Transferring the relief image into the underlying substrate involves either etching or deposition to create monolithic device features. Layer by layer, this overall process is repeated many times to build an integrated circuit.

The communication of information from the photomask to the photoresist is not straightforward. For projection lithography, an incredibly complex lens system collects the diffracted light produced by the mask and redirects it to form an image at the substrate. This aerial image is imposed on a photosensitive polymer resist,[17] which reacts with light to form a latent chemical image. Depending on the photochemistry of the resist, the exposed areas are rendered either more or less soluble in a developer solution. Positive tone resists become more soluble in developer after irradiation, while negative tone resists become less soluble. Developing the resist film produces the final relief

image replica of the master pattern that is then transferred into the substrate. This process can be seen clearly in Figure 1.5.

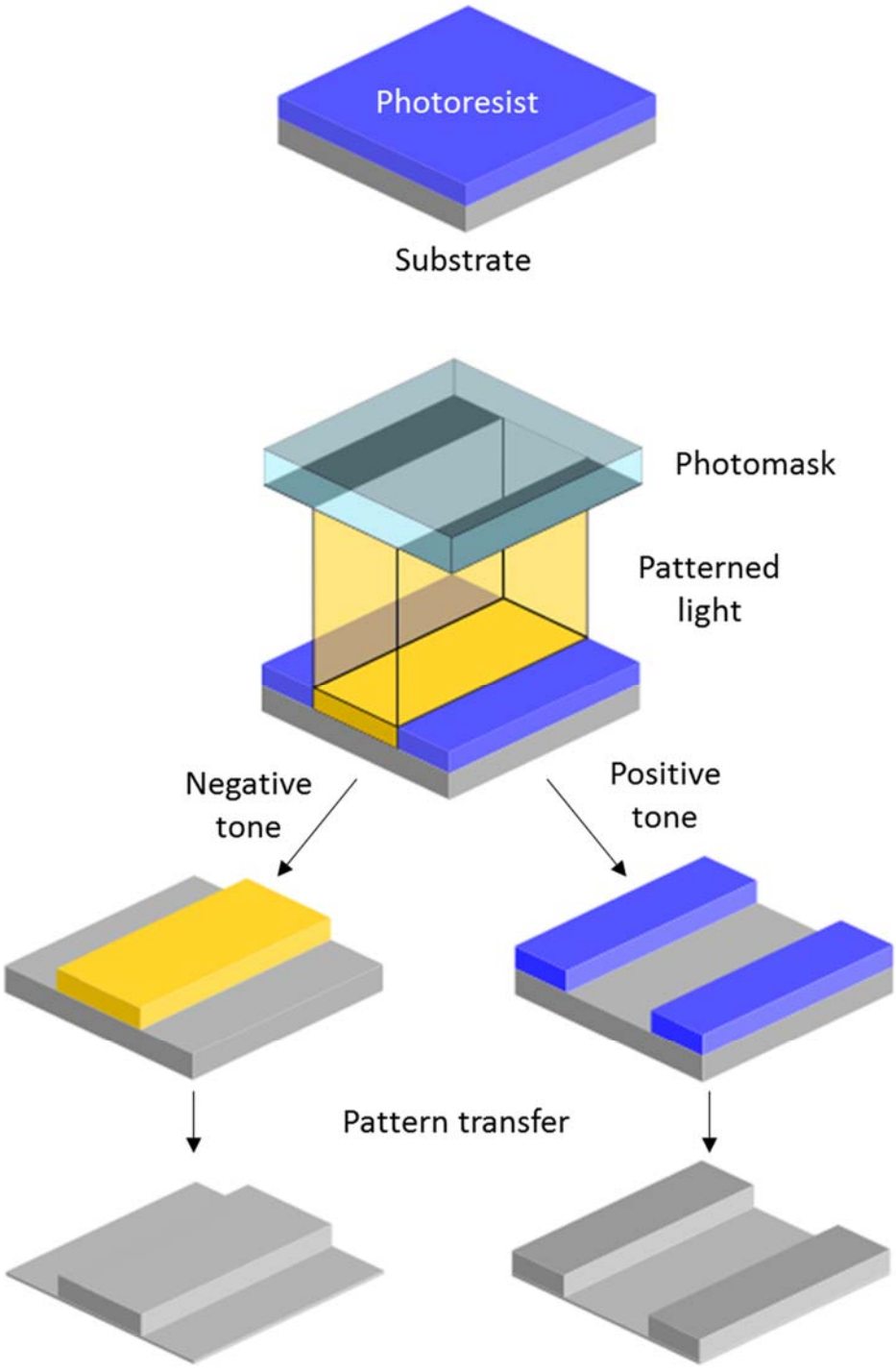

Figure 1.5: Cartoon schematic of photolithography process, including pattern transfer.

In the early days of lithography, contact printing was used to make circuit features with minimum dimensions on the order of tens of microns. To print these features, the mask was placed in direct contact with photoresist film and irradiated with light. Although contact printing reproduced mask patterns with high fidelity, the lifetime of the masks suffered from contamination issues as a result of direct contact with the photoresist films.[18] This process was ultimately abandoned in favor of proximity printing, in which a carefully-controlled micron-sized gap was held between the wafer and photomask during exposure. This gap solved much of the contamination issue, but introduced near-field diffraction that limited imaging resolution. Although the mask was less likely to collect debris from the photoresist, particles from the air could not be prevented from landing on the surface of the mask, which still limited their manufacturing lifespan.

Because both of these systems required 1:1 mask features and could not be protected from contamination, projection lithography tools were eventually developed that would allow mask makers to fabricate 4:1 mask features that were minimized using 4x reduction imaging.[19] Thin membranes, known as pellicles, were also invented that prevented dust and debris from landing on the mask, greatly improving their lifetime.[20]

1.3 Minimum Resolution

The minimum resolution for a projection lithography process is determined by the limitations of diffraction. As light passes through narrow spaces in a photomask, plane waves of light near feature edges spread out and away from the surface. To reproduce the original image, the diffracted light must be collected by an optical system that refocuses

the image on the wafer. Because the objective lens can only have a finite size, it cannot capture all of the light that is diffracted from the mask pattern; thus, some of the original information contained in the mask is lost.[16]

In the far field diffraction limit, a 1:1 line/space grating produces a sinusoidal aerial image at the wafer. Forming this interference pattern requires at least two diffraction orders to be collected by the objective lens. For the example of a diffraction grating, Rayleigh's law (Equation 1.1) limits the minimum pitch of two points on the line/space pattern before printing an image becomes impossible.

$$R = \frac{k_1 \lambda}{NA} \tag{1.1}$$

where R is the minimum half-pitch resolution, λ is the wavelength of light, NA is the numerical aperture of the lens, and k_1 is a lumped coefficient that accounts for additional process conditions which improve resolution (off-axis illumination, phase-shift masks, etc.). With the introduction of immersion lithography in 2008, λ and NA have been fixed at 193 nm and 1.35, respectively. Off-axis, dipole illumination, and other optical tricks for improving the aerial image have reduced k_1 to a minimum value of 0.3. This puts a hard resolution limit of about 40 nm half pitch on current lithographic processes.

1.4 Optical Lithography Beyond 193 nm Immersion

Anticipating the need to continue scaling down feature sizes, the lithography community has pursued 157 nm and 13.5 nm light sources for next-generation patterning

tools. Both of these technologies have proven extremely difficult to implement in manufacturing for the reasons enumerated below.

Like 248 and 193 nm, 157 nm lithography was explored because that is the characteristic emission wavelength of an excimer laser (F_2).[21] Many materials are not transparent at 157 nm, including organic polymers and the fused silica used to make lenses and photomasks. Therefore, new materials were required for all optical elements, including the photoresist. Although it was nearly impossible to find a resist material that was completely transparent, several fluorinated polymer structures were identified that provided reasonable performance.[22] CaF_2 was identified as a replacement for the fused silica used in 193 nm optics, as the transmission of CaF_2 at 157 nm is greater than 99%.[23] The two biggest problems that ultimately proved fatal for this technology were the lack of a suitable pellicle material and the intrinsic birefringence of CaF_2.

Polymeric pellicles were desired that were completely transparent to 157 nm light. Unfortunately, 157 nm photons have enough energy to break almost any organic bond, which leads to photodarkening upon exposure and a loss of transparency.[24] Soft pellicles had maximum lifetimes of about 100 wafers before they had to be replaced.[25] Although this was a major technical issue, the real nail-in-the-coffin for 157 nm was the undesirable material properties of CaF_2. The intrinsic birefringence of CaF_2 was first identified in 2001 by John Burnett at the National Institute of Standards and Technology (NIST).[26] In his 2001 paper on the properties of CaF_2 and BaF_2, he reported that the birefringence of these materials was negligible at wavelengths greater than 200 nm, but increased by nearly an order of magnitude near 157 nm. Several solutions to this problem

were proposed, including carefully controlling the crystallographic orientation of the CaF_2 used in the lenses, but the cost and complexity of designing the optics was ultimately prohibitive. Two years after Burnett's paper was published, 157 nm lithography was dead.[27]

After declaring their intention to abandon 157 nm technology, Intel decided to extend the lifetime of 193 nm exposure tools while simultaneously pursuing extreme ultraviolet (EUV) lithography.[27] At the time, EUV faced enormous technological challenges, and many were skeptical or even angry about the decision to abandon the worldwide effort to realize 157 nm lithography. At the inaugural International EUV Symposium in 2002, Intel claimed that EUV would probably be ready for manufacturing in 2007, and announced a per-scanner target cost of approximately $20 million. Upon hearing this information, one symposium participant reportedly said that he was, "surprised the audience didn't break out laughing, it was so unrealistic."[28] In 2017, EUV scanners are still not yet manufacturing-ready, and reported tool costs are already close to $100 million.[29]

Figure 1.6: An EUV lithography system manufactured by ASML.

Unlike 248 nm and 193 nm lithography, EUV lithography does not have a high power light source. Instead, it was designed around the observation that X-ray mirrors can be made from deposition of alternating layers of molybdenum and silicon. Reflection enables projection printing with reduction optics; however, each mirror only reflects 65% of incident photons, so an extremely "bright" X-ray source is required for high throughput. Short of a miniaturized synchrotron,[30] no light source has been identified that is capable of meeting throughput requirements for high-volume manufacturing. In addition, because defects buried within the MoSi multilayers cannot be repaired, mirrors

must be made flawlessly; otherwise, the entire circuit design must be adjusted to accommodate even a single aberration. As of 2017, a perfect mirror for EUV lithography has yet to be made.

Figure 1.7: A photograph of a MoSi multilayer mirror used for EUV lithography.

Many other challenges make EUV prohibitively expensive for manufacturing, including the design of new pellicles[31] and metrology systems for inspecting mask blanks.[32] Photoresist materials are not currently considered a gating challenge for the successful implementation of EUV; however, current resist designs are fundamentally

limited at the minimum resolution of EUV tools. Chapter 6 discusses a new type of resist design that could be used in the future to overcome these limitations.

1.5 Other High Resolution Patterning Techniques

1.5.1 Electron Beam Lithography (EBL)

No matter how sophisticated photolithography becomes, it is inherently limited to printing only the information contained in the photomask. To initialize the printed pattern, a method of directly writing the circuit layout must first be established. Before writing tools were invented, circuit layouts were drawn by hand on films like Rubylith and pasted to a drafting board. The large circuit pattern was photographed and reduced such that the resulting image printed 1:1 circuit features. In the 1960's, SEMs were modified with controllers that could deflect and "blank" the electron beam to create patterns. Since then, dedicated e-beam write tools have been developed for both high resolution and high throughput applications.[33] Here, the advantages and disadvantages of electron beam lithography will be discussed in comparison to optical lithography.

The most notable advantage of electron beam lithography is its resolution capabilities. Because the de Broglie wavelength of an electron (5.5 pm at 50 keV and 3.8 pm at 100 keV) is so much smaller than that of UV photons, the e-beam diameter for sophisticated Gaussian beam tools can be smaller than 2 Å. These tools are somewhat limited, however, because they must address the wafer one pixel at a time. Some applications, such as photomask fabrication, do not need such small pattern sizes and instead require greater throughput for manufacturing. To meet the needs of the

semiconductor industry, shaped beam or vector scan tools were developed for faster scanning over larger field sizes. As the name implies, the beam shape is fixed to a certain geometry consisting of tens or even hundreds of pixels, and in some tools, the shape of the beam can be adjusted depending on the geometry of the required pattern. Patterns for electron beam lithography are written in CAD software. Recently, new tools have become available that make the pattern design process easy by parameterizing cells most commonly found in microelectronic devices.[34]

A typical direct-write EBL tool (Figure 1.8) consists of an emission gun from which electrons are extracted and accelerated through a column. In the column, electromagnetic plates manipulate the beam size and shape to focus it onto the substrate.

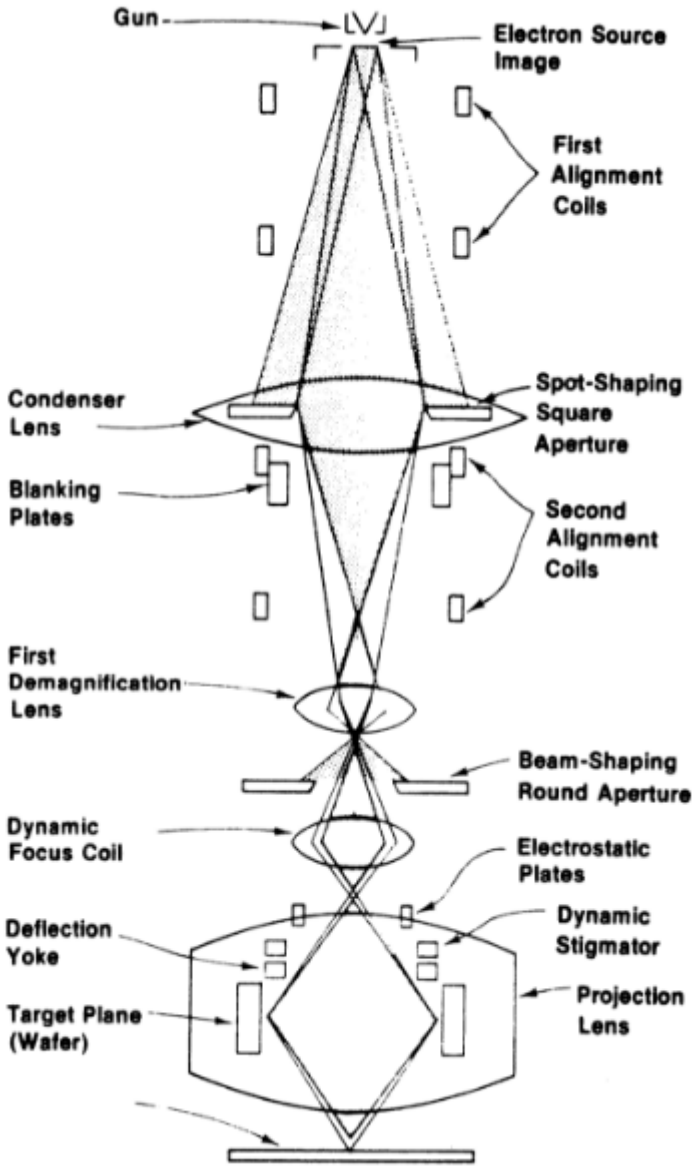

Figure 1.8: Vertical layout of typical shaped e-beam tool.[35]

Unlike photons, electrons are charged particles, meaning they repel each other and cannot be focused to an infinitely small point. This is a fundamental problem that limits the resolution of all EBL tools. In addition, electrons scatter as they interact with

the resist (forward scattering) and the underlying substrate (backscattering) (Figure 1.9).[36] The amount of each type depends on the accelerating voltage being used, but both types degrade the quality of the latent image. Forward scattering results in beam spreading as electrons initially travel through the resist. Line widths are enlarged as a result, and this effect is magnified at lower accelerating voltages, when electrons have a greater chance of interacting with the atoms in the resist. Backscattering is caused by electrons reflecting from atoms deep inside the substrate and re-exposing the resist, sometimes microns away from the original exposure. The effect of backscattering is greater at higher accelerating voltages and greatly depends on the feature density of the pattern being printed. For most device-related structures, proximity correction software must be used to compensate for this effect.

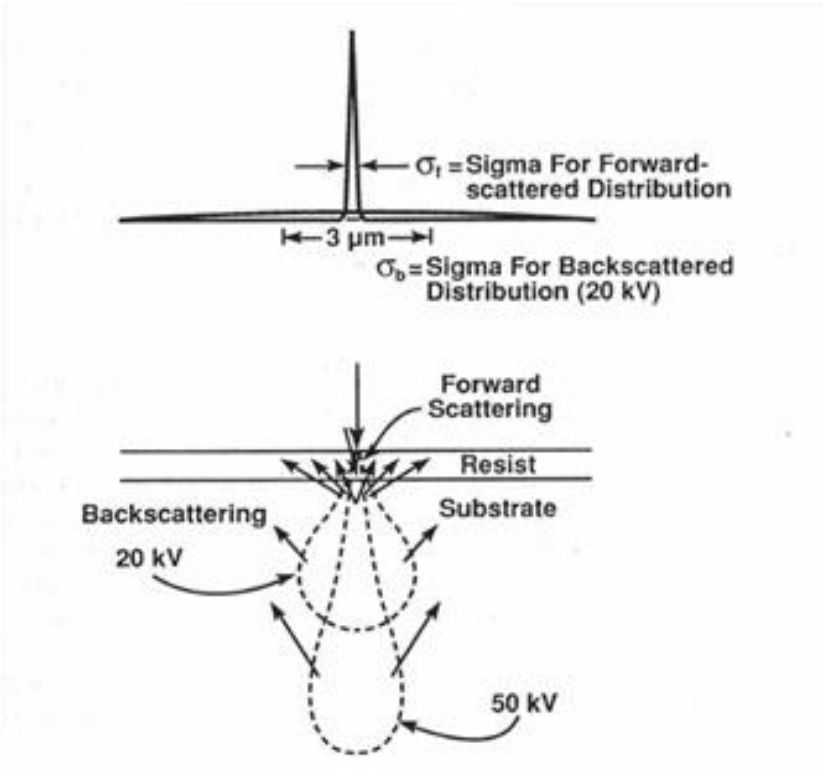

Figure 1.9: A depiction of forward and backscattering phenomena which occur when high energy electrons interact with the resist and substrate.

Because EBL is a serial process, the primary trade-off for high resolution is low throughput. Even with variable shape beams, writing a complete photomask can take more than 24 hours. During this time, beam instabilities can lead to patterning errors and focus drift. In addition, because tools can only pattern a certain field size before the wafer has to be moved to a new location, stitching errors can occur where two fields meet. During long exposures, tools must periodically pause and recalibrate to ensure faithful reproduction of the designed pattern.

As lithographic processes move towards model-based OPC[37] and "inverse lithography",[38] defining sub-resolution mask patterns of arbitrary shape and size will become increasingly important. Mask manufacturers will be required to improve the reliability and throughput of their EBL write processes to continue being profitable. However, direct write EBL systems will continue to be the foundation of photomask patterning for decades to come.

1.5.2 Nanoimprint Lithography (NIL)

NIL is a direct contact lithography process which uses the topography of a pre-patterned template to mechanically stamp features in an organic resist. Because the relief image in the resist is created by physical contact, the minimum achievable feature size for NIL is only limited by the resolution of the process used to pattern the template. For example, the height profile of a single-walled carbon nanotube can be transferred into a polymeric resist using this technique.[39] Figure 1.10 plots minimum achievable resolution versus throughput for available lithography techniques. NIL breaks the paradigm of trade-offs between accessing small feature sizes and generating patterns quickly.[40]

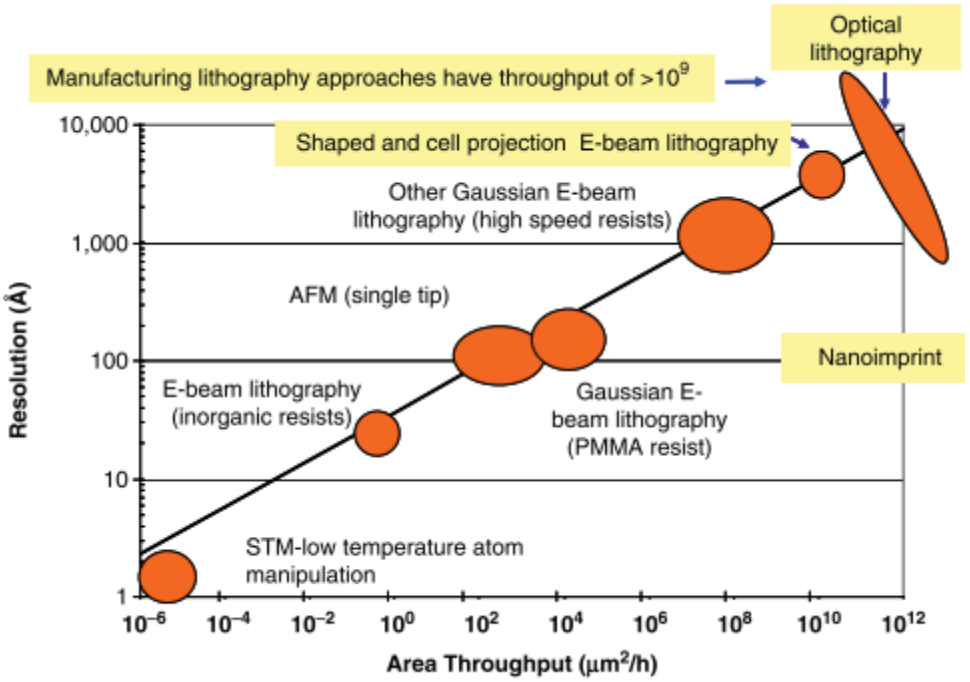

Figure 1.10: Plot of resolution versus area throughput for various lithography techniques. Reproduced with permission from Sreenivasan, S.V. *et al*. *MRS Bull.* **2008**, *33*, 854–863. Copyright 2008 Materials Research Society.

There are several variations of NIL; two of the most popular are thermal NIL and UV-NIL. Thermal NIL was first demonstrated by Chou et al[41] to fabricate 25 nm holes in a pre-casted PMMA film. UV-NIL instead starts with a photopolymerizable monomer which can be cured after filling in the template and photocuring with UV light. Step-and-flash imprint lithography (S-FIL) was developed at the University of Texas as a step-and-repeat variant of UV-NIL.[42] The S-FIL process can be seen in Figure 1.11.

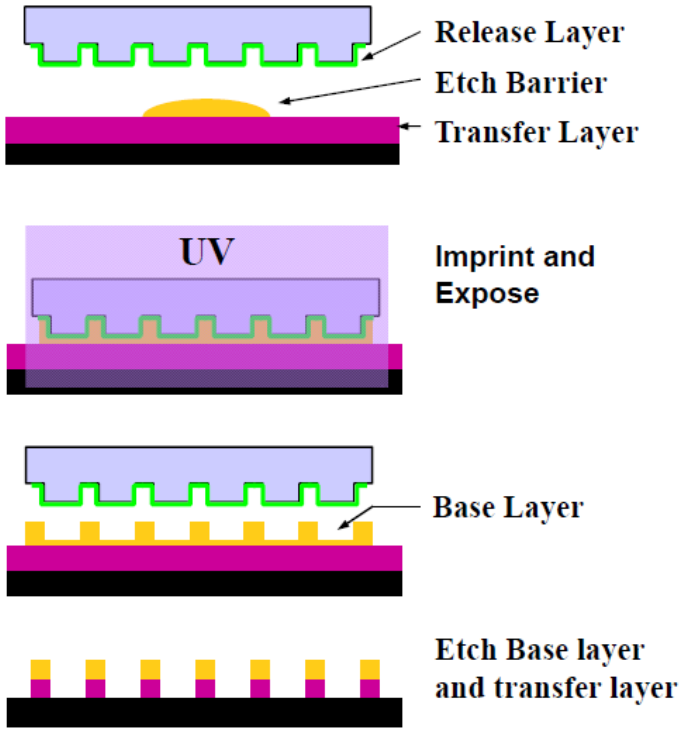

Figure 1.11: The S-FIL process flow for generating nanoscale features.

While NIL can achieve significantly better resolution than optical lithography, several technical challenges have prevented its widespread adoption in the semiconductor industry. The lifetime of an S-FIL template depends on how well particle contamination is controlled. The template can easily become fouled with polymeric debris if the interfacial interactions between the resist and template are not controlled during the separation process. Because the template must be perfectly planar with the substrate to ensure uniform patterning, even one particle on the surface can cause failure. Manufacturers have gone to great lengths to remove any sources of particle contamination from commercial S-FIL systems, including in-line filtration systems for

the NIL resist as well as special coatings and pre-treatments for mechanical parts to reduce particle generation. Other issues with NIL, including alignment, throughput, and partial field imprinting have been largely solved. Since NIL is a 1:1 patterning process, some argue that fabricating the template via electron beam lithography poses significant challenges at very high resolutions. However, photomasks used in optical lithography incorporate sub-resolution assist features to improve the aerial image, which also require high-resolution e-beam patterning.

1.5.3 Block Copolymer Lithography

Block copolymer (BCP) self-assembly has gained significant attention in a wide variety of fields including lithography[43], nanofiltration[44], and electrolyte membranes[44,45]. In thin films, BCPs can self-assemble into different morphologies with feature sizes on the order of several to hundreds of nanometers[46]. The self-assembled patterns and morphologies can be used to template nanoparticle growth[47] and surface functionalization[48], or to transfer patterns into an underlying substrate[49,50].

BCPs are especially well-suited for lithography because they combine large-area patterning capability with the critical reduction in feature size that is difficult to achieve with photolithography alone due to diffraction phenomena. Perhaps the most promising future applications for BCP patterning are the production of next-generation storage media[51], FinFET architectures[52], and contact holes for current integrated circuit designs[53]. Directed self-assembly integrates well with current 193 nm immersion processes and does not require new equipment or tools to achieve high resolution patterning. However,

BCP lithography still has many challenges to overcome before it can be implemented in commercial manufacturing.

One of these challenges is the alignment of BCP domains in thin films. Rather than forming ordered arrays of lines and spaces, BCP patterns (both perpendicular lamellae and parallel cylinders) tend to look like fingerprints in thin films as a result of BCP confinement. These patterns can be seen in Figure 1.12.

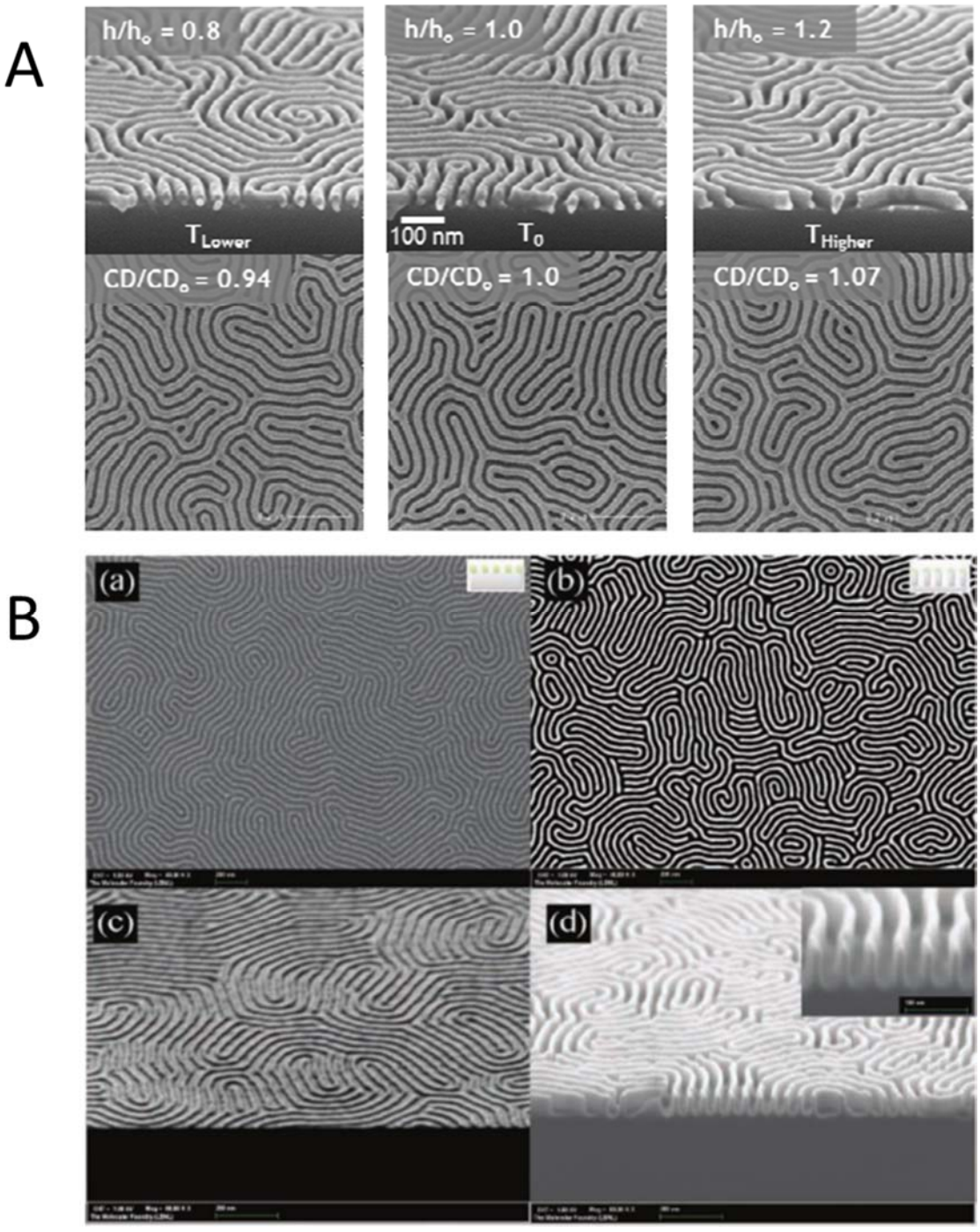

Figure 1.12: Block copolymer fingerprint patterns. (A) Lamellae-forming PS-*b*-PMMA[54] (B) parallel PS-*b*-P2VP cylinders etched into silicon.[55]

High-resolution lithography requires strict tolerances for pattern placement and overlay error to achieve acceptable manufacturing yields. Fingerprint patterns cannot be aligned with features underneath the BCP film, so controlling the alignment of BCP domains is a key prerequisite to their use in semiconductor manufacturing. Directed self-assembly (DSA) must be used to spatially control the placement of BCP domains. Most DSA processes begin by patterning the substrate with sparse chemical[56] or topographical[57] guiding features. This pre-patterning can be accomplished by a number of lithography technologies, including optical-, electron beam-, or nanoimprint lithography. Annealing a BCP film on top of the guiding features induces BCP domains to align in a preferential direction. By carefully tailoring the dimensions and surface chemistry of the guiding pattern, an overlying BCP film can be made to replicate many device-relevant features[58–60] with low pattern registration error.[61]

Because DSA requires a pre-patterning step, the BCP must somehow improve the pre-pattern to justify its fabrication cost. One of the central arguments for DSA stems from the fact that BCPs are capable of increasing both the density and resolution of the guiding pattern. This is demonstrated more clearly in Figure 1.13. In addition, DSA processes can repair defects and misplaced features from the initial lithography step[62,63] (Figure 1.14). This becomes increasingly important as lithography tools are forced to operate close to their resolution limits.

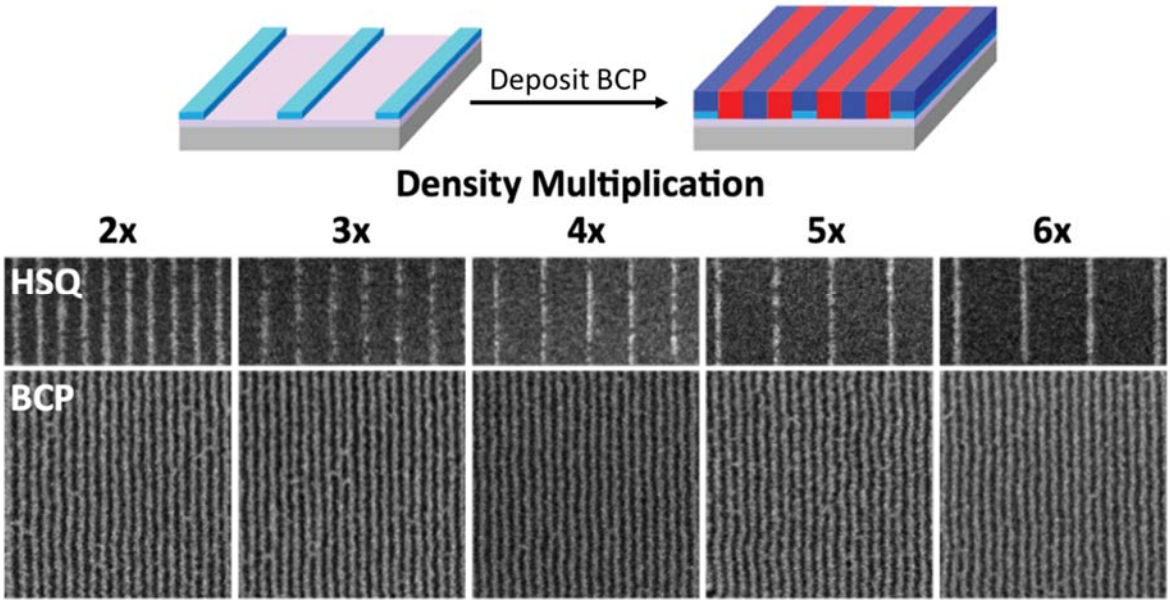

Figure 1.13: Density multiplication of sparse HSQ guide lines patterned by electron beam lithography.[64]

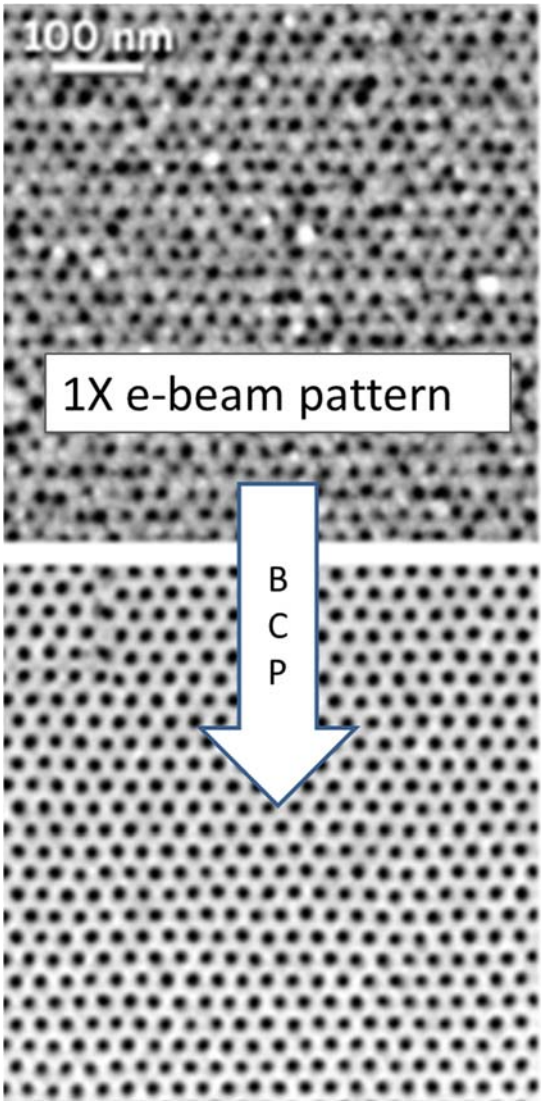

Figure 1.14: SEM images of DSA process where assembling a BCP film on top of a poor pre-pattern can repair defects and improve feature size uniformity.[62]

BCPs must also integrate well with current manufacturing processes to be a viable nanopatterning alternative. In addition to forming small structures, using thermal annealing to achieve perpendicular features is preferable to solvent annealing. Imparting

inherent etch resistance between the two blocks also improves subsequent pattern transfer processes. To address these requirements, the Willson group has designed a family of silicon-containing, high-χ BCPs that can access 5 nm half-pitch feature sizes with intrinsic etch resistance between the two blocks. A full description of these materials can be found in Chapter 2.

Chapter 2: Materials for High Resolution Lithography

The goal of this chapter is to provide a brief overview of photoresist and BCP material design. The limitations of materials used in lithography processes today are identified and, where appropriate, specific chapters in this dissertation are referenced that describe new materials capable of improving on current designs.

2.1 PHOTORESIST DESIGN

Novel polymer resists are always required to meet the specific challenges associated with patterning at different wavelengths of light. All photoresists must serve two functions: they must change solubility upon exposure to radiation, and they must "resist" some harsh etching process that can be used to transfer the relief image into the exposed substrate.

2.1.1 Negative-tone Resists

Some of the earliest resists used for photolithography were negative-tone resists that crosslinked upon exposure to light.[65] The first lithograph was made by Nicéphore Niépce in 1839 using Bitumen of Judea, a tar-like residue containing non-volatile petroleum compounds.[66] Bitumen of Judea hardens with prolonged exposure to sunlight, but unexposed regions can be washed away using oil of lavender. The potential of the lithographic process was demonstrated when Niépce produced a grayscale image of his French courtyard after 8 hours of exposure on a sunny afternoon.

From these humble beginnings, photoresist technology evolved through several generations of negative-tone materials, including gelatin dichromate,[67]

poly(vinylcinnamate),[68,69] and KTFR,[70] a bisazide/rubber blend that dominated the photoresist market for 15 years. As feature sizes continued decreasing, however, a fundamental flaw with these negative tone resists was discovered: a phenomena known as "snaking", which results from polymer features swelling during development (Figure 2.1).

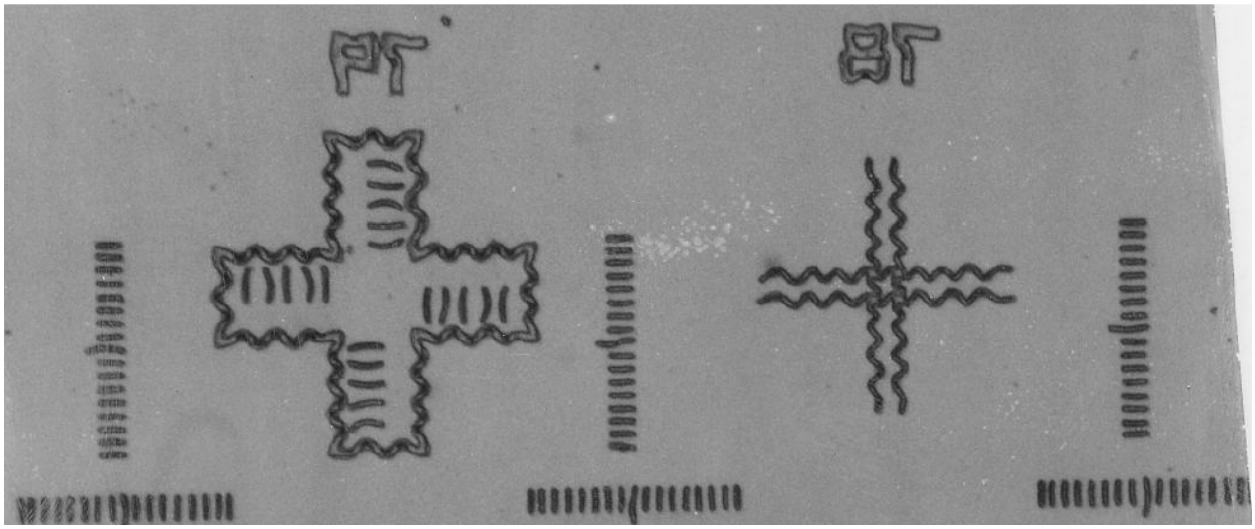

Figure 2.1: "Snaking" that results from polymer features swelling in the development solvent.[71]

Feature irregularity due to this wiggling made accurate pattern placement impossible and forced lithographers to search for a new type of photosensitive polymer. Ideally, the resist would not switch solubility by changing molecular weight; rather, solubility should be modified by changing the chemical structure of the resist, such that the unexposed polymer regions would be completely insoluble in the developer to avoid swelling.

2.1.2 DNQ/Novolak

The solution to this problem was eventually identified by Oskar Süβ, a German chemist at the Kalle company in the 1940's. While developing new materials for blueprint papers, he realized the photochemical potential of diazo compounds for lithography. Süβ observed that blends of diazonaphthoquinone (DNQ) and a tacky resin called Novolak were slow to dissolve in basic solution until they were exposed to UV light. It was immediately recognized that the DNQ acted as a photoswitchable dissolution inhibitor for Novolak. This behavior was the key to formulating the first positive tone resists that did not swell in developer, since the unexposed regions of the film were completely insoluble in aqueous base.

DNQ/Novolak resists were successful in part because of their high contrast, resolution, and etch resistance. Their contrast stems from the fact that the photoproduct of DNQ, indene carboxylic acid, actually accelerates the rate of development of Novolak in areas exposed to light. This effect can be seen in the Meyerhoffer plot[72] in Figure 2.1. Resist formulations with higher loadings of unexposed DNQ decrease the dissolution rate possibly due to hydrogen bonding between the two components.[73] The indene carboxylic acid produced after exposure is soluble in base.

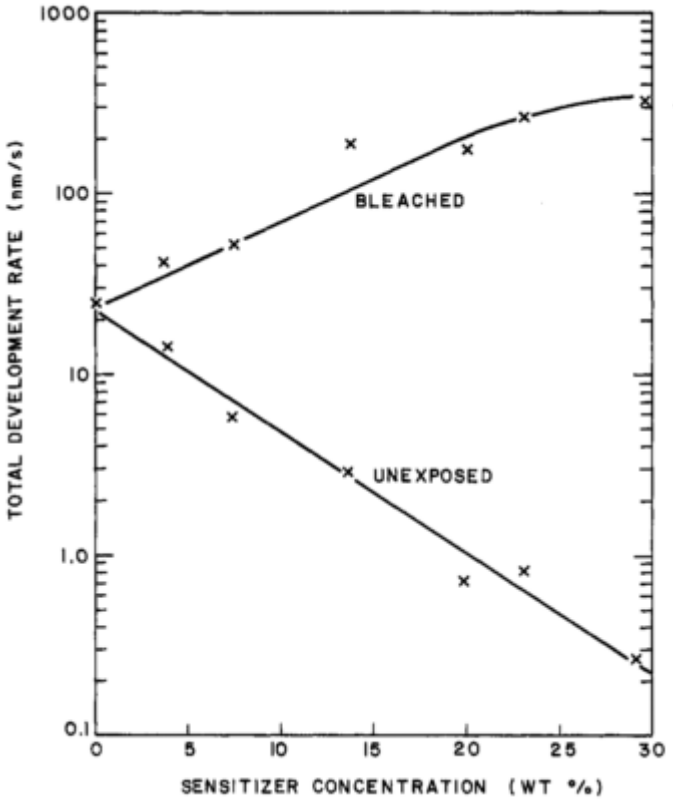

Figure 2.2: The Meyerhofer plot for DNQ/Novolak. It demonstrates that the photoproducts of DNQ accelerate the development rate of Novolak compared to the development rate of the pure polymer. Unexposed DNQ reduces the development rate of Novolak. Here "bleached" means fully exposed. Reproduced with permission from Meyerhofer, D. *IEEE Trans. Electron Devices* **1980**, *27*, 921–926. 2011 IEEE.

DNQ/Novolak photoresists were ubiquitously adopted in semiconductor manufacturing with the advent of projection lithography. The high pressure mercury lamps used to expose DNQ/Novolak at 436 and 365 nm were not photon-limited at those wavelengths, so resist sensitivity was not a gating factor for manufacturing. As the

semiconductor industry looked towards 248 nm lithography, however, the DNQ/Novolak system was no longer viable. The power output of a mercury lamp at 248 nm is an order of magnitude less than that at 365 nm. Each DNQ molecule requires at least one photon absorption for photochemistry to occur, meaning many photons are required to modify resist solubility. In addition, DNQ is opaque at 248 nm and does not photobleach significantly during exposure. As a result, resist films required excess light to fully expose the entire thickness of the film. These overexposed features had sloped sidewalls after development (Figure 2.3) which are undesirable for manufacturing. A new resist was required that had a higher quantum efficiency and was transparent enough to provide a uniform cross-section of light throughout the film. Other photoactive compounds were eventually developed that solved the photobleaching problem,[74] but with quantum efficiencies of only 0.3, they were still too slow for photon-limited 248 nm light sources.

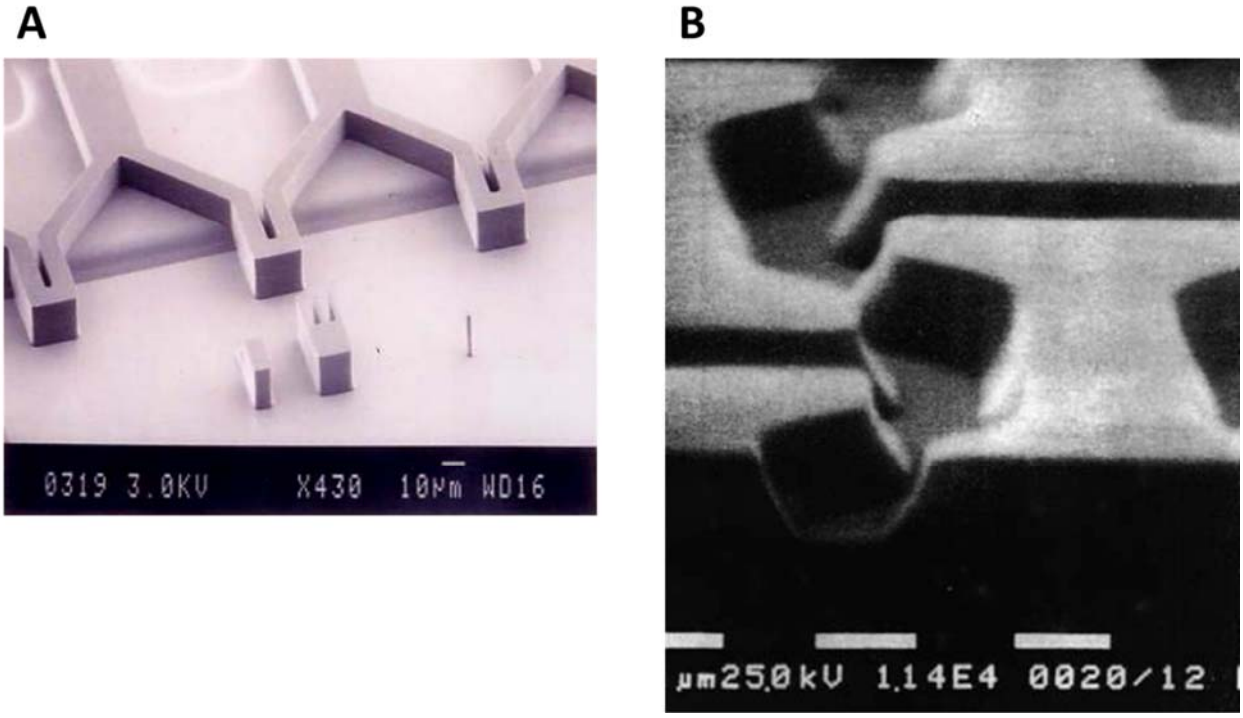

Figure 2.3: Developed features in DNQ/Novolak films after imaging at (A) 365 nm and (B) 248 nm. The sloped sidewalls in (B) can be attributed to the opacity of DNQ/Novolak at 248 nm.[75]

2.1.3 Chemically Amplified Resists (CAR)s

The development of the chemically amplified resist (CAR)[71] was a watershed moment for photoresist technology and has enabled the continued march towards ever-smaller printed feature sizes. The basic design principle is simple: a single photochemical reaction activates a catalyst inside the resist film. The catalyst then initiates a cascade of chemical changes with the matrix polymer via a simultaneous diffusion and reaction mechanism.[76] The net result of the single photochemical reaction can be several hundred deprotection or crosslinking reactions which change the solubility of the resist.[77] Thus, orders of magnitude less light is required for imaging.

One of the first acid-catalyzed resists was a dual tone system based on melamine/Novolak/DNQ blends.[78] The resist could be patterned in either a negative or positive-tone configuration, and exhibited nonlinear dose response which produced steep sidewall profiles at low exposure doses (Figure 2.4).

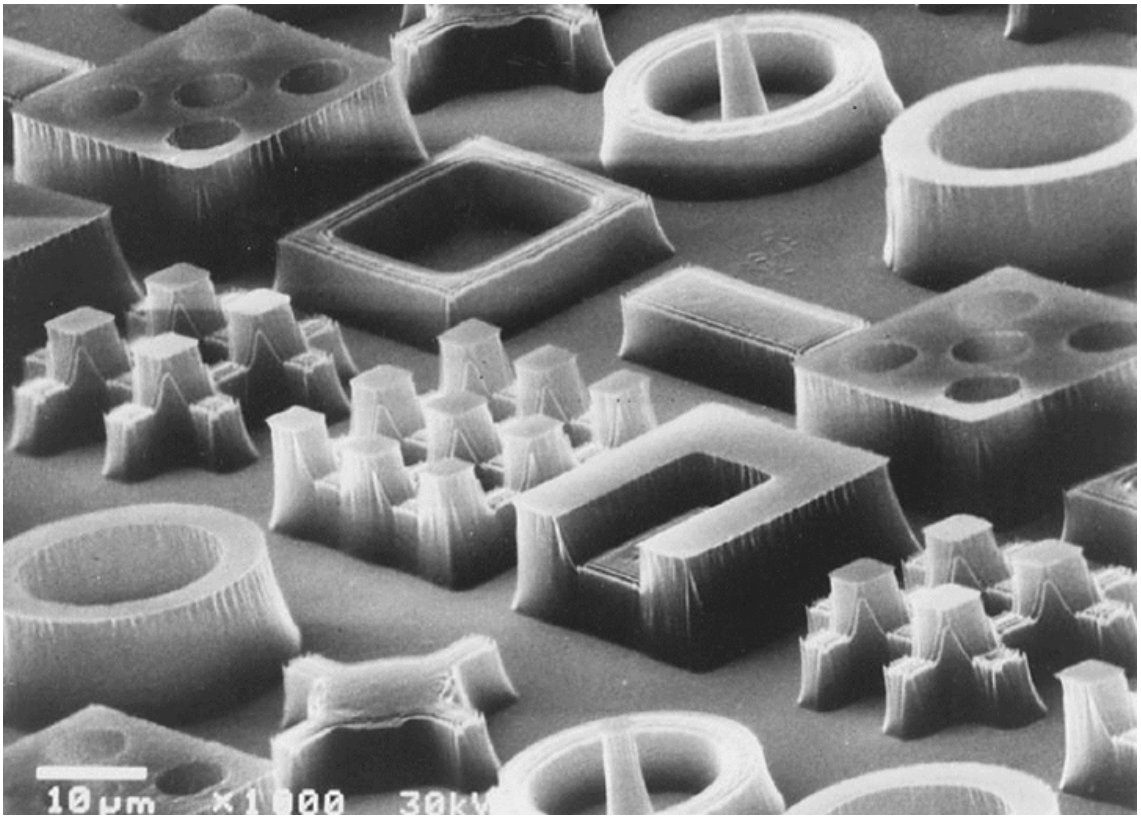

Figure 2.4: Photoresist features printed in melamine/Novolak/DNQ resist blends.[78]

No recorded evidence exists of a positive-tone chemically amplified resist until 1973. A patent filed by G. H. Smith at 3M detailed the invention of a THP-protected Novolak resin which could be rendered soluble in basic developer after reacting with

strong acid produced by an onium photoacid generator (PAG).[79] However, this resist system was never commercialized.

The credit for the first commercial CAR typically goes to Willson, Frechet, and Ito, who pioneered the first use of a protected poly(hydroxystyrene) matrix protected by a tert-butoxycarbonate functional group.[80] In the presence of strong acid and heat, the tBoc group decomposes to form isobutene and carbon dioxide, liberating the base-soluble phenol. PHOST also has the added benefit of being nearly transparent at 248 nm. The nonlinear response produced by chemical amplification made the resist two orders of magnitude more sensitive than DNQ/Novolak.[81] The CARs used today for 193 nm lithography use a very similar acid-catalyzed deprotection principle. However, the absorption of PHOST at 193 nm limits its usefulness in current manufacturing. Instead, methacrylate systems were developed which are more transparent and utilize tert-butyl ester protection chemistry rather than tBoc groups.[82]

CARs achieve sensitivity via a catalytic reaction between a photo-activated strong acid and a reactive polymer matrix. For chemical amplification, the catalyst must diffuse and react with many protected polymer sites; however, the stochastic nature of this mass transport also creates roughness in the final developed pattern.[83] As feature sizes approach the diffusion length of the acid catalyst, this characteristic roughness becomes unmanageable[84] without significantly reducing the sensitivity of the resist. The CAR design is fundamentally limited by this trade-off between resist speed and pattern quality.[85,86] A more detailed discussion on the limitations of CARs for next-generation

lithography can be found in Chapter 6, as well as a description of a new resist design that may overcome this fundamental trade-off.

2.2 Block Copolymer Materials Design

BCP self-assembly offers unique advantages that are especially appealing for nanopatterning applications, including access to sub-5 nm features in thin films[87–89] and sub-nm feature uniformity[90] over large areas. On planar substrates, BCP films can provide templates for fabricating nanostructured features like highly selective membrane pores[44] and dense nanowire arrays.[91] However, with the appropriate pre-patterned surface, BCP self-assembly can also be leveraged to dramatically enhance both the density and minimum feature size of patterns produced by traditional photolithography.[62]

2.2.1 Block Copolymer Thermodynamics

Diblock copolymers (BCP)s consist of two chemically distinct homopolymer domains (blocks) bound by a single covalent bond.[46] Frequently, the two blocks are immiscible and spontaneously phase-separate to minimize unfavorable blockwise interactions. However, because the polymer domains are tethered together, dissociation on the macro scale (> 1 μm) is impossible. Instead, BCPs self-assemble into a limited number of nanoscale morphologies in bulk and thin films.[92] Allowed morphologies for diblock copolymers include spheres, hexagonally-packed cylinders, gyroid networks, and lamellae. Three variables govern the location of these different structures on a theoretical phase diagram[93] (Figure 2.5A): the relative volume fraction of each block (f_A, f_B) and the product of χ and N, where χ is the Flory-Huggins interaction parameter[92] which captures,

to a certain extent, the degree of chemical incompatibility between the two blocks. N is the overall degree of polymerization of the block copolymer. χ, N , and the ratio of the two blocks can be controlled using synthesis to create custom BCP materials with prescribed behavior and properties.

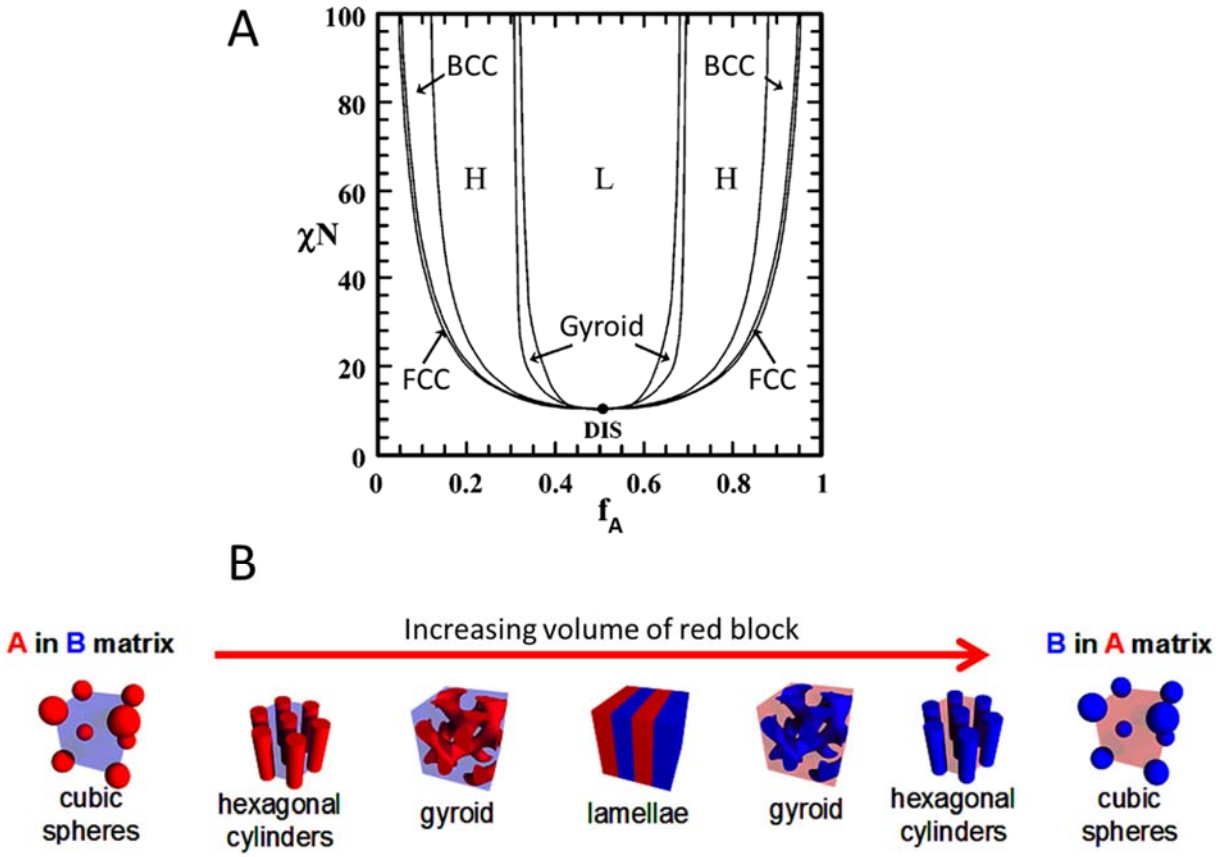

Figure 2.5: (A) Theoretical phase diagram for diblock copolymers. Reproduced with permission from Cochran, E. W. *et al*. *Macromolecules* **2006**, 39, 2449–2451. Copyright 2006 American Chemical Society. (B) Cartoon depiction of different available morphologies for diblock copolymers

Lamellae (lines and spaces) and hexagonally-packed cylinders are the most useful features for lithographic applications. These morphologies have a uniform cross-section when oriented perpendicular to the substrate, which provides a larger process window for pattern transfer via reactive ion etching (RIE). In addition, naturally-produced line/space and via patterns can template a number of relevant circuit features like transistor "fins"[52] and interlayer contact hole connections.[53,94,95]

BCP structures repeat over large length scales and have a natural periodicity (L_0). For lithographic applications, L_0 determines the resolution of the patterned features resulting from BCP self-assembly. The minimum resolution of any BCP material is governed by two scaling laws (Eq. 2.1 and 2.2).

$$L_0 \sim N^{2/3}\chi^{1/6} \qquad \text{Eq. 2.1}$$

$$\chi N > 10.5 \qquad \text{Eq. 2.2}$$

L_0 increases as both N and χ increase, but scales more strongly with N. This makes sense intuitively; as polymer chains become smaller, self-assembled domains should correspondingly decrease in size. However, feature sizes cannot be minimized arbitrarily. Below χN = 10.5, known as the order-disorder transition (ODT), polymer blocks will not phase separate, instead preferring to form disordered, homogenous materials. To produce the smallest possible feature sizes for lithography, blocks should be chosen to maximize χ while minimizing N such that Eq. 2.2 is satisfied.

2.2.2 Self-Assembly in Thin Films

The film thickness of the BCP as well as the interfacial interactions at the substrate and top surface control BCP self-assembly in thin films. Depending on the state of these three variables, BCPs generally adopt an orientation either parallel or perpendicular to the substrate.[96] Non-preferential, or "neutral" surfaces, balance the surface tension of each block such that neither block prefers to form a wetting layer.[97] Surfaces of this sort promote the formation of perpendicular features. In addition, if the film thickness of the BCP is not commensurate with L_0, confinement between two surfaces can frustrate BCP domains into standing up vertically.[98] It should be noted that perfectly neutral interfaces produce perpendicular features at all film thicknesses.[99] Since parallel features are lithographically useless, self-assembly processes must be designed to carefully control the interfacial energy at the substrate and free (top) surface.

The ideal lithography process for a lamellae-forming BCP is depicted in Figure 2.6. First, a BCP film is deposited onto a substrate via spin coating. In this state, blocks are phase-separated but lack long-range order. During a subsequent thermal annealing process, the BCP domains reorganize into either parallel or perpendicular features, depending on which is more thermodynamically favorable. Thermal annealing is preferred to solvent annealing[100] because it is a fast, scalable, and repeatable process that does not require inventing new equipment for high volume manufacturing. After annealing, one block is selectively removed from the BCP film to create a sacrificial etch mask, which can be used to transfer the relief image into an underlying substrate.[49]

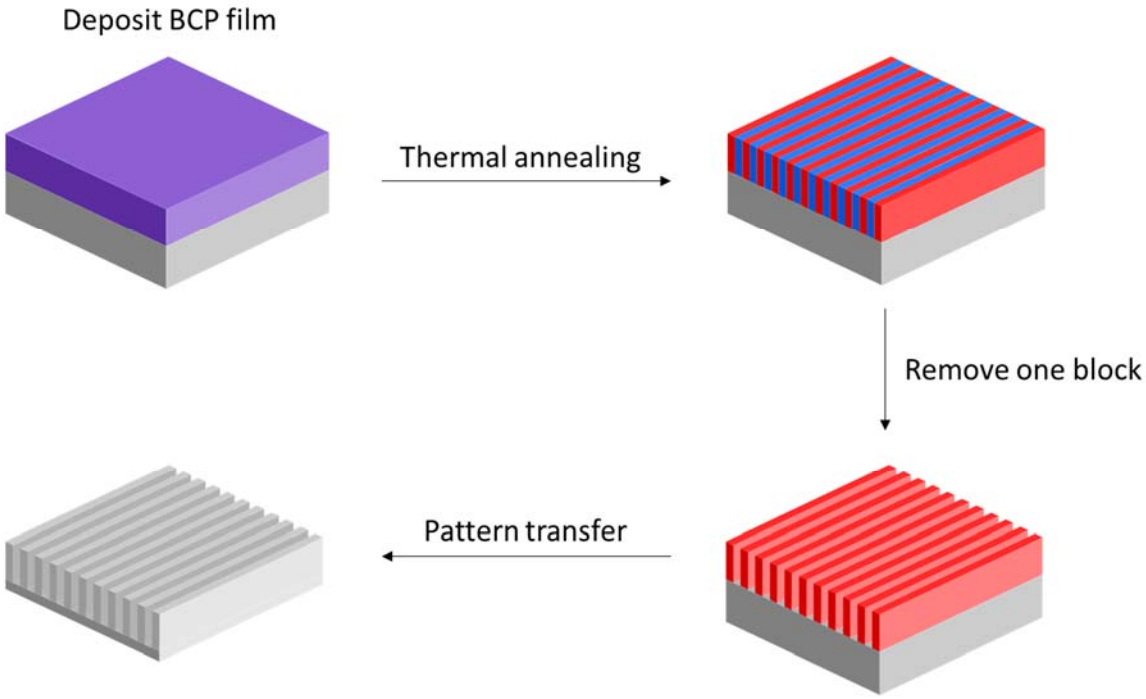

Figure 2.6: Cartoon schematic of ideal BCP lithography process

In practice, this type of process rarely works. Most substrates are not neutral for BCPs; for example, the native oxide film found on silicon wafers is highly polar and generally wets the more hydrophilic block in any BCP system. Thus, annealing BCP films on top of an unmodified substrate usually results in the formation of parallel features, as depicted by arrow 2 in Figure 2.7.

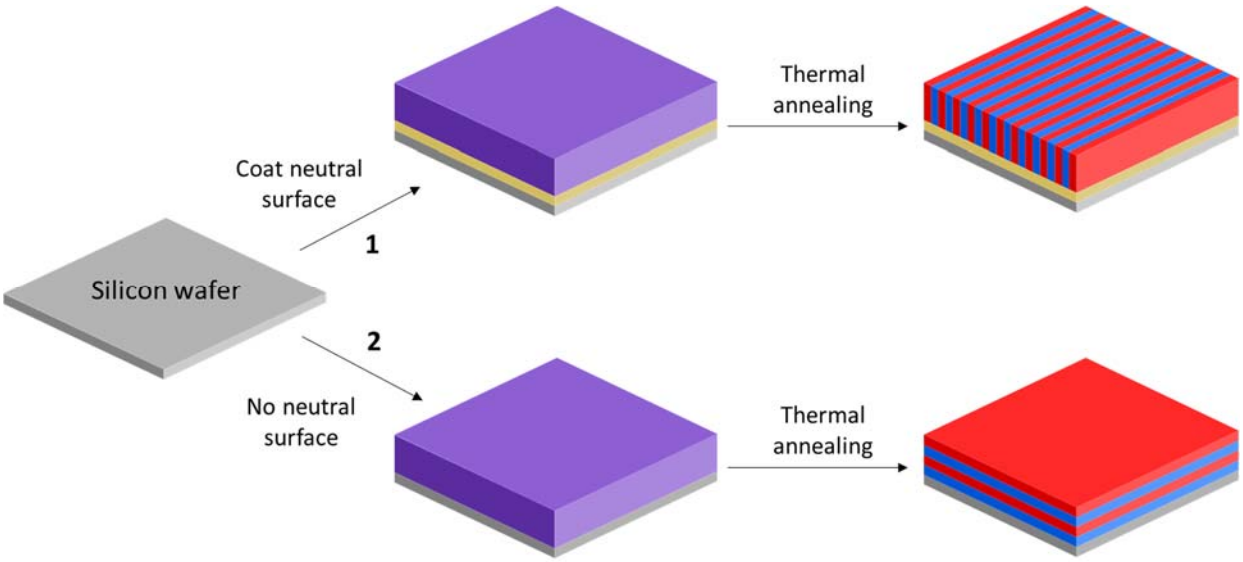

Figure 2.7: Over-simplified cartoon depicting BCP self-assembly in thin films. Lamellae-forming BCPs can form either parallel or perpendicular features, depending on the surface energy of the underlying substrate.

In most self-assembly processes, a neutral bottom coat is first applied to the substrate before depositing the BCP film (Figure 2.7, arrow 1). These surfaces are usually polymers which are capable of crosslinking[101,102] or grafting to the substrate[103,104] so they are not dissolved during BCP spin coating. Carefully controlling the composition of random copolymers can produce neutral surface coatings that are specifically tuned for individual BCP materials.

2.2.3 Limitations of PS-*b*-PMMA

The process depicted by arrow 1 in Figure 2.7 can be used to orient poly(styrene)-*block*-poly(methyl methacrylate) (PS-*b*-PMMA). The surface energies of PS and PMMA are approximately equal in air at high temperatures,[105] meaning that the free interface is

neutral for the BCP during thermal annealing. This property is exceedingly rare among BCP materials, and it is the main reason why PS-*b*-PMMA is the most studied material for BCP lithography. However, due to its relatively modest χ value, the minimum full pitch resolution for lamellae-forming PS-*b*-PMMA is approximately 20 nm,[106] which cannot sustain manufacturing for future generations of microelectronics devices. In addition, the poor etch selectivity between PS and PMMA limits pattern transfer into an underlying substrate, since high aspect ratio etch masks are difficult to generate without coating very thick BCP films.[90]

Ultimately, these limitations disqualify PS-*b*-PMMA as a long-term lithography solution. In response, so-called "high-χ" BCPs[107] have been heavily investigated because they offer access to high resolution features in thin films (< 5nm). BCPs can be further improved by incorporating etch-resistance moieties such as silicon[108] or tin[109] into the structure of one of the blocks. In the Willson group, we have produced a family of silicon-containing BCPs capable of improving on the material properties of PS-*b*-PMMA without discarding its key advantage: the ability to generate perpendicular features using thermal annealing.

2.3 Silicon-containing Block Copolymers

2.3.1 The Path to Smaller Feature Sizes

In the final ITRS roadmap published in 2015,[110] several options were listed for scaling below 7 nm half pitch resolution for future manufacturing nodes. This list of options include EUV quadruple patterning, high-NA EUV, directed self-assembly,

nanoimprint lithography (NIL), and 193 nm octuple patterning. Directed self-assembly stands out from these options because it does not require new process infrastructure, and does not involve a lot of costly and complex process steps like those found in quadruple or octuple patterning.[111]

Resolution requirements become even more stringent looking beyond semiconductors to the hard disk drive industry. According to the most recent ASTC roadmap,[112] bit-patterned media will need to be capable of reaching areal densities of at least 7 Tb/in^2 by 2023. According to geometric analysis, to avoid the extra, costly processing steps required for SADP, BCP materials will need to achieve a minimum resolution of 10 nm full pitch.[113]

To design materials capable of meeting these standards, the component blocks must be chosen judiciously to maximize χ while still remaining amenable to orientation control in thin films. Our group works primarily with BCPs made from styrenic monomers. The chemistry of styrene can be readily modified by appending various moieties, including silicon-containing groups, to the aromatic ring. In this way, blocks can be made progressively hydrophobic or hydrophilic, which increases the driving force for self-assembly and ultimately leads to higher χ values and smaller feature sizes. A progression of BCPs that have been made in our group can be seen in Figure 2.8. Using this strategy, we have achieved 5 nm half-pitch lamellae structures in thin films using PVBD-*b*-PDSS (Figure 2.8), which meets resolution goals for both the semiconductor and hard disk drive industries. Chapter 3 describes the processes we have developed for directed self-assembly and pattern transfer of 10 nm PVBD-*b*-PDSS.

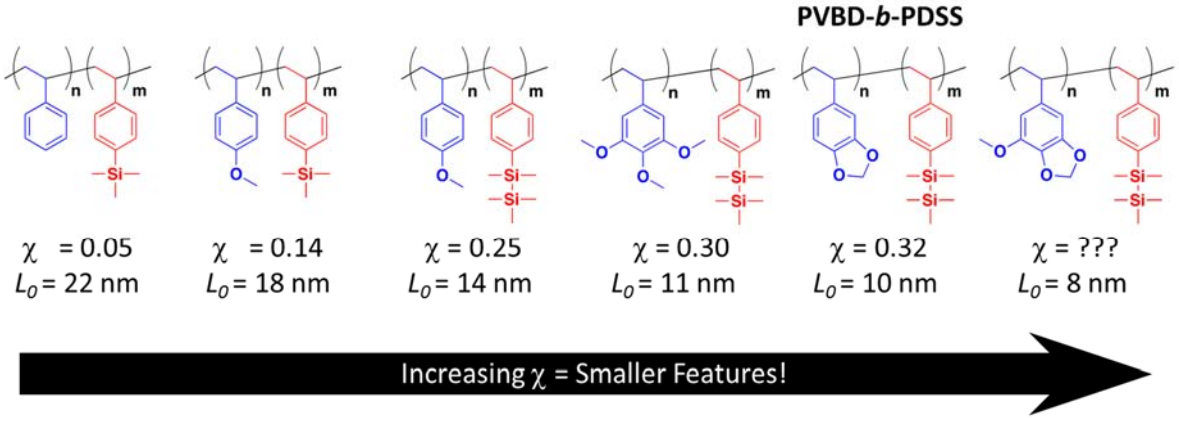

Figure 2.8: Progression of styrenic block copolymers made in the Willson group.

2.3.2 Orientation Control

Although modifying substrate surfaces for BCP self-assembly has been well-established, controlling the free (air) interface remains a significant challenge for BCP systems other than PS-*b*-PMMA. High-χ BCPs are especially difficult to orient perpendicularly, since large enthalpic blockwise interactions usually correlate with large difference in block surface energies. In general, three strategies exist for modifying the free interface for BCP thin films: 1) solvent annealing,[100] 2) surfactant additives,[114] and 3) polymeric top coats.[99,115] Of these options, top coats can be deposited by routine spin coating and are simple to synthesize. In addition, solvent annealing and surfactant additives are capable of altering the morphology of BCP assembly by preferential swelling of one block. The Willson group has developed a library of top coat materials based on the polarity-switching mechanism of maleic anhydride.[99] This strategy allows us

to cast polymeric top coats from orthogonal solvents like MeOH and H_2O, which do not disturb the BCP film during spin coating. After baking at high temperature, the top coat film undergoes a reaction that reduces its polarity and promotes perpendicular BCP orientation. These materials have been key to enabling the self-assembly of silicon-containing BCPs in thin films. Top coat materials were vital to the success of the DSA process described in Chapter 3. Brush materials that are capable of selectively grafting to thin chromium films and creating neutral surfaces are described in Chapter 4.

2.3.3 Etch Resistance and Pattern Transfer

Any BCP system for lithography must demonstrate a fundamental compatibility with etch processing and pattern transfer. Transferring features less than 10 nm wide into an underlying substrate by etching requires a BCP system with good etch selectivity between the two blocks and the underlying substrate. BCPs which incorporate inorganic elements such as silicon[108] and tin[109] in one block form etch-resistant crusts during oxygen- or fluorine-based RIE, which can function as protective barriers and impart etch selectivity between BCP domains. Recent progress in the RIE processing of BCPs containing inorganic elements demonstrates that pattern transfer can be achieved using a variety of etch conditions.[54,116]

To mitigate complications associated with wet or dry etching, BCPs could also potentially be designed to contain a depolymerizable block. Polymers of this sort can be caused to depolymerize at elevated temperatures when exposed to specific stimuli. As a result of degradation, the low celling block self-develops as the monomer vaporizes,

leaving behind a relief image of the BCP film. Two polymer systems that could be potentially useful as self-developing BCPs are described in Chapter 5.

Chapter 3: Directed Self-Assembly and Pattern Transfer of 5 nm Block Copolymer Lamellae

The possible patterning applications enabled by BCP lithography extend to both the semiconductor and data storage industries, where high-resolution features are required for manufacturing next-generation devices. This chapter specifically discusses how BCPs offer advantages for enabling bit-patterned media for magnetic information storage technology, and possible schemes for implementing directed self-assembly using nanoimprint lithography (NIL) to define the guiding pattern.

3.1 INTRODUCTION

The function and cost of microelectronic devices have continuously improved during the last 40 years, largely due to the ability to fabricate ever-smaller structures in silicon. Improvements in the patterning process that has traditionally been used to fabricate these devices, photolithography, has enabled this scaling. However, the progress in improving the resolution of photolithography has reach its physical limitations. The resolution limit of a single pass of 193 nm immersion lithography, which is the most advanced technology deployed for high volume manufacturing, is ~40 nm half pitch. Driven by a relentless pursuit for higher resolution patterning, manufacturers of microelectronics devices are now considering using the nanoscale self-assembly of block copolymers (BCPs) to pattern next generation devices.[43]

The directed self-assembly (DSA) of BCP films requires pre-patterning of the substrate surface with sparsely spaced guidelines. Orientation of BCPs in the presence of these guidelines results in a density multiplication of the pre-pattern with minimum

feature sizes well beyond the capabilities of traditional photolithography.[62] These patterns provide the templates for many of the most demanding next generation patterning applications including production of patterned media (BPM)[113,117] for hard disk drives, and FinFETs [52] and contact holes[94] for microelectronics.

To achieve the highest possible resolution from self-assembly, the chemical structure of a BCP must be carefully designed to maximize the chemical incompatibility between blocks (often measured by the Flory-Huggins interaction parameter, χ). Polystyrene-*block*-poly(methyl methacrylate) (PS-*b*-PMMA) is the most studied BCP system for lithography applications because it readily adopts a perpendicular orientation of lamellae or cylinder morphology during thermal annealing.[118] Although processing PS-*b*-PMMA is simple, it suffers from a low χ parameter that limits its ultimate resolution to ~11 nm half-pitch features.[106] Unfortunately, these features do not fully satisfy the hard disk drive industry's resolution goals[112]. Consequently, there is increasing demand for the development of "high-χ" BCPs that are capable of forming sub-10 nm features.[108,119–121] In particular, 5 nm half-pitch BCP features have garnered special interest[107] because these dimensions rival the resolution of combined litho/multiple patterning processes operating at their technological and economic limits.[111] Lamellae-forming BCPs are also particularly interesting because they provide a uniform through-film cross-section, which affords a larger process window than cylinders for full BCP development and subsequent substrate etching.[122]

Although BCPs of different chemistries have been shown to reach the sub-10 nm threshold (as referenced previously), some of these BCP systems fail to satisfy two other

properties needed for facile processing: direct etch contrast between the BCP components and the perpendicular orientation of the BCP features by thermal annealing. Work in our group has focused on designing BCPs with minimum feature sizes that scale into the sub-10 nm regime[108] but also satisfy these two other prerequisites. These include BCPs that incorporate inorganic elements such as silicon[108] and tin[109] in one block that resist specific plasma etch chemistries and enable development of a BCP film into a sacrificial etch mask.[54,116] After development, the resilient features also enable the transfer of high aspect ratio patterns into an underlying substrate. BCP orientation control by thermal annealing is desirable for applications in manufacturing because it introduces no new equipment and is generally fast and reliable. We note that for many high-χ BCPs, solvent annealing is the only choice for controlling BCP orientation in thin films.[100] While solvent annealing can be effective on the lab-scale, the process is disadvantageous for high-volume manufacturing because of increased capital costs, safety considerations, and time required to qualify new processing equipment and methods. Therefore, a key design parameter of our high-χ BCPs was to require only thermal annealing to generate perpendicular features. To accomplish this, spin coat-able, polarity-switching top coats were introduced to control domain orientation during thermal annealing.[99] This orientation control strategy is compatible with full 300 mm wafer processing, with drop-in compatibility on existing all-track processing integration schemes.[123]

3.2 Pattern Transfer of 5 nm BCP Features

3.2.1 Reactive Ion Etching (RIE)

The focus of this chapter is the pattern transfer and DSA of a new block copolymer that is capable of forming 5 nm half-pitch lamellae. Figure 3.1 demonstrates the pattern transfers of PVBD-*b*-PDSS fingerprint patterns through a chromium hard mask and into an underlying film of spin-on carbon (SOC) film. In this experiment, an 18 nm thick PVBD-*b*-PDSS film oriented by thermal annealing was subjected to a CO_2-based RIE process, which removed the PVBD block. During this process, the PDSS block is gradually oxidized to form an SiO_x crust that impedes further etching.[116] After completely removing the PVDB block, the remaining etch mask was comprised of approximately 8 nm of PDSS and neutral brush (Figure 3.1A). The BCP etch mask was then subjected to a Cl_2/O_2-RIE to break through the thin chromium film and etch into the underlying SOC layer. Evidence for the success of this transfer can be seen in the tilted-view SEM image in Figure 3.1B. The thickness of the BCP mask before and after the Cr breakthrough etch is approximately 26 nm. Since the BCP mask did not lose any thickness during the second etch, it can be assumed that the difference in the aspect ratio of the etched features in Figure 3.1A & 3.1B is a result of complete transfer through the Cr layer and subsequent etching into the underlying SOC layer. There is some evidence of a small amount of bridging after the Cl_2/O_2 etch, but this process has not yet been fully optimized. RIE processing of grating structures as small as 5 nm in width is unprecedented and has not been extensively studied due to the significant challenge of fabricating such small structures using traditional lithography. Fully optimizing the RIE

processes on 5 nm length scales is beyond the scope of this work and will be a key challenge for the success of BCP lithography in this regime. However, this process shows proof of concept that 5 nm BCP features can serve as an etch mask, and can be used to pattern inorganic and organic underlayers.

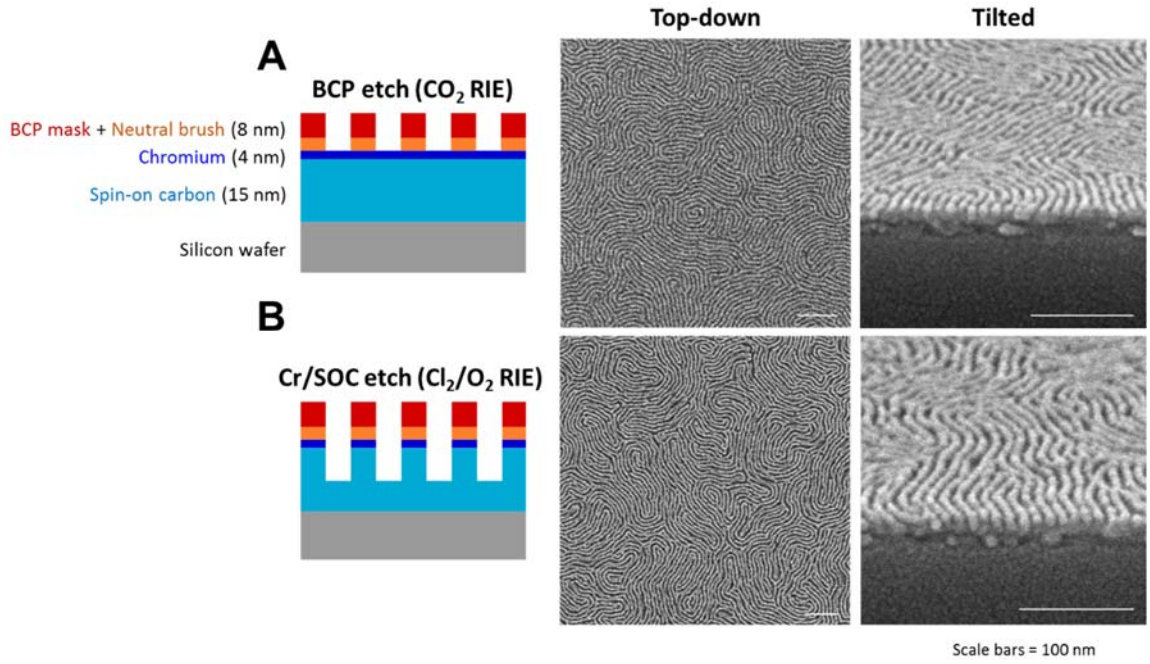

Figure 3.1: Top-down and tilted view SEMs of (A) fully developed 5 nm domains on top of a Cr/SOC-coated silicon wafer and (B) transferred patterns after the Cl_2/O_2 etch process. An oxidizing RIE process was used to completely remove the PVBD block in (A). The full height of the mask in (A) and (B) is approximately 26 nm. Scale bars = 100 nm.

3.2.2: Pattern Transfer via Molecular Transfer Printing

Molecular transfer printing (MTP)[124,125] is a potentially interesting technique for transferring DSA patterns with complex through-film structures. In this process, a chemical "copy" of the *top* surface of a BCP film can be transferred to another substrate,

effectively ignoring any morphological defects at the bottom interface which might prevent efficient pattern transfer. Once the "master" wafer has been copied, another BCP film can be coated over the chemical pattern to make "daughter" wafers which reproduce the original "master" film when annealed. This solution is excellent for film stacks with underlying topography, since the copy of the original DSA pattern will naturally be transferred to a flat substrate, potentially simplifying subsequent etch processing without losing any pattern information.

The work described herein is based on a process originally developed for replicating PS-*b*-PMMA films.[126] A schematic of the materials and process used for MTP can be seen in Figure 3.2. A pre-assembled PVBD-*b*-PDSS film on top of a nanoimprint guiding pattern was coated with a thin film of PSSMA (Figure 3.2A). When exposed to light, the sulfonyl azide group in the PSSMA structure is converted to a reactive nitrene intermediate, which quickly crosslinks with itself and any polymer in contact with the film. As a result, approximately 1-7 nm of the underlying BCP film is permanently grafted to the PSSMA mat after exposure. PSSMA can be directly spin-coated from methanol on the BCP after forming the trimethylamine polymer salt.

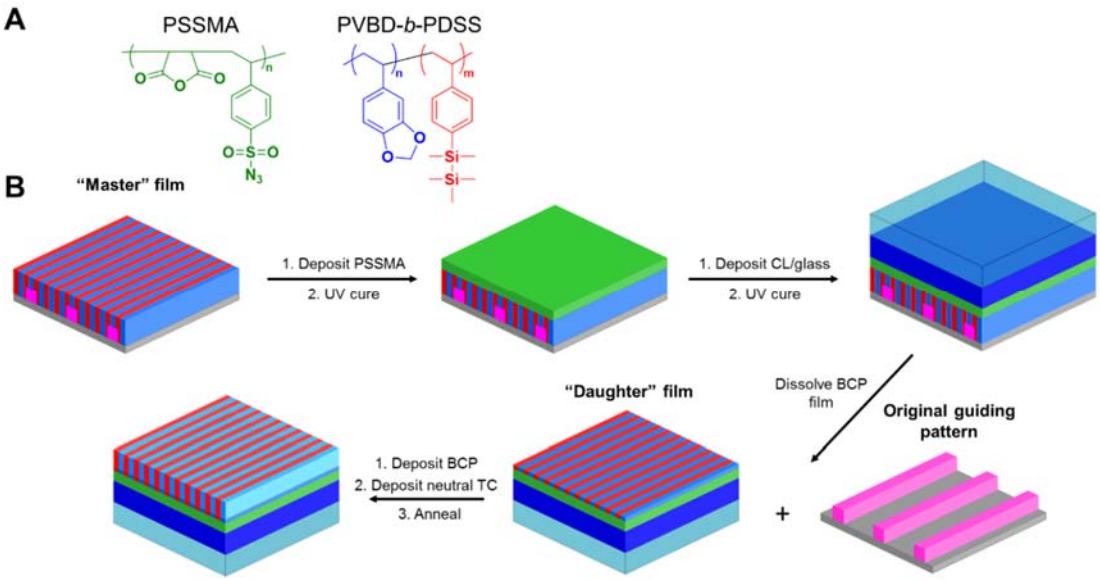

Figure 3.2: (A) Materials and (B) MTP process used for replication of DSA films. CL stands for "conformal layer".

After coating, the PSSMA film was placed in a nitrogen atmosphere and UV cured using a high-pressure mercury lamp. Once fully crosslinked, a single drop of a photocurable mixture of acrylate monomer and free radical initiator was deposited directly onto the film stack to act as a conformal layer (CL). A glass slide was added on top of the CL liquid drop, and pressure was applied to evenly spread the fluid over the entire film. The glass slide and the PSSMA/BCP film stack were then bonded by curing the CL using UV light. The purpose of the CL creates a planar surface between the glass slide and the PSSMA, ensuring good adhesion between the two surfaces.

Once hardened, the only soluble portion of the film stack was the BCP film. The bottom nanoimprint template attached to the silicon wafer could be separated from the PSSMA/CL/glass slide by sonicating in toluene overnight. After isolating the glass slide, a new BCP film and neutral top coat were sequentially spun-cast on top of the grafted

chemical copy of the original DSA pattern. The film stack was then annealed and etched in oxygen plasma for SEM imaging.

The BCP assembly obtained in the final "daughter" film can be seen in Figure 3.3. The topography of the original NIL pattern can be seen clearly in the replicated BCP film. The bright rectangles in the top row of SEM images contain perpendicular BCP assembly. Unpatterned NIL resist borders these subfields in the original pattern, which produce parallel features that are transferred to the "daughter" film. However, when the DSA quality was studied at higher magnifications, it can be clearly seen that many defects in the BCP assembly were created as a result of the transfer. Some areas of the "daughter" film do appear to show aligned features, however, which is encouraging and suggests it may be possible to optimize this process further to obtain acceptable DSA quality. Unfortunately, due to the limited availability of aligned PVBD-*b*-PDSS films and the large number of experiments that would required to improve this MTP process, this option was not pursued further.

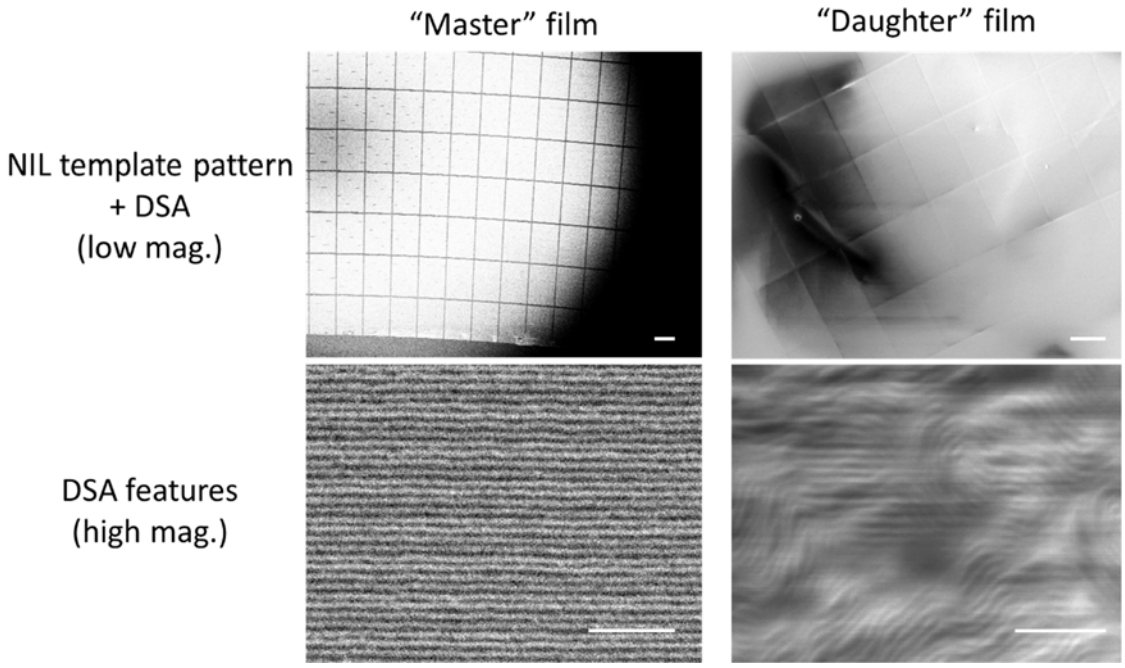

Figure 3.3: Results from the MTP process depicted in Figure 3.2. The images in the top row demonstrate that the large sub-fields of the original NIL pattern could be copied with good fidelity. However, the DSA obtained from the "daughter" film contained many defects, although some DSA was evident. The distortion seen in the "daughter" film SEM images is due to charging effects from the underlying glass substrate. The scale bars correspond to 100 μm and 100 nm for the top and bottom row of images, respectively.

3.3 DIRECTED SELF-ASSEMBLY

3.3.1 Process Flow

High-resolution lithography requires strict tolerances on pattern placement, overlay error and defect density to enable acceptable manufacturing yields. For BCPs, DSA is required for producing lithographically interesting structures relevant to device manufacturing. Numerous DSA schemes that use lithography to pattern chemical[56] or topographical[57] guide features have been reported. By carefully tailoring the dimensions

and surface chemistry of the guiding patterns, BCP films can be induced to produce many device-relevant features[58–60] with low pattern registration error.[61] In addition, DSA processes can repair defects and misplaced features from the guide pattern lithography.[62,63] Typically, guiding features for DSA are designed such that they have little or no topography (chemo-epitaxy).[125,127,128] However, so-called hybrid chemo-/grapho- epitaxy DSA schemes[129–131] purposely incorporate some topography in the guiding features to provide an additional constraining force to help achieve the desired alignment. These hybrid structures are more challenging to fabricate, but there is some evidence that combining topography with chemical pre-patterns reduces defects in self-assembly.[123,131]

Figure 3.4 shows the materials and the process steps used to align the 5 nm BCP features with PVBD-*b*-PDSS. First, a silicon wafer was coated either with a native oxide film or 2-3 nm of sputtered chromium, which is a standard hard mask material used for manufacturing of nanoimprint lithography (NIL) templates. A commercial acrylate-based NIL resist was used to pattern the guiding lines for DSA, with line widths of approximately 18 nm and pitches ranging from 40 to 50 nm. The ~8 nm-thick residual layer of NIL resist remaining between the guiding lines after patterning was removed using an oxidizing plasma etch. This breakthrough etch process (herein referred to as the trim etch) was also employed to simultaneously reduce both the height and width of the NIL guide lines. In some experiments, a polymeric brush was grafted to the substrate between the NIL features to neutralize the surface that was exposed during the trim etch. PVBD-*b*-PDSS was then spin-coated from methyl isobutyl ketone (MIBK), and then the

trimethylamine (TMA) salt of a neutral top coat copolymer was spin coated from methanol on top of the BCP. Thermal annealing was conducted at temperatures greater than 180°C, which initiates a reaction in the top coat to eliminate TMA and generate a neutral surface that is not preferential for either block.[115] After annealing, the top coat and PVBD block were removed by etching with oxygen plasma. Samples were then inspected using top-down SEM.

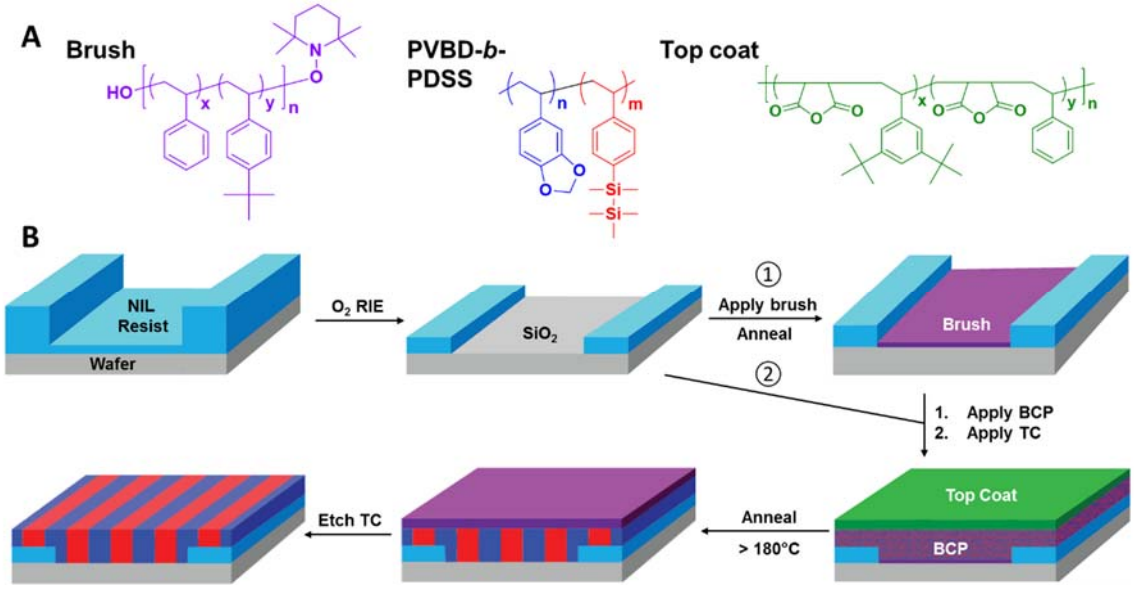

Figure 3.4: Schematic showing the materials (A) and process steps (B) used for producing directed self-assembly of 5 nm features. Arrow 1 and 2 describe the process flow with and without a grafted brush, respectively.

Four parameters significantly affected the quality of the DSA obtained by this process: presence or absence of a neutral brush layer, the ratio of BCP film thickness to NIL feature height, trim etch time, and the pitch of the NIL resist features. In most DSA process flows, i.e. the chemoepitaxial LiNe process,[132] a photoresist pattern is transferred into an underlying polymer mat to form preferential guide stripes, which anchor a

specific domain of the BCP. Afterwards, the photoresist is removed to expose the un-etched top surface of the underlying polymer. This top surface serves as a chemical guide stripe for the BCP. However, NIL produces a cross-linked polymer after patterning that cannot be removed using solvent. In this case, the NIL resist itself must be used as the guiding pattern.[133]

3.3.2 Initial DSA results

Figure 3.5 shows SEM images of the NIL lines before brush spin coating and grafting.

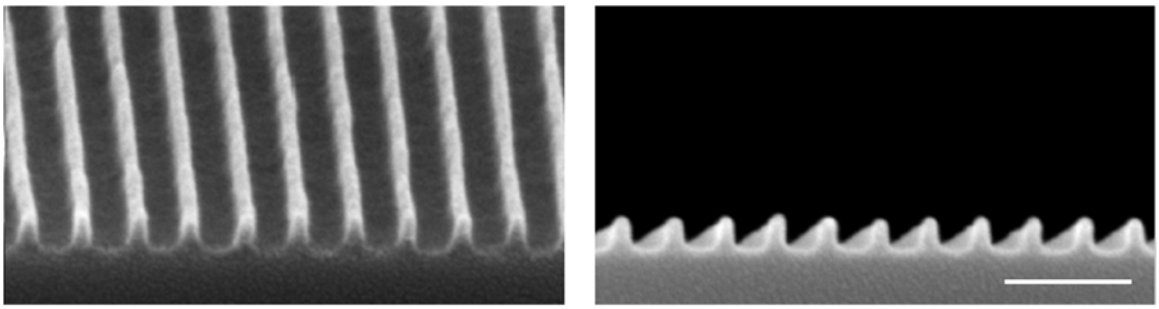

Figure 3.5. Tilted and cross-sectional SEM images of unetched NIL lines. Scale bar = 100 nm for both images.

In Figure 3.6, a polymer brush was applied to the NIL-patterned wafer by spin coating and then baked at 250°C. The presence of this neutral brush facilitates perpendicular BCP orientation. Unfortunately, the results of this process showed only well-oriented BCP domains which were weakly aligned *perpendicular*[134,135] to the direction of the guide lines. Most DSA processes rely on the chemical contrast between the guide line and substrate for alignment. These micrographs suggest that the brush

binds to both the NIL resist (oxidized during the trim etch) and the oxide substrate, which quenches the chemical contrast of the guide patterns. Since the brush polymer did not react selectively with the interspace surface, we attempted to achieve chemical contrast between the NIL guide lines and the substrate by foregoing the brush and etching the resist in oxygen plasma to increase its polarity relative to the substrate. For this process, BCP films were deposited directly onto the NIL resist without first grafting a neutral brush layer (arrow 2 in Figure 3.4B). On un-etched NIL lines, thin BCP films filled the interspaces and formed ladder structures aligned perpendicular to the direction of the trenches. No fingerprint patterns formed in regions where the NIL resist was flat, which suggests that confinement between the rigid NIL trenches produces the driving force for perpendicular BCP orientation. When the NIL resist lines were briefly trim etched, the direction of the assembly switched to form traditional graphoepitaxy structures aligned parallel to the NIL lines (Figure 3.6B). Etching the NIL lines apparently caused the exposed surfaces to become highly preferential for the polar PVBD block and facilitated the formation of DSA in the ideal direction. When PVBD-*b*-PDSS was assembled in non-patterned regions of the etched wafer, no perpendicular features were observed (Figure 3.8A), indicating that oxidized NIL resist is preferential for one component of the BCP. This result suggests that a highly preferential surface from the oxidized guide stripe is sufficient to control the direction of BCP alignment.

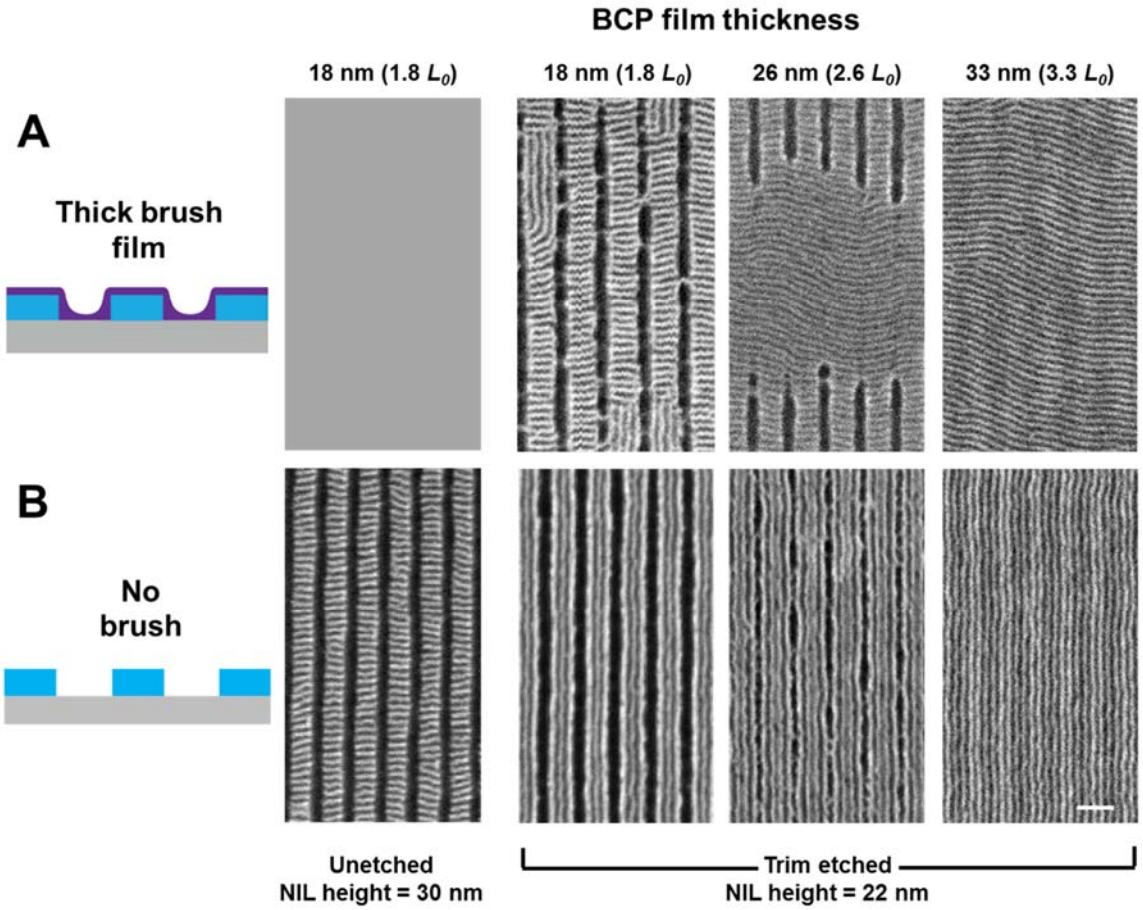

Figure 3.6: SEMs of BCP assembly on tall NIL features. The images in (A) were taken from samples in which a layer of brush was grafted to the substrate and rinsed before spin-coating the BCP film. The sample corresponding to the box in the first column was not imaged. The images in (B) were taken from samples prepared without grafting a neutral brush to the substrate. All BCP films were annealed at 190°C for 2 minutes. Scale bar = 50 nm.

Graphoepitaxial structures are sub-optimal for patterning applications since a portion of the surface is forfeited to accommodate the guiding pattern. Therefore, the DSA process was shifted towards chemoepitaxial assembly by increasing the BCP film thickness at a constant NIL feature height. As the film thickness increased, the BCP

gradually overfilled the trenches until the domains completely covered the surface of the NIL lines, as seen in Figure 3.6B. Even with a relatively thick BCP film (3.3 L_0), the DSA persisted over large areas. This patterning regime is perhaps most accurately described as hybrid chemo-/grapho- epitaxy, a relatively unexplored type of DSA process[123,129,131] compared to the panoply of studies describing either pure chemo- or graphoepitaxy. Although highly ordered line/space patterns can be created using this process, etch transfer of these structures could be challenging because features on top of tall guiding lines may not etch completely, leading to uneven and incomplete transfer of the BCP pattern.

3.3.3 Process Optimization

A series of experiments was performed to determine whether high quality DSA could still be achieved with shorter NIL guide lines (with and without a surface modifying brush). Longer trim etch times were used to shrink the lateral and vertical dimensions of the NIL features while the BCP film thickness was kept constant at 33 nm (3.3 L_0). The images in Figure 3.8A show the results of these DSA experiments without using a neutral brush treatment. Nearly defect-free self-assembly was observed by top-down SEM when the BCP was assembled on NIL features taller than 6 nm (as measured by AFM). When the NIL features were etched below 6 nm, the BCP lamellae adopted an orientation parallel to the substrate, indicating that the topographic driving force for self-assembly was mostly extinguished. This experiment was repeated with a two step brush grafting process that included a brief 150°C bake prior to the high-temperature grafting

bake at 250°C (previous studies have shown that brush grafting density can be controlled by varying the time and temperature of the brush annealing step[53,136]). The final brush thickness was also kept as low as possible (< 3 nm by ellipsometry) by spin coating the brush polymer from a very dilute solution at high spin speeds. The images in Figure 3.8B show the DSA resulting from this modified grafting process. Unlike the results in Figure 3.6A, nearly perfect registration between the BCP domains and the NIL lines was achieved with the modified grafting process. Figure 3.7 demonstrates that performing a soft bake at 150°C is necessary for generating this sort of alignment.

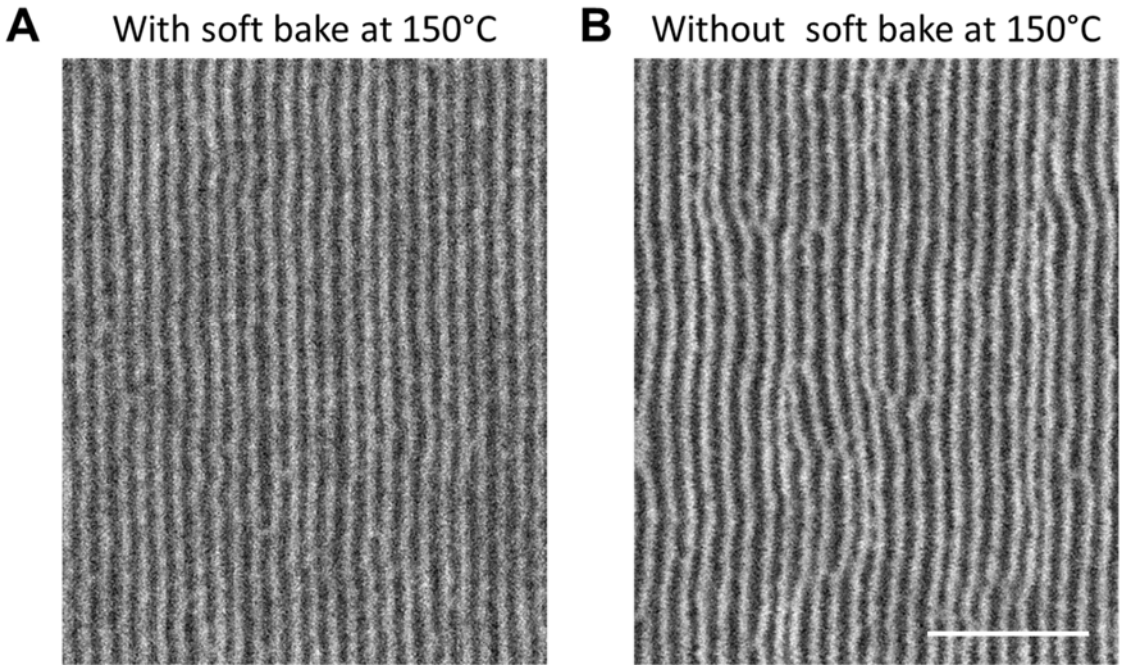

Figure 3.7: (A) SEM image of BCP DSA after grafting a thin brush layer (3 nm) by annealing at 150°C for 10 mins and then annealing at 250°C for 5 mins. (B) SEM image of BCP DSA using the same process to prepare the sample shown in (A), but without the 10 min bake at 150°C. The improvement in DSA quality seen in (A) could be the result of the polymer brush flowing away from the NIL lines during the soft bake at 150°C, improving the selectivity of the grafting reaction during the 250°C bake. Scale bar = 100 nm.

Similar to the experiments without a brush, the quality of the DSA diminished as the height of the NIL lines was reduced. The DSA transitioned to fingerprint patterns when the NIL features were less than 6 nm tall. Apparently, the sparse deposition of the brush is sufficient to selectively modify the substrate and thereby generate perpendicular features despite removing much of the topographical driving force. This result further

reinforces the importance of the height of the guiding pattern as an important variable for the BCP alignment process.

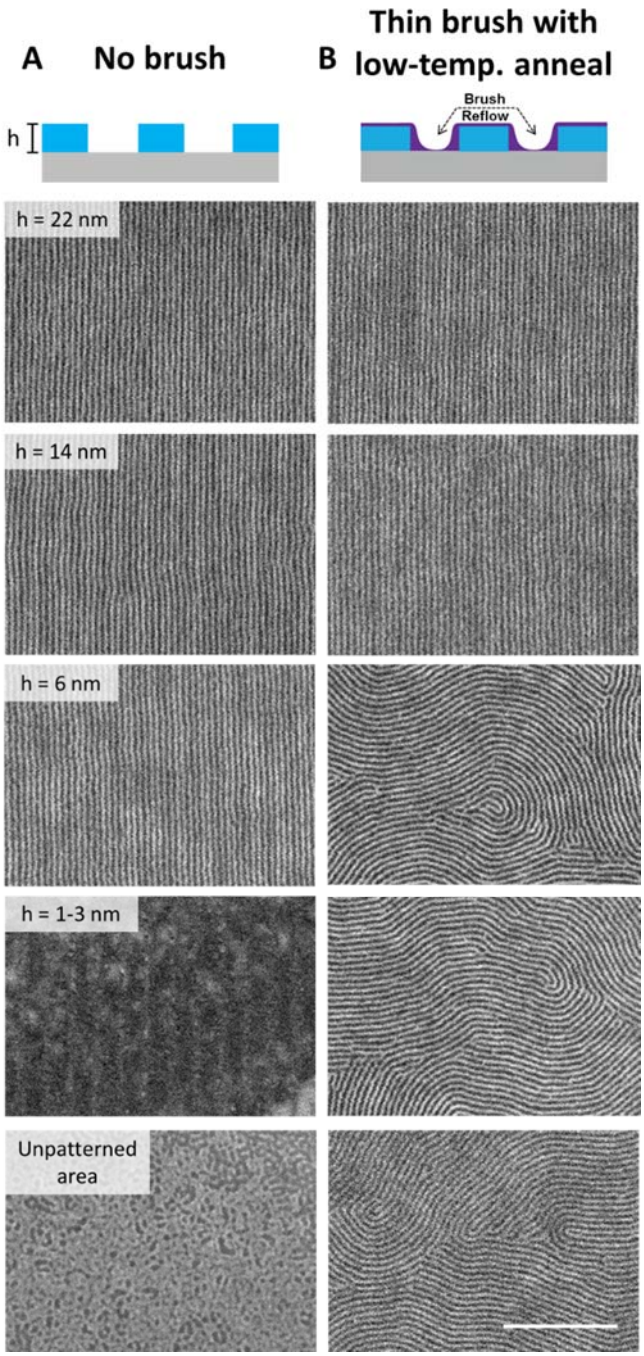

Figure 3.8. SEMs of BCP assembly on substrates patterned by NIL, demonstrating how DSA quality is affected by NIL feature height. "h" is the average height of the NIL lines for both images in a given row, as measured by AFM. All BCP films were 33 nm (3.3 L_0) thick and were annealed at 190°C for 2 minutes. Scale bar = 200 nm.

Figure 3.9 shows a quantitative analysis of DSA quality for NIL resist heights between 6 and 12 nm and also illustrates how pitch affects BCP alignment. DSA performance was assessed by analyzing top-down SEM images using custom computer software.[123] The score represents an estimate of the number of pixels in a given image that participate in DSA, normalized to the total number of pixels. An image with no obvious visual defects obtained a raw score of approximately 60%, while an image of random fingerprint patterns typically scored around 10%. The scores in Figure 3.9 have been normalized assuming a perfect score is approximately 60%.

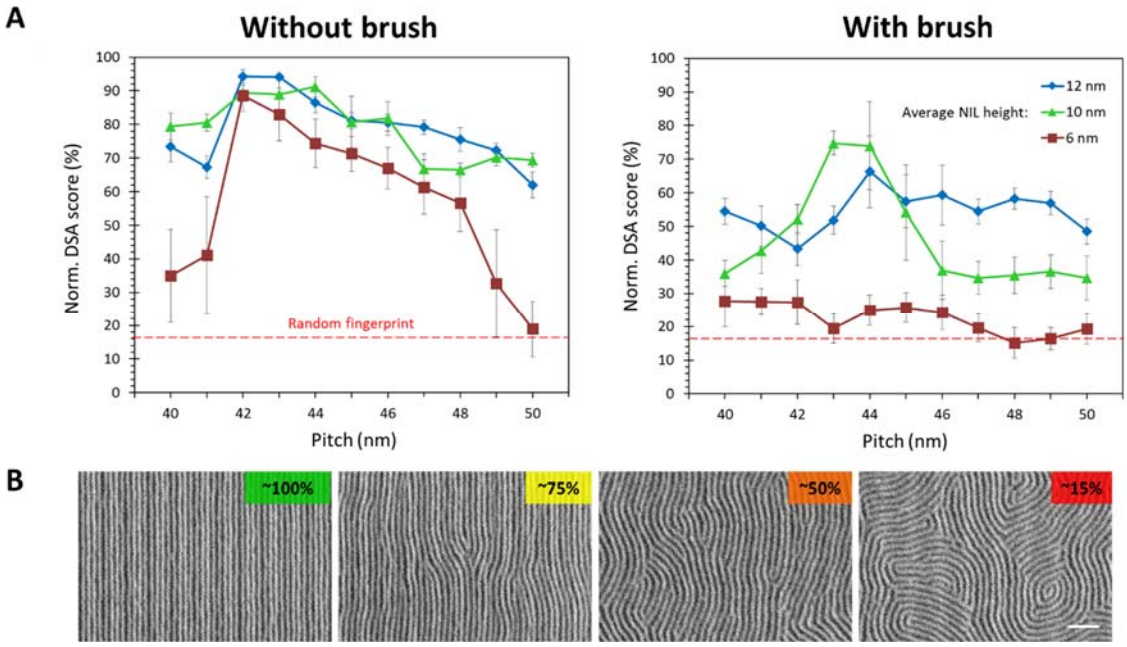

Figure 3.9: (A) A quantitative comparison of DSA quality between samples produced with and without brush. The DSA score (y-axis) is calculated using custom computer software and represents the normalized average percentage of pixels participating in DSA. Error bars correspond to ±1 standard deviation from the mean score. The lines connecting the points are only meant to be visual aids, not to indicate a continuous relationship between individual pitches. The red dotted line represents the average score of a random fingerprint pattern. (B) Representative SEM images that approximately correspond to the normalized score in the colored box. All samples used a BCP film thickness of 33 nm and were annealed at 205°C for 10 min. Scale bar = 50 nm.

Features with pitches between 42 and 44 nm produced the highest quality DSA for samples with and without brush. The process without a brush consistently produces DSA with fewer defects based on top-down analysis, even for non-ideal pitches. The discovery of the wider process window for the no-brush process was surprising, and prompted further investigation.

3.3.4 Cross-section Analysis Using STEM/EELS

To study the through-film structures of the BCP domains, representative samples of DSA films from both processes were cross-sectioned by focused ion beam milling. The cross sections were then imaged using scanning tunneling electron microscopy (STEM) with a simultaneous measurement of electron energy loss spectroscopy (EELS). The objective of this analysis was to understand how the BCP was interacting with the substrate surface by mapping the elemental composition of the cross-sectioned film. Figure 3.10 shows the results of the cross-sectional STEM EELS experiments for three different substrate surfaces (chromium, SiO_2 with and without brush), and demonstrates the need for carefully studying the through-film structure of any BCP system designed for lithography (the tilting of the domains in all three figures is most likely an artifact of thermal drift seen in other STEM EELS studies of soft materials,[131] especially since there is no corroborating evidence of tilted domains from other analyses).

The most striking difference between the samples with and without brush is the BCP behavior near the substrate. The BCP domains travel through the entire film in Figure 3.10A, implicating the importance of the brush in controlling BCP orientation. In contrast, the BCP forms a wetting layer on the samples without a brush: a very thin, carbon-rich layer of polymer can be seen touching the substrate in Figure 3.10B and 3.10C, indicating that the polar PVBD block wets the oxide surface of Si and Cr. In addition, a ~5 nm layer of PDSS lies above the PVBD block, which is undesirable. It is unclear whether this thin layer of organosilicon polymer would prevent successful pattern transfer. Previous results[108] have shown that organosilicon polymers etch quickly when

first exposed to oxidizing plasma, and only after extended etching does enough SiO_x accumulate in the polymer film to form a substantial etch mask.[116] It is plausible that pattern transfer can be achieved for the orientation of domains in Figure 3.10B. However, pattern transfer at the 5 nm length scale in DSA samples is more complex and is outside the scope of this manuscript.

Another interesting difference between the three STEM/EELS results is the position of the BCP domains in relation to the NIL lines at the free surface. Samples assembled on SiO_2 (Figure 3.10 A&B) have PVBD and PDSS domains that appear to alternate aligning over the guide line. This is indicative of a mismatch between the natural periodicity of the BCP and the periodicity of the NIL guide lines at the pitches sampled. The sample prepared on chromium (Figure 3.10C) was imaged at a different pitch and the misalignment has disappeared.

Applying a brush before BCP assembly offers clear advantages for processing DSA films; however, the non-selective grafting of the brush to the NIL lines produces defective BCP alignment. Efforts are underway to develop brush chemistry and processing that offers contrast in the form of different reactivity with the substrate and the etched resist, such that the surface energy of these materials can be tuned separately. That work will be reported in a separate paper.

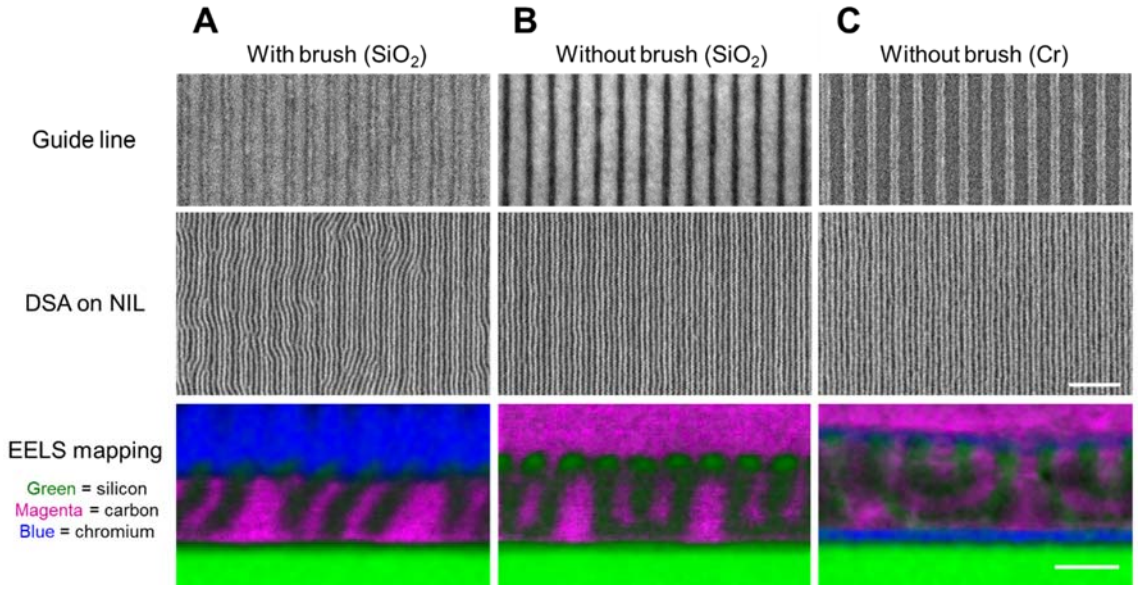

Figure 3.10. Images of NIL guide lines (top), BCP self-assembly (middle) and cross-sectional STEM in conjunction with EELS mapping (bottom) for three surfaces investigated in this study: (A) SiO_2 with brush, (B) untreated SiO_2, and (C) thin Cr_xO_y (2 nm) on SiO_2. The height of the NIL lines for the samples made on SiO_2 and Cr_xO_y is approximately 12 nm and 8 nm, respectively. BCP features for the samples made on SiO_2 were etched before STEM analysis, while the sample made on Cr_xO_y was not. The starting BCP film thickness for all three samples was approximately 33 nm. The samples on SiO_2 were annealed at 190°C for 2 min, while the sample prepared on Cr_xO_y was annealed at 205°C for 10 min. Scale bar for the top-down SEM images is 100 nm. Scale bar for the cross-section EELS images is 15 nm.

3.4 CONCLUSIONS

We present a report of 5 nm DSA using a lamellar BCP guided by NIL-fabricated guidelines. Perpendicular orientation of PVBD-*b*-PDSS was achieved using only thermal annealing and sequential spin coating processes to deposit neutral surface treatments at the substrate and/or the free interface. DSA quality was affected by multiple factors, but arguably the most important was the presence or absence of a neutral brush at the substrate interface. Absence of the brush polymer promoted nearly defect-free assembly

over large areas with guiding patterns thin enough for subsequent pattern transfer. However, the high surface energy of SiO_2 and oxidized chromium caused through-film defects and produced a thin BCP wetting layer at the substrate surface. Grafting a neutral brush to the interspace surface eliminated the through-film defects caused by the highly polar substrate. However, the chemical contrast between the NIL lines and the substrate was also reduced because the brush grafts to both surfaces. Future work will focus on optimizing the brush chemistry and processing to further minimize the height of the NIL features required for defect-free DSA and achieve selective functionalization of the substrate.

3.5 EXPERIMENTAL

3.5.1 Materials

The synthesis of the VBD monomer and the neutral brush are described below. Synthetic procedures for the block copolymer and top coat are described elsewhere.[115] Solvents were purchased from Sigma Aldrich and used as received.

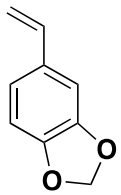

5-vinylbenzo[*d*][1,3]dioxole- A 1L round bottom flask was equipped with a stir bar and flame dried. Triphenylphosphonium iodide (119.0 g, 293.1 mmol, 1.1 eq) and dry THF (300 mL) were added under nitrogen. The slurry was cooled to 0˚C in an ice bath. Potassium *tert*-butoxide (32.9 g, 293.1 mmol, 1.1 eq) was added under nitrogen portionwise. The white slurry turned bright yellow. Piperonal (40.0 g) was dissolved in 100 mL of dry THF and added slowly

via syringe needle. After 5 minutes, the slurry became white. After 1.5 hr, TLC showed that there was still unconsumed piperonal. An additional 10.7 g of triphenylphosphonium iodide and 3.0 g of *tert*-butoxide was added the reaction vessel. The reaction was stirred for an additional 3.5 hrs. TLC showed that that the piperonal was completely consumed. The reaction was quenched with 5 mL of water. The solids were filtered off, and the solvent was removed *via* rotary evaporation. The crude product was passed through a plug of silica using 1:9 ethyl acetate:hexanes as the eluting solvent. The solvent was removed using rotary evaporation and the product was dried *in vacuo*. The monomer was distilled (BP: 46-49˚C at 27 mTorr) prior to anionic polymerization to yield 33.9 g (86% yield) as colorless oil. ^{1}H-NMR (400 MHz; $CDCl_3$): 6.97 (d, J = 1.7 Hz, 1H), 6.85-6.83 (m, 1H), 6.77 (d, J = 8.0 Hz, 1H), 6.63 (dd, J = 17.5, 10.8 Hz, 1H), 5.96-5.95 (m, 2H), 5.58 (dd, J = 17.5, 0.8 Hz, 1H), 5.14 (dd, J = 10.8, 0.8 Hz, 1H). ^{13}C-NMR (400 MHz; $CDCl_3$): 147.9, 147.3, 136.3, 132.1, 121.1, 111.9, 108.2, 105.4, 101.0. HRMS (CI) m/z for $[M]^+$ calcd for $C_9H_8O_2$ 148.0524; found 148.0521.

The anionic polymerization procedures used to synthesize PVBD-*b*-PDSS have been reported elsewhere.[115]

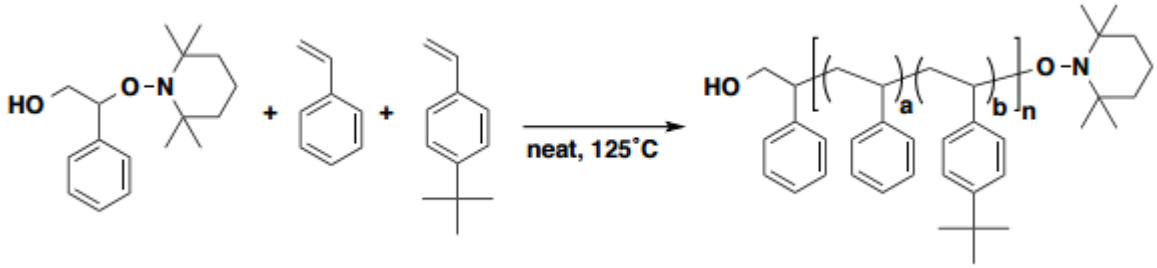

Neutral brush polymer- Inhibitor was removed from all monomers with basic alumina. A round bottom flask equipped with a condenser was charged with a stir bar, the NMP initiator[137] (0.38 g, 1.66 mmol, 1 eq), styrene (8.30 g, 8.30 mmol, 47.9 eq) and 4-tert-butylstyrene (25.49 g, 147.9 mmol, 88.3 eq). The solution was degassed by sparging with nitrogen for 30 minutes. The degassed solution was then placed in an oil bath and stirred at 125˚C. After 18.6 hrs, the reaction vessel was quenched to 0˚C. The polymer solidified upon cooling. Approximately 150 g of THF was added to dissolve the polymer. Precipitation two times in 1200 mL of methanol resulted in a fine white powder. The polymer was dried at 60˚C under vacuum overnight. The mass of the recovered polymer was 19.6 g (57%).

3.5.2 Guide line preparation

150 mm <100> silicon wafers were purchased from WRS materials and either used as received or first coated with a thin film of sputtered chromium (2-3 nm). Chromium deposition was performed using an AJA International ATC 2200-V sputtering system. A 20 nm-thick acrylate-based NIL resist film was deposited onto the wafers and subsequently imprinted using a Molecular Imprints Imprio HD 2200 Nanopatterning

System. The NIL template produced a pre-pattern with spaces between 40 and 50 nm in pitch in an annular band approximately 2.4 mm wide. Each patterned region was approximately 100 x 200 um in size and only contained lines with a single pitch. Trim etching was performed by exposing the NIL resist to an oxygen-based plasma in an Oxford Plasmalab System 100 etcher. Generally, wafers were trim etched by covering ¾ of the wafer with another blank wafer so only one quarter section of the wafer was exposed to RIE at a time. In this way, 4 different etch splits could be run on the same wafer. Some samples were characterized by AFM and SEM analysis after trim etching.

3.5.3 BCP and top coat processing

Spin coating and annealing were performed on a Brewer Science 100CB spin coating/hot plate station. BCP films of various thicknesses were spun from MIBK onto the trim-etched guide lines. To achieve grapho-epitaxy, BCP films were spun from a 0.9 wt% solution at 3000 rpm. Thicker films could be spun from 1.2 wt% solutions at 2000 rpm to cause the BCP to overfill the NIL lines. A 15 nm film of a top coat in TMA-salt form was subsequently spin-coated from methanol directly onto the BCP film. For the highest quality DSA, the film stack was annealed at 205°C for 10 mins on an open air hotplate. For SEM analysis, the film stack was then exposed to an oxygen-based RIE step for 90 s to fully remove the top coat and lightly oxidize the PDSS domains. For pattern transfer processes, the excess top coat material was first removed by stripping in aqueous TMAH for 30 s, followed by rinsing with water and IPA for 15 s each. The exposed BCP

film was then exposed to an oxidizing etch on a Lam Flex RIE tool. The pattern was transferred into underlying Cr and spin-on carbon films using sequential RIE processes.

3.5.4 Thin film analysis

SEM micrographs of NIL patterns, BCP films and chromium templates were obtained using a Raith150-Two system operating at an accelerating voltage of 10 kV. AFM height data was obtained from a Bruker system operating in tapping mode. Cross-sectional STEM and EELS images were obtained from Nanolab Technologies, CA. Film thickness measurements were made on a Nanometrics reflectometer (model # 1000-01195). SEM images were scored using custom computer software.

3.6 Acknowledgements

Yusuke Asano synthesized the block copolymer and top coat used in this chapter. Michael Maher synthesized the neutral brush. XiaoMin Yang, Michael Maher, and Greg Blachut contributed a large amount of time and effort to develop and optimize the DSA process. Steve Sirard developed all of the etch processes used for pattern transfer. Special thanks to Nanolab Technologies for generating the STEM/EELS images.

Chapter 4: Selective Surface Modification using Polymer Brushes

Polymer brushes are capable of reacting with hydrophilic surfaces like SiO_2 to create "neutral" interfaces that promote perpendicular block copolymer (BCP) orientation.[103] Even a thin layer of polymer attached to the substrate can prevent the BCP film from "seeing" the surface and forming unwanted wetting layers. Similar to crosslinkable surface treatments (XSTs), the composition of random copolymer brushes can be tuned to create non-preferential surfaces. Unlike XSTs, however, brushes are capable of grafting selectively to certain substrates without creating conformal films. The brush only reacts with the surface and not with other brush polymer chains. This property is required for many DSA processes where the neutral layer must be deposited *after* the guiding features are patterned.[138] The selectively of the grafting reaction can even be adjusted to favor the substrate over other materials on the surface; however, this is not always the case.

This chapter describes the limitations of polymer brushes for DSA on silicon substrates. Our studies indicate that polymer brushes can be grafted selectively in the presence of some, but not all materials. This selectivity depends greatly on how the substrate is processed beforehand. For applications where selectivity cannot be achieved between SiO_2 and polymer guidelines, we propose replacing silicon oxide with a thin film of oxidized chromium. Based on the studies in Section 4.3, oxidized Cr (Cr_xO_y) reacts readily with organic molecules and polymer brushes at low temperature. The first

experiments for the grafting studies on chromium were performed by Greg Blachut, and more information on this initial work can be found in Chapter 5 of his dissertation.

4.1 Introduction and Brush Synthesis

The term "brush" typically refers to any polymer that can be chemically or physically tethered to a surface.[139] These polymers are useful for controlling the surface properties of bulk and nanoscale materials,[140] and applications for polymer brushes range from stabilizing colloidal particle solutions[141] to providing corrosion resistance for metal surfaces.[142] Brush films usually consist of a monolayer of tethered polymer chains which are capable of mitigating strong interactions between intimate surfaces. Because polymer chains occupy a finite volume, the attachment process tends to produce a monolayer of densely-packed molecules, which stretch away from the surface to minimize the energetic penalty for self-interaction. This polymer chain stretching causes the brush film to exhibit unusual properties not found in polymer solutions or melts.[143]

The characteristics of brush films are largely determined by how the polymer chains are attached to the surface.[144] Processes for chemically bonding polymers to a surface can be roughly divided into two categories: "grafting to"[145–147] and "grafting from".[148,149] For brevity, physical grafting processes are not considered here. "Grafting to" processes involve a chemical reaction between a surface and a polymer. The brush polymer is typically functionalized at one end of the polymer chain. The grafting reaction between the surface and the polymer can take place immediately if the materials are reactive enough.[150] However, some energy is usually required to encourage covalent

bonds to form. For instance, hydroxyl-terminated polymers react with SiO_2 surfaces during thermal annealing at high temperatures (>200°C).[151] Polymer molecules typically react with surfaces as random coils instead of elongated chains. Therefore, the chain packing density for "grafting to" processes tends to be lower than for "grafting from" processes.[140] However, brush surfaces can be generated very quickly and reproducibly, since conformal polymer films can be deposited by spin coating. High temperature annealing also produces uniformly saturated surfaces.

"Grafting from" processes grow polymer chains directly from the surface. The initiators for polymerization are usually attached to the surface chemically or generated by other reactive processes.[152,153] Since small molecule initiators can cover surfaces at high densities, the resulting brush grafting density is also much greater. However, it can be difficult to characterize the molecular weight and dispersity of "grafted from" polymers after polymerization. In addition, the time, variability, and safety associated with growing polymer films from a surface is not suitable for some manufacturing processes.

For DSA applications, brush uniformity is important for consistent processing; thus, "grafting to" processes are preferred. The most common brush-substrate chemistry is the reaction between silicon oxide and a terminal hydroxyl end group.[154] At high temperatures, the end of the polymer chain reportedly undergoes dehydration to form an Si-O bond with the surface.[155] Hydroxyl-terminated polymers with controlled molecular weights and compositions can be synthesized by a variety of polymerization techniques, and examples are shown in Scheme 4.1.

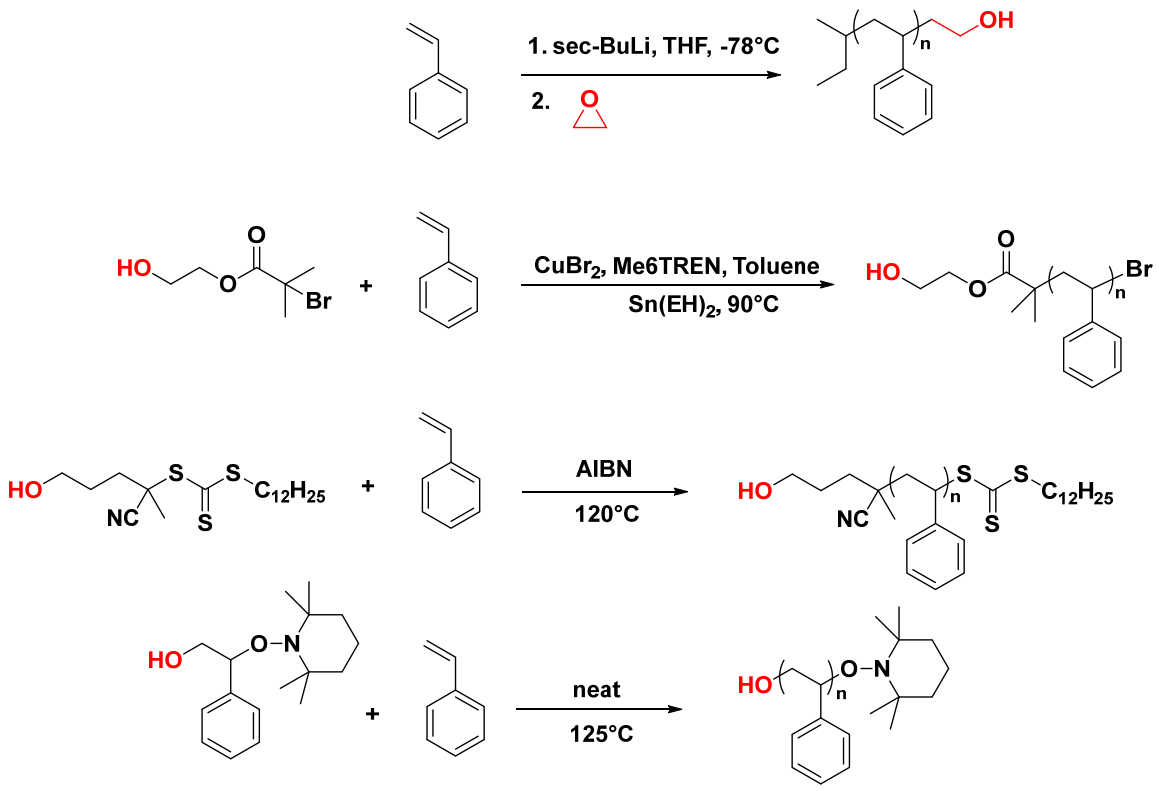

Scheme 4.1: Different synthetic routes for making hydroxyl-terminated polymers. Both anionic and controlled free-radical polymerization can produce polymers with controlled molecular weights and compositions.

The wetting behavior of a brush polymer film can be controlled by synthesis. Random copolymers of chemically distinct monomers can produce surfaces that are "neutral" and promote the formation of perpendicular BCP features. Hawker et al.[154] was the first to demonstrate that random copolymers of styrene and methyl methacrylate could be used to balance the surface interactions of PS and PMMA. As a result, brush polymers have become important materials for BCP lithography, especially for processes where a neutral surface is desired in some, but not all areas of the substrate.[123,129,131,138]

4.2. THE LIMITS OF BRUSH POLYMERS FOR DIRECTED SELF-ASSEMBLY

Many DSA processes used in high volume manufacturing utilize sparse, lithographically-defined pre-patterns to guide BCP domains. In some processes, the pre-pattern must be fabricated first to achieve the feature sizes required for alignment. Consequently, the regions between the pinning lines must be rendered neutral after the patterning step is completed. This is typically accomplished by grafting a brush polymer film to the interspace surfaces. It is usually desirable to only graft brush to the exposed substrate to avoid polluting the surface of the guiding feature. The chemical contrast between the pre-pattern lines and the background neutral surface is critical for producing defect-free alignment, especially for chemoepitaxy processes.[56]

In a typical "LiNe" process flow,[132] the top and side surfaces of the guiding pattern are fully exposed to the brush polymer during the grafting step. However, a report by Williamson et al[156] claims that the oxidized portion of the sidewall does not chemically react with hydroxyl-terminated polymers. This selectivity means three-tone chemical patterns can be created, as depicted in Figure 4.1.

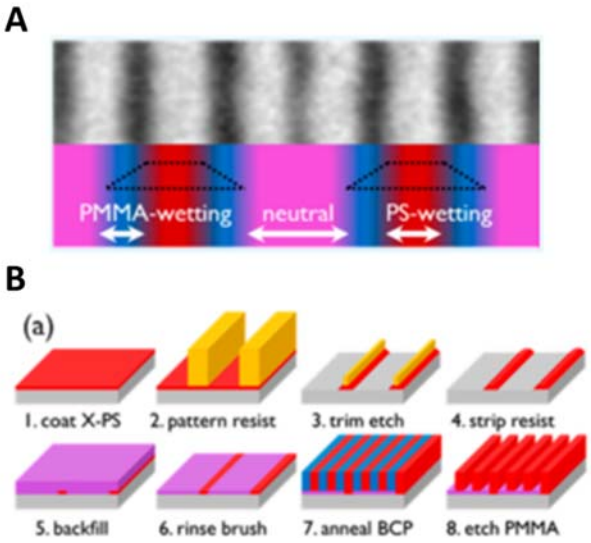

Figure 4.1: (A) A CD-SEM image and cartoon depicting the three-tone guiding patterns used for DSA. (B) The process used for creating three-tone patterns. Reproduced with permission from Williamson, L. *et al*. *ACS Appl. Mater. Interfaces* **2016**, 8, 2704–2712. Copyright 2016 American Chemical Society.

Results from our group have corroborated the results from Williamson et al., to an extent. Researchers at HGST demonstrated that polystyrene could be used as the material for both the pinning lines and the background substrate surface for DSA.[131] However, this is only possible if the sidewalls of the pinning line have been previously oxidized by a trim etch step. Similar to the LiNe flow, a preferential polymer mat is first patterned and etched to create the guiding features before backfilling the exposed substrate with a polymer brush. This process can be seen more clearly in Figure 4.2. The excellent BCP alignment achieved by this double-sidewall guided process is proof positive that the polystyrene brush used in this study can be grafted to a substrate without bonding significantly to another oxidized polystyrene surface. Without this selectivity, the guiding

interfaces depicted in Figure 4.2B would be smothered by the brush and unable to promote BCP alignment.

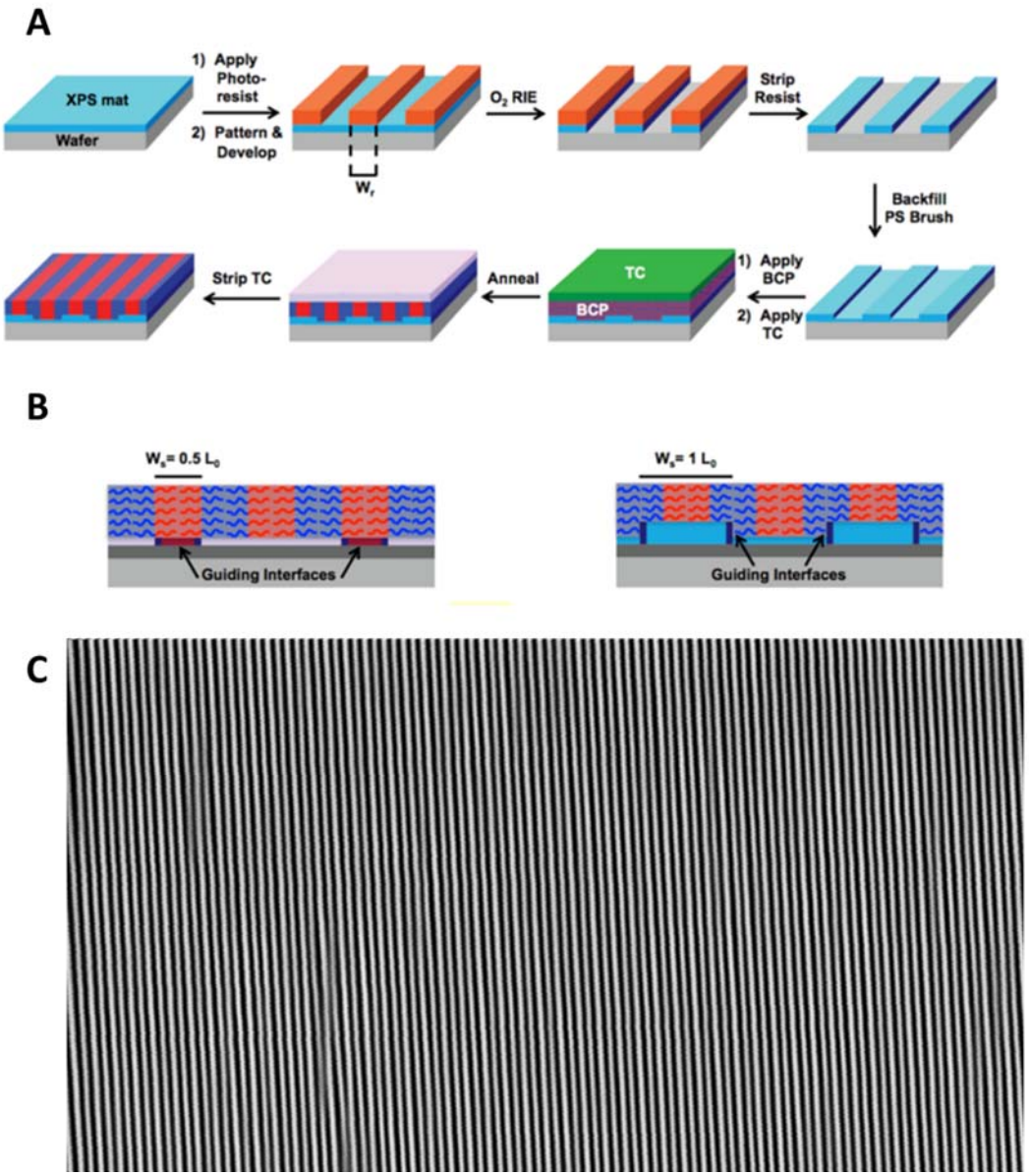

Figure 4.2: (A) The process for creating sidewall-guided DSA. (B) A cartoon depicting how the oxidized sidewalls interact with the block copolymer domains. (C) Line/space patterns from BCP assembly which have been transferred into a silicon substrate. Reproduced with permission from Cushen, J. *et al*. *ACS Appl. Mater. Interfaces* **2015**, *7*, 13476–13483. Copyright 2015 American Chemical Society.

These results are further corroborated by experiments performed at UT, which can be seen in Figure 4.3A. A hydrophobic brush was spun coat on various substrates and annealed at high temperatures to induce bonding between the brush and the surface. After removing the brush, a thin film of PMOST-*b*-PDSS BCP was deposited on the surface and annealed to produce island/hole features. The BCP behavior served as a diagnostic test for probing the wetting behavior of the surfaces before and after treatment with the brush.[115] Both polystyrene (PS-XST) and tert-butylstyrene (PtBuSty-XST) were tested in this study. PS-XST and the corresponding oxidized surface wet the polar PMOST block, as evidenced by the formations of island topography after depositing and annealing a 1.75 L_0 BCP film. A hydrophobic brush was applied to the oxidized PS-XST surface and annealed at 250°C for 5 minutes. In the control experiment, this brush polymer wets the PDSS block when grafted to a bare SiO_2 surface. When this brush was applied and annealed on the oxidized PS-XST surface, no change in wetting behavior was observed for the BCP, indicating the no reaction took place between the brush and the oxidized surface.

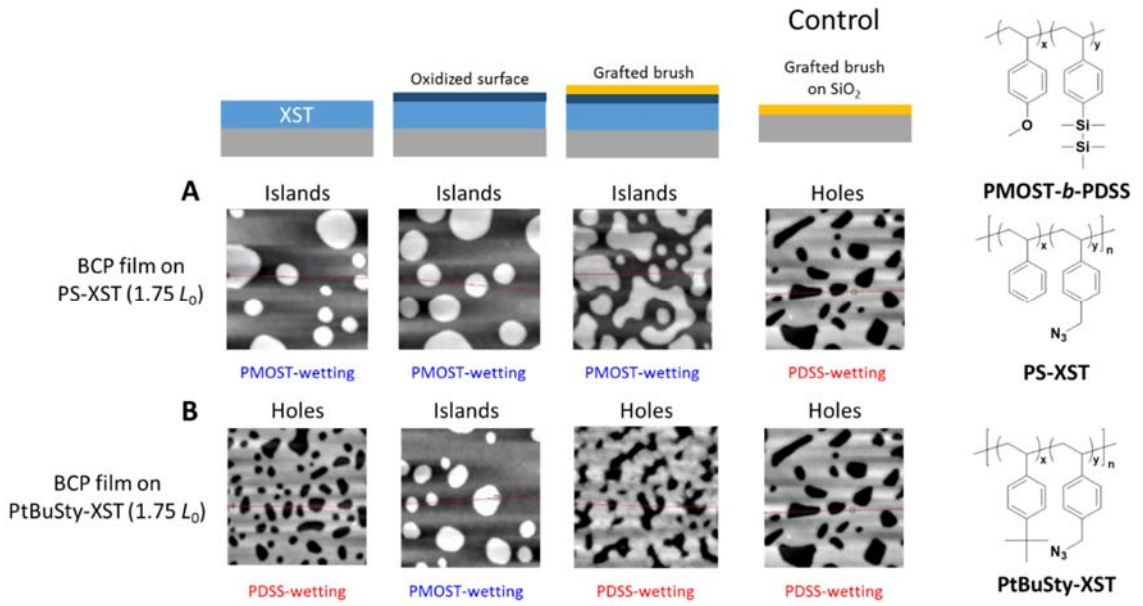

Figure 4.3: Results from an experiment to determine if polymer brushes react with oxidized polymer surfaces. The wetting behavior of the surface was determined by depositing BCP films on top of various surfaces and thermally annealing the samples in air to produce island/hole topography. The resulting films were imaged by AFM. Samples were made using both a (A) PS-XST and (B) PtBuSty-XST polymer surface. BCP films were annealed at 180°C for 10 mins and the brush grafting step was performed at 250°C for 5 mins.

The same experiment was repeated with a PtBuSty-XST, which is non-polar and normally wets the silicon-containing block. When oxidized, the PtBuSty-XST wets the polar PMOST block. However, after attempting to graft a hydrophobic brush to the surface, the wetting behavior switches again to wet the PDSS block, indicating that the brush does attach to the surface enough to cause a practical change in wetting behavior. This type of non-selective grafting could negatively affect the performance of a DSA process where brush polymer is capable of reacting with oxidized polymer surfaces at high temperatures. For example, the DSA process described in Chapter 3 is limited by

this type of non-selective grafting between the substrate and oxidized nanoimprint lithography (NIL) resist features.

When selectivity cannot be achieved with saturated surface grafting, it may be possible to find a small time/temperature window where the substrate can be rendered neutral without significantly affecting the chemistry of the guiding pattern.[136] However, a more elegant solution would be to find a brush/substrate chemistry with a lower activation energy. At lower grafting temperatures, the amount of bonding that takes place between organic materials might be significantly diminished, which would create more selective grafting between the brush and substrate. In the course of our search for such a surface, we found that oxidized chromium films are very reactive with organic materials at low temperatures. The rest of this chapter details the experiments performed to determine how thin films of oxidized chromium could potentially be used to improve the selectivity of grafting processes.

4.3 Selective Grafting Chemistry on Chromium Thin Films

Our inspiration for testing oxidized Cr films came from recent studies[157–159] demonstrating that small molecules with specific functionalities can be covalently attached to oxidized CrN surfaces. Activating the CrN surface with plasma allowed both alkene- and alkyne-functionalized hydrocarbons to chemically react with the strongly oxidizing surface. In addition to the length of the alkyl chain, the authors observed that the temperature used for the grafting step changed the water contact angle of the modified CrN surface. Increasing the temperature of the reaction increased the hydrophobicity of

the resulting surface, ostensibly because the alkene/alkyne functional groups react more quickly with the surface at higher temperatures and produce more densely packed films.

A number of small molecules were screened to determine if the same type of grafting reaction could be achieved on oxidized Cr films. The goal of this study was to determine which types of chemical moieties were capable of modifying the Cr surface, and then compare the surface energies of both Cr and oxidized NIL resist after treatment to determine if any contrast in surface modification could be achieved. Water contact angle (WCA) measurements were used to obtain rough estimates of surface energy. The variability inherent to all goniometry measurements made quantitative analysis impossible; however, WCAs are useful for tracking general trends produced in experiments like the ones described below.

The first series of experiments was performed using alkene and alkyne compounds, which are known to bond well to CrN surfaces. Figure 4.4 shows the measured water contact angle of Cr_xO_y and NIL surfaces after treatment. Wafer coupons coated with a thin layer of Cr were briefly exposed to oxidizing plasma, and then immediately placed in a beaker filled with one of the molecules depicted in Figure 4.4, which had been preheated to 100°C on a hotplate. After 1 minute in the bath, the wafer was removed, rinsed with MIBK, and baked at 180°C for 1 minute to drive off any solvent not chemically bonded to the surface. This bake step also served as a model process step for the BCP annealing process. The water contact angle of the untreated Cr wafer was less than 15°.

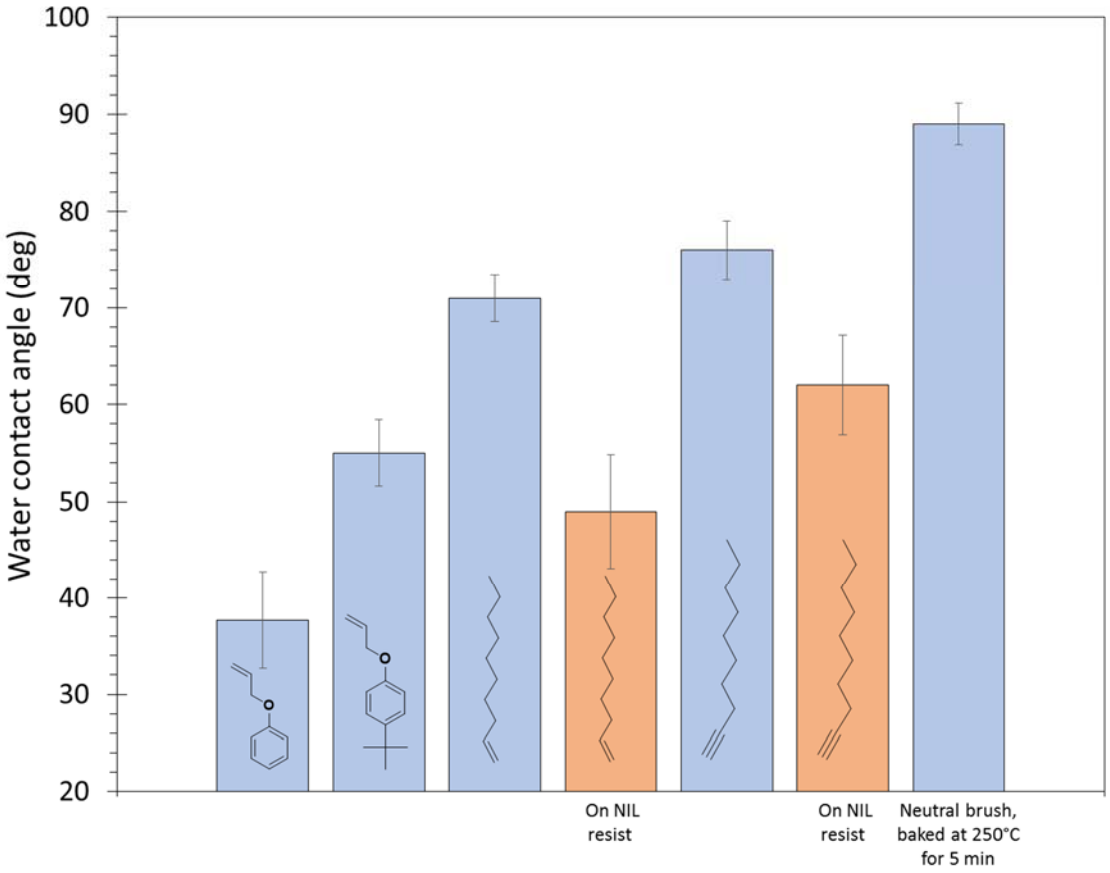

Figure 4.4: Water contact angles for Cr_xO_y and NIL surfaces after reacting with various alkene and alkyne functionalized compounds at 100°C. The data colored in orange represents NIL resist samples.

In line with the reported results for CrN films, all of the molecules tested with alkene or alkyne functional groups improved the hydrophobicity of the Cr surface. The extent of the WCA change depended on the chemical structure of the molecule being tested. To create analogs of the monomer components of the BCP, several phenyl allyl ethers were synthesized by the reaction shown in Scheme 4.2. These were tested instead

of the original styrene monomers, since styrenes tend to autopolymerize at high temperatures.

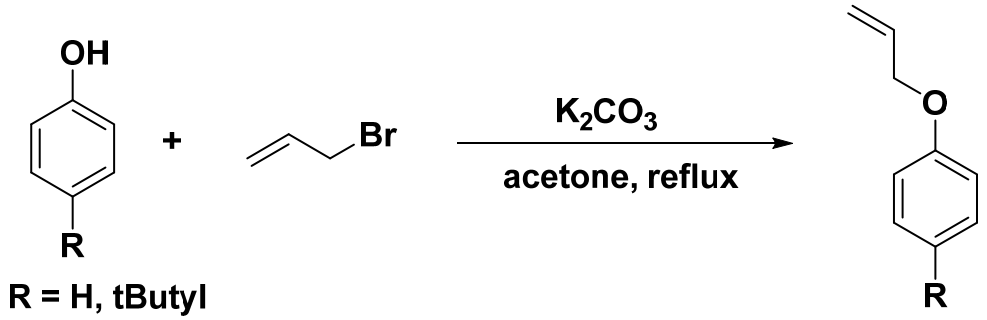

Scheme 4.2: Synthesis of phenyl allyl ethers.

The surfaces produced by the phenyl allyl ethers tended to be less hydrophobic than surfaces produced by 1-decene and 1-decyne, which have longer hydrocarbon chains. Importantly, when oxidized NIL resist was subjected to the same grafting procedure using 1-decene and 1-decyne, the resulting WCA was less than that of the Cr sample. However, the difference was less for 1-decyne, indicating alkynes may be less selective than alkenes for this particular application. As a reference measurement, a typical poly(styrene-*r*-tert-butylstyrene) brush capable of producing a "neutral" surface for BCPs was deposited and grafted to Cr_xO_y to determine the approximate WCA for a surface that promotes perpendicular BCP orientation. The WCA for the neutral brush was significantly higher than any of the surfaces produced using small molecules, but it's difficult to compare the efficacy of the treatments by WCA alone without testing to see whether or not the substrate can produce perpendicular BCP domains.

Ultimately, processing wafers by submersion in chemical baths at high temperatures is dangerous, so this strategy was abandoned in favor of using functionalized polymer brushes. Polymers produce thicker grafted films, which can potentially act as a more effective buffer layer between the BCP and the hydrophilic surface. Since alkenes are more capable of distinguishing an oxidized Cr_xO_y and NIL film, a set of alkene-functionalized random copolymers of styrene and divinylbenzene was synthesized according to Scheme 4.3.

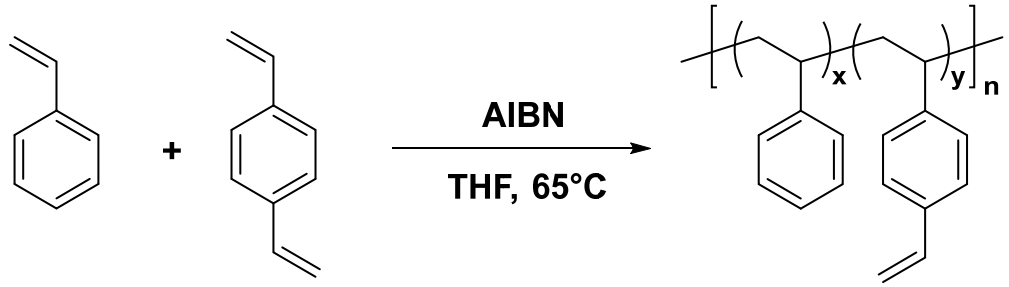

Scheme 4.3: Synthesis of poly(styrene-*r*-divinylbenzene) brushes

Incorporating vinyl groups directly into the polymer structure is a straightforward method of synthesizing materials with alkene functionality. However, if the polymerization conversion becomes too high, these materials can crosslink in solution. Several feed ratios of styrene to divinylbenzene were tested and it was determined that a 5 mol% loading of DVB could be polymerized for 1 hr without significant crosslinking. Several of these copolymers were testing using the grafting procedure mentioned previously at different temperatures, and the results of this study can be seen in Figure 4.5.

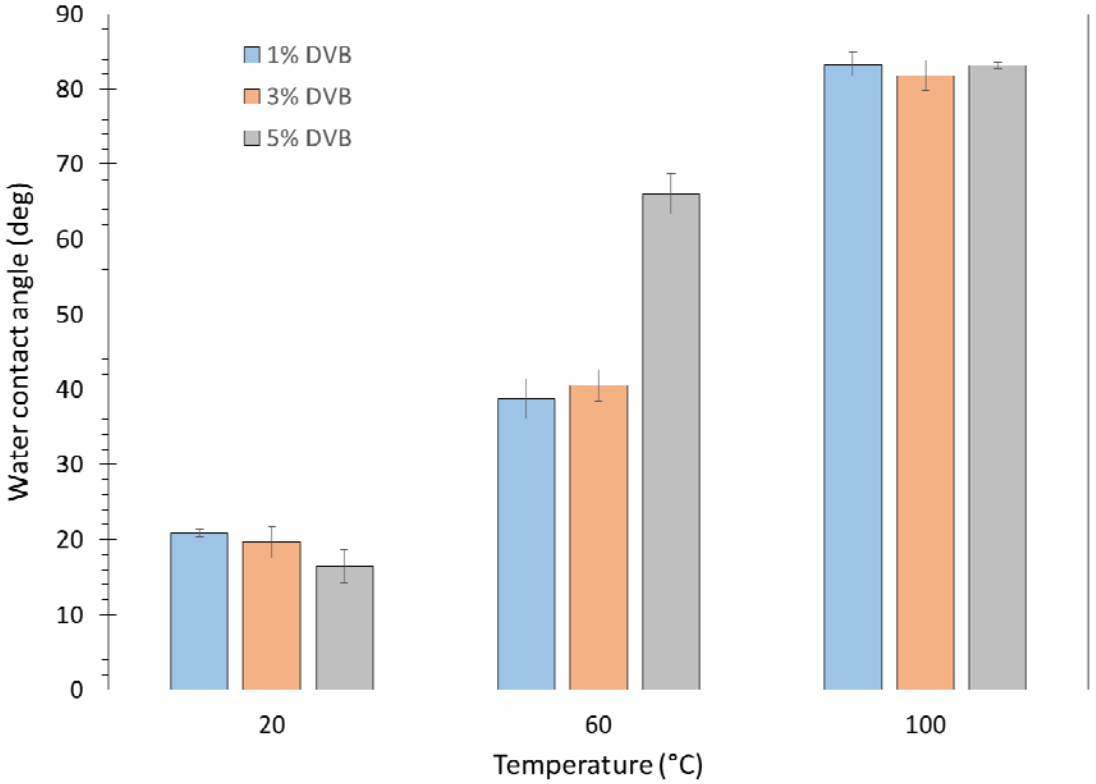

Figure 4.5: Water contact angle measurements taken after grafting various P(Sty-*r*-DVB) copolymers to Cr_xO_y films at 20, 60, and 100°C.

These results confirm that temperature plays a major role in changing the surface energy of the resulting Cr film, although the percentage of functional groups does not seem to have a major effect on the surface energy modification. This indicates the reaction between the Cr surface and polymer is potentially very sensitive to even small concentrations of reactive functional groups in the polymer film. In addition, the WCA obtained at 100°C are much closer to the WCA produced by the neutral polymer from Figure 4.4.

The results obtained for the 5% DVB polymer were compared to several other PS homopolymers synthesized by different polymerization methods. The results of this study can be seen in Figure 4.6.

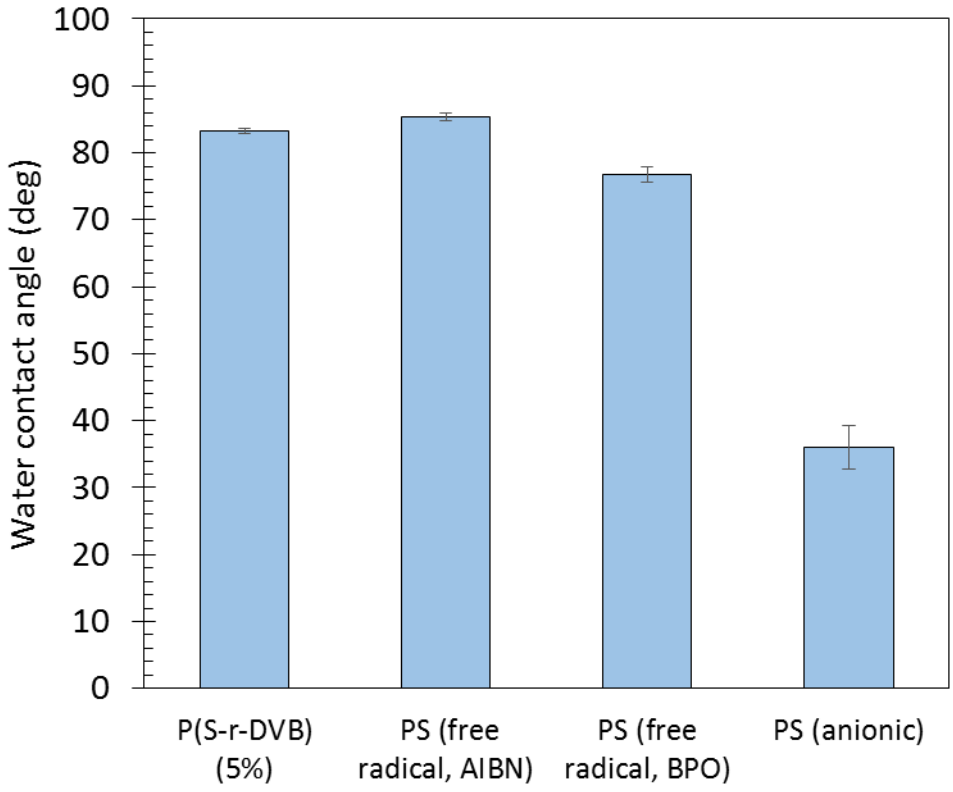

Figure 4.6: WCAs produced after reacting P(S-*r*-DVB) and various polystyrene homopolymers with Cr_xO_y surfaces at 100°C for 1 min. The two PS homopolymers synthesized by free radical polymerization were made using different free radical initiators.

Surprisingly, it was discovered that pendant alkenes were not required to create surfaces that had WCAs similar to the neutral brush polymer. Polystyrene homopolymers made by free radical polymerization initiated by AIBN or benzoyl peroxide may contain terminal nitrile or acetate groups, which could react with Cr surfaces similarly to alkyne

moieties. Indirect evidence for this hypothesis was also provided by testing a polystyrene homopolymer made by anionic polymerization, which should contain no functional groups besides aromatic rings and hydrocarbons in the polymer backbone. This polymer modified the Cr surface to a much smaller extent than either the free radical polymers or the P(S-r-DVB). Because the only chemical difference between the anionic PS and the free radical PS is the chemistry of the end group, the residual functionality from the AIBN/BPO may play a role in promoting surface attachment.

Although the extent of surface attachment for the anionic PS polymer was relatively small, it was still unusual that the WCA changed at all, given the lack of functional groups available for reaction. To exclude the possibility that the solvent from the polymer solution was responsible for reacting with the Cr surface and increasing the WCA, a film of anionic PS was dried in a vacuum oven at room temperature for 30 min to remove any residual solvent trapped in the film after spin coating. After annealing at 100C for 1 min, the measured WCA was 31.2 ± 1.2, indicating that the polymer itself was at least partially adsorbing to the Cr surface. Because the resulting WCA for the anionic PS was similar to the WCA obtained after testing the analogous phenyl ether small molecule in Figure 4.4, a number of other small molecules with no obvious functionality were tested to determine the scope of the reactions that modify the Cr_xO_y surfaces. The results of those tests can be seen in Figure 4.7.

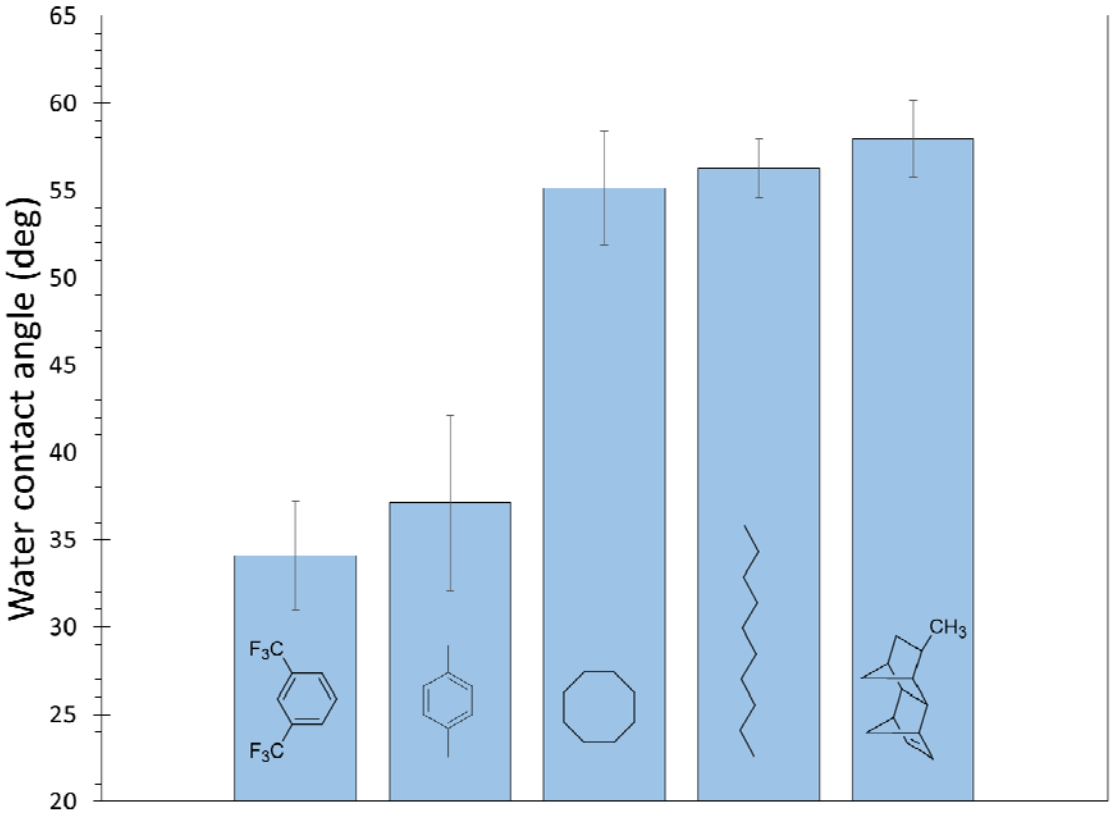

Figure 4.7: Measured WCAs after reacting Cr_xO_y films with various aliphatic and aromatic molecules without obvious functionalities. The films were processed in the same way as the samples from Figure 4.4. Freshly oxidized Cr films were placed in a beaker pre-heated to 100°C containing 5 mL of each compound. After one minute, the films were removed, rinsed with MIBK, and baked at 180°C for 1 min. The WCA was measured in triplicate for each sample.

Remarkably, pure hydrocarbons like n-decane and cyclooctane were capable of increasing the WCA of Cr_xO_y films to 56.3 ± 1.7° and 55.1 ± 3.3°, respectively (unmodified Cr_xO_y films have a contact angle of 15°). The mechanism behind this modification is not understood; however, because the WCAs for the Cr_xO_y films treated with xylenes and bis(trifluorobenzene) are significantly different from the films treated

with aliphatic molecules, the possibility that the experimental procedure is causing this unexplained difference is unlikely. The volatility of these compounds at 100°C makes them very unsuitable for DSA applications. However, this interesting surface chemistry could be explored in the context of other applications.

We decided to pursue two polymer families for further testing: the hydroxyl-functionalized brushes used for the DSA process described in Chapter 3, and copolymers synthesized by free radical polymerization using AIBN as an initiator. Given the hydroxyl-terminated polymers are much more challenging to synthesize than the free radical polymers, we were interested to see if their performance as brushes was comparable. Demonstrating that the hydroxyl-functionality is not necessary for robust surface modification would be an important result from a manufacturing standpoint.

The grafting selectivity that could be achieved using both polymer systems was evaluated by attempting to graft polymers from both families to both oxidized Cr and NIL surfaces. The results of these experiments can be seen in Figure 4.8.

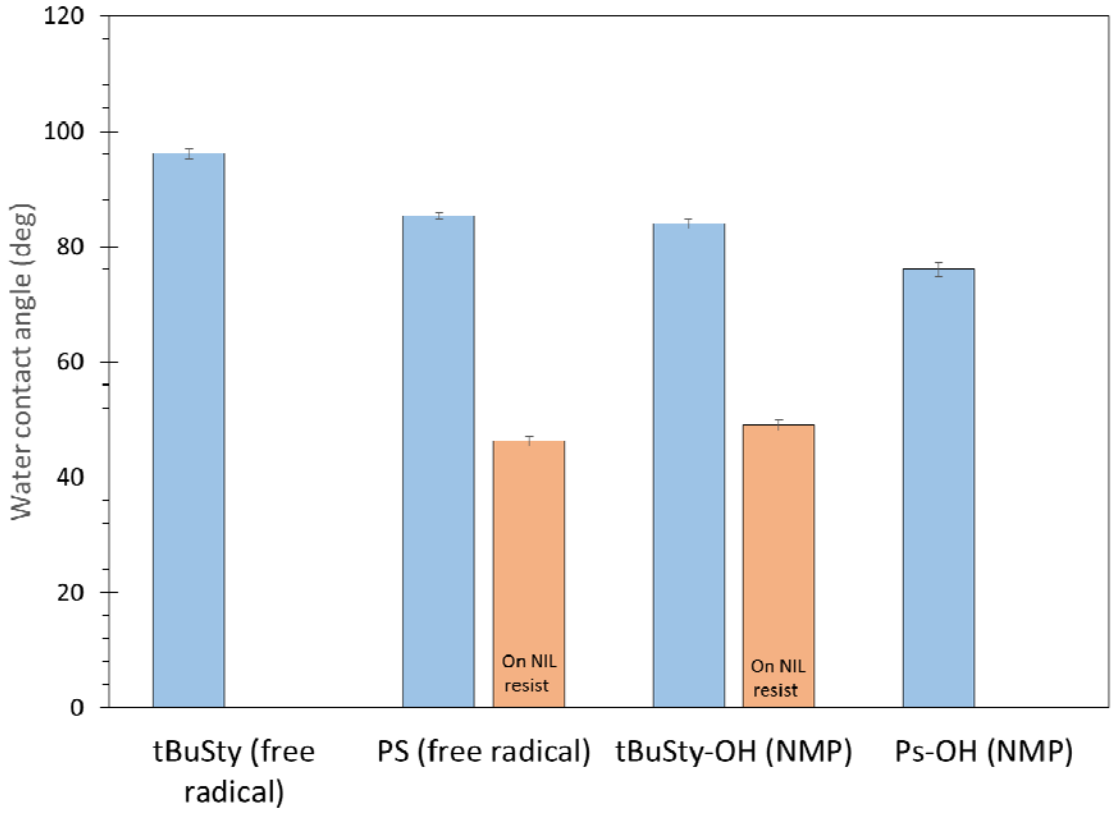

Figure 4.8: WCA results for polystyrene and poly(tert-butylstyrene) made by free radical and nitroxide-mediated polymerization (NMP). Polymer films were spun onto oxidized Cr and NIL films and processed by heating to 100°C for 1 minute, then rinsing with MIBK and baking again at 180°C for 1 minute.

In general, polymers made by free radical polymerization tend to produce more hydrophobic surfaces than the corresponding –OH terminated polymers made by nitroxide-mediated polymerization (NMP). For this small sample size, the WCAs for the surfaces produced by the free radical polymers are approximately 15° higher than the corresponding surfaces produced using the NMP materials. The amount of grafting selectivity achieved by both systems is comparable, however. For the free radical PS and

NMP tBuSty-OH, the WCA difference between the Cr_xO_y and the oxidized NIL is about 40°.

Ultimately, the purpose of grafting these polymers to Cr films is to create surfaces that facilitate the perpendicular orientation of BCP features. The islands/holes thin film test is a useful diagnostic technique for determining the wetting behavior of interfaces. In this case, the islands/holes test was used to determine an approximate window for neutrality based on the composition of the brush as well as the grafting temperature.

The results of the islands/holes experiments using PVBD-*b*-PDSS as a test material can be seen in Figures 4.9-12 below. For each sample, the standard procedure for grafting was carried out using the annealing temperature listed above each column. Afterwards, a PVBD-*b*-PDSS film was deposited on top of the Cr/brush film at the film thickness indicated by the L_0 for each row. Then, the film was baked at 180C for 10 min to form the topographical features. The terraced films were analyzed by AFM to determine the wetting behavior of the substrate.

From this experiment, it can be clearly seen that both the temperature of the grafting anneal and the composition of the brush affect which block wets the substrate. Multiple film thicknesses were tested for each annealing temperature to confirm the wetting behavior. While some of the results were obvious, others produced features which were self-contradictory or showed no features at all. The more straightforward results typically occurred at the more extreme boundary temperatures, while results that were more inconclusive appeared for the median temperatures.

In general, as the amount of tBuSty in the brush composition increased, the temperature required to produce a PDSS-wetting surface decreased. This result makes intuitive sense knowing that a 100% tBuSty brush annealed at 250°C on SiO_2 creates a PDSS-wetting film. For all samples, as the temperature increased, the WCA of the oxidized Cr film increased as well. Although these data are not shown here, the WCA does level off around 95°, regardless of the grafting temperature used.

All films gave full 1.0 L_0 features as measured by AFM. No half features were observed, which made identifying a definitive neutral surface somewhat difficult. However, the inconclusive results were bracketed by samples which produced obvious wetting behavior, so it was tentatively assumed that the polymer films grafted at these temperatures might be close to neutral.

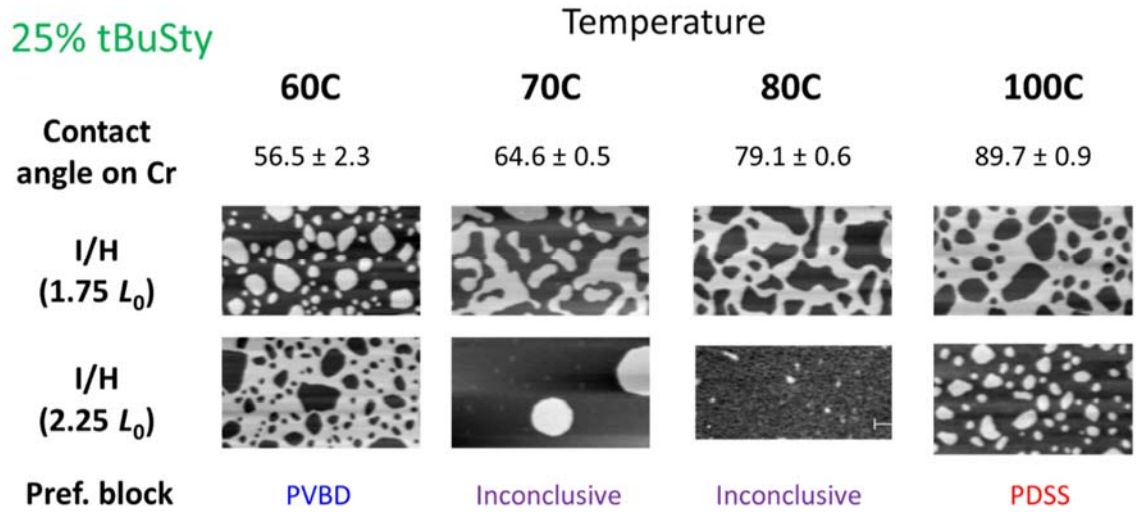

Figure 4.9: WCAs and AFM scans showing island/hole results for grafted surfaces using a 25:75 tBuSty:Styrene copolymer synthesized by NMP. The brush was grafted at several temperatures to determine the approximate window for neutrality.

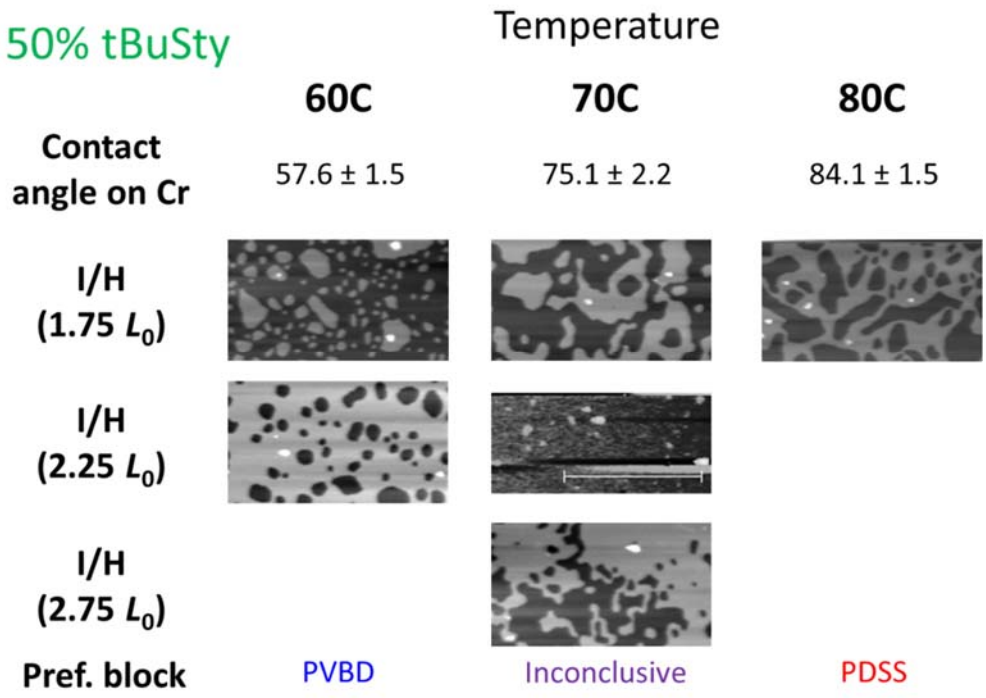

Figure 4.10: WCAs and AFM scans showing island/hole results for grafted surfaces using a 50:50 tBuSty:Styrene copolymer synthesized by NMP.

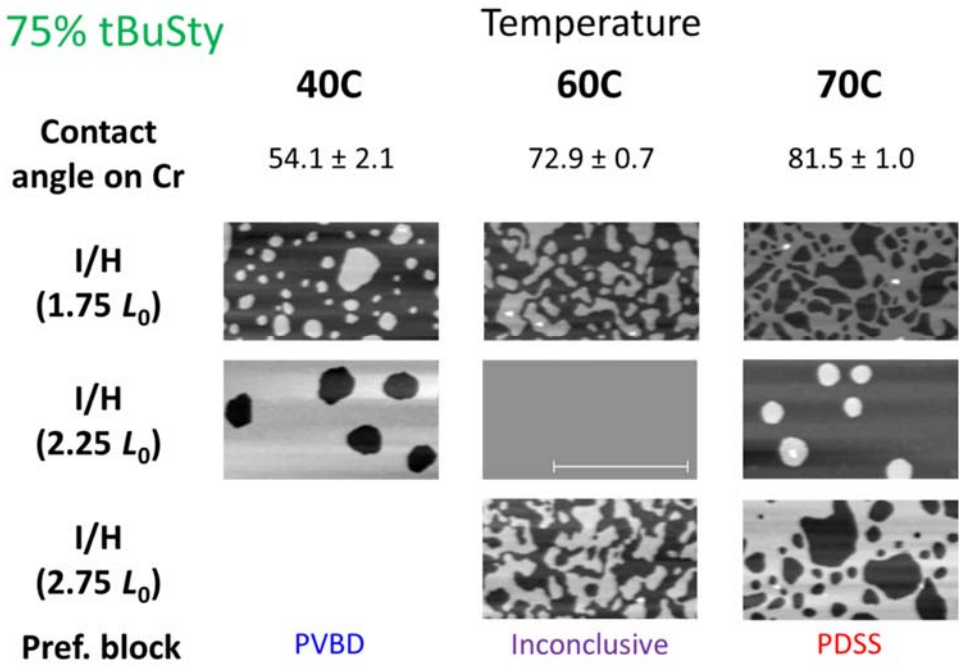

Figure 4.11: WCAs and AFM scans showing island/hole results for grafted surfaces using a 75:25 tBuSty:Styrene copolymer synthesized by NMP.

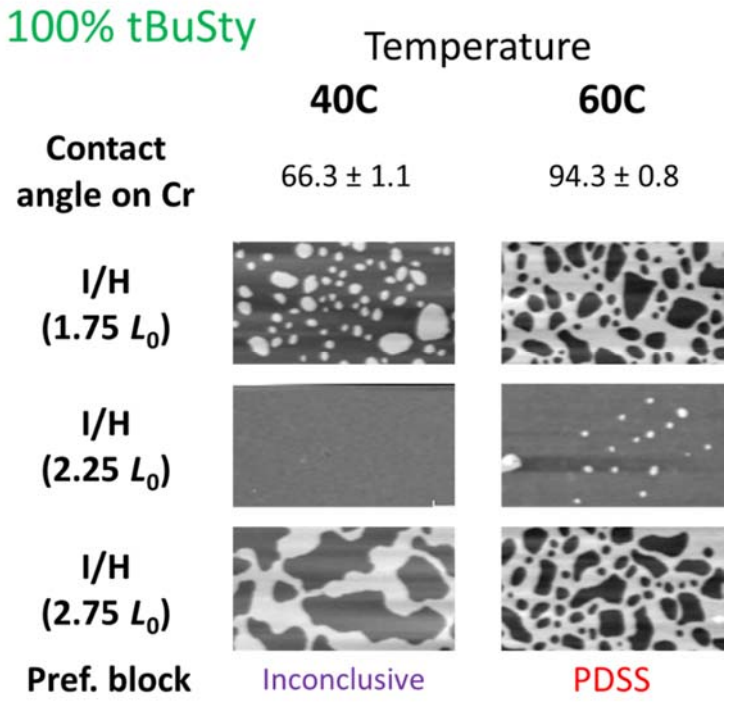

Figure 4.12: WCAs and AFM scans showing island/hole results for grafted surfaces using a 100% tBuSty copolymer synthesized by NMP.

To test the hypothesis that the "inconclusive" samples might indicate a neutral surface, BCP film stacks containing a neutral top coat and Cr-grafted brush films were annealed at 180C for 5 min, and subsequently etched and examined by SEM for perpendicular BCP structures (Figure 4.13).

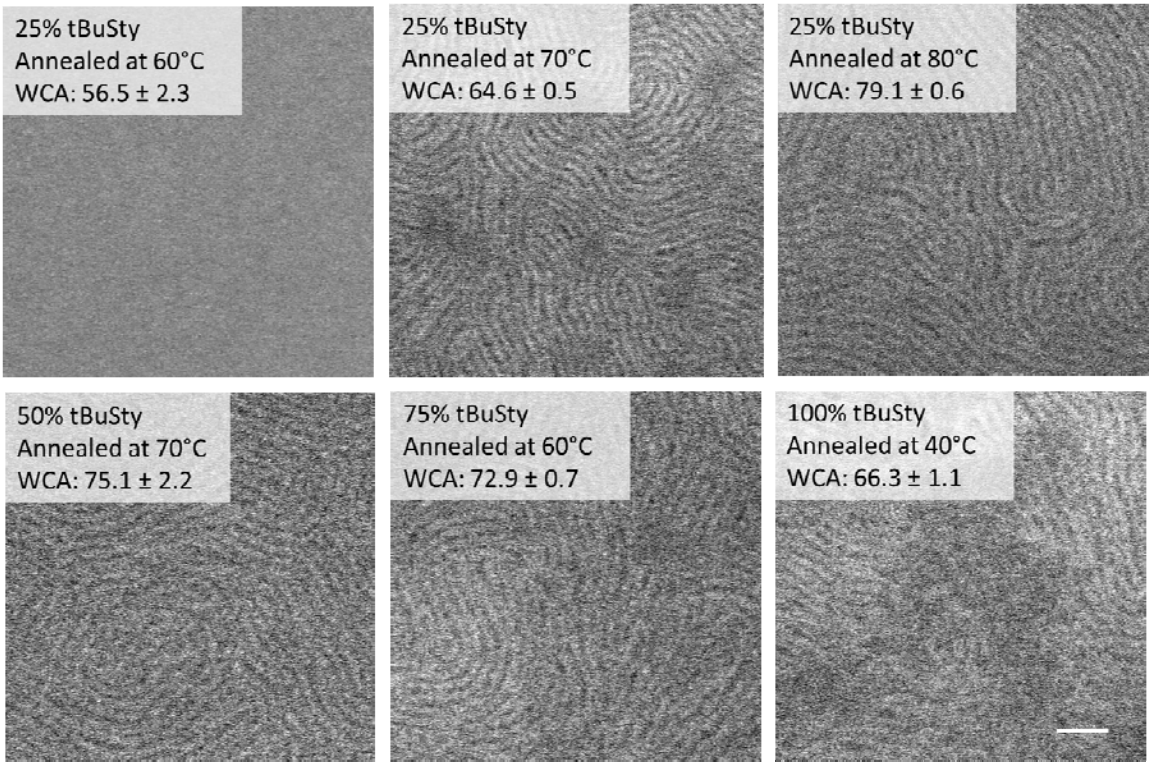

Figure 4.13: SEMs of BCP films sandwiched between a neutral top coat and a polymer-grafted Cr film. With the exception of the sample in the top right, every polymer composition/grafting temperature combination corresponds to an "inconclusive" result by the islands and holes test. Scale bar = 50 nm.

As a control, one of the annealing temperatures that produced a PVBD-wetting surface was used to attempt to generate perpendicular structures. As expected, only featureless films were produced after annealing, indicating parallel BCP orientation. The brush annealing temperatures that produced inconclusive results, in general, produced perpendicular BCP structures. For a few of the samples, patchy features indicative of non-uniform surface wetting could be seen.

For DSA applications, it has been shown that slightly off-neutral surfaces are desirable, since the preferential guide stripe affects the ratio of polar-to-nonpolar blocks

that's on the interspace surface. To determine if it was possible to produce parallel features using a PDSS-wetting condition, the 100% tBuSty brush was annealed at much higher temperatures to potentially induce more grafting and produce a more hydrophobic surface. These results can be seen in Figure 4.14.

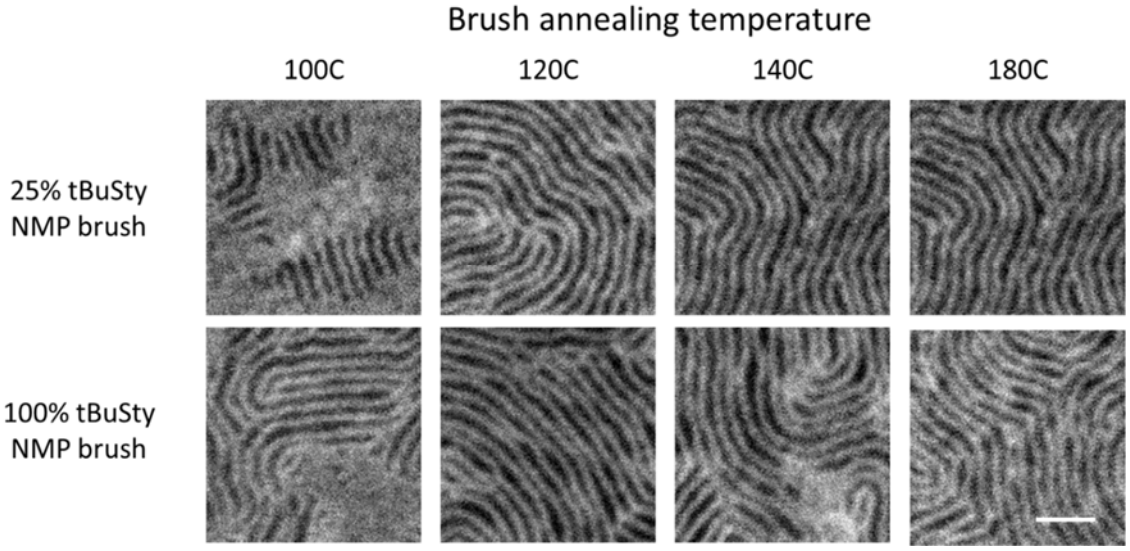

Figure 4.14: SEM micrographs of BCP films annealed between a neutral top coat and a PtBuSty-treated Cr film. The brush films grafted at high temperatures still produce perpendicular BCP lamellae. Scale bar = 50 nm.

The 25% tBuSty brush has been demonstrated to be neutral for PVBD-*b*-PDSS, so the fact that the BCP forms perpendicular features for even high annealing temperatures is expected. However, even the 100% tBuSty brush, which demonstrated preferential wetting behavior by islands/holes, produced perpendicular features at grafting temperatures as high as 180°C (although at higher temperatures, some patchy assembly was observed). While this contradicts the behavior from the islands/holes

experiments, the presence of the top coat could be driving the formation of perpendicular structures even in the presence of a preferential bottom substrate.

A similar set of experiments has also been performed for the polymers made by free radical polymerization. However, the samples have not yet been fully characterized, so these data will be published elsewhere.

To demonstrate that the surface energies of NIL resist and oxidized Cr could be tuned independently, samples of both surfaces were subjected to the same polymer grafting procedure and used as substrates for BCP orientation. The results of the experiment can be seen in Figure 4.15.

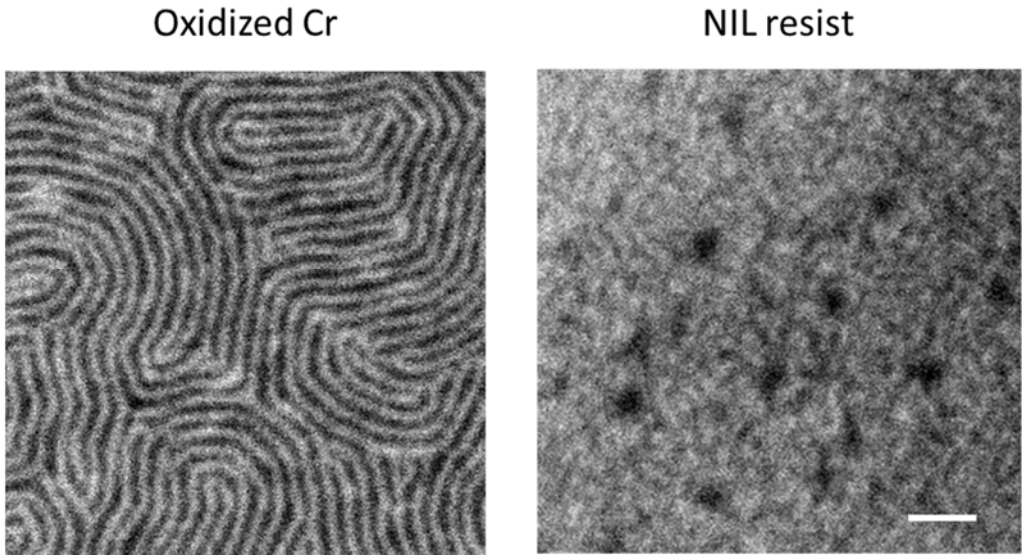

Figure 4.15: SEM micrographs of BCP assembly on oxidized Cr and NIL films after treatment with the same polymer brush at 100°C. After sequentially spin coating an 18 nm thick film of BCP and neutral top coat, the samples were annealed at 180°C for 5 mins. Scale bar = 50 nm.

After grafting a neutral brush to both surfaces at 100°C for 1 minute, only the oxidized Cr film was modified enough by the brush to produce perpendicular BCP features. The featureless film observed on the NIL resist indicates that one block of the BCP wets the bottom surface, ostensibly the polar block. This result is an encouraging sign that a practical difference in BCP wetting behavior can be created by exploiting the low temperature grafting of functionalized brush polymers to oxidized Cr films.

4.4 CONCLUSIONS

In summary, the limits of selective grafting between oxidized polymer surfaces and SiO_2 were explored. Under certain conditions, hydroxyl-terminated polymers are capable of selectively reacting with SiO_2 in the presence of etched organic materials, depending on the chemical composition of the etched material. In cases where selectivity cannot be obtained by process optimization, thin films of oxidized chromium may be used to graft polymer brushes at lower temperatures. Because the rate of the chromium-polymer reaction appears to be much faster than the rate of the corresponding polymer-polymer reaction at low temperatures, selective surface modification can be obtained.

A number of functional groups are capable of grafting to oxidized Cr films, including alkenes, alkenes, alcohols, nitriles, and possibly even purely aliphatic molecules. Small molecules tend to affect surface energy less than polymer films. The extent of modification to the oxidized Cr surface can be controlled by changing the grafting temperature and the composition of the grafted polymer. For BCP applications, a neutral process window can be found to produce perpendicular orientation in thin films

using these variables. Importantly, perpendicular BCP structures are not produced on corresponding films of NIL resist that have been subjected to the same grafting procedure. These results are encouraging for improving the DSA process described in Chapter 3. Future work will include auditioning these processes using real NIL structures for DSA. The performance of the selective grafting process will be evaluated based on the defectivity and through-film structure of the BCP domains after DSA processing.

4.5 EXPERIMENTAL

4.5.1 Materials

The synthesis of the NMP brushes used for the grafting studies has been reported elsewhere.[123] Solvents used for spin coating and removing excess brush were purchased from Sigma Aldrich and used as received. All chemicals used for the synthesis of the phenyl allyl ethers and free radical polymers were purchased from commercial sources. Styrene monomers were passed through an alumina plug before polymerizing to remove inhibitor.

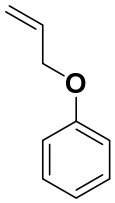

Phenyl allyl ether – A 2 L, 3 neck round bottom flask was equipped with a magnetic stir bar, reflux condenser, and addition funnel. Phenol (94 g, 1 mol) and 800 mL of acetone were added and the solution was heated to 50°C. Anhydrous potassium carbonate (165.8 g, 1.2 mol) was added in large portions and stirred. After 10 minutes, allyl bromide (121 g, 1 mol) was added dropwise *via* addition funnel over the course of 1 hour. Once the addition was complete, the heterogeneous

mixture was heated to reflux, stirred for 2 hrs, and then cooled to room temperature. The solids were filtered off, and the solvent was removed *via* rotary evaporation. The crude oil was dissolved in 500 mL of diethyl ether and washed several times with sat. K_2CO_3 to remove any residual phenol. When TLC showed the phenol had been completely removed, the solution was washed with 200 mL of water and dried over $MgSO_4$. The solids were filtered and the solvent was removed via rotary evaporation. The resulting oil was purified by vacuum distillation (BP: 75°C at 13 mTorr) to yield 102 g (76% yield) as a colorless oil. NMR spectra matched values reported in literature.[160]

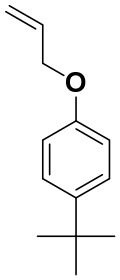

Allyl p-cymyl ether – Prepared as described for phenyl allyl ether using 4-tert-butylphenol instead of phenol. Isolated 91 g (61% yield) after vacuum distillation (BP: 129°C at 10 mTorr). NMR spectra matched values reported in literature.[161]

.

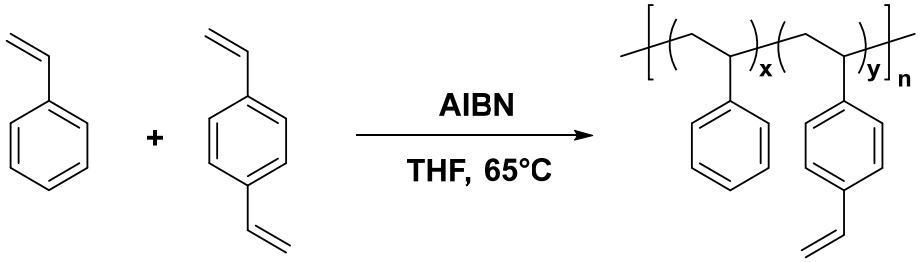

P(S-*r*-DVB): Three flame dried round bottom flasks equipped with magnetic stir bars and water condensers were charged with styrene (10.0 g, 96.0 mmol, 0.95-0.99 eq.), divinylbenzene (0.01-0.05 eq.), AIBN (0.01 eq.), and THF (50 mL). The solutions was

degassed by bubbling nitrogen for 30 mins, then plunged into an oil bath at 65°C for 75 minutes. The flasks were quenched in ice water to stop the polymerization. The THF was removed via rotary evaporation at 40°C until only a few mL remained. The polymer was precipitated three times from THF into MeOH and filtered to remove any monomer impurities. The resulting powder was dried *in vacuo*, and 100-800 mg (1-8% yield) of dry polymer was obtained.

4.5.2 Brush Processing

Unless otherwise noted, all samples were processed similarly. Thin films of chromium or NIL resist were briefly oxidized (10 s) in a plasma cleaner. Samples were then immediately placed in a bath (small molecule compound) or used as a substrate for spin coating a brush polymer from a MIBK solution. The samples were then heated at the prescribed temperature (100°C unless otherwise noted) for 1 minute. After heating, the samples were rinsed using MIBK, blown dry using pressurized N_2, and placed on a hotplate at 180°C for 1 minute. Afterwards, WCA measurements were made in triplicate using a goniometer.

4.5.3 Thin Film Analysis

WCAs were measured using a Rome-Hart NRL C.A. Goniometer. AFM scans were obtained using an Asylum MFP-3D Origin operating in tapping mode. A Brewer CEE 100CB Spincoater was used to coat all thin films. Ellipsometry was performed with a J.A. Woollam Co, Inc. VB 400 VASE Ellipsometer with wavelengths from 382 to 984

nm and a 65° angle of incidence. A Zeiss Supra 40 VP scanning electron microscope operating at 5 kV with the in-lens detector and a working distance of 2-5 mm was used to collect all SEM data. Brightness and contrast for all SEMs were uniformly enhanced using commercial image editing software.

4.6 ACKNOWLEDGEMENTS

The groundbreaking experiments for this project were done by Greg Blachut. Thank you for letting me continue the work you started. The NMP brushes were synthesized by Greg Blachut and Michael Maher. Special thanks goes to Benjamin Hausmann and Emily Young for your help with the island/hole experiments and characterization.

Chapter 5: Self-developing Block Copolymers for Lithographic Applications

5.1 Introduction

One of the most important steps in any BCP lithography process is transferring the BCP pattern into an underlying substrate.[49,162] To achieve the cleanest possible transfer, one block copolymer domain must first be removed selectively from the assembly to reveal a relief image. Selectively removing one block is normally accomplished in one of two ways: a chemical development using selective solvents,[163] or a dry etch using reactive ion etch (RIE) processes.[54,164]

Consider PS-*b*-PMMA. Thurn-Albrecht et al.[165] was the first to demonstrate that PMMA domains can be removed selectively by first exposing BCP films to UV light, followed by washing with acetic acid. This process is chemically selective because the PMMA block undergoes scission when irradiated with UV light, so the low molecular weight fragments of PMMA are dissolved under conditions in which PS is insoluble. This type of development has been generalized to include polymers that are joined by a photocleavable junction,[166,167] such that exposure to radiation followed by washing with selective solvent leads to the complete removal of one block. This process works well for features with low aspect ratios or perpendicular cylinder features that are embedded in a matrix of the other block. However, for lamellae features with high aspect ratios, capillary forces and swelling in the non-degradable block can lead to pattern collapse.[90] Figure 5.1A shows the effect of developing high aspect ratio PS-*b*-PMMA films using solvent.

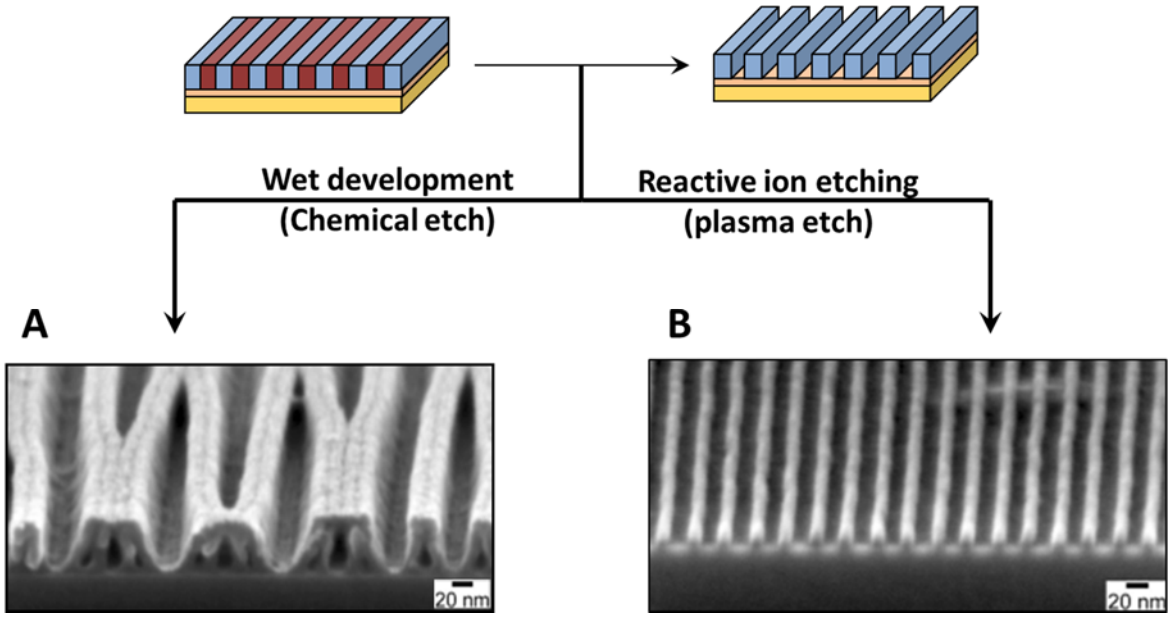

Figure 5.1: Identical PS-*b*-PMMA films developed using (A) exposure to UV light followed by acetic acid washing and (B) oxygen-based RIE process. Reproduced with permission from Ruiz, R. *et al*. *ACS Nano* **2011**, *5*, 79–84. Copyright 2011 American Chemical Society.

For lithography, maintaining pattern fidelity throughout the pattern transfer process is critical. To avoid capillary forces causing feature collapse, plasma etching is often used to selectively remove the block with least etch resistance. Although this type of process maintains image quality throughout development, most BCPs consist of purely organic blocks, which tend to etch at similar rates in plasma environments. Etch selectivity can be imparted on BCP systems by incorporating inorganic elements such as silicon[108] or tin,[109] but generally some of the BCP etch mask is still lost during the first few seconds of etching.[116] As feature sizes continue to scale down, etch mask height becomes more important for retaining a reasonable process window for pattern transfer.

Figure 5.1B shows a BCP film with the same starting thickness as in 5.1A, but treated with a plasma etch process instead of solvent washing. The height of the BCP mask has been significantly diminished to completely remove the PMMA block.

So-called "self-developing" polymers[168] are materials that can combine the advantages of both wet and dry feature development. These polymers depolymerize rapidly and vaporize upon exposure to a selective stimulus. Many such materials have been developed for lithography such as polycarbonates,[169–172] polyformals,[173,174] polyaldehydes,[71,175,176] and nitrocellulose.[177] Typically, self-developing polymers are designed to either react directly with light or with strong photoacid produced after exposure. In each case, neither solvent nor plasma etching is required to generate an image in the resist, which means high aspect ratio features can potentially be developed without causing feature collapse. In principle, the other block can also be designed to be chemically inert to the stimulus that triggers depolymerization in the other block, preserving the perfect chemical selectivity of solvent-based development.

This chapter discusses two polymer systems we have investigated for self-developing BCP materials: poly(phthalaldehyde)s and poly(α-methylstyrene)s. Few studies have been reported on self-developing systems of this sort in BCP architectures; even fewer exist for specific applications for lithography. Often, the synthesis of these self-developing materials requires special conditions for polymerization, since many such polymers are prone to degradation if not handled carefully. Therefore, incorporating these materials into a BCP architecture was a major challenge in this work. Ideas for future work are included that are focused on making our BCP systems perform better.

5.2 POLY(PHTHALALDEHYDE)

Poly(phthalaldehyde) (PPHA) is one of the most studied polymers in the field of depolymerizable materials.[175,178–181] Due to its rapid degradability in both solution and in thin films, PPHA has found a number of applications in transient electronics,[176] sensors,[181] and lithographic patterning.[182] o-Phthalaldehyde can be polymerized via ring-closing polymerization below -40°C (the ceiling temperature) to form a polymer backbone comprised of acetal bonds. Both anionic and cationic initiators can be used to synthesize PPHA. While anionic initiators tend to produce linear polymers, cationic polymerization creates cyclic polymers that grow via ring-expansion polymerization.[178] Terminating an anionic polymerization below -40°C traps the active polymer chain end and prevents depolymerization when the polymer is allowed to warm to room temperature.

Triggering PPHA depolymerization can be accomplished by a variety of stimuli, depending on how the monomer is polymerized and the chemical nature of the end group. PPHA is perhaps most sensitive to catalytic amounts of strong acid. The acetal groups in the PPHA backbone readily hydrolyze in low pH environments. After rupturing the backbone, a cascade of ring-opening reactions quantitatively converts polymer chains into monomer. Cleaving the end cap also induces a head-to-tail depolymerization, which can be exploited to render PPHA sensitive to other chemical triggers. End caps such as allyl carbonates,[180] silyl ethers,[181,183] and o-nitrobenzyl moieties[180] have all been employed to synthesize PPHA that degrades in response to Pd(0), fluoride ions, and UV light, respectively.

The rapid change in molecular weight after initiating the depolymerization reaction is a source of chemical amplification that can be leveraged for photolithography.[175] Some of the first chemically amplified resists were formulated by blending PPHA with photoacid generators (PAG)s. Work done at IBM in the 1980's demonstrated that PPHA/PAG blends functioned as extremely sensitive positive tone resists for DUV and electron beam lithography.[184] This resist system owes its sensitivity to two sources of chemical amplification: 1) acid diffusing and reacting with many different PPHA polymer chains after exposure, and each polymer chain depolymerizing after reacting. The depolymerization of PPHA is exothermic; in fact, enough heat is produced during depolymerization to volatilize monomer from the solid state, meaning PPHA films can "self-develop" during the exposure process. While this resist was incredibly "fast", it suffered from poor stability in solution, outgassing in the exposure tool which caused contamination, and poor etch resistance as a homopolymer matrix.

Although PPHA was never commercialized as a photoresist, it was an important demonstration that depolymerizable polymers could be utilized for lithography. The goal of this work was to incorporate PPHA into a BCP architecture, such that the PPHA domains could be "self-developed" upon exposure to photogenerated acid. The degradation of PPHA into monomer provides a mechanism for perfect chemical selectivity when developing BCP patterns. However, a number of challenges made it difficult to realize this particular application for PPHA, including polymer synthesis, the low thermal stability of PPHA, BCP characterization, shelf life, and BCP orientation control in thin films. Although not all of these challenges were met in this study, an

approach is described for potentially solving these issues and suggestions are provided for future work on this system.

5.2.1 o-phthalaldehyde

5.2.1.1 Monomer and Homopolymer Synthesis

o-phthalaldehyde is commercially available but cannot be polymerized without careful purification. PHA slowly degrades in atmospheric conditions, and the degradation products can quench anionic polymerization initiators or initiate chain-transfer reactions that reduce the molecular weight of the polymer product.[185] Initial attempts to purify the monomer by recrystallization were low-yielding and generally failed to improve the melting point of the recovered solid. We discovered that sublimation at temperatures of 45-50°C produced highly pure monomer that polymerized readily at low temperatures.

The monomer's polymerization behavior was studied by reacting o-PHA with sodium phenyl-methanolate at -78°C (Scheme 5.1). Sodium phenyl-methanolate was formed by reacting benzyl alcohol with sodium hydride prior to mixing with o-PHA in solution.

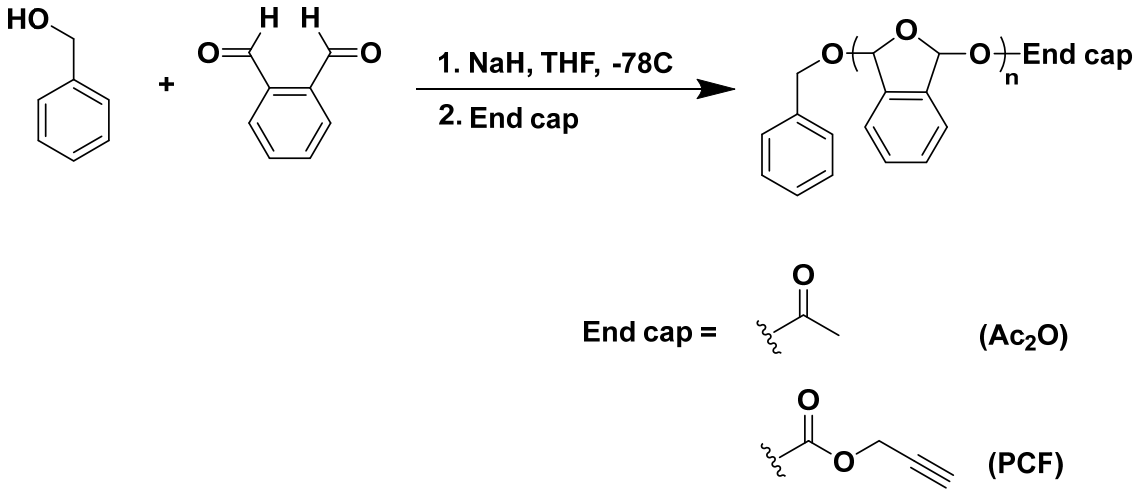

Scheme 5.1: Typical PPHA polymerization using the benzyl alcohol/NaH initiator system

Table 5.1: PPHA homopolymer characterization data

Target M_n (kDa)	Actual M_n (kDa)[a]	Đ[a]	Mass Yield (%)	End capping reagent
20.0	11.8	1.34	47%	Ac_2O[c]
20.0	12.8	1.30	21%	PCF[d]
20.0	17.4[b]	2.46	49%	PCF

[a] Determined by GPC relative to a PS standard, dn/dC = 0.059
[b] Polymerization was run using o-PHA purified by sublimation (m.p. = 55°C)
[c] Acetic anhydride
[d] Propargyl chloroformate

Despite efforts to rigorously purify the monomer, including multiple sublimations, the yield of these polymerizations usually did not rise above 50%. This behavior could be attributed to the equilibrium nature of the polymerization reaction. In addition, these polymers often showed signs of degradation after a few weeks, even as a precipitated powders.

Subsequent polymerization attempts were preceded by washing all glassware with strong aqueous base beforehand to remove any potential acidic contaminants, as well as rigorous drying of the glassware and solvent to remove any protic species capable of quenching the initiator. While these measures did improve the stability of the dried polymer powders, all PPHA samples slowly depolymerized over the course of a few days when dissolved in solution, regardless of the synthetic technique used. In addition, it was difficult to control the molecular weight and dispersity of PPHA.

In hindsight, the issues associated with controlling the polymerization probably could have been avoided by carefully storing the monomer after sublimation. Because PHA readily hydrolyzes in air, storing it in a glove box immediately after recovery probably would have significantly improved the resulting polymerization efficiency. In addition, other anionic initiators like the phosphazene base P_2-tBu, have been demonstrated to provide more control over molecular weight than the benzyl alcohol/NaH system. P_2-t-Bu was eventually used as a base to initiate the polymerization of 4,5-dichlorophthalaldehyde, as described further below.

5.2.1.2 Block Copolymer Synthesis

Despite issues with controlling the molecular weight of the PPHA homopolymer, attempts were made to initiate the polymerization of the block copolymer using a hydroxyl-terminated macroinitiator (Scheme 5.2).

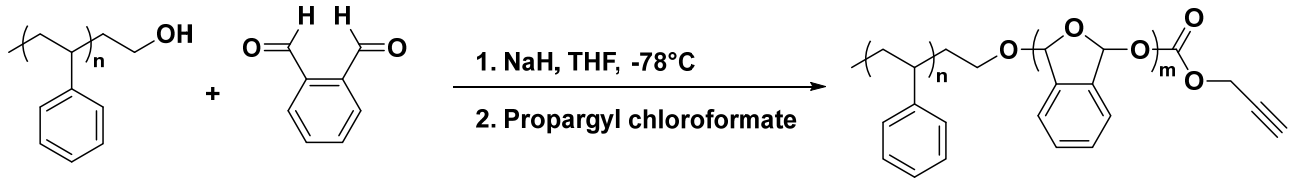

Scheme 5.2: PS-*b*-PPHA synthesis using PS-OH as a macroinitiator.

Polystyrene was chosen as the second block because it can be made using a number of polymerization techniques, including anionic polymerization.[186] Although the polymerization of o-PHA can be initiated using organolithium compounds, like the styryl anion, previous experience with o-PHA informed our choice to use alkoxide initiators instead. Thus, PS-OH macroinitiator was synthesized by terminating the anion of "living" polystyrene chains with ethylene oxide.

As with the PPHA homopolymer reactions, the PS-OH was mixed with NaH to form the alkoxide initiator prior to addition to the monomer solution. GPC data for a typical BCP polymerization reaction can be seen in Figure 5.2.

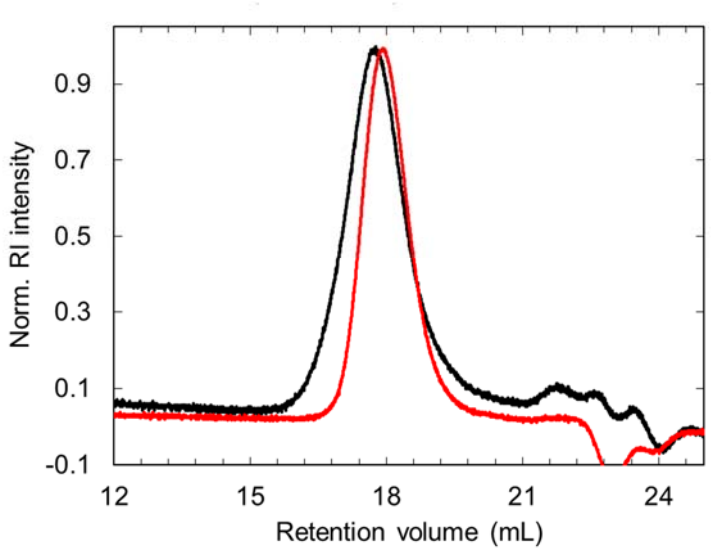

Figure 5.2: Representative GPC traces for PS-OH (red), M_n = 2.5 kDa, Đ = 1.02 and the PS-PPHA BCP product (black) from the reaction depicted in Scheme 6.2. The small peak shift towards lower retention volume indicates low conversion for the polymerization.

Although there is some evidence for BCP formation from Figure 5.2, the conversion of o-PHA to polymer is low. This could be due to the fact that at -78°C, the hydroxyl end group on the polystyrene initiator is not accessible for initiating PPHA polymerization. Increasing the concentration of the monomer solution improves the reaction yield, but it was observed that o-PHA solutions with concentrations greater than 2.0 M crystallize from THF at -78°C. Ultimately, this strategy was abandoned in favor of a modular BCP synthesis described later in this section.

5.2.2 4,5-dichlorophthalaldehyde

Because of the limited solution lifetime of PPHA, we sought to synthesize a derivative of PPHA that would be less sensitive to handling and processing. As discussed in Chapter 7, our collaborators at Penn State discovered that installing chlorine atoms on the aromatic ring of o-PHA significantly improved the solution stability of the corresponding homopolymer[187,188] (Figure 5.3).

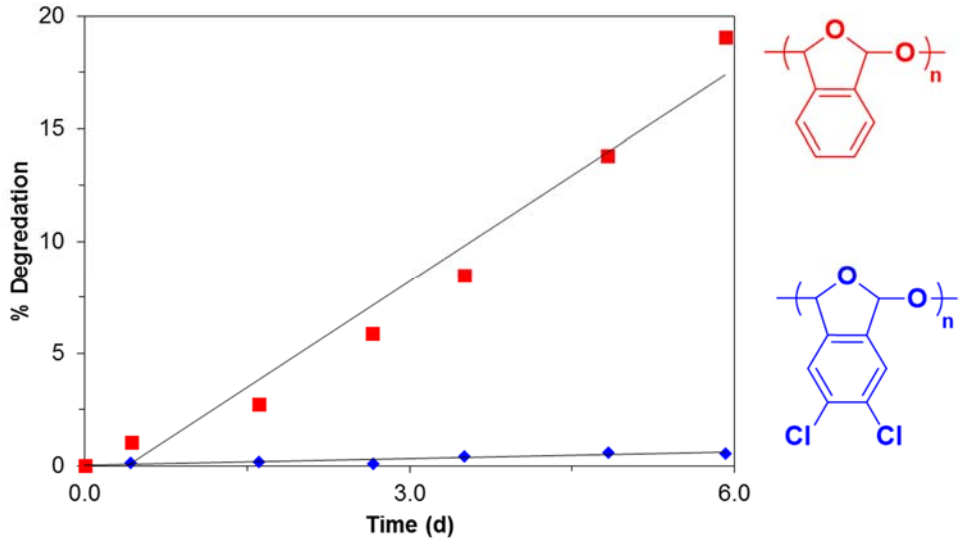

Figure 5.3: Effect of aromatic ring substituents on solution stability of PPHA. Special thanks goes to Dr. Anthony DiLauro for generating the data for this plot.

5.2.2.1 Monomer and Homopolymer Synthesis

4,5-Dichlorophthalaldehyde (PHA-Cl_2) can be synthesized in two steps starting from 4,5-dichlorophthalic acid (Scheme 5.3). It should be noted that the Swern oxidation (step 2) is perhaps the only oxidation capable of yielding the dialdehyde product without over-oxidation or formation of a cyclic lactone. The purification techniques required for PHA-Cl_2 were similar to those required for o-PHA. However, in addition to sublimation,

PHA-Cl_2 had to be recrystallized from cyclohexane to achieve sufficient purity for polymerization.

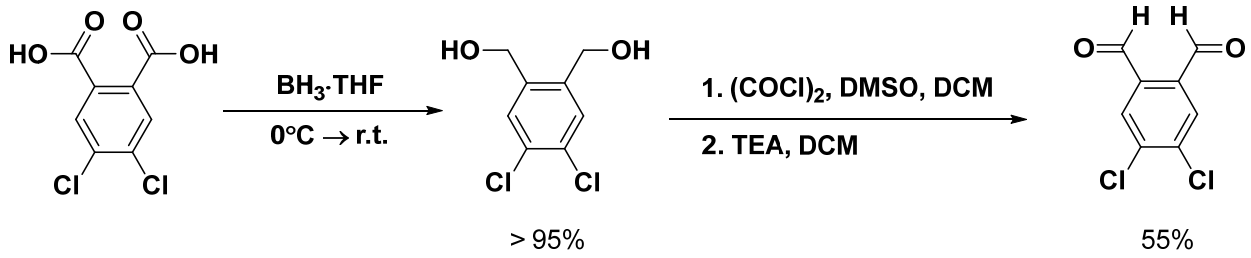

Scheme 5.3: Synthesis of 4,5-dichlorophthalaldehyde

Researchers at Penn State also discovered that phosphazene base/alcohol initiator systems efficiently polymerized PHA-Cl_2 with much higher yields and control over end-group functionalization than corresponding polymerizations using other strong bases like NaH.[187] The difference between the two initiators may have to do with the non-coordinating nature of the phosphazene base, which exerts less influence over the propagating anion due to its size.

PPHA-Cl_2 homopolymers were synthesized with various terminal functionalities using P_2-tBu/BnOH as the initiating system (Scheme 5.4). These end caps were made chosen to make the resulting polymers amenable to “click” chemistry.

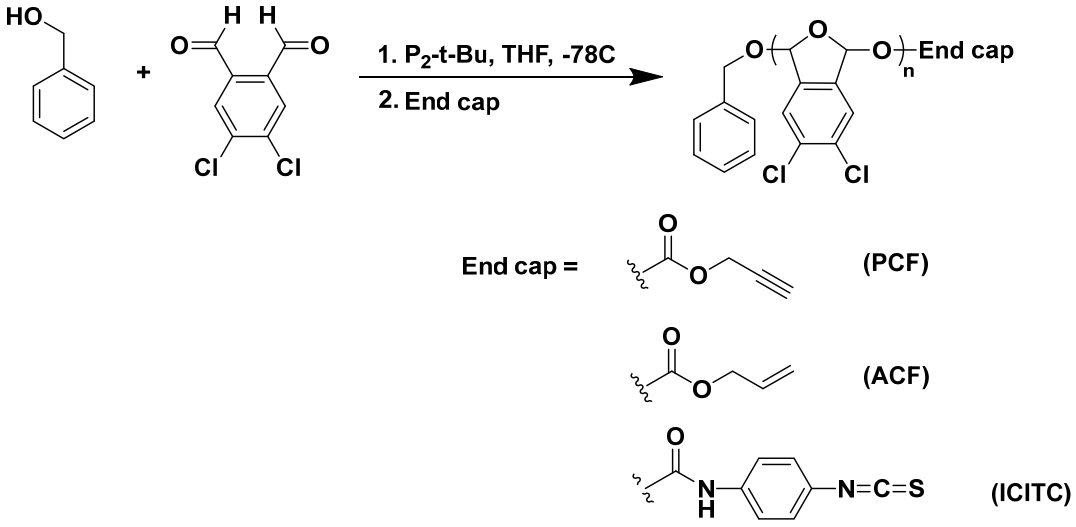

Scheme 5.4: Synthesis of PPHA-Cl_2 using the P_2-t-Bu/benzyl alcohol system

Table 5.2: PPHA-Cl_2 homopolymer characterization data

Targeted Mn (kDa)	Actual Mn (kDa)[a]	Đ[a]	Mass yield (%)	End capping reagent
5.0	3.4[b]	1.08[b]	47	PCF
20	3.2	1.68	60	ACF[d]
20	5.3	1.26	50	ICITC[e]
100	6.9[c]	1.50	59	ICITC

[a] Determined by GPC relative to a PS standard, dn/dC = 0.185
[b] Determined by MALDI-FT-ICR analysis
[c] Before terminating the polymerization, a small amount of pyridine was added
[d] Allyl chloroformate
[e] p-Isocyanatophenyl isothiocyanate

Despite targeting relatively high molecular weights, it was difficult to achieve significant conversion of the PHA-Cl_2 monomer. This could have resulted from the well-known chain transfer reaction o-PHA is known to undergo when polymerized for

extended periods of time. It should be noted that polymerizations initiated with the benzyl alcohol/NaH system failed to produce any polymer.

5.2.2.2 Block Copolymer Synthesis

Early attempts to synthesize BCPs from PHA-Cl_2 followed previous attempts to synthesize PS-PHA using the macroinitiator approach (Scheme 5.5). Despite using a more effective initiating system, no BCP formation could be detected by GPC analysis (Figure 5.4).

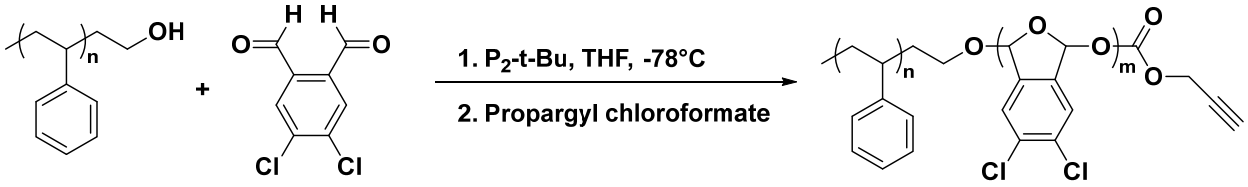

Scheme 5.5: PS-*b*-PPHA-Cl_2 synthesis using PS-OH as a macroinitiator.

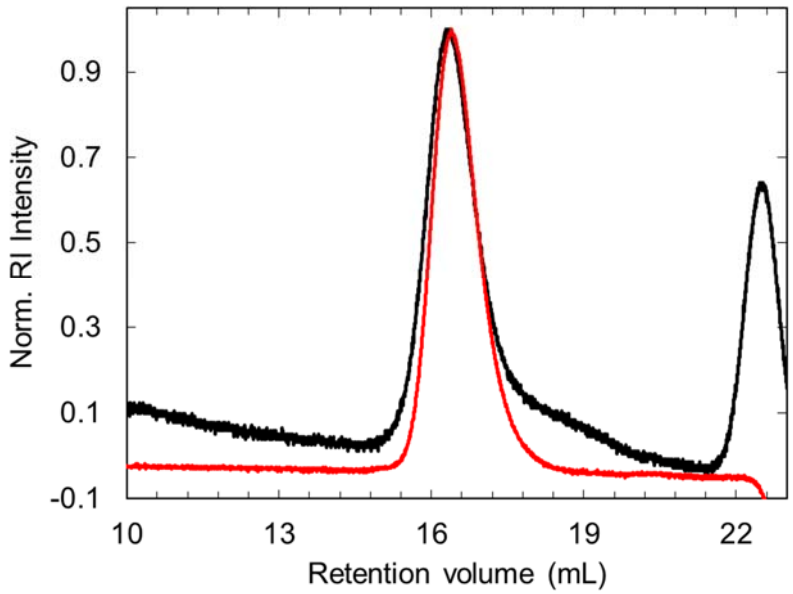

Figure 5.4: Representative GPC traces for PS-OH (red), M_n = 7.0 kDa, Đ = 1.07 and the PS-PPHA BCP product (black) from the reaction depicted in Scheme 6.2. The small peak shift towards lower retention volume indicates low conversion for the polymerization.

Rather than initiate the polymerization of the PPHA-Cl_2 block from a PS macroinitiator, it is also theoretically possible to synthesize the BCP in the opposite configuration, using a functionalized PPHA-Cl_2 as the initiator for the polymerization of PS (Scheme 5.6). For instance, PS can be synthesized by a number of controlled radical polymerization techniques which have been demonstrated to produce well-controlled BCP materials. Practically, however, this strategy is limited by the low thermal stability of PPHA-Cl_2 (Figure 5.5). Despite improving on the stability of unmodified PPHA, we

assumed that even modest polymerization temperatures of 90°C would cause degradation of the PPHA-Cl_2 block, so this route was not pursued.

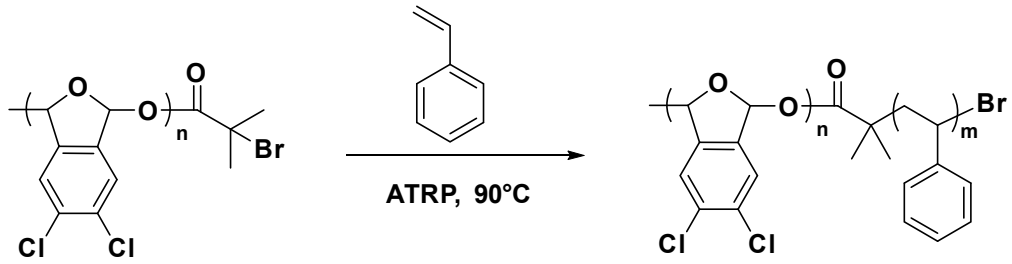

Scheme 5.6: Possible synthetic route to PS-*b*-PPHA-Cl_2 using PPHA-Cl_2 as a macroinitiator.

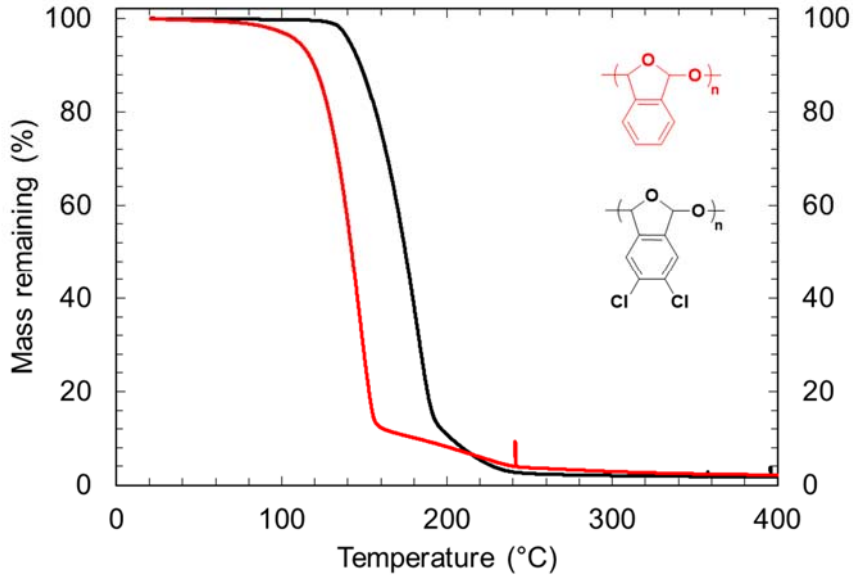

Figure 5.5: Thermogravimetric analysis (TGA) traces for PPHA(red) and PPHA-Cl_2 (black). The structures corresponding to each trace have been drawn for clarity.

Instead of growing one block using the other as a macroinitiator, BCPs can also be synthesized by coupling two homopolymers together using well-established "click" chemistry.[189,190] This technique is often used when homopolymer blocks are made by incompatible polymerization techniques. One of the most common "click" reactions for producing BCPs is the Cu(I)-catalyzed azide-alkyne cycloaddition.[191] In this reaction, azides react readily with terminal alkynes in the presence of Cu(I) halide salts.

PPHA-Cl_2 was synthesized with a terminal alkyne group by capping the alkoxide chain end with propargyl chloroformate (Scheme 5.4). However, attempts to couple this homopolymer to azide-terminated styrene failed to yield any BCP product, producing only PHA-Cl_2 monomer as a result. The reason for this depolymerization is unclear; at the time, it was believed that the Lewis acidity of the Cu(I) catalyst may have been responsible for "unzipping" the PPHA-Cl_2. It should be noted that recently, several reports has been published describing the synthesis of PPHA BCPs made using azide-alkyne click chemistry.[192,193]

Before starting this work, the only previously reported example of a BCP with a PPHA block was made using selective isocyanate-isothiocyanate coupling reactions.[194] While not technically recognized as a "click" reaction, the study reported to couple Surfonamine polymers (amino-functionalized ethylene oxide/propylene oxide copolymers) with PPHA in high yields. Isothiocyanate-functionalized PPHA-Cl_2 was synthesized by capping alkoxide chain ends with p-isocyanatophenyl isothiocyanate (Scheme 5.4). The alkoxide species reacts much faster with isocyanates than isothiocyanates, which minimizes homopolymer coupling as a result of two polymer

molecules reacting with the same terminating molecule. Amines can react readily with isothiocyanates, so PS-NH_2 was prepared by reducing PS-azide with $LiAlH_4$. Subsequently mixing PPHA-isothiocyanate and PS-NH_2 in DCM (Scheme 5.7) cleanly afforded the BCP product (Figure 5.6A)

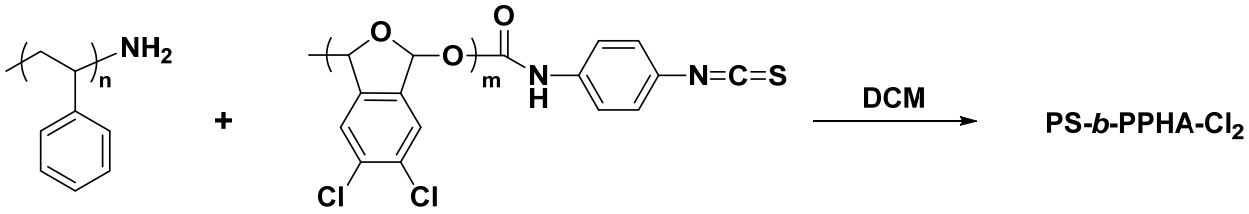

Scheme 5.7: PS-*b*-PPHA-Cl_2 synthesis using amine-isothiocyanate coupling chemistry.

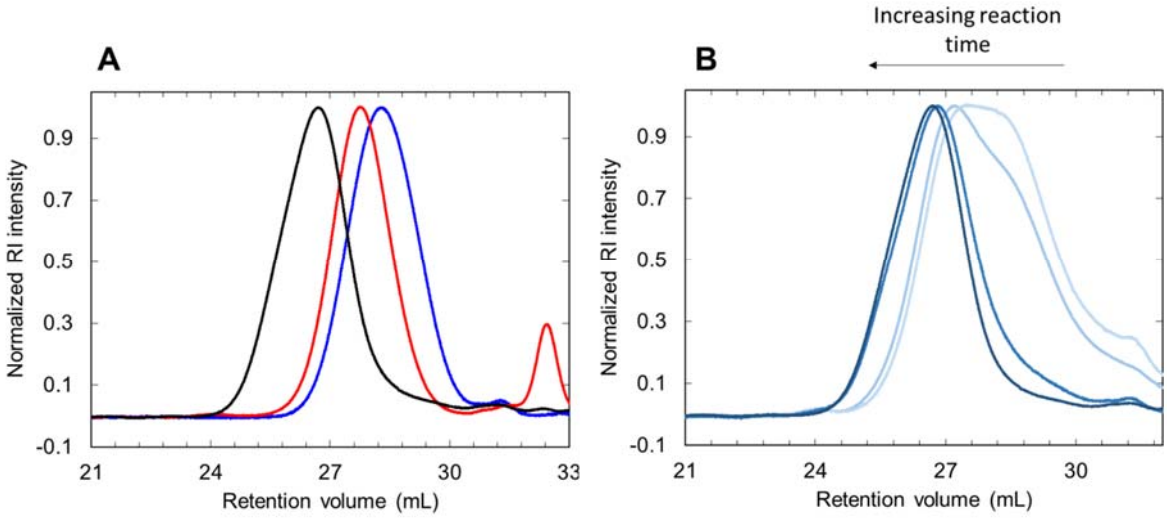

Figure 5.6: (A) GPC traces for PS-NH_2 (red, M_n = 10.1 kDa, Đ = 1.1), PPHA-isocyanate (blue, M_n = 5.3 kDa, Đ = 1.26), and the PS-*b*-PPHA-Cl_2 BCP product (black). The PS-NH_2 was modified by reaction with phenyl isocyanate prior to GPC analysis. (B) GPC traces of the BCP product taken at various reaction times. Starting from 1 hr (lightest blue), the plot shows the kinetics of the amine-isothiocyanate coupling reaction until it reaches completion after approximately 24 hrs (darkest blue).

To further demonstrate that the coupling reaction resulted in the formation of BCP, the PPHA block was removed by treatment with trifluoroacetic acid (Scheme 5.8). The depolymerization of the PPHA-Cl_2 block was monitored by both GPC and NMR (Figure 5.7). The decrease in molecular weight of the coupling product after treatment with acid is evidence that the BCP was synthesized.

Scheme 5.8: Depolymerization of the PPHA-Cl_2 block using trifluoroacetic acid

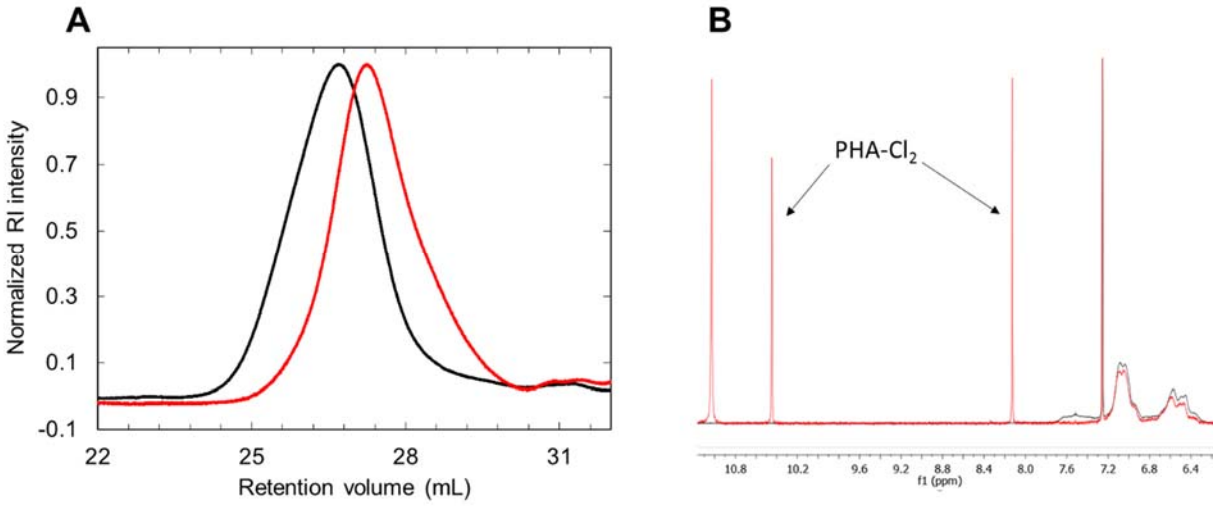

Figure 5.7: (A) GPC traces of PS-*b*-PPHA-Cl_2 before (black) and after (red) treatment with trifluoroacetic acid. (B) NMR spectra of PS-*b*-PPHA-Cl_2 before (black) and after (red) treatment with trifluoroacetic acid. The presence of peaks corresponding to the PHA-Cl_2 monomer confirmed the clean degradation of the PPHA-Cl_2 block.

5.2.2.3 BCP Self-assembly

To produce self-assembled BCP features, it is necessary to anneal the BCP so that polymer chains have sufficient mobility to reorganize into domains with long-range order. This can be accomplished by either heating the BCP above its T_g[136] or exposing the BCP to an saturated atmosphere of solvent vapor.[100] Unfortunately, the T_gs of both PPHA and PPHA-are above their degradation temperature, which makes thermal annealing impossible. Therefore, solvent annealing was used to induce self-assembly.

Two PS-*b*-PPHA-Cl_2 samples were annealed in acetone vapor for 1 hour and subsequently analyzed by small angle X-ray scattering (SAXS). SAXS is a useful technique for probing the nanostructure of soft materials on the order of 1-30 nm, which makes it excellent for determining the natural domain spacing of self-assembled BCPs in bulk. The SAXS data for the PS-*b*-PPHA-Cl_2 samples can be seen in Figure 5.8.

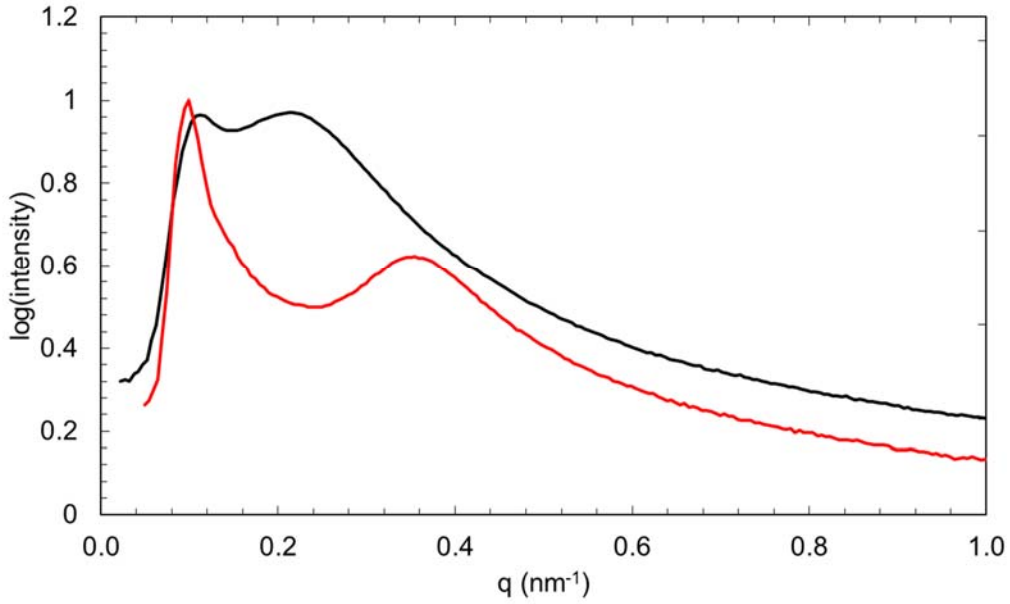

Figure 5.8: SAXS data for two PS-*b*-PPHA-Cl_2 samples annealed in acetone vapor for 1 hour: $PS_{10.1}$-*b*-PPHA-$Cl_{2,\ 5.3}$ (red), $PS_{10.1}$-*b*-PPHA-$Cl_{2,\ 7.9}$ (black)

The difference in the location of the peaks on the x-axis is due to the difference in the size of the BCP. Unfortunately, the broad primary scattering peaks indicate no long range order was present in the samples after annealing. Changing the annealing solvent did not produce more defined peaks. The GPC traces for one of the BCP samples before and after the SAXS measurement can be seen in Figure 5.9. The depolymerization observed by GPC may explain why the SAXS data did not indicate the presence of ordered BCP domains.

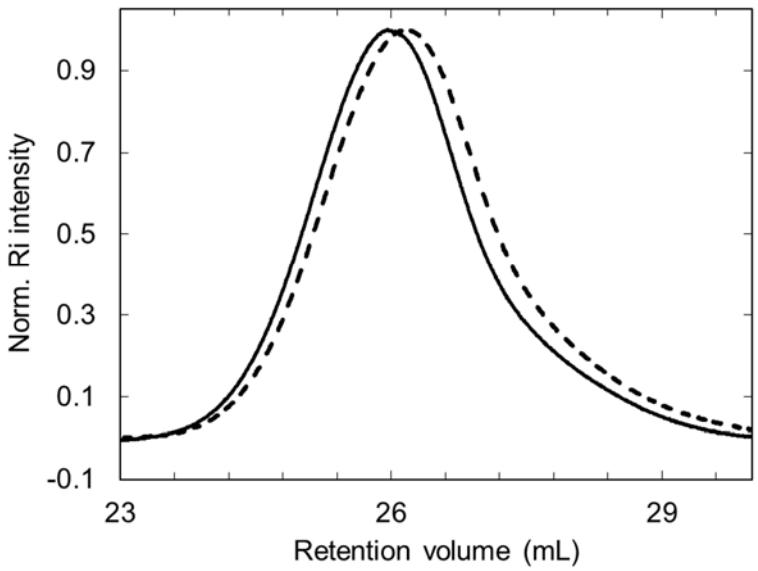

Figure 5.9: GPC traces of $PS_{10.1}$-*b*-PPHA-$Cl_{2, 7.9}$ before SAXS measurement (solid) and after (dashed). The peak shift towards higher retention volumes indicates depolymerization may have resulted from exposure to X-ray radiation

Attempts were also made to solvent anneal thin films of PS-*b*-PPHA-Cl_2 to produce ordered domains. Various solvents, underlayer coatings, annealing times, and BCP film thicknesses were tested; however, no phase-separated structures were ever observed by top-down SEM or AFM. It is difficult to say why this BCP system did not form nanoscale features. Solvent annealing is more complicated than thermal annealing and requires controlling more experimental variables for success. However, because neither BCP sample was ordered according to SAXS analysis, it is likely that the degree of polymerization of the BCP was not high enough to achieve phase separation. Future work for this particular BCP system would first require establishing good control over the molecular weight of the PPHA-Cl_2 homopolymerization so BCPs with higher molecular

weights could be synthesized. Unfortunately, as of the publication of this document, the 4-isocyanato phenylisothiocyanate end cap required for the amine-isothiocyanate coupling reaction has been discontinued, so this reagent would either need to be synthesized from scratch, or a new coupling chemistry would be required.

5.3 POLY(METHOXY A-METHYLSTYRENE)

α-Methylstyrene polymers and copolymers have a number of applications for pressure-sensitive adhesives[195] and resist materials for electron beam lithography.[196] Perhaps the most remarkable property of α-methylstyrene is its unusually low ceiling temperature (61°C, $[M]_0$ = 1.0 M).[197] The addition of the methyl group to the benzylic position of styrene decreases the ceiling temperature by nearly 330°C. The clean thermal decomposition of poly(α-methylstyrene) (PAMS) is well-known[198,199] and has been leveraged to make nanostructured foams in high T_g materials[200,201] and sensitive acid-degradable photoresist compositions.[202]

PAMS has also been previously incorporated into BCP materials for lithographic patterning. Ober et al.[203–205] have demonstrated that PAMS domains can be selectively removed from BCP films by irradiation with large doses of light and subsequent annealing in vacuum. While the process successfully created nanostructured films, the large amount of energy required for complete degradation leaves room for improvement. In truth, PAMS is actually quite stable when end-capped and does not begin thermal degradation until nearly 300°C.[198] It is only when an *active* polymer chain end is generated that PAMS begins depolymerizing. UV light may be responsible for main

chain cleavage in the PAMS backbone which generates active chains, but this does not appear to be a very sensitive trigger. Ideally, a controlled initiation event could be used to trigger depolymerization quickly and quantitatively.

In his studies with PAMS derivatives, Ito et al.[202] also noticed that these polymers did not respond to heat or strong acid unless prepared using specific conditions. Ito observed that cationic polymerization of poly(hydroxy α-methylstyrene) produced polymers which depolymerized when exposed to strong acid. He reasoned that terminating the cationic polymerization with methanol led to the formation of a double bond at the end of the polymer chain. Terminal double bonds react with strong acid to form tertiary carbocations which initiate depolymerization above the ceiling temperature. However, terminating cationic polymerization of α-methylstyrene derivatives with methanol does not produce the phenylallyl-functionalized polymer quantitatively. Synthesizing a polymer that depolymerizes completely requires fully functionalizing every polymer chain with an end cap that facilitates depolymerization. Thus, we hoped to improve on Ito's original work by designing polymers that could be synthesized by anionic polymerization but are still sensitive to the strong acid trigger by installing a phenylallyl group at the polymer chain end (Scheme 5.9).

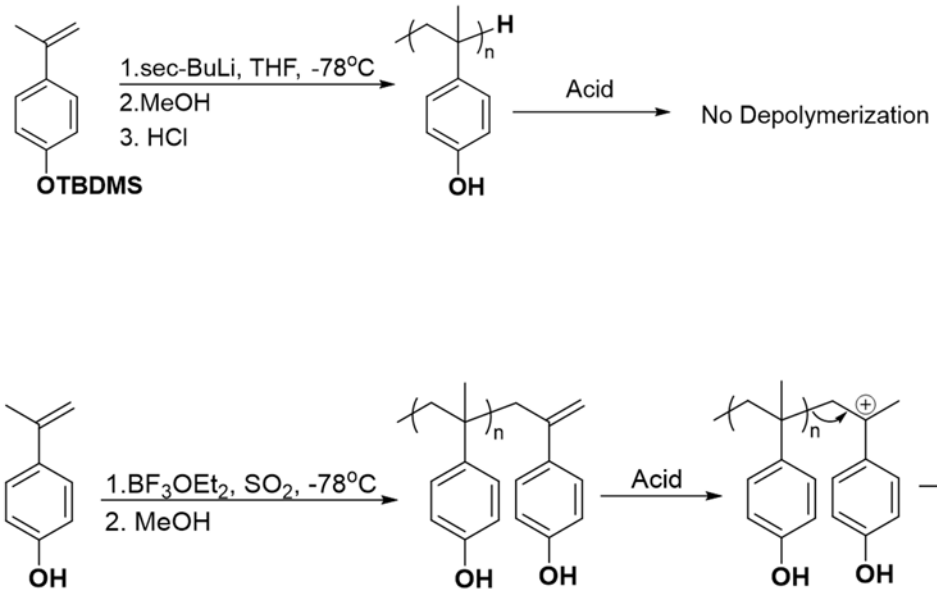

Scheme 5.9: Ito's observation that only poly(hydroxyl α-methylstyrene) made by cationic polymerization could be degraded using strong acid catalyst.[202]

Ito primarily studied poly(hydroxyl α-methylstyrene) due to its analogous structure to the poly(4-hydroxystyrene) resins used for 248 nm chemically amplified resists. However, hydrogen bonding from the phenol group can lead to undesirable BCP self-assembly in thin films. For our purposes, we chose to synthesis poly(methoxy α-methylstyrene) (PMAMS), a structural analog to the polymer originally studied by Ito that does not have hydrogen bond donating groups in the polymer backbone. The polymerization of PMAMS has not been reported previously in the literature.

5.3.1 PMAMS Homopolymer Synthesis

To test the effectiveness of poly(methoxy α-methylstyrene) (PMAMS) as an unzipping polymer, the structure of the end group had to be modified so that it could react with strong acid in thin films. Synthesizing PMAMS by normal anionic polymerization techniques, like the route shown in Scheme 5.10, produces polymers that are inert in acidic conditions.

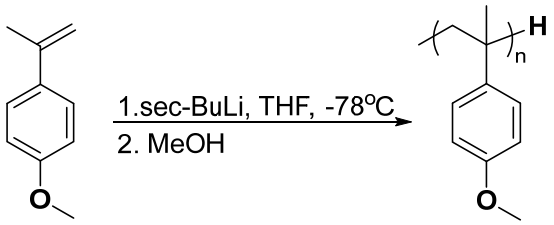

Scheme 5.10: Typical anionic polymerization of methoxy α-methylstyrene. PMAMS terminated with a hydrogen atom behaves as a stable polymer.

Two strategies were identified for quantitatively installing an alkene group at the end of the polymer structure. The first was the post-polymerization reaction of PMAMS with NBS to replace the terminal hydrogen with Br, followed by the elimination of Br to produce a double bond. The overall reaction can be seen in Scheme 5.11, and the MALDI spectra of poly(α-methylstyrene) before and after reaction with NBS can be seen in Figure 5.10.

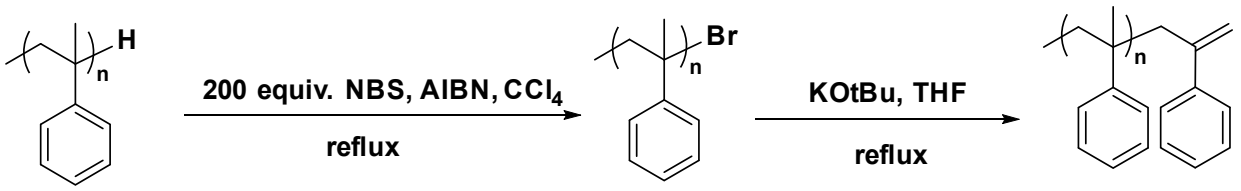

Scheme 5.11: Synthesis of alkene-terminated poly(α-methylstyrene) by bromine substitution and subsequent elimination.

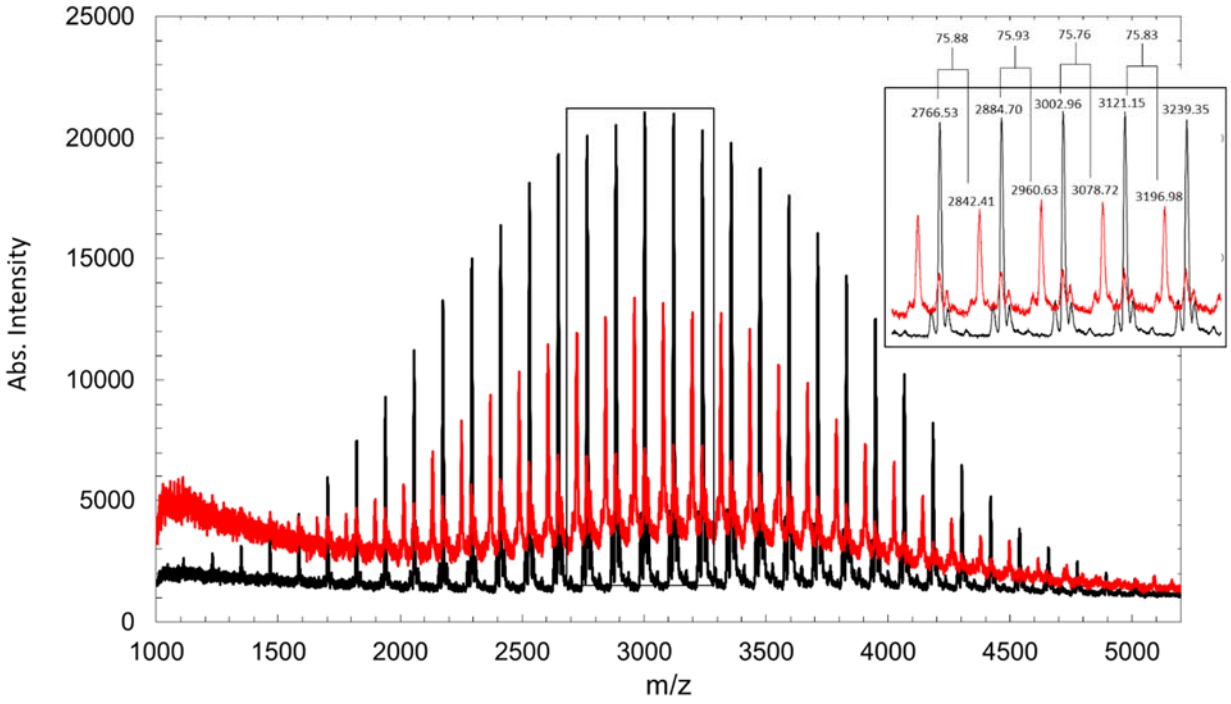

Figure 5.10: MALDI spectra for PAMS homopolymer before (black) and after (red) reaction with NBS as drawn in Scheme 5.11

Although MALDI data of the polymer after the substitution reaction showed the addition of 76 amu, approximately corresponding to the substitution of hydrogen with bromine, it could not be determined by NMR whether this substitution had taken place at

the end of the polymer chain or somewhere else on the polymer structure. Furthermore, reacting the brominated poly(α-methylstyrene) with KOtBu to form the double bond produced a mixture of polymer structures with different mass distributions (Figure 5.11). The convolution of the polymer distributions made characterizing the product nearly impossible. Another route was required that could produce the alkene-terminated polymer cleanly and ideally in a single step.

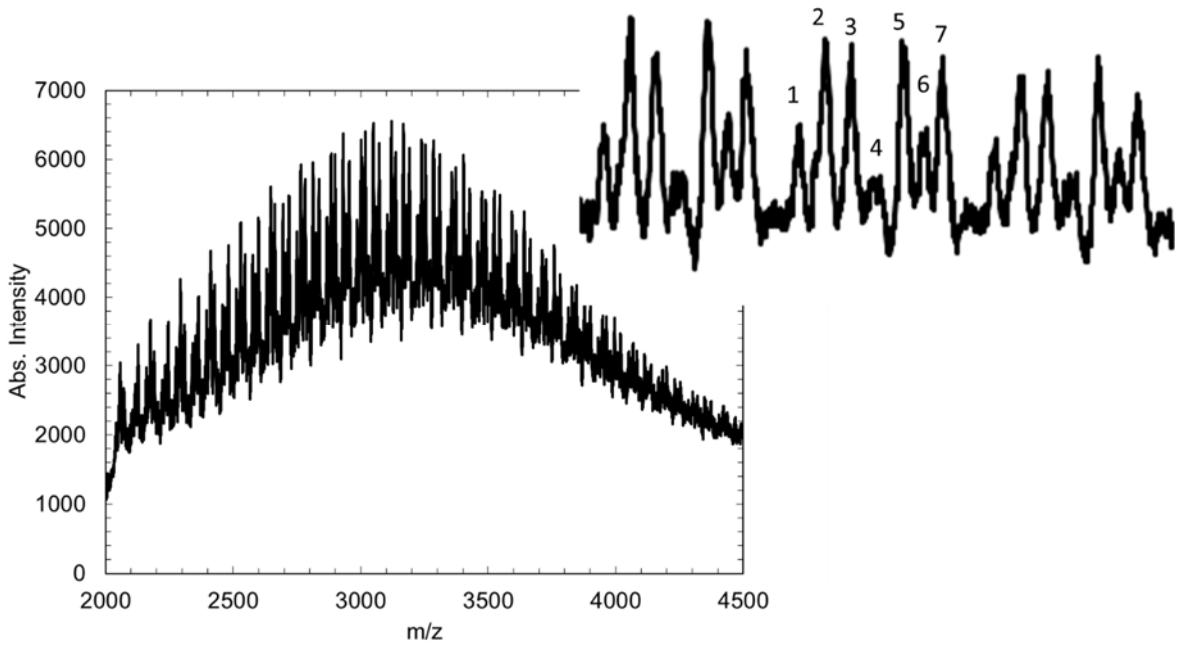

Figure 5.11: MALDI spectra of brominated PAMS after reaction with KOtBu.

Previous reports[206,207] have demonstrated that phenylallyl groups can be installed quantitatively at the end of α-methylstyrene polymers by reaction with 2-phenylallyl halide derivatives like the one shown in Scheme 5.12. By judiciously choosing the

reaction conditions, it is possible to isolate pure 2-phenylallyl bromide, albeit in modest yield.

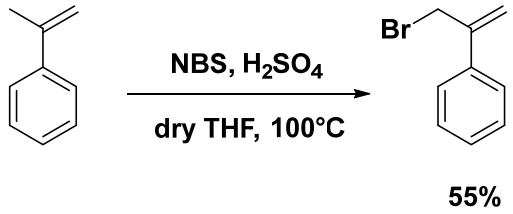

Scheme 5.12: Synthesis of 2-phenylallyl bromide.

To synthesize 2-phenylallyl-functionalized PMAMS, the living anion of methoxy α-methylstyrene was generated by adding sec-BuLi to a THF solution of methoxy α-methylstyrene at -78°C. Immediately upon adding sec-BuLi, the solution turned dark brown and the color persisted for the length of the polymerization. After about 20 minutes, the anion was quenched by dropwise addition of 2-phenylallyl bromide. The dark brown color instantly disappeared, indicating the end capping reaction occurred quickly and cleanly. GPC analysis revealed a monomodal distribution of molecular weights with low dispersity, indicating no coupling took place during termination (Figure 5.12B). As a control for the acid exposure experiments, a control was also synthesized that was terminated with MeOH (Figure 5.12A).

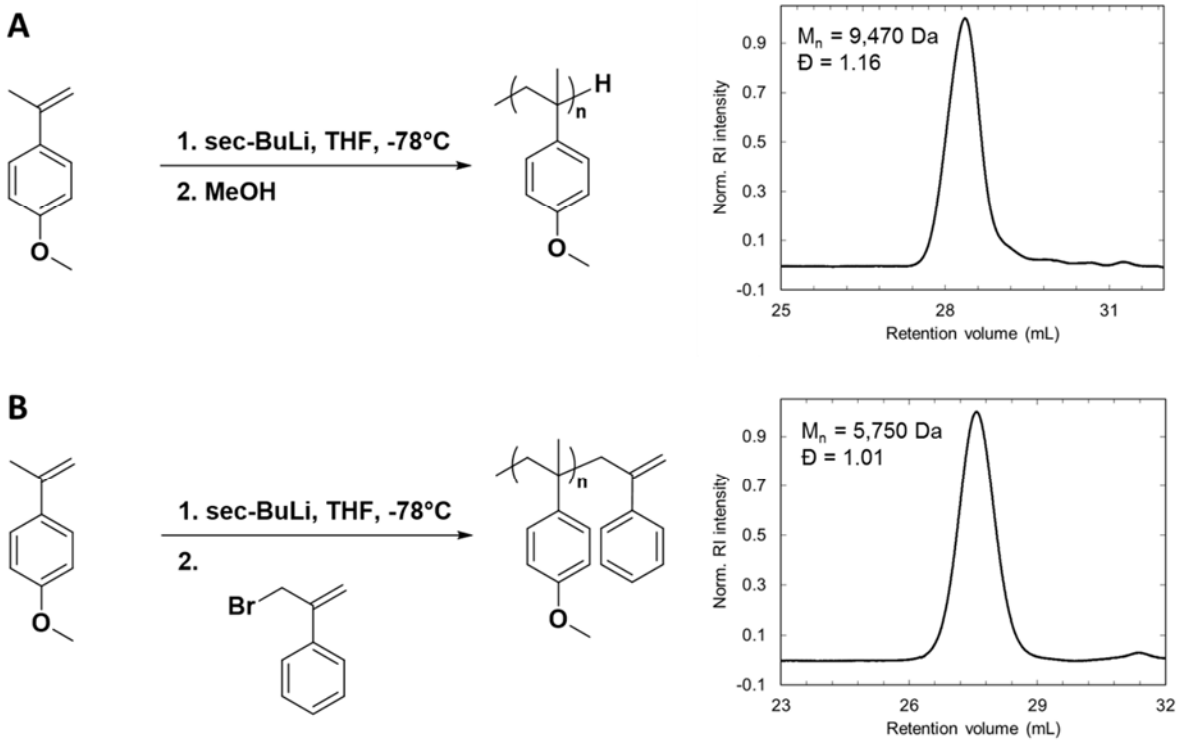

Figure 5.12: Synthesis of PMAMS homopolymers by anionic polymerization. PMAMS with (A) hydrogen end groups and (B) phenylallyl end groups could be synthesized with good control over molecular weight and dispersity

5.3.2 Thin Film Depolymerization Experiments

To test the hypothesis that the 2-phenylallyl end cap could render PMAMS sensitive to strong acid, both polymers in Figure 5.12 were blended with 5 wt% TPS-nonaflate and cast onto bare silicon substrates to form thin films. After a post-apply bake at 100°C, the polymer films were subsequently irradiated with 1000 mJ/cm^2 of broadband UV light from a high-pressure Hg lamp source to completely react the photoacid generator. Samples were then immediately baked on a hot plate at 100°C for 1 minute.

The film thicknesses of blanket films before and after exposure + bake can be seen in Table 5.3.

Table 5.3: Experimental details and thin film characterization for PMAMS depolymerization experiments

Polymer	PAG loading (wt%)	Initial thickness (nm)	Thickness after PAB (nm)	Exposure Time (s)	Thickness after PEB (nm)	% Thickness Lost
H-end cap	5%	124.3	117.6	10	111.1	5.5
Alkene end cap	5%	165.8	158.3	10	1.5	99
Alkene end cap	0%	130.8	123.8	10	123.6	0.1
Alkene end cap	5%	165.8	158.3	0	156.5	1.1

Each control experiment listed in Table 5.3 did not result in significant film thickness loss after exposure or baking at 100°C. However, the phenylallyl-substituted PMAMS completely depolymerized, leaving only a small amount of residue on the wafer that amounted to 1% of the starting film thickness. This is strong evidence that Ito's original hypothesis was correct. Furthermore, it was exciting to see that this depolymerization was possible in thin films, and it occurred within seconds of placing the wafer on the hotplate.

To illustrate the lithographic capabilities of this polymer, a 25 μm line/space grating mask was placed on top of polymer films and irradiated with various doses of UV light. Optical micrographs of the films after post-exposure bake can be seen in Figure 5.13.

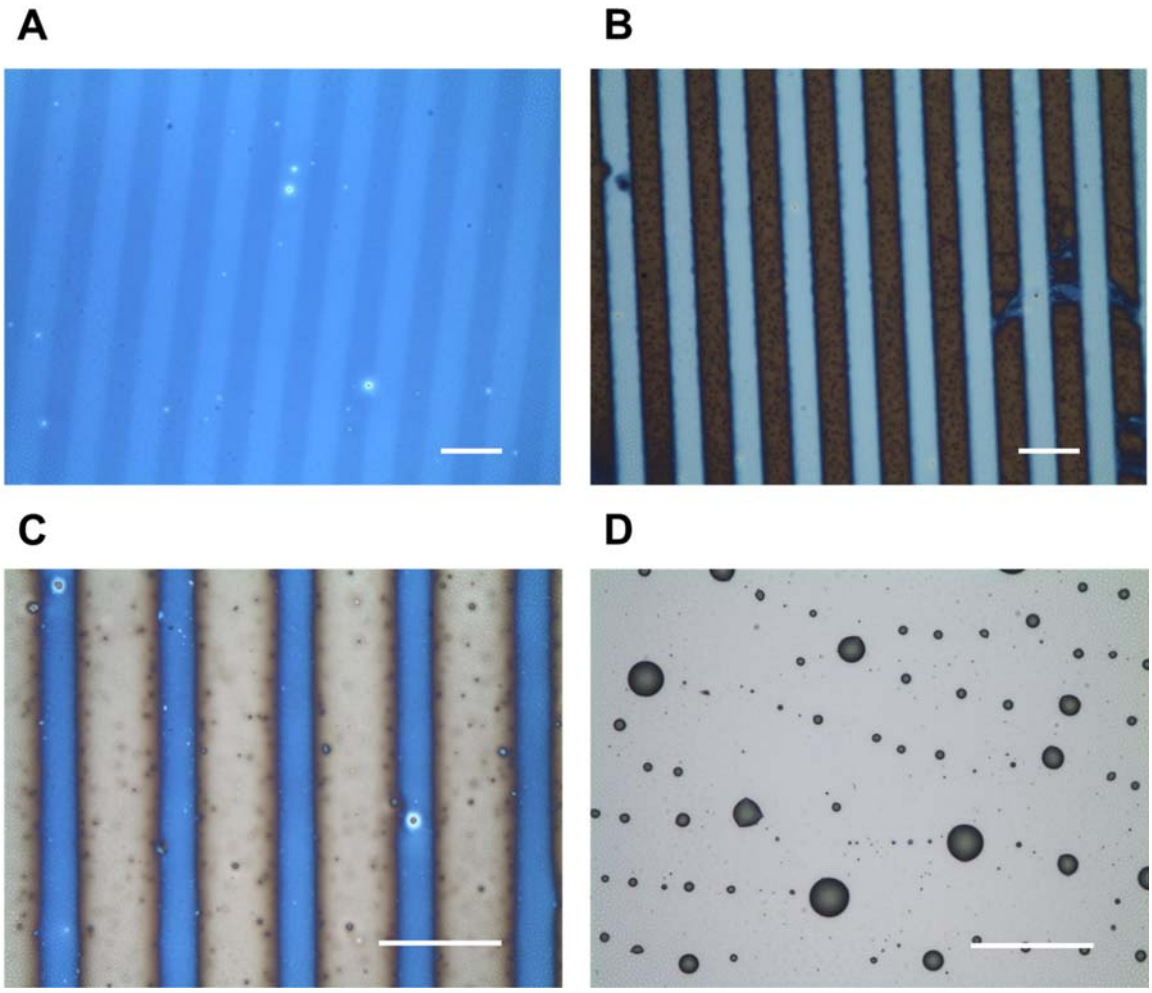

Figure 5.13. Optical micrographs of PMAMS films after exposure to UV light and annealing at 100°C for 1 minute. All polymer films were loaded with 5% TPS-nonaflate PAG (A) PMAMS-H exposed to 135 mJ/cm^2 (B)) PMAMS-alkene exposed to 135 mJ/cm^2 (C) PMAMS-H exposed to 270 mJ/cm^2 (D) PMAMS-alkene exposed to 1,135 mJ/cm^2. Scale bars = 50 μm

For BCP lithography, the unzipping block must undergo rapid depolymerization in thin films, but it must also be thermally stable enough for BCP annealing at temperatures >180°C and have an accessible T_g below it degradation temperature. The

TGA and DSC data in Figure 5.14 shows that phenylallyl-PMAMS has a degradation temperature over 300°C with a T_g = 152°C, making it an excellent candidate for this application. In addition, when phenylallyl-PMAMS was blended with p-toluenesulfonic acid, the polymer's onset degradation temperature decreased dramatically to about 100°C, matching the experimental results in thin films.

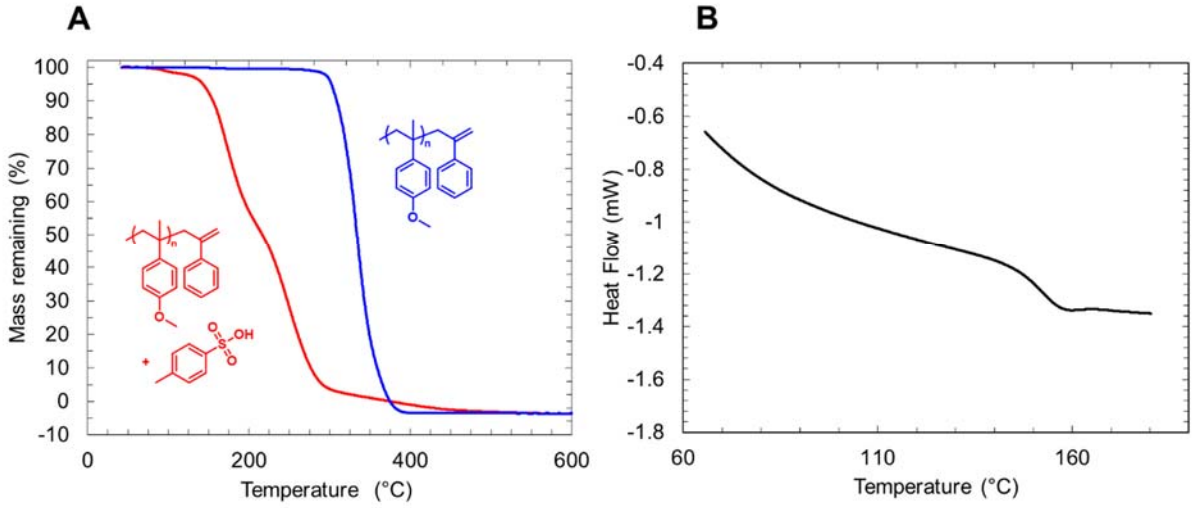

Figure 5.14: Thermogravimetric (TGA) data (A) and differential scanning calorimetry (DSC) data (B) for phenylallyl-PMAMS. The heating curve in (B) was the second run in the DSC experiment.

To understand how the structure of the monomer affected the degradability of the resulting polymer, several α-methylstyrene derivatives were synthesized, polymerized, and terminated with phenylallyl end caps. Each polymer was then blended with photoacid generator, and blanket films were exposed under similar conditions to the ones described for the initial PMAMS depolymerization experiment. Figure 5.15 was generated by

plotting the normalized film thickness lost after post-exposure bake against the dose supplied to the polymer film.

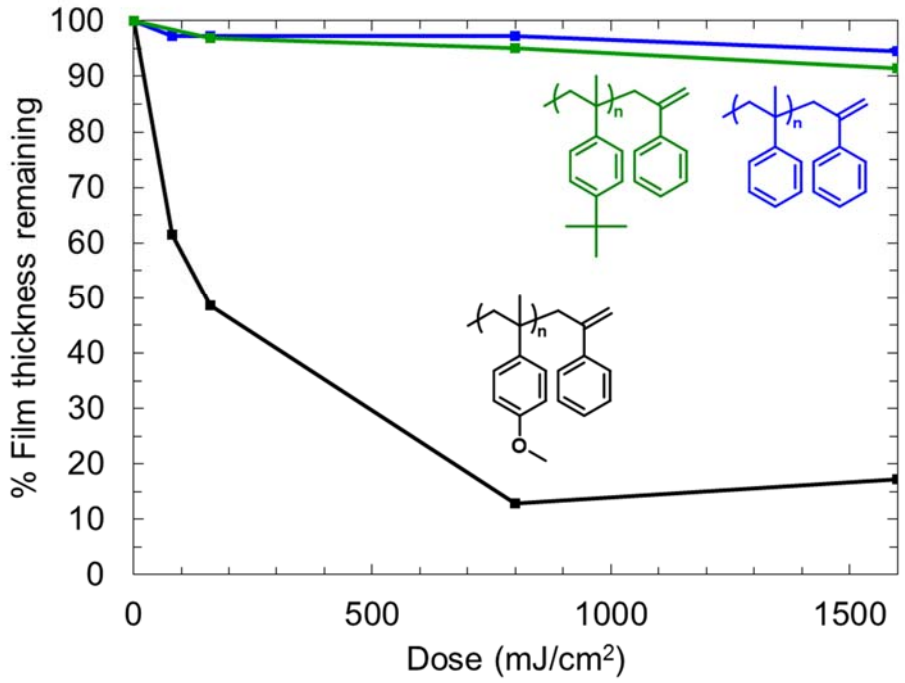

Figure 5.15: Plot showing the effect of ring substitution on the degradability of several poly(α-methylstyrene) derivatives. Although not well understood at the time, it is hypothesized that the PMAMS polymer did not depolymerize fully in this experiment due to the presence of minute quantities of airborne organic base in the lab where the exposure and post-apply bake was performed.

From the data in Figure 5.15, it seems clear that a strongly electron-donating group is required to facilitate the depolymerization of phenylallyl-functionalized α-methylstyrene polymers. Electron donating groups at the ortho and para positions on the

aromatic ring stabilize carbocation intermediates formed at the benzylic position. Since the rate of depolymerization is proportional to the speed of the initial reaction with the end cap, this could explain why PMAMS depolymerizes much more rapidly than the other derivatives tested. Although the presence of the methoxy group facilitates depolymerization, it also causes problems for synthesizing BCP by sequential anionic polymerization, which will be discussed in the next section.

5.3.3 Block Copolymer Synthesis

BCPs with well-controlled molecular weights, dispersities, and volume fractions are readily made by sequential anionic polymerization of styrenic monomers.[186,208] Typically, the polymerization of one block can be initiated directly from the first block if the polymerization order is considered carefully. To enable the depolymerization of the PMAMS block, the phenylallyl functionality must be located at the end of the polymer chain, meaning the PMAMS block must polymerized second. However, the propagating anion during the polymerization of methoxy α-methylstyrene is tertiary benzylic with an electron donating group on the aromatic ring. This carbanionic species is very unstable, and to create a tertiary anion from a secondary anion like the one produced by normal styrene polymerizations requires overcoming a large activation energy barrier. This problem is more clearly illustrated in Scheme 5.13. GPC data from a typical BCP synthesis is shown in Figure 5.16.

Attempting to initiate the polymerization of PMAMS from a number of styryl anions, including polystyrene and poly(trimethylsilylstyrene), largely failed. Even

attempting to initiate the PMAMS polymerization from a α-methylstyryl anion failed to produce any BCP product. Initiating from an even more unstable tertiary anion, like p-N,N-dimethylamino-α-methylstyrene, might produce the reaction energy profile required for successful polymerization. However, appending electron donating groups to the monomer structure tends to make the resulting polymer more hydrophilic. A BCP design with two hydrophilic blocks would almost certainly have a low χ parameter and require high molecular weights to create ordered BCP structures. Due to the difficulties of synthesizing PMAMS BCPs by sequential anionic polymerization, this strategy was abandoned in favor of a modular BCP synthesis.

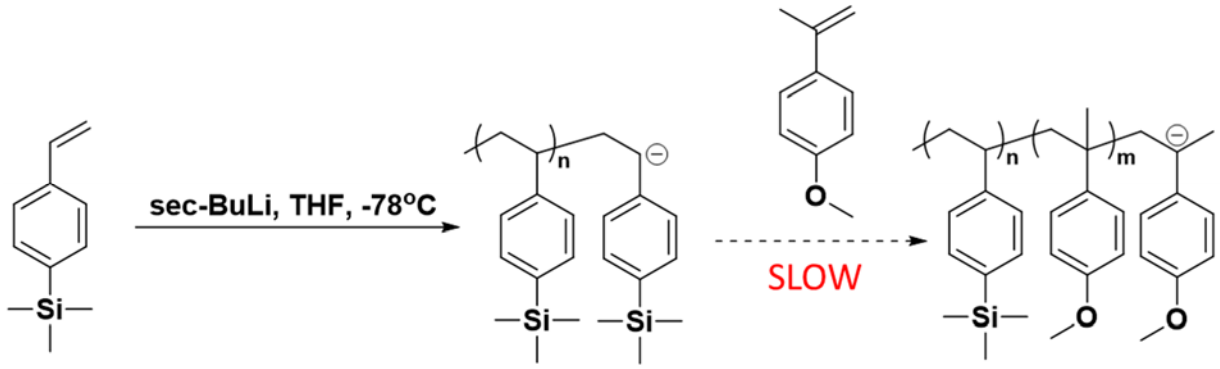

Scheme 5.13: Attempted synthesis of PTMSS-b-PMAMS by sequential anionic polymerization. Initiating the PMAMS block from a styryl anion largely failed due to the instability of the propagating tertiary anion.

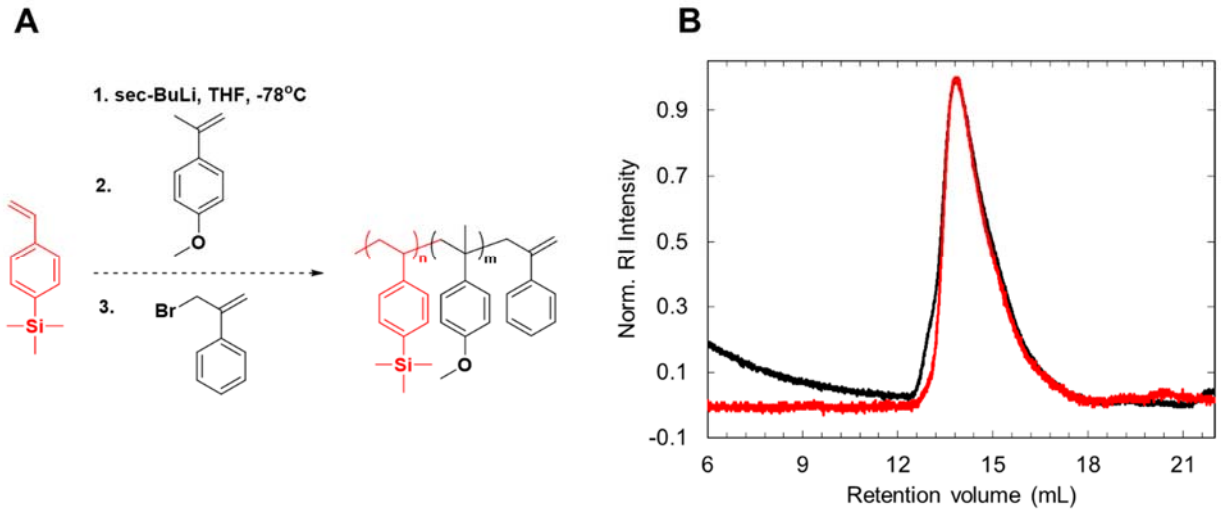

Figure 5.16: (A) reaction scheme for anionic polymerization of phenylallyl-functionalized PTMSS-*b*-PMAMS. (B) GPC traces for the PTMSS aliquot (red) and product after sequential addition of methoxy α-methylstyrene and 2-phenylallyl bromide (black).

As discussed in the section on the synthesis of PPHA BCPs, coupling chemistry can be used to synthesize BCPs from homopolymers with incompatible polymerization methods. We envisioned synthesizing PTMSS/PtBuSty and PMAMS homopolymers separately, functionalized with an azide and alkyne group, respectively. Cu(I)-catalyzed azide-alkyne cycloaddition chemistry could then be used to "click" the two homopolymers together to form the desired BCP architecture.

Azide-functionalized PTMSS/PtBuSty polymers are routinely made by ATRP followed by substitution of the terminal bromine atom with sodium azide (Scheme 5.14). To synthesize alkyne-functionalized PMAMS, a new end capping molecule was designed that incorporated both terminal alkyne and phenyl allyl moieties (Scheme 5.15).

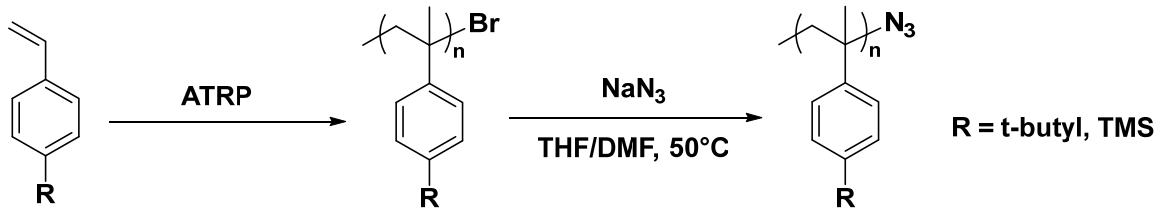

Scheme 5.14: Synthesis of azide-terminated blocks for "click" chemistry

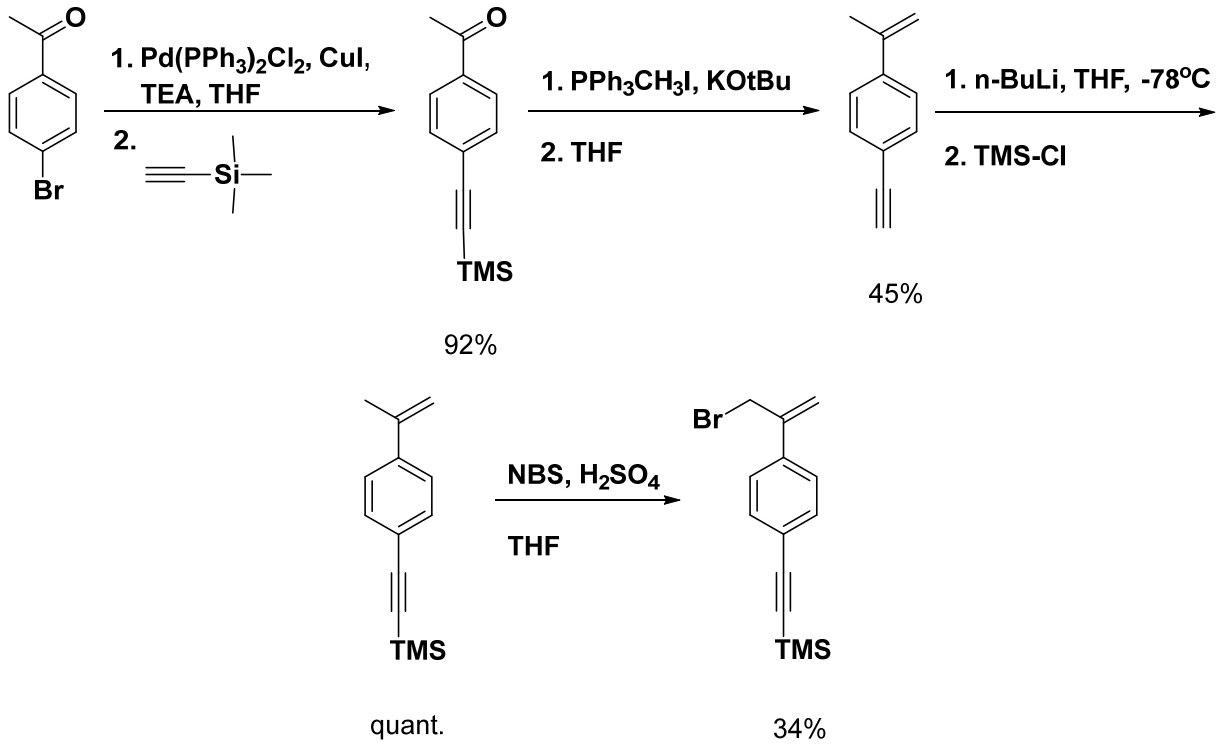

Scheme 5.15: Synthesis of end cap for PMAMS polymerization than includes both terminal alkyne and phenyl allyl moieties.

The synthesis of the end cap begins by substituting bromoacetophenone with a TMS-protected alkyne using Sonagashira coupling. The product was then converted to

the α-methylstyrene derivative using Wittig olefination. During the Wittig reaction, the TMS protecting group was removed. The terminal alkyne proton of the product is slightly acidic and readily removed by styryl anions. To limit the number of possible side reactions during termination, the terminal alkyne was re-protected by first deprotonating with n-BuLi and immediately adding TMS-Cl. Initiating the polymerization of the α-methylstyrene group with n-BuLi is orders of magnitude slower than the lithium-proton exchange with the terminal alkyne, so the protected alkyne was afforded quantitatively. Finally, bromination at the allylic position yielded the final end cap product. It should be noted that the bromination step must be performed last. In atmospheric conditions, phenyl allyl bromides are potent lachrymators!

Before coupling the azide- and alkyne-functionalized polymers together, it was necessary to first remove the TMS-protecting group from the terminal alkyne (Scheme 5.16). Figure 5.17 shows MALDI data before and after deprotecting a low molecular weight PMAMS homopolymer using tetra-n-butylammonium fluoride.

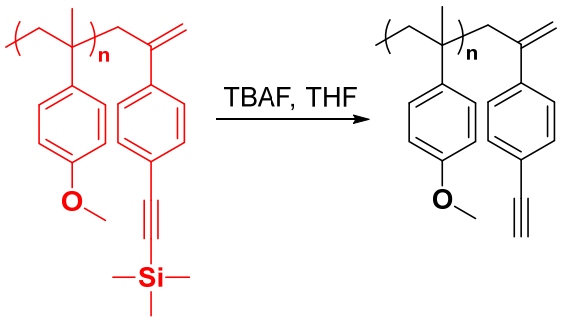

Scheme 5.16: Deprotection of terminal alkyne group using TBAF

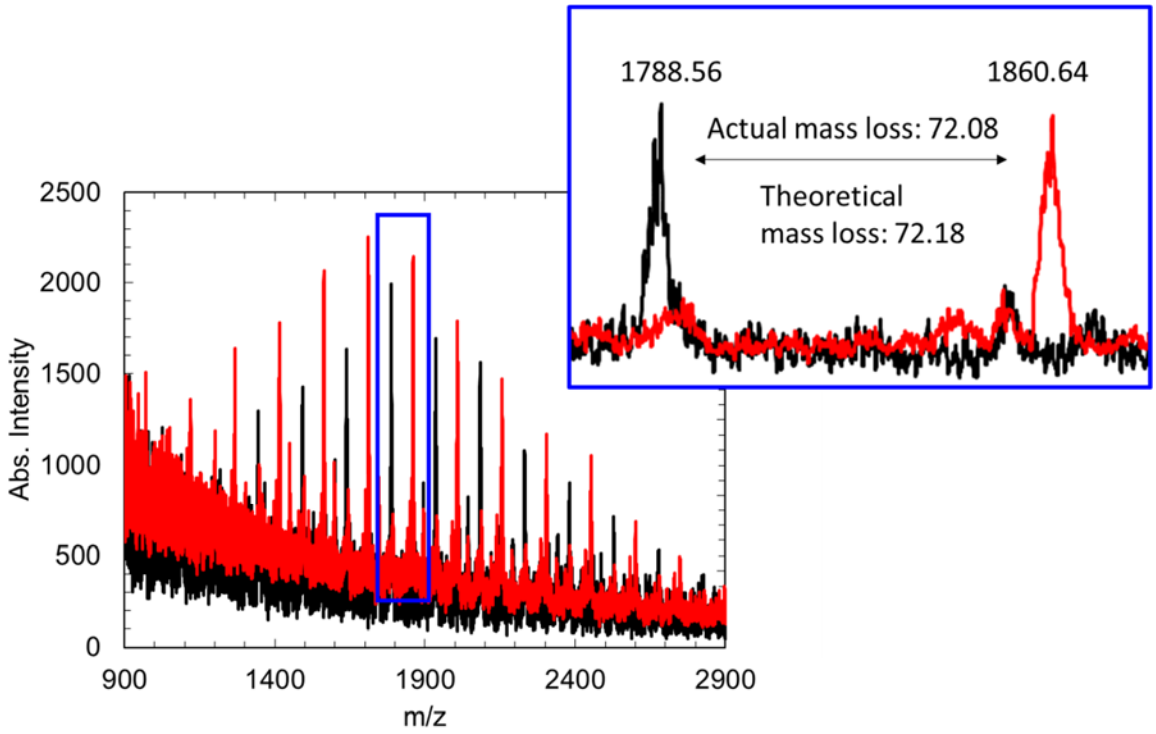

Figure 5.17: MALDI spectra before and after deprotection of the terminal alkyne group. The colors correspond to the polymers in Scheme 5.16.

PMAMS-*b*-PtBuSty and PMAMS-*b*-PTMSS were synthesized using the click reaction depicted in Scheme 5.17. Although the extent of the coupling reactions were generally high, residual amounts of unreacted homopolymer could be removed by washing with selective solvents such as hexanes for PTMMS and PtBuSty and DMF or acetonitrile for PMAMS homopolymer.

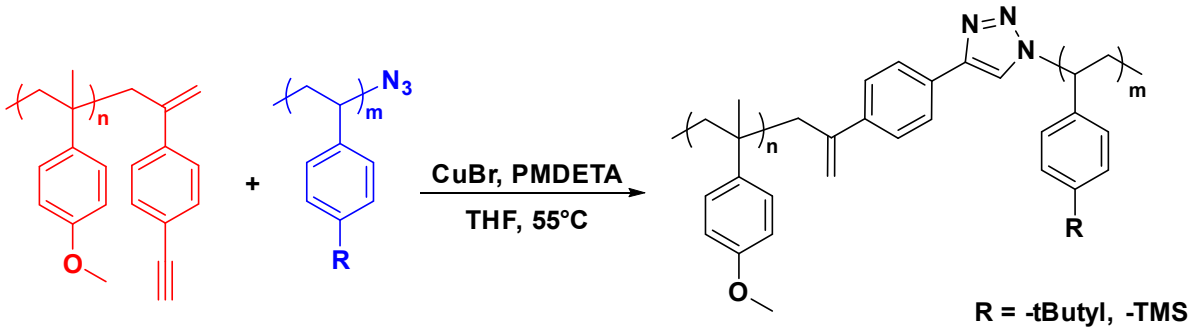

Scheme 5.17: Synthesis of PMAMS BCPs using Cu(I)-catalyzed azide-alkyne click chemistry

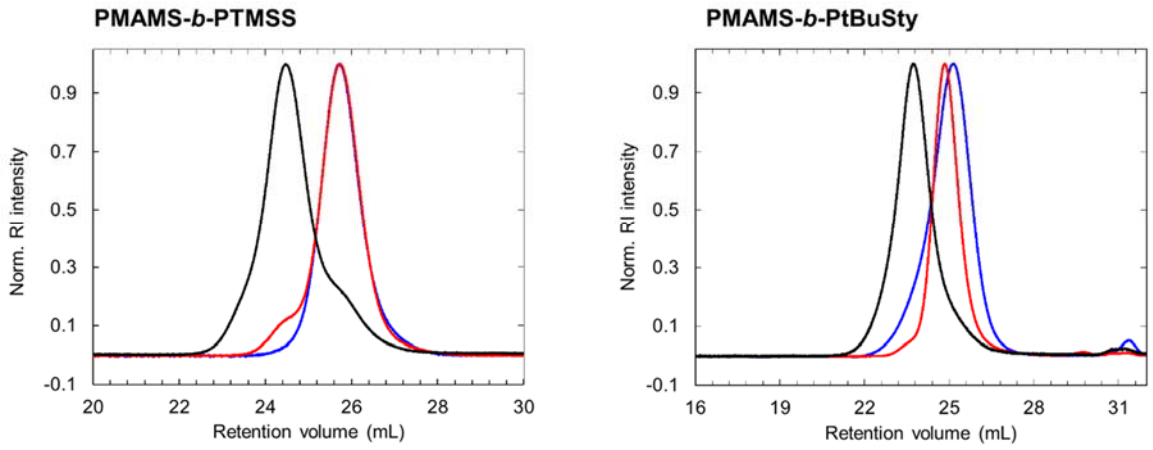

Figure 5.18: GPC traces for PMAMS-alkyne (red), PTMSS/PtBuSty-azide (blue), and BCP products after purification with selective solvent washing (black). The colors of the GPC traces correspond to the colors in Scheme 5.17.

Table 5.4: Characterization data for the polymers presented in Figure 5.18. M_n and Đ values were calculated from GPC using dn/dc values reported at the end of this chapter. Volume fractions were calculated from NMR. L_0 values were calculated using data from island/hole experiments and AFM characterization of island/hole films

	$M_{n,PMAMS}$ (kDa)	$Đ_{PMAMS}$	$M_{n,block\ B}$ (kDa)	$Đ_{block\ B}$	$M_{n,BCP}$ (kDa)	$Đ_{BCP}$	f_{PMAMS}	L_0 (nm)
PMAMS-*b*-PTMSS	18.7	1.06	17.5	1.02	33.6	1.12	0.48	24
PMAMS-*b*-PtBuSty	30	1.03	33.7	1.15	59.2	1.07	0.43	25

5.3.4 Thin Film Self-assembly of PMAMS-*b*-PTMSS

With PMAMS BCPs in hand, experiments were performed to characterize the thin film self-assembly behavior of these materials. NMR analysis suggested that these BCPs had the correct volume fractions of each block to produce lamellar structures in thin films. Small-angle X-ray scattering (SAXS) is a common way to probe the self-assembly of BCPs in bulk. However, upon annealing and exposing PMAMS BCPs to hard X-ray radiation, it was observed that these materials depolymerized. This led to inconclusive SAXS results.

Instead, the self-assembly behavior was tested by using island/hole experiments. In the presence of preferential surfaces, lamellae-forming BCPs can form wetting layers at both the bottom and free interfaces. This drives the formation of parallel lamellae. At incommensurate film thicknesses, the parallel lamellae will terrace and form either island or hole structures to avoid stretching of polymer chains.[209,210] The type of terracing formed depends on the wetting conditions of both surfaces as well as BCP film thickness, and the presence of islands or holes acts as a diagnostic test for the relative polarity of a given substrate.[115] Tracking the appearance and disappearance of terraced features can also be useful for elucidating the natural periodicity of a BCP (L_0).

Optical micrographs for the island/hole test for both PMAMS-*b*-PtBuSty and PMAMS-*b*-PTMSS BCPs can be seen in Figure 5.19. Despite forming I/H on bare SiO_2, the PMAMS-*b*-PtBuSty BCP did not form islands/holes on any other surfaces that were tested, making it very difficult to identify neutral surfaces for perpendicular BCP assembly. Neutral surfaces were identified for PMAMS-*b*-PTMSS using methods

previously reported.[211] Perpendicular structures were generate by confining a BCP film between these surfaces and annealing at high temperatures. The features produced by these experiments can be seen in Figure 5.20. These BCP features were developed using oxygen plasma, and the PTMSS block provided intrinsic etch resistance for this demonstration. However, the ultimate goal would be to generate analogous structures using strong acid catalysis and thermal development instead of plasma etching.

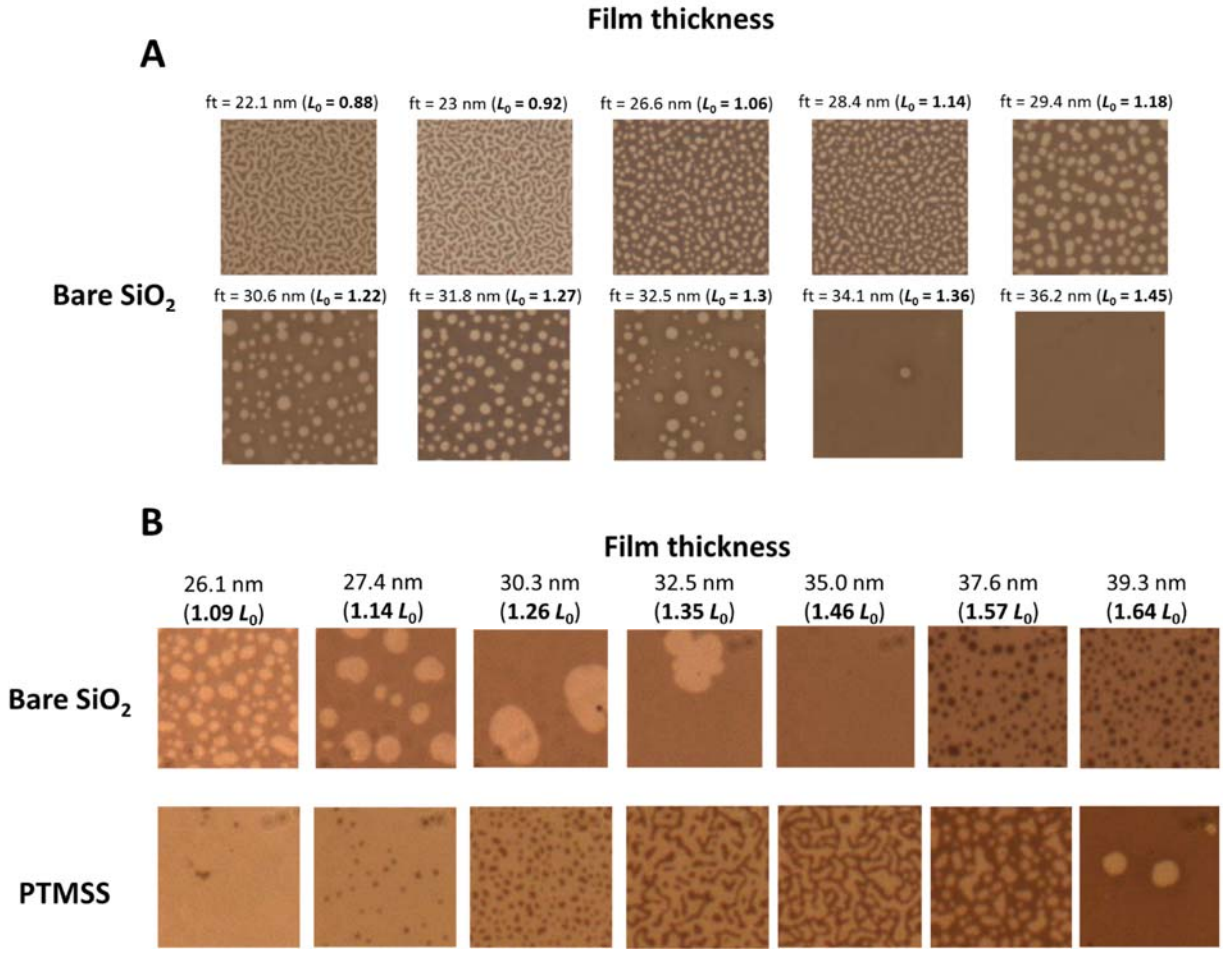

Figure 5.19: Optical micrographs showing island/hole terracing for (A) PMAMS-*b*-PtBuSty and (B) PMAMS-*b*-PMAMS on different substrates and at various BCP film thicknesses.

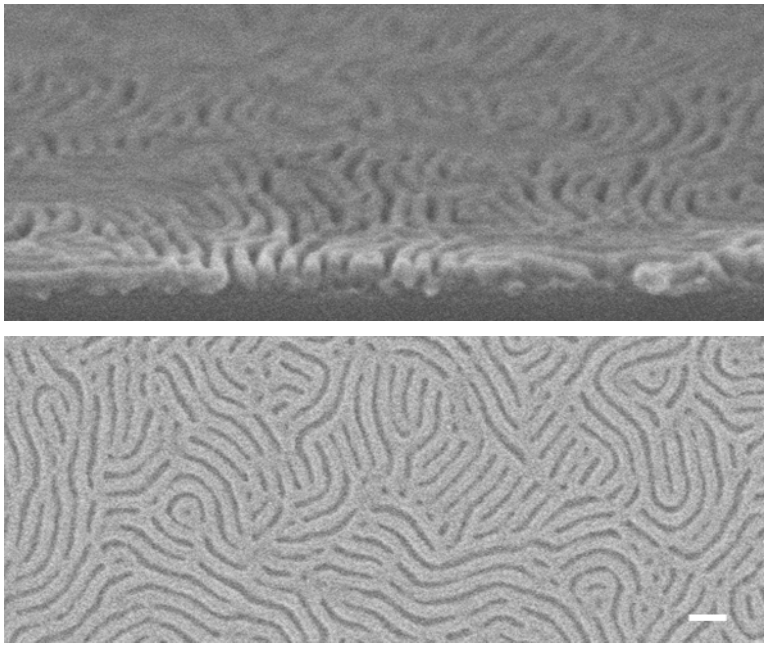

Figure 5.20: SEM images of perpendicular structures formed by annealing PMAMS-*b*-PTMSS between neutral surfaces at 200°C for 5 minutes. Scale bar = 50 nm

Unfortunately, blending PAG with PMAMS-*b*-PTMSS did not produce perpendicular structures in thin films. This could be caused by the PAG interfering with the self-assembly of the BCP as it segregates into one domain, affecting BCP morphology. Instead, oriented BCP films were exposed to strong acid vapor using a custom experimental apparatus built and provided by Lam Research (Figure 5.21).

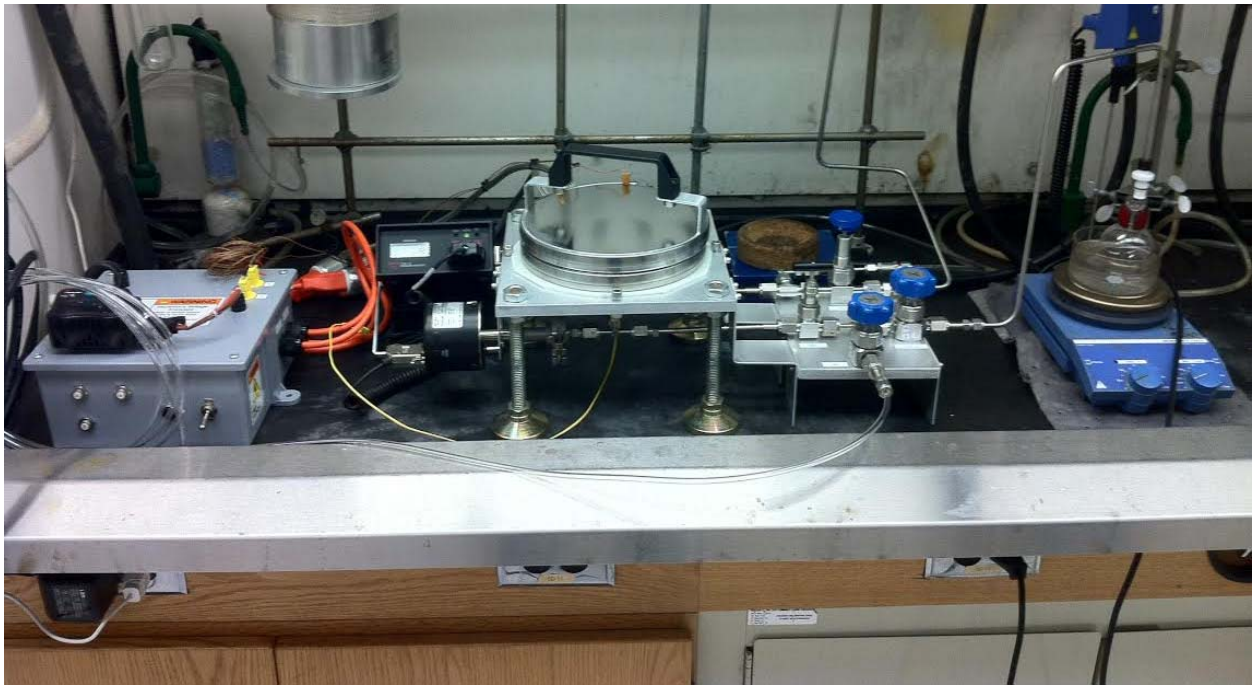

Figure 5.21: Acid exposure chamber used for exposing BCP films to either triflic acid or HBr vapor. BCP films are placed inside the chamber in the middle of the image. This chamber can be heated to promote depolymerization.

SEM images of developed BCP films exposed to triflic acid under various conditions can be seen in Figure 5.22. Films were either underdeveloped and not completely depolymerized, or feature collapse was evident in films that had been exposed to too much acid vapor. The feature collapse could be due to monomer byproducts or acid vapor swelling BCP domains. No process window could be identified where perfectly developed features were achieved.

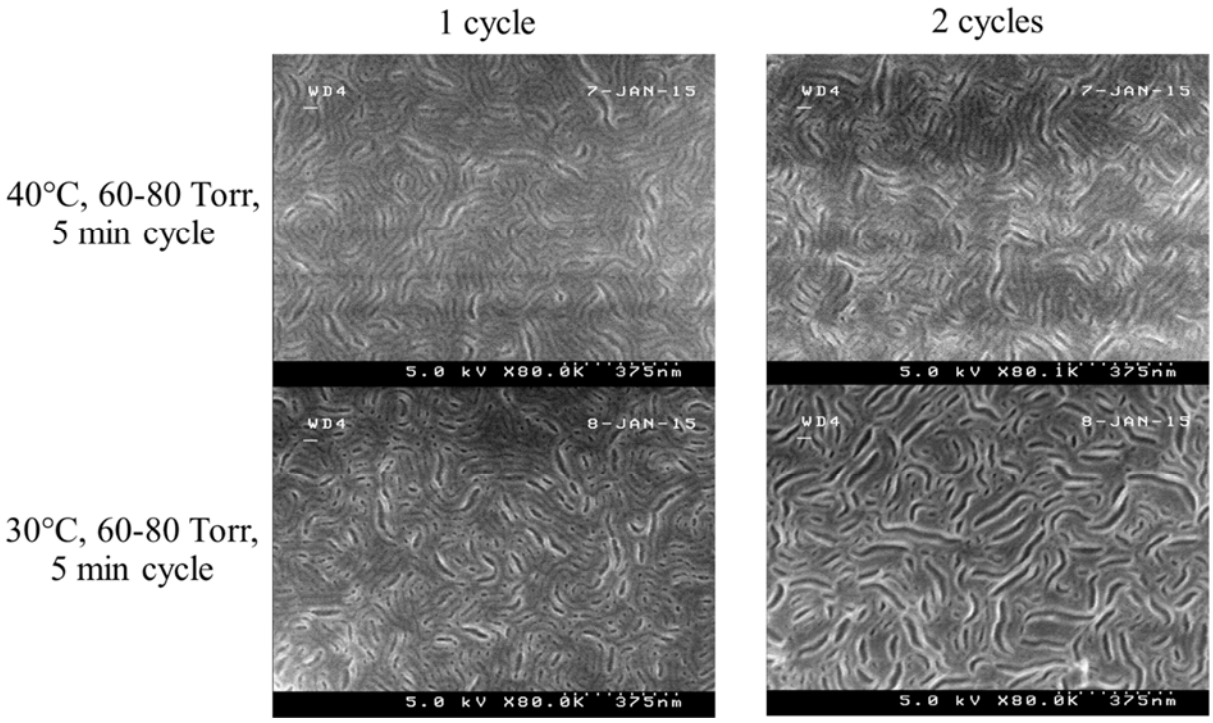

Figure 5.22: SEM images of PMAMS-*b*-PTMSS films after exposure to triflic acid at different temperatures and pressures. In each experiment, thin films were pumped down in the chamber, exposed to acid vapor at the listed temperature and pressure, and then purged using N_2 for 2 minutes. This constituted a single cycle.

Although it was promising to see that the PMAMS block could be successfully removed using acid vapor, the collapsed line/space patterns were not desirable for lithography applications. To improve on this design, more work needs to be done to identify an acid catalyst capable of blending with the BCP and initiating the depolymerization of PMAMS without swelling the BCP film. In addition, the cylinder-forming PMAMS-*b*-PTMSS may be less prone to pattern collapse in thin films and allow for a successful demonstration of the self-developing BCP concept.

5.4 CONCLUSIONS

Poly(4,5-dichlorophthalaldehyde) (PPHA-Cl_2) and poly(methoxy α-methylstyrene) (PMAMS) were synthesized by anionic polymerization and incorporated into a block copolymer (BCP) structure by reacting it with another homopolymer via coupling chemistry. By carefully selecting the chemistry of the end group, the BCP synthesis could be performed with very good efficiency. Low molecular weight homopolymers of PPHA-Cl_2 and PMAMS depolymerize when exposed to acid and heat. However, the corresponding block copolymers were difficult to assemble in thin films, and PMAMS-*b*-PTMSS did not depolymerize fully without causing unacceptable pattern collapse. To improve on this work, more control is needed over the polymerizations of the homopolymers to synthesize more well-defined block copolymer materials.

5.5 EXPERIMENTAL

5.5.1 Instrumentation

NMR spectra were recorded on a Varian Unity Plus 400 MHz instrument. Chemical shifts are reported in ppm downfield from TMS using the residual solvent as an internal standard (CDCl3, 1H 7.26 ppm). GPC data were collected with an Agilent 1100 Series isopump and autosampler with a Viscotek VE 2001 triple detector and THF as an eluent at 23°C. Three I-series mixed bed high-MW columns were calibrated relative to PS standards. Small-angle x-ray scattering (SAXS) measurements were collected using a Molecular Metrology instrument equipped with a high brilliance rotating copper anode

source (Kα radiation, λ = 1.5418 Å) and a two-dimensional 120 mm gas filled multiwire detector. Vertical focus was acquired with a single crystal germanium mirror, and horizontal focus and wavelength selection was made with an asymmetrically cut Si(111) monochromator. The beam was calibrated using silver behenate with its primary reflection peak set at 1.076 nm^{-1}.

Ellipsometry was performed with a J.A. Woollam Co, Inc. VB 400 VASE Ellipsometer with wavelengths from 382 to 984 nm and a 65° angle of incidence. AFM scans were obtained using an Asylum MFP-3D Origin operating in tapping mode. A Brewer CEE 100CB Spincoater was used to coat all thin films. A Zeiss Supra 40 VP scanning electron microscope operating at 5 kV with the in-lens detector and a working distance of 2-5 mm was used to collect all initial SEM data.

5.5.2 Syntheses

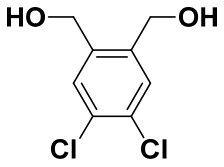

4,5-dichlorobenzene-1,2-dimethanol – A 1 L, three-neck round bottom flask was equipped with an addition funnel, Schlenk line inlet, and magnetic stir bar. The apparatus was flame dried and purged with N_2 (3x). The flask was charged with dry THF (40 mL) and 4,5-dichlorophthalic acid (11.0 g, 46.8 mmol) and cooled to 0°C using an ice bath. BH_3·THF (121.6 mL, 1M solution) was added dropwise from the addition funnel over a period of 1 hour. Once the addition was complete, the flask was warmed to room temperature and the solution was stirred for an additional 24 hours. The flask was then cooled to 0°C again and the addition funnel was charged with a 1:1 THF/H_2O solution (40 mL). The THF/H_2O was

added dropwise over a period of several minutes to quench excess BH_3·THF. The rate of addition was controlled to minimize the amount of H_2 gas produced by the quenching reaction. Once bubbles stopped evolving, the flask was removed from the ice bath and the contents were transferred to a 1 neck, 1 L round bottom flask. The THF was removed *via* rotary evaporation. The residue was redissolved in ethyl acetate and washed with H_2O (100 mL). The aqueous layer was separated and extracted with ethyl acetate (20 mL, 3x). The combined organic layers were washed with sat. brine (100 mL), dried over $MgSO_4$, and filtered to remove any solids. The solvent was removed *via* rotary evaporation to afford nearly pure 4,5-dichlorobenzene-1,2-dimethanol as a chalky, white powder (9.2 g, 44.4 mmol, 95% yield). ^{1}H-NMR (400 MHz, DMSO-d_6): δ 7.56 (s, 2H), 5.32 (t, 2H), 4.47 (d, 4H). HRMS (CI) m/z for $[M]^+$ -H_2O calcd. for $C_8H_8Cl_2O_2$ 187.98; found 187.9796.

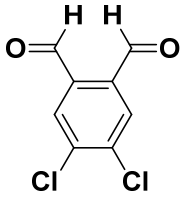

4,5-dichlorophthalaldehyde – A 250 mL, three-neck round bottom flask was equipped with an addition funnel, Schlenk line inlet, and magnetic stir bar. The apparatus was flame dried and purged with N_2 (3x). The flask was charged with DCM (35 mL) and oxalyl chloride (2.7 g, 21.2 mmol) and cooled to -78°C in a dry ice/IPA bath. A solution of DMSO (3.32 g, 42.5 mmol) in DCM (6 mL) was added dropwise over a period of 15 minutes. The resulting solution was stirred for 10 minutes after the addition was complete. A solution of 4,5-dichlorobenzene-1,2-dimethanol (2.01 g, 9.66 mmol) in DCM (10 mL) was added dropwise (note: the diol was not completely soluble in DCM) and stirred for 30 minutes after the addition was

complete. Triethylamine (17.1 g, 169.0 mmol) was added to the flask dropwise and the solution was stirred for 10 minutes after the addition was complete. The flask was then transferred to a water ice bath, stirred for 2 hours, and then warmed to room temperature, quenched with 200 mL of H_2O, and transferred to a separatory funnel. The aqueous layer was separated and extracted with DCM (100 mL, 2x). The organic layers were combined, washed with sat. $NaHCO_3$ (100 mL), sat. brine (200 mL), and dried over $MgSO_4$. The solvent and residual trimethylamine were removed *via* rotary evaporation, and the crude product was purified by column chromatography on silica gel (7:3 hexanes/ethyl acetate). The recovered product was recrystallized twice from cyclohexane to afford 4,5-dichlorophthalaldehyde (1.08 g, 5.31 mmol, 55% yield) as light yellow needles. ^{1}H-NMR (400 MHz, $CDCl_3$): δ 10.46 (s, 2H), 8.05 (s, 2H). ^{13}C-NMR (400 MHz; $CDCl_3$) δ 189.93, 139.1, 135.32, 133.08. HRMS (CI) m/z for $[M]^+$+H calcd. for $C_8H_4Cl_2O_2$ 201.96; found 202.9668.

Monomer purification for PPHA polymerization: Both o-phthalaldehyde and 4,5-dichlorophthalaldehyde were sublimed at 50°C overnight to isolate purified monomer. An additional recrystallization from cyclohexane was required before 4,5-dichlorophthalaldehyde could be polymerized.

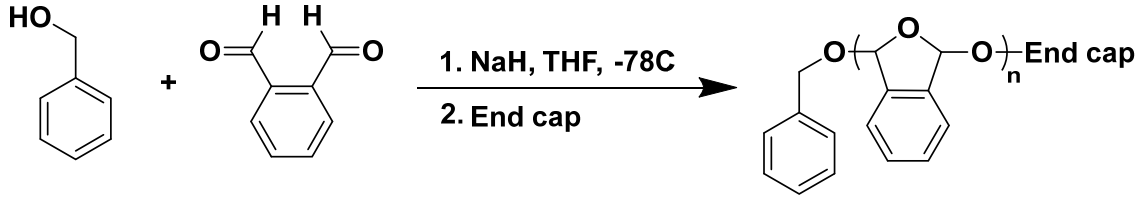

Typical PPHA polymerization initiated with benzyl alcohol/strong base: A three neck, 25 mL round bottom flask was equipped with a magnetic stir bar, a Schlenk line inlet, and two rubber septa. The flask was flame dried and purged with N_2 (3x). One septa was removed to add phthalaldehyde (1.04 g, 7.68 mmol) to the flask and quickly replaced. The flask was subsequently evacuated and purged again with N_2 (2x). Dry THF (29 mL) was added to the flask and the solution was stirred until all phthalaldehyde had dissolved. The solution was then free-pump-thawed three times. A separate flame-dried flask was charged with benzyl alcohol (1.36 g) and THF (36 g) to make a stock initiator solution. NaH (740 mg) was added slowly to the stock solution to form the initiator. The polymerization flask was placed in a dry ice/IPA bath and stirred for 5 minutes to cool the phthalaldehyde solution to -78°C. A small amount of the initiator solution (605 mg) was added in one portion to the polymerization flask. The reaction was left stirring overnight at -78°C. To terminate the polymerization, 2 equivalents of end capping reagent were added to the polymerization flask and the solution was stirred for an additional hour at -78°C. The flask was removed from the dry ice bath and allowed to warm to room temperature. Most of the THF was removed *via* rotary evaporation until only a few mL remained. The polymer was precipitated into MeOH and filtered. The recovered polymer was dissolved in THF, reprecipitated in MeOH, and filtered (2x). The polymer was dried under high vacuum to yield a white powder (49% yield).

Polymerizations with P_2-t-Bu, PS-OH, and PPHA-Cl_2 were performed using the same experimental methods as described above.

PS-*b*-PPHA-Cl_2 synthesis: Isothiocyanate-functionalized PPHA-Cl_2 (1 equiv.) and amine-functionalized PS (1.1 equiv.) were added to a flask with DCM (10 mL) and a magnetic stir bar. The solution was stirred for 24 hours and the solvent was removed *via* rotary evaporation until 2 mL remained. The BCP product was precipitated into MeOH and filtered. The recovered polymer was dissolved in THF, reprecipitated in MeOH, and filtered. The polymer was dried under high vacuum to yield a white power (91% yield).

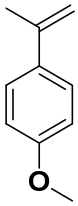

4-methoxy-α-methylstyrene - A 250 mL round bottom flask was equipped with a stir bar and flame dried. Triphenylphosphonium iodide (18.2 g, 44.9 mmol, 1.3 eq) and dry THF (80 mL) were added under nitrogen. The slurry was cooled to 0˚C in an ice bath. Potassium *tert*-butoxide (5.03 g, 44.9 mmol, 1.3 eq) was added under nitrogen portionwise. The white slurry turned bright yellow. A solution of p-methoxyacetophenone (5.2 g, 34.5 mmol, 1 eq.) in dry THF (15 mL) was added slowly via syringe needle. After 5 minutes, the slurry became white. The reaction was stirred for an additional 3.5 hrs. TLC showed that that the acetophenone was completely consumed. The reaction was quenched with 5 mL of water. The solids were filtered off, and the solvent was removed *via* rotary evaporation. The crude product was passed through a plug of silica using hexanes as the eluting solvent. The solvent was removed using rotary evaporation and the product was dried *in vacuo*. The monomer was distilled (b.p.: 78-80˚C at 4 mTorr) prior to anionic polymerization to yield 3.3 g (64% yield), which solidified upon standing to form a white, crystalline solid. ^{1}H-NMR (400 MHz, $CDCl_3$): δ

7.46-7.44 (m, 2H), 6.91-6.85 (m, 2H), 5.33 (m, 1H), 5.03 (m, 1H), 3.84 (s, 3H), 2.17 (m, 3H). ^{13}C-NMR (400 MHz; $CDCl_3$) δ 159.02, 142.51, 133.70, 126.56, 113.50, 110.62, 55.24, 21.88

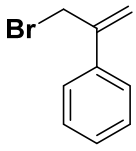

2-phenylallyl bromide – NOTE: This compound is a potent lachrymator. Take precautions when cleaning glassware used for synthesis. A 250 mL, three-neck round bottom flask was equipped with a reflux condenser, Schlenk line inlet, and magnetic stir bar. The flask was flame-dried and purged with N_2. The flask was first charged with dry THF (120 mL), then α-methylstyrene (4.55 g, 38.5 mmol, 1 eq.), N-bromosuccinimide (7.19 g, 40.4 mmol, 1.05 eq), and H_2SO_4 (378 mg, 3.85 mmol, 0.1 eq) were added sequentially. The flask was placed in a oil bath at 100°C and stirred for 6 hours. The flask was cooled to room temperature and most of the solvent was removed *via* rotary evaporation. The residue was diluted with hexanes (100 mL) and washed with H_2O (100 mL, 3x). The organic layer was separated, dried over $MgSO_4$, and filtered. The solvent was removed *via* rotary evaporation and the residue was purified via colum chromatography using hexanes as the eluting solvent. The product was dried *in vacuo* to yield 2-phenylallyl bromide (4.2 g, 55%) as a colorless oil. ^{1}H-NMR (400 MHz, $CDCl_3$): δ 7.52-7.49 (m, 2H), 7.41-7.32 (m, 3H), 5.57 (s, 1H), 5.50 (s, 1H), 4.39 (s, 2H). ^{13}C-NMR (400 MHz; $CDCl_3$) δ 144.31, 137.65, 128.54, 128.37, 126.11, 117.29, 34.20. HRMS (CI) m/z for $[M]^+$+H calcd. for C_9H_9Br 195.99; found 195.9888.

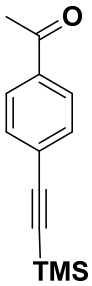

4'-(2-trimethylsilylethynyl)acetophenone – A 250 mL, three-neck round bottom flask was equipped with a Schlenk line input and a magnetic stir bar. The flask was flamed dried and purged with N_2. THF (50 mL), 4-bromoacetophenone (10.0 g, 50.2 mmol, 25 eq.), $Pd(PPh_3)_2Cl_2$ (1.40 g, 2.01 mmol, 1 eq.), CuI (191 mg, 1.00 mmol, 0.5 eq.), and triethlyamine (21 mL) were added under nitrogen. The solution was stirred for 5 minutes and placed in an ice bath. A solution of trimethylsilylacetylene (5.18 g, 52.8 mmol, 26.25 eq.) in THF (10 mL) was added dropwise over 30 minutes and stirred for an additional 30 mins. The solvent was removed *via* rotary evaporation and the residue was diluted with pentane (100 mL). The slurry was filtered through Celite and the solvent was evaporated. The crude product was purified by vacuum distillation (b.p. 96-98°C at 1 mTorr) to yield 4'-(2-trimethylsilylethynyl)acetophenone (9.9 g, 92% yield) as a white solid upon standing overnight. ^{1}H-NMR (400 MHz, $CDCl_3$): δ 7.90-7.85 (m, 2H), 7.55-7.50 (m, 2H), 2.58 (s, 3H), 0.24 (s, 9H). ^{13}C-NMR (400 MHz; $CDCl_3$) δ 197.53 , 136.53 , 132.24 , 128.38 , 128.17 , 104.10 , 98.31 , 26.88 , 0.02.

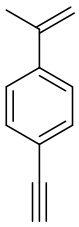

p-ethynylstyrene - A 250 mL round bottom flask was equipped with a stir bar and flame dried. Triphenylphosphonium iodide (21.0 g, 51.7 mmol, 1.3 eq) and dry THF (120 mL) were added under nitrogen. The slurry was cooled to 0˚C in an ice bath. Potassium *tert*-butoxide (5.8 g, 51.7 mmol, 1.3 eq) was added under nitrogen portionwise. The white slurry turned bright yellow. A solution of 4'-(2-trimethylsilylethynyl)acetophenone (8.61 g, 39.8 mmol, 1 eq.) in dry THF (20 mL) was

added slowly via syringe needle. After 5 minutes, the slurry became white. The reaction was stirred for an additional 3.5 hrs. TLC showed that that the acetophenone was completely consumed. The reaction was quenched with 5 mL of water. The solids were filtered off, and the solvent was removed *via* rotary evaporation. The crude product was passed through a plug of silica using hexanes as the eluting solvent. The solvent was removed using rotary evaporation and the product was dried *in vacuo*. The crude product was distilled (b.p.: 90-92˚C at 2 mTorr) to yield 2.55 g of p-ethynylstyrene (45% yield) as a colorless oil. ^{1}H-NMR (400 MHz, $CDCl_3$): δ 7.48-7.42 (m, 4H), 5.40 (s, 1H), 5.13 (s, 1H), 3.10 (s, 1H), 2.14 (s, 3H).

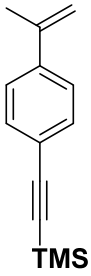

4'-(2-trimethylsilylethynyl)styrene – A 100 mL, three-neck round bottom flask was equipped with a Schlenk line inlet and magnetic stir bar. The flask was flame-dried and purged with N_2 (3x). p-ethynylstyrene (1.59 g, 11.1 mmol, 1 eq.) and THF were added and the flask was cooled to -78°C in a dry ice/IPA bath. n-BuLi (4.68 mL, 2.5 M solution) was added dropwise. The solution slowly turned dark green. Immediately after the n-BuLi addition was complete, TMS-Cl (1.57 g, 14.5 mmol, 1.3 eq.) was added dropwise. The solution slowly turned colorless as the TMS-Cl was added. After completing the addition, the solution was allowed to warm to room temperature. The solvent was removed *via* rotary evaporation and the crude product was distilled (b.p. 125°C at 0.4 mTorr) to yield 4'-(2-trimethylsilylethynyl)styrene (2.3 g, 95% yield) as a colorless oil. ^{1}H-NMR (400 MHz, $CDCl_3$): δ 7.44-7.38 (m, 4H), 5.40 (s, 1H), 5.12 (s, 1H), 2.13 (s, 3H), 0.25 (s, 9H).

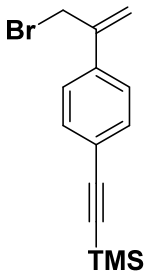

4'-(2-trimethylsilylethynyl)styrene bromide – Synthesized using the same reaction conditions as 2-phenylallylbromide, except starting with 3.7 g of 4'-(2-trimethylsilylethynyl)styrene. The product was isolated as an off-white solid (330 mg, 34% yield). ^{1}H-NMR (400 MHz, $CDCl_3$): δ 7.50-7.40 (m, 4H), 5.55 (d, 2H), 4.36 (d, 2H), 0.25 (s, 9H). HRMS (CI) m/z for $[M]^{+}$+H calcd. for $C_{14}H_{17}BrSi$ 292.03; found 292.0277.

Purification for anionic polymerization

α-methylstyrene and methoxy-α-methylstyrene - Two 500 mL Schlenk flasks were loaded with di-n-butylmagnesium (ca. 1.5 mL for every 5 g monomer) in a glove box and the solvent was removed in vacuo on a Schlenk line. Monomer was distilled trap-to-trap through a flame-dried short path into the first dry di-n-butylmagnesium Schlenk flask and the slurry was stirred for an hour at room temperature (since methoxy-α-methylstyrene is a solid at room temperature, this part was skipped). Monomer was trap-to-trap distilled into the second di-n-butylmagnesium Schlenk flask and stirred (except in the case of methoxy-α-methylstyrene). Finally, monomer was trap-to-trap distilled into a flame-dried Schlenk flask and stored in a glovebox freezer.

Solvent purification - Tetrahydrofuran was passed through a Pure Solv MD-2 solvent purification system containing two activated alumina columns to remove trace water and a copper supported redox catalyst to remove oxygen. The purified THF was added to a 500 mL Schlenk flask directly from the purification system. For making solutions of

methoxy-α-methylstyrene, methylcyclohexane was distilled trap-to-trap over n-BuLi which had previously been dried *in vacuo*.

PMAMS polymerization

A 500 mL glass reactor, charged with a stir bar, was flame-dried under high vacuum and purged with argon gas (5x). Attached to the ports were a glass thermocouple well, a solvent flask, two glass blanks, and a glass arm with inlets to the Schlenk line, pressure gauge, and rubber septum. Purified THF (100 g) was added and the solvent was magnetically stirred. The reactor was cooled to -78 °C with a dry ice/IPA bath while maintaining a 3 psig overpressure of argon in the reactor. sec-BuLi (0.3 mL of a 1.4 M solution in hexanes, 0.42 mmol, 1.0 eq.) was then added via syringe. One hour later, a solution of methoxy-α-methylstyrene (6.24 g, 42 mmol, 100 eq.) was added via syringe. 2-phenylallylbromide (198 mg, 1 mmol, 2.4 eq.) was then added via syringe and the solution color disappeared after just a few drops. The solution was stirred for an additional 5 minutes, then transferred to a 250 mL round bottom flask. Most of the solvent was removed *via* rotary evaporation until approximately 10 mL remained. The polymer was then precipitated into methanol and the resultant white powder was dried in vacuo. The total recovered mass was 4.0 g. For α-methylstyrene, the conversion went to nearly 100%.

NBS-bromination of α-methylstyrene – PAMS (1.0 g, 0.33 mmol) was added to a 100 mL round bottom flask with CCl_4 (30 mL). N-bromosuccinimide (11.75 g, 66 mmol) and

AIBN (0.66 mmol) were added to the flask which equipped with a reflux condenser and subsequently placed into an oil bath at 90°C. The solution was stirred for 4 hours and cooled to room temperature. Solids were filtered off and the solvent was removed *via* rotary evaporation. The residue was redissolved in THF (6 mL), precipitated in MeOH, and filtered (3x). The slightly orange polymer powder was dried *in vacuo* (0.82 g).

Azide-alkyne click reaction – Equal equivalents of alkyne-functionalized PMAMS and azide-functionalized PTMSS/PtBuSty were added to a flask with 1.5 equivalents of Cu(I)Br and PMDETA, and 20 mL of THF. The solution was stirred overnight at 55°C. The solution was cooled to room temperature and filtered through a short plug of alumina using THF as the eluting solvent. Solvent was removed *via* rotary evaporation until a few mL remained. The polymer solution was precipitated into MeOH and filtered. Homopolymer impurities were removed by either washing the collected polymer with hexanes or DMF/acetonitrile mixtures. After precipitating again into MeOH, the powder was dried overnight *in vacuo*.

5.6 ACKNOWLEDGEMENTS

Chris Bates assisted with the first PPHA homopolymer syntheses. Special thanks goes to Anthony DiLauro for generously teaching me how to make 4,5-dichlorophthalaldehyde. I would also like to thank Anthony Engler for his help in lab during the time this work was completed. Steve Sirard developed the etch process for PMAMS-*b*-PTMSS and imaged the fingerprint patterns. Also, special thanks goes to the researchers at Lam who designed and built the acid vapor chamber setup.

Chapter 6: A Chemically Amplified Resist without Catalyst

This chapter describes our efforts to design a new type of resist that realizes amplification via depolymerization rather than catalysis. Drastic changes in molecular weight can effect a solubility change without requiring diffusion. However, the self-immolative or "unzipping" polymer that is responsible for depolymerizing must be carefully designed to degrade under specific conditions and must meet established standards for normal resist processing, including etch resistance and thermal stability. The aromatizing polyester described in this chapter functions as an exceptionally sensitive positive-tone resist for electron beam lithography (EBL) when blended with a robust matrix polymer. High resolution patterns were produced with reasonable line edge roughness after optimizing the lithography process. We are cautiously optimistic that this type of system could serve as a model for the design of a new family of resist materials for electron beam and even extreme ultraviolet (EUV) lithography.

6.1 INTRODUCTION

6.1.1 Chemically Amplified Resist Design

The evolution of photolithography can be documented by the progressive reduction in the wavelength of light used for projection exposure tools.[212] Each transition requires new resist materials to meet the specific challenges of enabling photochemistry at different wavelengths.[65] The transition from 365 to 248 nm lithography was particularly challenging from a materials standpoint. Resists for 365 nm lithography did not have to have high quantum efficiencies, because high pressure Hg lamps have

excellent power output at 365 nm. Hg lamps do produce light at lower wavelengths; the lowest characteristic emission for Hg lamps is found near 250 nm (Figure 6.1). Although patterning at 248 nm provided a significant resolution increase, the power output at this wavelength is an order of magnitude lower than the available power at 365 nm. This means much longer exposure times are needed for patterning resists with the same dose requirement. This problem could have been (and eventually was) solved by retrofitting exposure tools with more powerful KrF excimer lasers operating at 248 nm,[213] but at the time these light sources were not compatible with manufacturing equipment. Even if more light was available, traditional i-line resists were opaque at 248 nm and did not significantly photobleach during exposure. This led to features with unacceptably sloped sidewalls after development. A new type of resist was required that could be imaged using very low doses of DUV light.

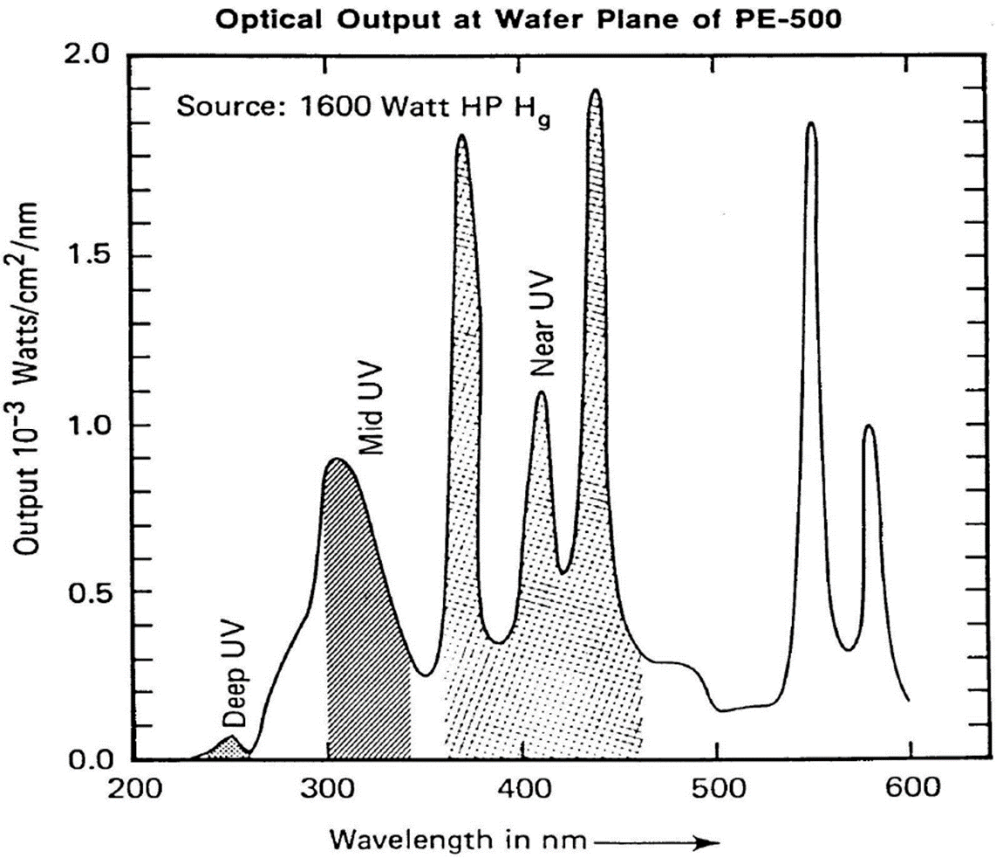

Figure 6.1: Spectral power output of high pressure Hg light source.

The photoactive compound in i-line resists is a diazonaphthoquinone (DNQ), which is converted to an indene carboxylic acid upon exposure to light in humid environments (Scheme 6.1). The rate of this reaction is directly proportional to the radiation dose supplied to the resist, because each DNQ molecule must absorb at least one photon for chemistry to occur. As a result, large numbers of photons are required to produce enough indene carboxylic acid and effect a solubility switch in the exposed areas. Photon availability is not an issue at the major characteristic emission wavelengths of mercury (436 and 365 nm), but posed a serious challenge at 248 nm.

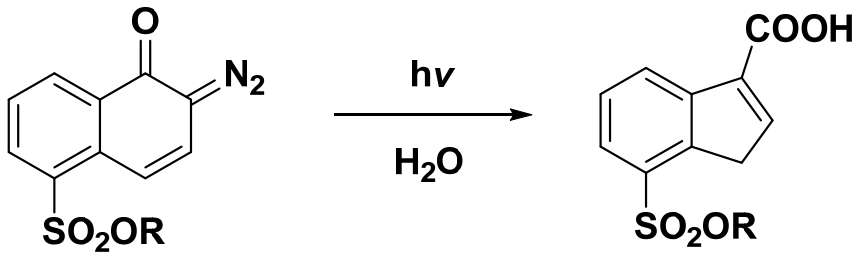

Scheme 6.1: Reaction scheme for the conversion of diazonaphthoquinone (DNQ) to indene carboxylic acid

The solution to this problem came from the realization that the *effective* quantum yield of a photoresist could be greatly enhanced by catalysis.[214] CARs operate by a more efficient mechanism than DNQ/Novolak resists: instead of directly effecting a chemical change in the resist, exposure to light activates a photoacid generator (PAG) inside the polymer film. As a result, information from the aerial image at the resist surface is transferred into a latent image of strong acid. During the subsequent post-exposure bake, the acid simultaneously diffuses and deprotects many reactive sites in the polymer matrix. This diffusion process is the key to chemical amplification[76] and increases the effective quantum yield of the initial photoreaction to well above one.

Unfortunately, this diffusion process is also responsible for blurring the latent image. During the post-exposure bake (PEB), the photoacid diffuses laterally into areas of the film not originally exposed to light. The stochastic nature of this mass transport process results in roughness and line placement errors in the final developed pattern. Because resist speed and roughness are intrinsically linked by the photoacid diffusion, a

fundamental trade-off between throughput and pattern quality exists for any catalyst-based CAR used in semiconductor manufacturing.

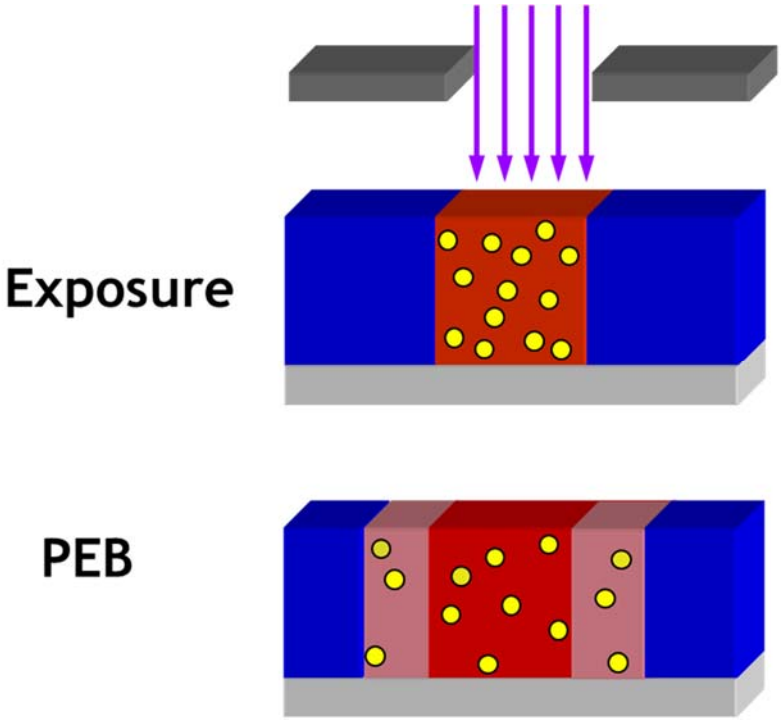

Figure 6.2: Cartoon depicting the bias/blur problem with CARs

This zero sum game is famously captured by the "triangle of death", also known as the RLS triangle (Figure 6.3A). The three sides of the triangle represent resist speed, resolution, and roughness in the developed pattern. These variables are not independent; they are linked by the mechanism of diffusion. Therefore, no amount of optimization can improve one leg of the triangle without affecting the other two sides. Heuristically speaking, the area of the triangle must remain constant. For instance, improving the speed of the photoresist requires more catalytic action, but increasing the diffusion length of the photoacid blurs the latent image and produces linewidth errors. The sensitivity of the

resist can be lowered by introducing basic "quenchers"[215,216] or polymer-bound PAG[217] to improve image quality. However, these modifications come at the price of lower throughput. Various figures-of-merit have been introduced to attempt to quantify the performance of a resist for sensitivity, line edge roughness, and resolution. These include Wallow's Z-factor[86] and the KLUP number.[218]

To make matters worse, RLS problems will be exacerbated as the industry shifts to EUV. Even faster resists will be required to compensate for a dim light source, but the resist must also pattern features with high resolution and stringent standards for roughness and critical dimension control.

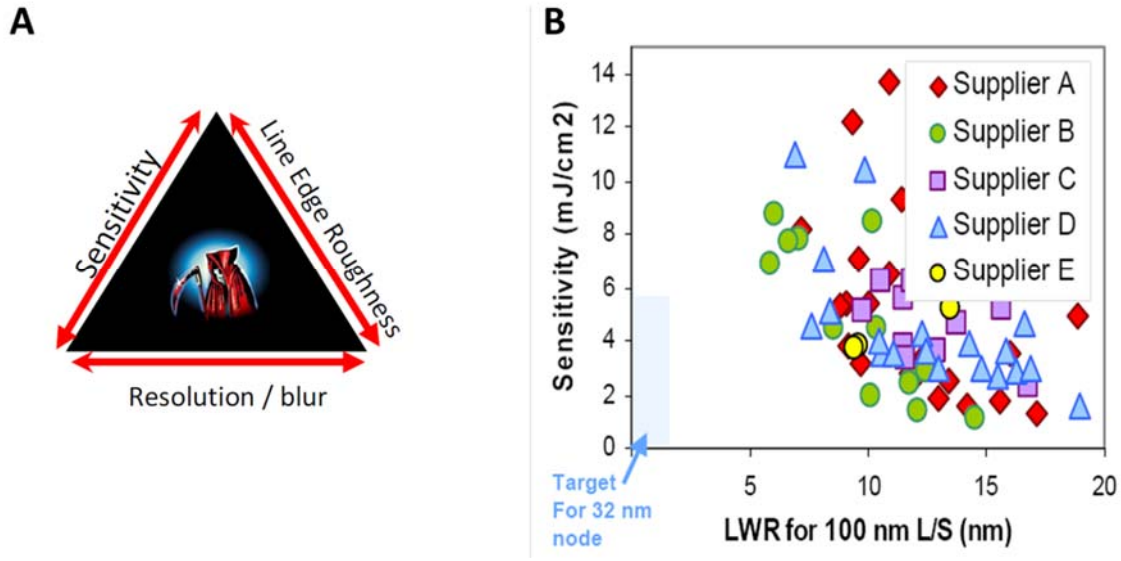

Figure 6.3: (A) The "triangle of death", depicting the relationship between resist sensitivity, resolution, and line edge roughness. (B) Graph that plots the sensitivity of commercially available CARs against LWR measurements. An "exclusion zone" exists in the lower left corner of the plot, which is a demonstration of how difficult it is to design a CAR that prints patterns quickly and with high fidelity.

6.1.2 Amplification Via Depolymerization

Catalysis is not the only way to achieve chemical amplification, however. For example, light or other stimuli can cause main chain scission reactions in the backbone of polymers that induces depolymerization. The resulting decrease in molecular weight of the polymer chains causes exposed regions of a resist film to become more soluble.[219] PMMA is an example of a polymer that undergoes main chain scission *without* depolymerizing at room temperature. Naturally, PMMA is a slow resist for the same reasons that DNQ/Novolak is slow; one photon is required to break one chemical bond, meaning large doses of radiation are required for complete resist exposure. However, certain materials, known colloquially as "unzipping" polymers, are capable of completely depolymerizing even if only one bond in the polymer backbone is ruptured.[220,221] Drastic changes in molecular weight can thus be leveraged for substantial gain, because one photochemical event leads to the breaking of many chemical bonds.[222,223] But, since the degradation process is confined to only one molecule, no diffusion is required to produce a solubility switch. The low-molecular weight byproducts of depolymerization can even vaporize afterwards, producing a self-developing image during exposure or the post-exposure bake.[168,173,177,224]

To understand why certain polymers are so prone to degradation, it's important to define the phenomena known as ceiling temperature.[225,226] Every polymerization can be thought of as an equilibrium reaction which has a temperature-sensitive equilibrium constant. Naturally, there exists a certain temperature for every polymerization where equilibrium is balanced between propagation and depolymerization. Here, at the ceiling

temperature, the rate of propogation equals the rate of depolymerization. For many monomer/polymer systems, such as polystyrene, the ceiling temperature is high enough that the polymerization reaction at normal conditions is practically irreversible. However, for some systems, the ceiling temperature is so low that the polymerization must be chilled to extreme temperatures to produce any polymer whatsoever.

Practically speaking, if active polymer chain ends exist below the ceiling temperature, monomer will preferentially add to the end of the chains and increase the molecular weight of the polymer. If the same active chain end is heated above the ceiling temperature, the equilibrium shifts to favor free monomer, and polymer chains will depolymerize as a result. This cycle can be repeated indefinitely as long as the ends of polymer chains are free to react with monomer. This phenomena can be exploited to create amplification in the following way: if a polymer chain is capped below the ceiling temperature, it is no longer free to participate in this equilibrium. When heated above the ceiling temperature, the polymer is thermodynamically driven to depolymerize, but can't because it is kinetically trapped by the end group. To initiate depolymerization, a new active polymer chain must be created, which requires cleaving either the end group or any bond in the polymer chain. If this cleavage occurs significantly above the ceiling temperature, the polymer will depolymerize quickly.

Poly(phthalaldehyde) (PPHA) is a well-known example of an unzipping polymer capable of producing amplification via depolymerization.[175,181] The acetal bonds in the PPHA backbone react with acid in extremely dilute concentrations. Work at IBM in the 1980's showed that PPHA could be formulated with photoacid generator to create

tremendously sensitive positive tone resists.[168,182] Examples of some of the patterns that could be produced with this resist can be seen in Figure 6.4. This system owes its speed to two sources of chemical amplification: the photoacid diffusing and reacting with many polymer chains, and each polymer chain completely depolymerizing after reacting with acid. While minimum doses of 2.4 mJ/cm^2 and 1 μC/cm^2 were achieved with DUV and electron beam lithography, respectively, PPHA did pose some challenges. Like PMMA and other polymers that degrade easily, PPHA has poor intrinsic etch resistance, limiting its utility for manufacturing. In addition, PPHA is not stable in solution and tends to depolymerize regardless of how carefully it is stored.

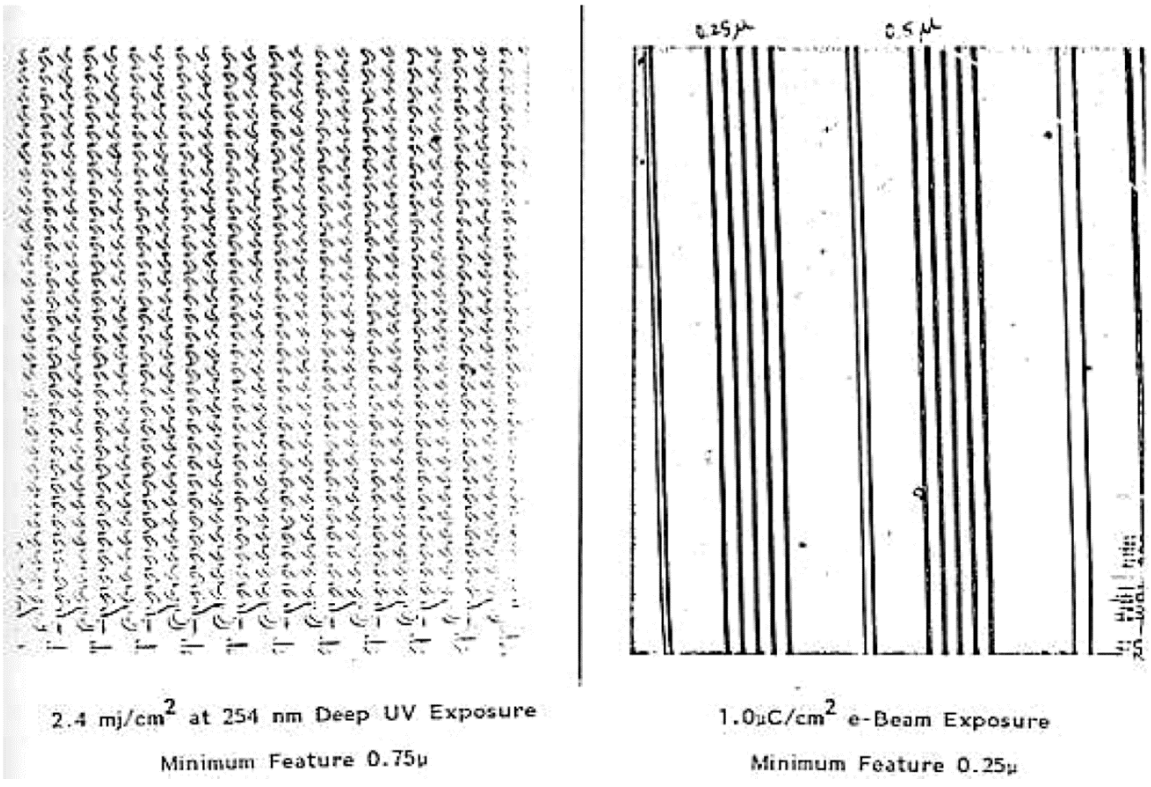

Figure 6.4: Examples of patterns printed in PPHA/PAG blends using DUV and e-beam exposure.[77]

To solve the issues associated with PPHA and other unzipping polymers, we envision combining the natural amplification of these materials with another type of resist design in which a matrix polymer is blended with a photoactive dissolution inhibitor.[227,228] The matrix polymer provides robust mechanical properties and resistance during RIE processing, and the photoactive compound undergoes a chemical change to increase dissolution rate in the exposed areas of the resist. Traditional i-line resists lack the sensitivity and resolution required for HVM, which is the original reason they were replaced with CARs. However, substituting DNQ with an unzipping polymer that acted as a dissolution inhibitor could create a complete resist system that potentially solves the fundamental problems with CARs.

6.1.3 Candidates for "Unzipping" Resists

We were inspired by the sensitivity exhibited by resist systems like the PPHA/PAG blends. To adopt this design, several material requirements had to be met. These include finding an unzipping polymer that had the following properties:

1) Specific and efficient depolymerization in thin films. Many polymers are capable of unzipping quickly in solution, but depolymerize slowly as a solid. A fast photoresist must either degrade immediately upon exposure or during a subsequent post-exposure bake so that the depolymerization is not the gating process during development. This usually means the ceiling temperature of the polymer should be near or below room temperature.

2) Inherent sensitivity to high energy radiation. To avoid the problems associated with CARs, the unzipping polymer cannot rely on a catalyst to initiate depolymerization. Unzipping polymers that are not inherently sensitive to radiation can be augmented with a photosensitive end cap.

3) Thermal stability for normal photoresist processing (i.e. soft bake to remove solvent)

4) Phase compatibility with a matrix polymer. This requirement is particularly challenging, as most binary polymer blends are not phase compatible with one another. Polymers can be encouraged to blend by decreasing the molecular weight of the homopolymers or by modulating the amount of hydrogen donating/accepting groups in the polymer structure. However, these are not guaranteed to create miscible blends, and it is very unusual to find polymers that can form binary resist systems. In addition to being phase compatible, the unzipping polymer must also inhibit the dissolution of the matrix polymer in an appropriate developer and the monomer must not.

Unfortunately, no documented materials could be found in the literature that met all the requirements for such a resist system. Attempts have been made to commercialize PPHA/Novolak and poly(olefin sulfone)/Novolak[229–231] blends in the past, but these systems tend to suffer from spontaneous degradation and opacity at 248/193 nm exposure wavelengths. In addition, PPHA and poly(olefin sulfone)s are not inherently sensitive to UV light (although poly(olefin sulone) is remarkably sensitive to electron beam radiation).

With collaborators at Penn State, a number of new unzipping polymers were synthesized and their structures can be seen in Figure 6.5. Each of the polymers had advantages and disadvantages relative to our application, but in general they had to meet the four requirements listed above.

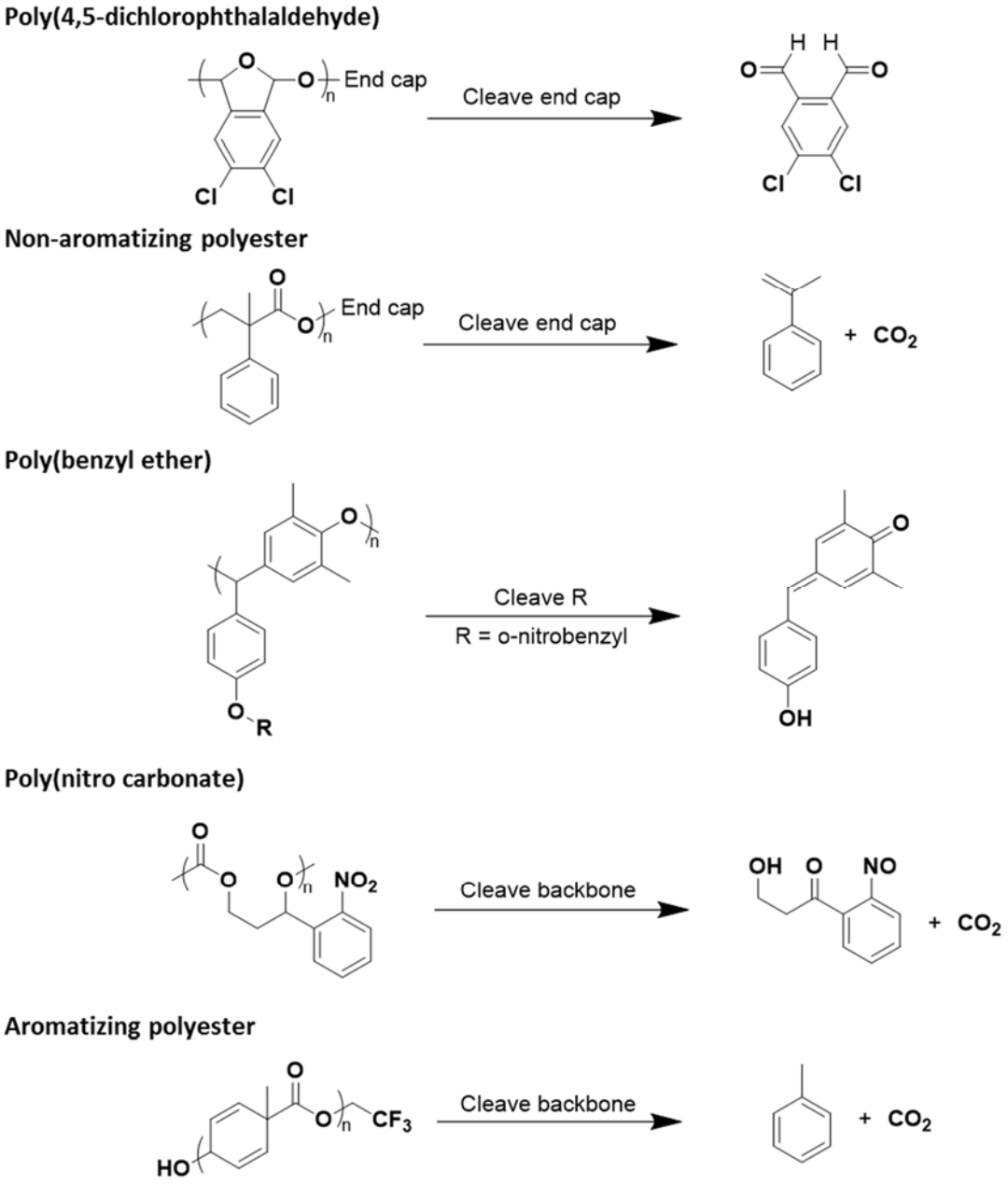

Figure 6.5: Examples of novel unzipping polymers developed for this project

Poly(4,5-dichlorophthalaldehye)[188] is a derivative of the original PPHA structure described earlier. The dichloro derivative improves on the performance of unmodified

PPHA by increasing the shelf life of the polymer in solution. The non-aromatizing polyester was synthesized via ring-opening polymerization of the cyclic lactone and was designed to release carbon dioxide and α-methylstyrene upon depolymerization. Both of these systems were designed to incorporate a photosensitive end cap since the main polymer backbones were not intrinsically photosensitive. Unfortunately, both systems required large doses of radiation for patterning, disqualifying them for high sensitivity resist applications. The poly(benzyl ether) (PBE),[232] developed by researchers at Penn State, and the poly(nitro carbonate) incorporated light-sensitive moieties at every repeat unit in the polymer chain, increasing the concentration of photoreactive species in the resist film and greatly improving the sensitivity of the resist. Despite being patternable at reasonable doses of UV light, we were unable to identify a matrix polymer that was phase-compatible with even low-molecular weight PBE homopolymers. The poly(nitro carbonate) also responded well to UV light, but crosslinked during relatively short exposure times due to undesirable side reactions.

The system that best met the requirements for our photoresist system was the aromatizing polyester. It was serendipitously discovered that this polymer was intrinsically sensitive to both UV and electron beam radiation, and functioned as a sensitive positive-tone resist when blended with several matrix resins, including Novolak and poly(norbornene hexafluroralcohol) (PNBHFA). The polymer degrades when exposed to radiation to form toluene and carbon dioxide, and undergoes this transformation very efficiently under the right conditions.

6.2 Monomer and Polymer Synthesis

The synthetic routes to the monomer and polymer are depicted in Scheme 6.2. The monomer is available in reasonable overall yield starting from benzoic acid. The final trifluoro ester monomer can be polymerized by a transesterification reaction initiated by n-BuLi. The polymerization is driven to completion by removing the trifluoroethanol byproduct via distillation. Using this method, polymers with molecular weights of 1-15 kDa can be produced in gram-scale batches, depending on the reaction conditions and the enantiomeric purity of the starting monomer. While the details of both syntheses will be documented in a future publication, an enormous thanks is owed to the chemists who worked very hard to design, synthesize, and scale up this polymerization. The efforts of Ryan Mesch, Wade Wang, Kensuke Matsuzawa, Wontae Joo, and Di Liu are greatly appreciated.

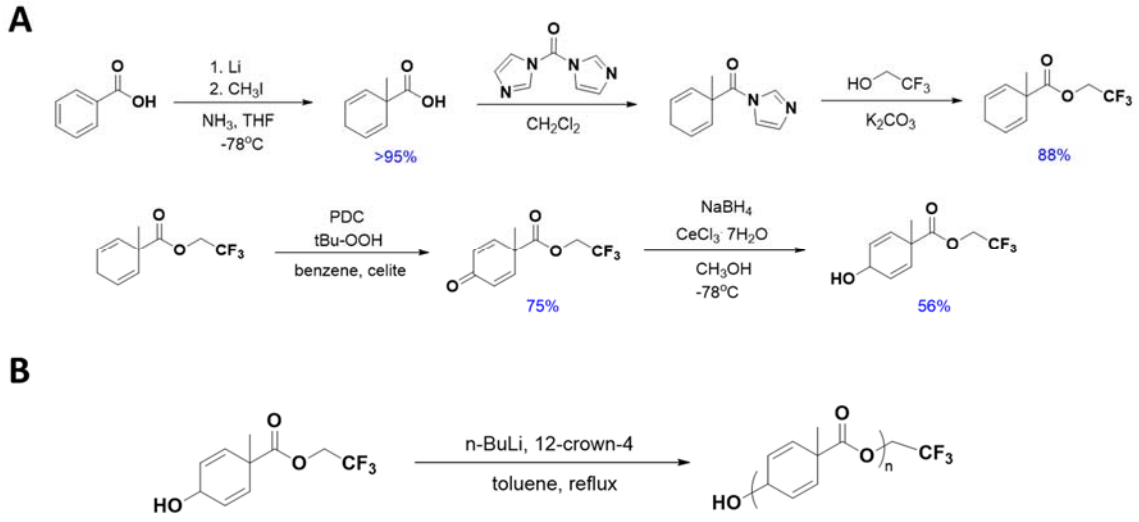

Scheme 6.2: Overall synthesis of the (A) monomer and (B) aromatizing polyester

Initially, it was believed the aromatizing polyester was not intrinsically photosensitive and would require a photolabile end cap to respond to radiation. O-nitrobenzyl functional groups could be installed at the end of the polymer by adding a small amount of monomer with the o-nitrobenzyl ester instead of the trifluoroethanol ester. However, when the control polymer without the o-nitrobenzyl group was exposed to UV light, the formation of toluene was observed by NMR, which can be seen in Figure 6.6.

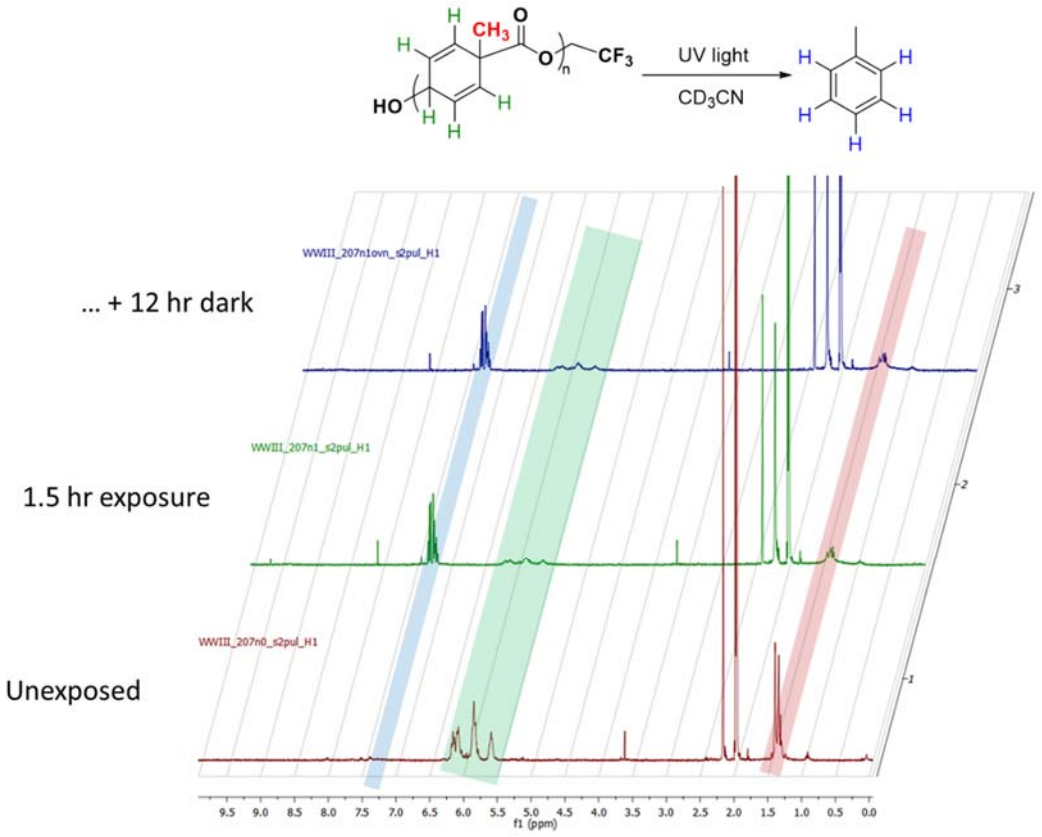

Figure 6.6: Multiple NMR spectra taken before and after exposing a solution of aromatizing polyester to UV light. The disappearance of the peaks labelled in green and red and the appearance of peaks labelled in blue indicate the polyester is demopolymerizing to form toluene. Furthermore, no photosensitive end cap is require to achieve degradation.

The peaks highlighted in red and green in Figure 6.6 correspond to characteristic protons on the polymer backbone. After exposure to broadband UV light, the intensity of these peaks diminishes, and aromatic protons corresponding to toluene begin to appear (highlighted in blue). Although no other side products were detected by NMR, not all of the polymer depolymerized, evidenced by the fact that the peaks corresponding to the polymer do not completely disappear. The NMR solution was stored for an additional 12

hours in the absence of UV light to determine if the depolymerization was simply slower than the timescale of the UV exposure. The presence of peaks corresponding to polymer in the NMR after this prolonged storage seems to support the conclusion that the depolymerization is not the rate-limiting step, but perhaps the quantum efficiency of the polymer is low when exposed to broadband UV light from a mercury lamp.

6.3 Initial Photopatterning Experiments

Despite depolymerizing in solution, the aromatizing polyester would not be useful for lithography if the same depolymerization did not occur readily in thin films. First, it was demonstrated that the aromatizing polyester could act as a dissolution inhibitor for Novolak in thin films (Figure 6.7).

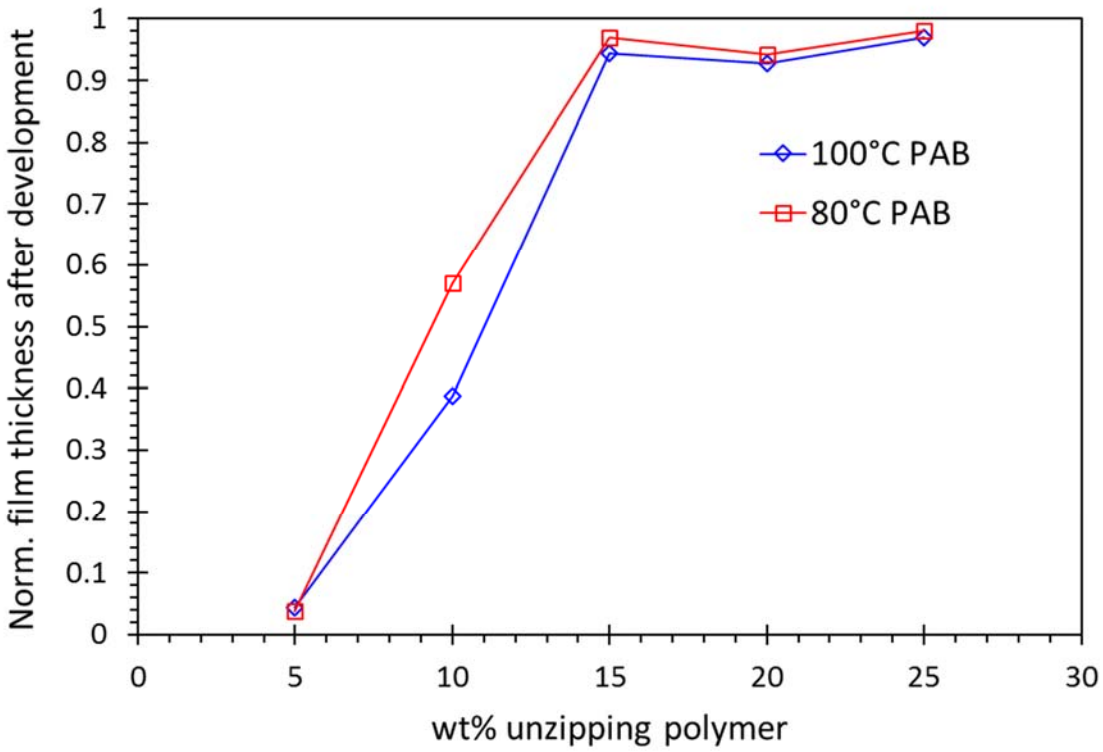

Figure 6.7: Dissolution curves for unzipping polymer/Novolak blend at two different PAB temperatures. Starting film thicknesses were between 60 and 70 nm. Films were developed in 2.38% TMAH for 1 min after the PAB.

Novolak is a common matrix resin for i-line resists. It is normally soluble in aqueous base. When blended with diazonaphtoquinone (DNQ), it becomes insoluble due to hydrogen bonding between the relatively hydrophobic DNQ and the phenol groups in the Novolak structure. Upon exposure to 365 nm light, DNQ undergoes a rearrangement to form a ketene that subsequently reacts with adventitious water to form a carboxylic acid group. The carboxylic acid is also soluble in aqueous base and actually increases the rate of dissolution of the Novolak in the exposed areas. By replacing the DNQ with the aromatizing polyester, the same type of behavior is essentially accomplished; however,

instead of one photochemical reaction causing one small molecule to undergo a chemical reaction, an entire polymer chain is depolymerized, causing a large change in molecular weight and achieving amplification. While it was encouraging to see that the unzipping polymer could inhibit the dissolution of Novolak at a relatively low concentration of 15 wt%, its initial lithographic performance as a UV resist was underwhelming (Figure 6.8). Based on the contrast curve in Figure 6.8A, the Novolak/unzip blend requires large amounts of UV light to become even moderately soluble in developer. In addition, the resist appears to photodarken with prolonged exposure. Only micron-sized features like the kind seen the optical micrograph of Figure 6.8B could be resolved in thin films, but not fully developed.

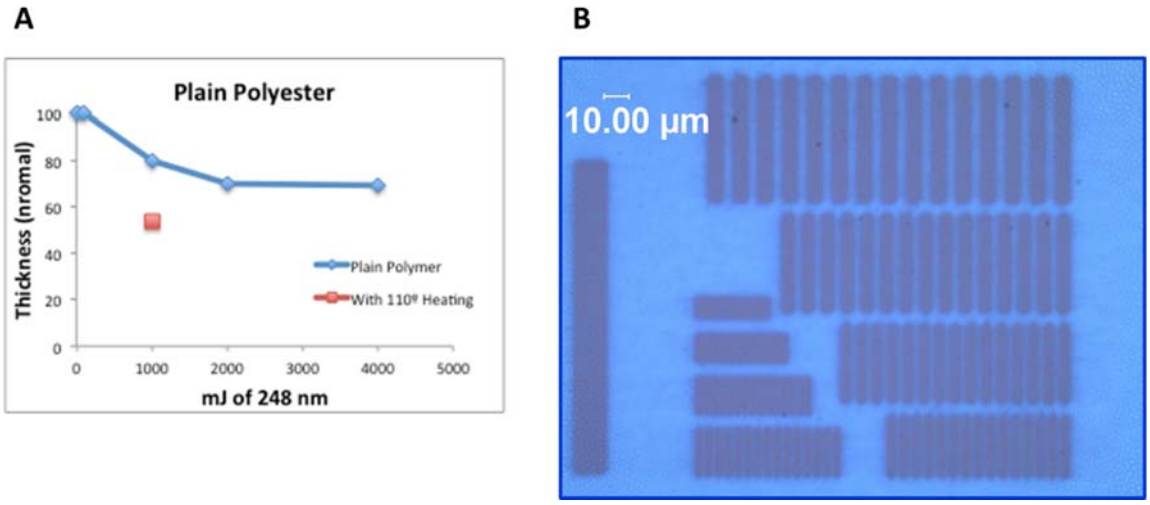

Figure 6.8: (A) Contrast curve data for the unzip/Novolak blend after exposure to 248 nm light. Films were exposed to various doses of UV light and developed in 2.38% TMAH for 1 minute after exposure. (B) an optical micrograph of micron-sized features printed in unzip/Novolak using 248 nm light.

While initially disappointing, it was hypothesized that perhaps the reason for the poor sensitivity was the relatively low energy of the exposing radiation. Since the resist was designed with the needs of EUV lithography in mind, it was auditioned as an EUV resist using the synchrotron at Lawrence-Berkeley National Labs as a source of EUV photons. The contrast curve of the resist can be seen in Figure 6.9. Despite the relatively large amount of dark loss and poor contrast, the 10 mJ sensitivity of the resist system appeared promising and warranted further testing.

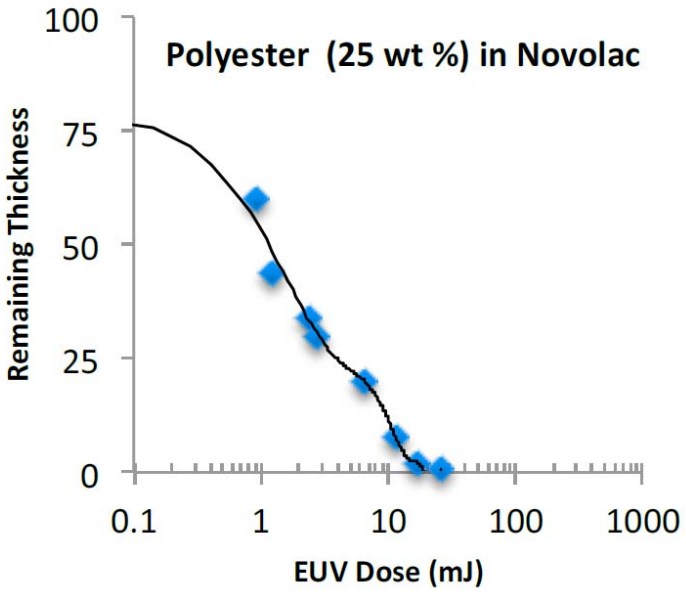

Figure 6.9: Contrast curve of 25% blend of unzip polymer in Novolak. Samples were exposed to varying doses of EUV radiation (synchrotron source) and developed in TMAH. Credit goes to Ryan Mesch for generating this data.[233]

6.4 Optimization of Resist Performance Using Electron Beam Lithography (EBL)

Because it can be difficult to access an EUV source for routine experiments, electron beam lithography was chosen as a surrogate patterning technique to further optimize the unzip/Novolak system. A high resolution electron beam lithography system was readily available for UT students to use at the Pickle Microelectronics Research Center (MRC). The proximity of the tool enabled us to quickly discover which process variables were important to control for optimum performance.

Initial e-beam exposure tests at 50 keV showed that the unzip/Novolak resist system was a remarkably sensitive positive-tone resist. The contrast of the unzip/Novolak blend (1.95) was comparable to the contrast of PMMA (2.46), a non-chemically amplified commercial e-beam resist, but the unzip/Novolak blend was approximately four times more sensitive. Contrast curves for both resist systems can be seen in Figure 6.10A. Normally, resists with greater sensitivities are more prone to line edge roughness in the final developed pattern. We were pleasantly surprised, however, that “crisp” 100 nm l/s patterns could be printed in the resist films at low doses (Figure 6.10B). With these initial results, we attempted to optimize the system to learn which process variables were important for best performance.

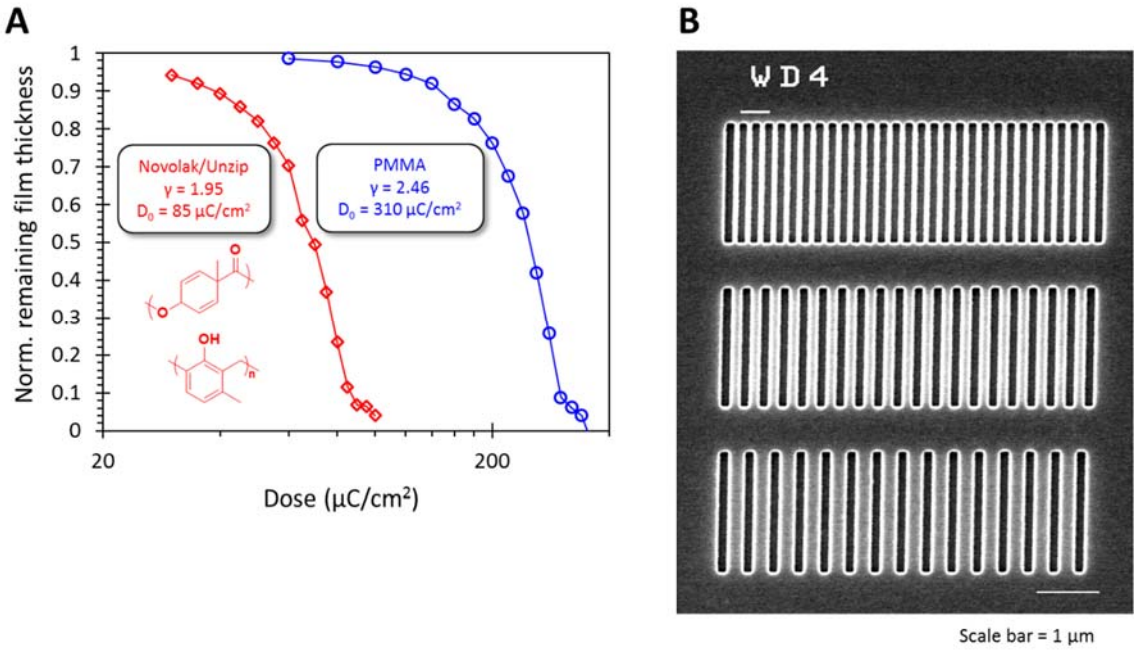

Figure 6.10: (A) E-beam contrast curves for PMMA and a 15% unzip/Novolak blend. The PMMA film was baked at 180°C for 2 mins prior to exposure and was developed in 1:3 MIBK:IPA for 1 min. The unzip/Novolak blend was baked at 95°C for 1 min prior to exposure and developed in 2.38% TMAH for 1 min. (B) 100 nm line/space patterns printed in the unzip/Novolak resist.

Initially, two quantitative response variables were considered for the optimization study: resist contrast and dose-to-clear. For comparison, several commercial resists, including PMMA, ZEP, and a 193 nm CAR were patterned using the same exposure conditions. The goal of the optimization study was to show the unzip/matrix blends could outperform commercially available resists in terms of sensitivity without sacrificing pattern quality in terms of line edge roughness. Several experimental factors were considered in the experimental design, including the weight percent of unzipping polymer in the resist blend, post-apply bake temperature, casting solvent, unzipping polymer

molecular weight, and whether Novolak or PNBHFA was used as the matrix resin. Table 6.1 summarizes the results of this experimental design. Contrast curves were generated by exposing 1 μm line/space patterns to a dose matrix that varied from 30-240 μC/cm^2. After developing the features, the topography produced by each dose region was measured by AFM and the normalized thickness loss was graphed on a semilog plot against dose. Contrast and dose-to-clear were calculated by fitting the straight line formed by the portion of the curve that intersects the x-axis. In addition, 100 nm, 1:1 line/space patterns were imaged using the same dose matrix as the larger patterns. After development, these were coated with a thin layer of metal and imaged by SEM to qualitatively determine the performance of the resist for high resolution patterns. The minimum printable feature size for the electron beam lithography tool at UT is approximately 20 nm, so a minimum test feature size of 100 nm was chosen to avoid conflating the roughness produced by the resist system with the quality of the aerial image produced by the tool operating near its resolution limits.

Table 6.1: A summary of the experiments that were performed to optimize the unzip/matrix system. Contrast and dose-to-clear (D_0) were chosen to be the response variables for this study. The results for PMMA and ZEP, commonly available e-beam resists, are provided for comparison. All films were developed for 1 minute, unless noted otherwise (PNBHFA). Contrast and D_0 data could not be collected for the third Novolak sample because features were essentially fully developed at the lowest possible exposure dose.

Matrix	wt% unzip	Casting solvent	PAB temp. (°C)	unzip Mn (kDa)	Developer conc. (wt%)	Contrast	D_0 (μC/cm²)
Novolak	15	PGMEA	80	7.0	2.38	2.72	114
Novolak	15	PGMEA	95	7.0	2.38	1.95	87
Novolak	15	PGMEA	110	7.0	2.38	N/A	N/A
Novolak	20	PGMEA	80	7.0	2.38	2.17	154
Novolak	20	PGMEA	95	7.0	2.38	1.8	113
Novolak	20	PGMEA	110	7.0	2.38	1.67	71
Novolak	25	PGMEA	95	7.0	2.38	2.24	137
Novolak	25	PGMEA	110	7.0	2.38	1.88	59
Novolak	15	2-ethoxyethyl acetate	80	7.0	2.38	1.88	111
Novolak	15	2-ethoxyethyl acetate	95	7.0	2.38	1.55	84
Novolak	15	ethyl lactate	80	7.0	2.38	2.25	115
Novolak	15	ethyl lactate	95	7.0	2.38	1.88	76
Novolak	15	PGMEA	80	2.5	2.38	2.18	122.2
Novolak	15	PGMEA	95	2.5	2.38	2	115
PNBHFA	15	2-ethoxyethyl acetate	80	7.0	1.82 (10 s)	1.6	76
PNBHFA	15	2-ethoxyethyl acetate	80	7.0	1.45 (60 s)	1.63	81
PNBHFA	15	2-ethoxyethyl acetate	95	7.0	1.82 (10 s)	1.8	52
PNBHFA	15	2-ethoxyethyl acetate	95	7.0	1.45 (60 s)	2.2	61
ZEP						4.24	90.5
PMMA						2.46	311

6.4.1 Effect of Post-apply Bake (PAB) Temperature

One of the most counter-intuitive results of this study was the effect of the post-apply bake temperature (Figure 6.11). Normally, the PAB is a useful step for removing residual solvent from the resist before exposure, whereas the PEB largely determines resist performance. In the case of this resist system, the PEB was detrimental to the

sensitivity of our resist, so resist films were developed immediately after patterning. However, for samples subjected to PABs at 80°C, 95°C, and 100°C, the dose required to clear the film decreases almost monotonically from 150 μC/cm^2 to 70 μC/cm^2 (Figure 6.11A). This is accompanied by corresponding decrease in contrast, however. As a result, more roughness is observed in 100 nm line/space patterns for the sample that was baked at 110°C (Figure 6.11B). This trade-off in speed and pattern quality can be attributed to polymer degradation at temperatures above 100°C (this is confirmed by thermogravimetric analysis data in Figure 6.12). When the unzip polymer is partially degraded, it loses its ability to inhibit the dissolution of Novolak, leading to faster dissolution in unexposed areas of the resist.

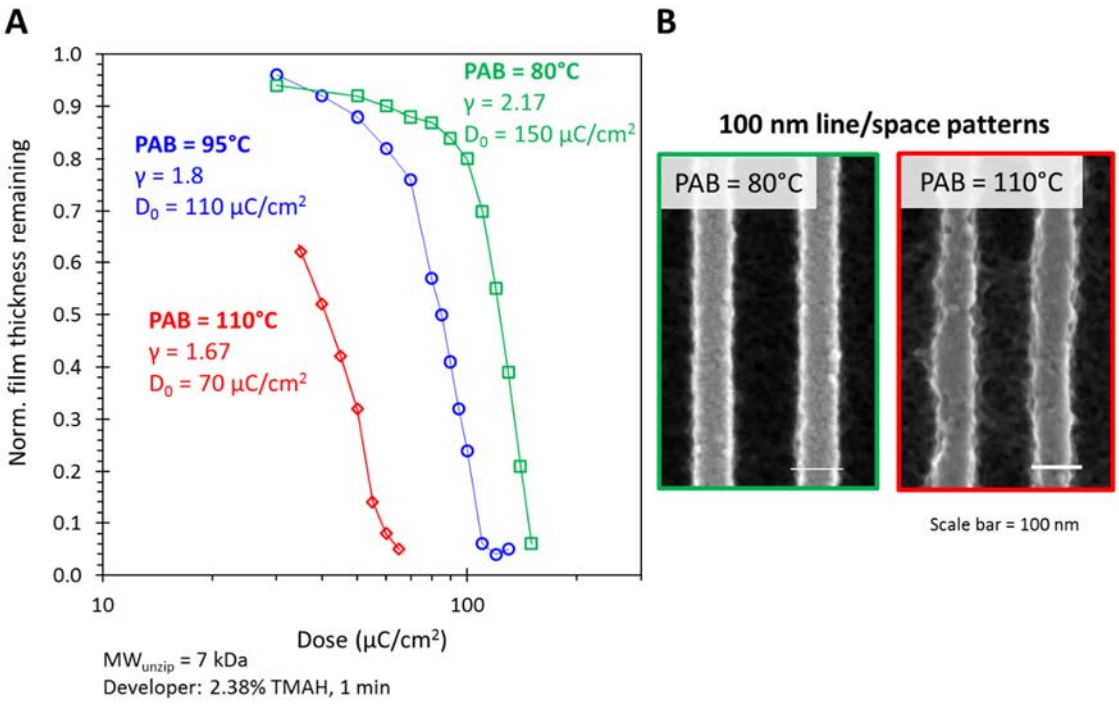

Figure 6.11: (A) Contrast curves for 20% unzip/Novolak blends baked at different PAB temperatures for 1 minute. (B) 100 nm line/space patterns imaged in samples that were post-apply baked at 80 and 110°C.

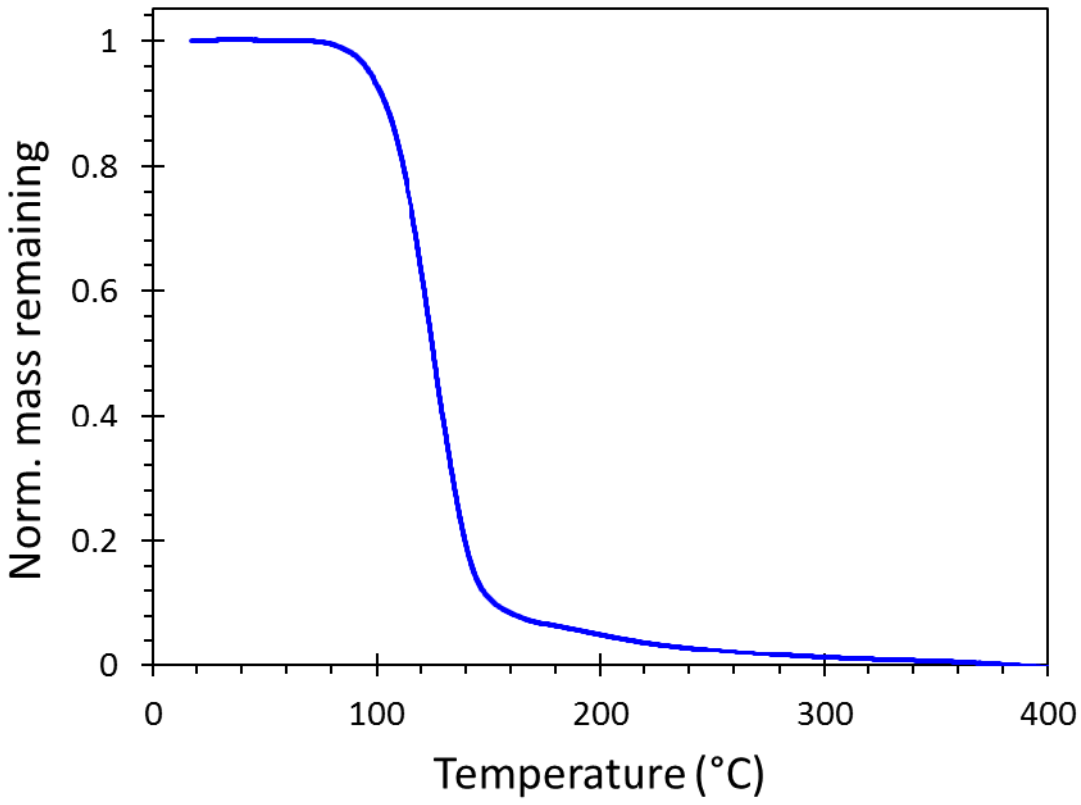

Figure 6.12: Thermogravimetric analysis (TGA) data for aromatizing polyester. Heating was performed under nitrogen atmosphere.

6.4.2 Effect of Post-exposure Bake (PEB) Temperature

As mentioned previously, baking unzip/Novolak films after exposure generally decreased the sensitivity of the resist. An interesting consequence of the PEB can be seen in Figure 6.13. In this optical micrograph, a dose matrix typically used for EBL experiments can be seen. Each region of line/space patterns was printed using a different dose. This particular sample was subjected to a PEB at 120°C for 5 minutes. After development, the brown background region has almost no resist film thickness

remaining; the areas that have been exposed are thicker than the surrounding film. After higher PEB temperatures/times, the unzip/Novolak blend acts as a negative tone resist!

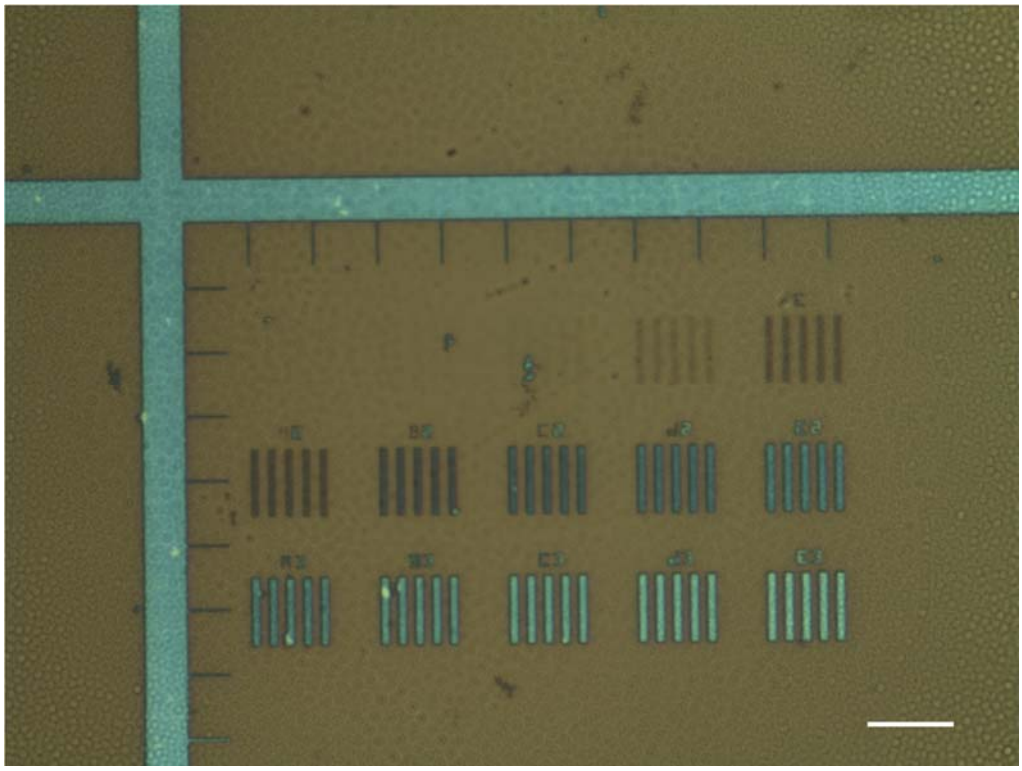

Figure 6.13: Optical micrograph of developed 1 μm features in unzip/Novolak after a PEB at 120°C for 5 min. In the dark background region, the unzip/Novolak has been completely developed away. The dose matrix increases going from left to right and top to bottom; the features that received the largest dose are crosslinked and retained full film thickness after development. Scale bar = 10 μm.

6.4.3 Effect of the Molecular Weight of Unzipping Polymer

Another unique process variable to this system is the molecular weight of the unzipping polymer. Assuming that the change in molecular weight is responsible for the resist's solubility switch, and the entire polymer chain depolymerizes regardless of molecular weight, then an increase in the sensitivity of the resist should be observed as

the molecular weight of the unzipping polymer is also increased. The contrast curves in Figure 6.14 demonstrate this effect. The formulation made with a 7 kDa unzipping polymer requires 30 μC/cm^2 less dose-to-clear than a formulation made with a 2.5 kDa unzipping polymer. Interestingly, the roughness of high resolution patterns also does not change drastically when larger polymers are used. This is a unique resist property, as typically any process change that increases the sensitivity of a chemically amplified resist leads to a decrease in pattern quality. Changing the molecular weight of the unzipping polymer could potentially provide a handle for decoupling speed and LER.

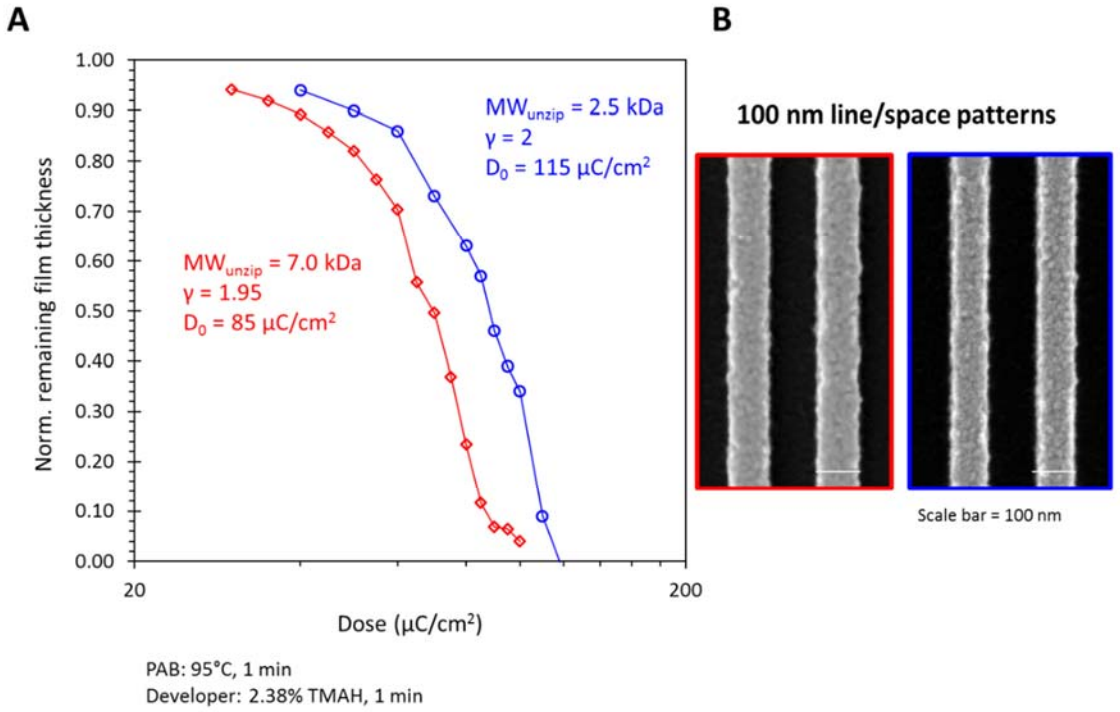

Figure 6.14: (A) Contrast curves for 15% unzip/Novolak blends containing unzip polymers with different molecular weights (B)) 100 nm line/space patterns imaged in samples that contained 7.0 kDa unzip polymer (red) and 2.5 kDa unzip polymer (blue).

6.4.4 Effect of changing the matrix resin

The factor that affected the resist performance most was changing the matrix resin. By chance, it was discovered that PNBHFA, which was originally developed for 157 nm lithography, was phase-compatible with the unzipping polymer. Compared to the Novolak blend, the 100 nm lines and spaces patterned in both resists are comparable in terms of quality (Figure 6.15), but the PNBHFA blend was patterned using almost seven times less dose. The reason behind this dramatic increase in sensitivity is unclear, but it has been shown that Novolak acts as a negative tone resist for EBL, which would result in a higher dose to clear for this positive tone system. Figure 6.16 shows contrast curves for a 15% unzip/PNBHFA blend developed using slightly different development conditions. For comparison, the contrast curve for a 15% unzip/Novolak blend is also shown. All samples were subjected to the same PAB temperature (95°C).

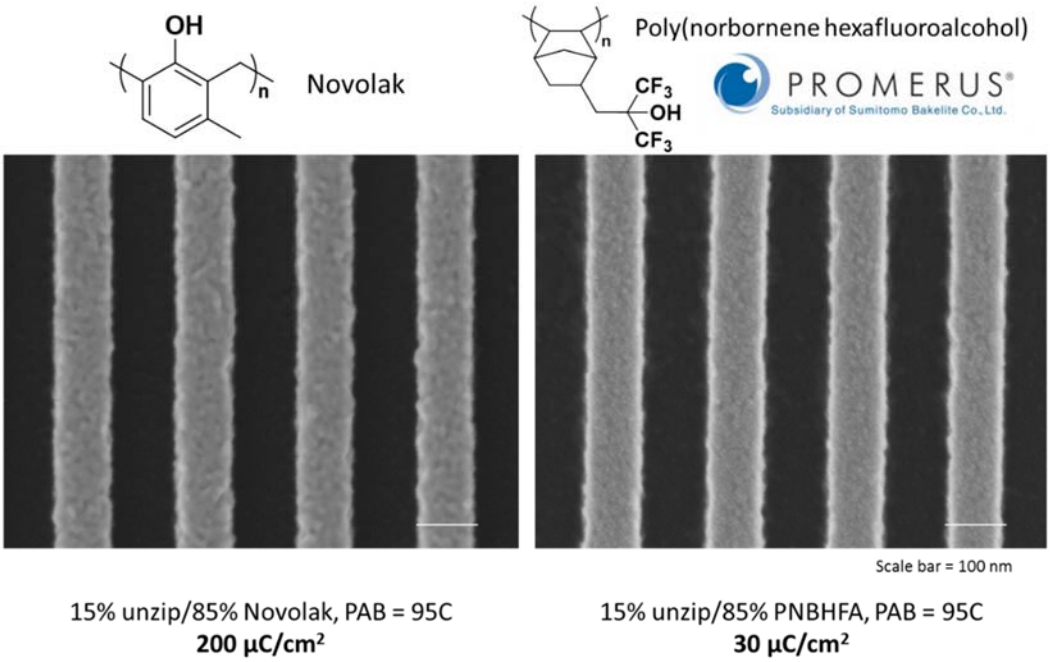

Figure 6.15: SEM micrographs of 100 nm lines and spaces patterned in 15% unzip/Novolak and unzip/PNBHFA blends. The dose-to-clear under each image represent the amount of dose required to completely develop 2:1 aspect ratio features.

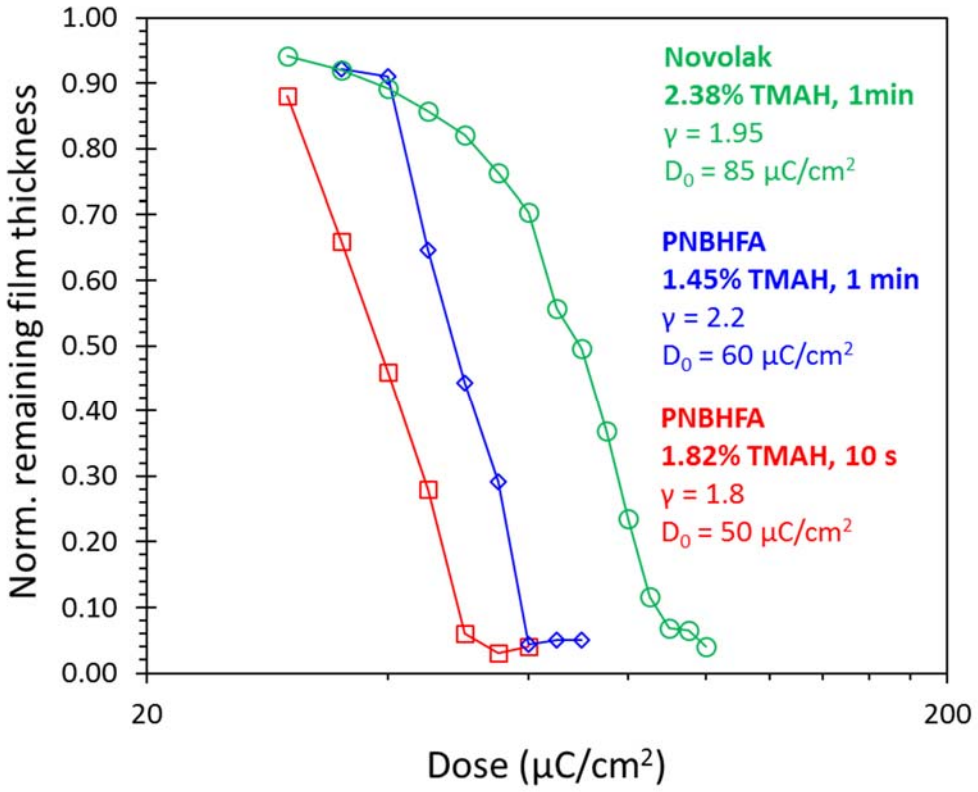

Figure 6.16: Contrast curves for two 15% unzip/PNBHFA blends developed using TMAH solutions with different concentrations. The contrast curve for a 15% unzip/Novolak blend is plotted for reference.

6.5 Etch Resistance Study

To ensure compatibility with manufacturing, it would be desirable to demonstrate that blending the aromatizing polymer with a robust matrix resin is required for achieving good etch resistance. To generate the data in Figure 6.17, blanket films of each resist formulation were exposed to a typical recipe used for oxide etching, and steady-state etch rates were normalized to the etch rate of thermal oxide. Overall, the unzipping resist blends performed satisfactorily. The selectivity of the Novolak/unzip resist was similar to

traditional i-line resist, near 3:1, and the performance of PNBHFA showed similar etch resistance to a typical acrylate-based CAR.

Some interesting transient etch behavior was also observed for the unzipping blends. In the first few seconds of etching, the unzipping formulations etch slightly faster than the steady state etch rate, and this could be attributed to an initial rapid degradation of the unzipping polymer. After this transient period, the etch rate slows down as the concentration of unzipping polymer decreased in the film.

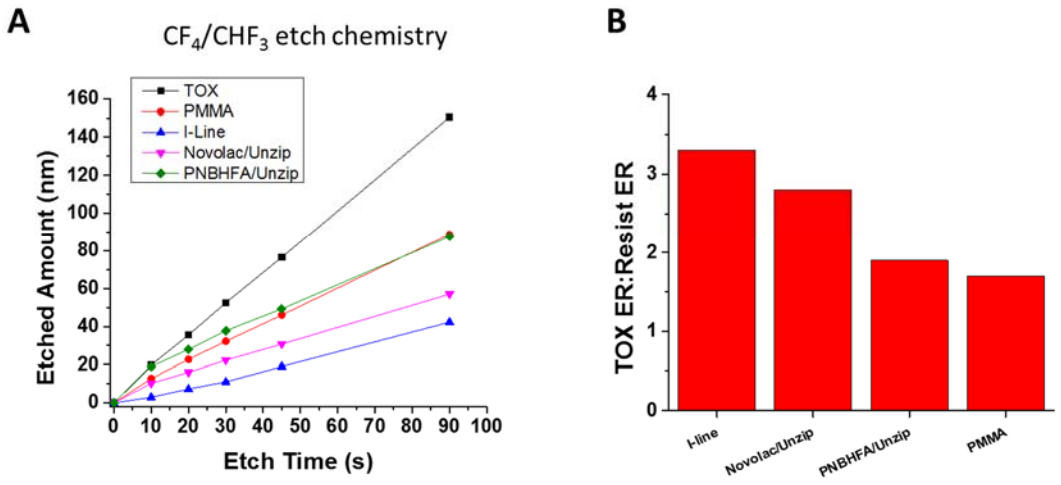

Figure 6.17: (A) Amount of polymer film etched plotted versus time for thermal oxide, PMMA, i-line resist (15% DNQ in Novolak), 15% unzip/Novolak, and 15% unzip/PNHFA blends. Films were exposed to CF_4/CHF_3 plasma chemistry, a common recipe for etching dielectric materials. Transient etch behavior can be seen in the first few seconds of etching the unzip blends. (B) Selectivity data for each of the resists studied. The selectivity is calculated by normalizing the steady-state etch rate of each resist to the steady-state etch rate of thermal oxide

6.6 LINE WIDTH ROUGHNESS (LWR) STUDY

In addition to improving the sensitivity of our resist, we were also interested in studying the line roughness produced by each of our unzipping formulations and comparing them to standard materials for EBL, including PMMA and ZEP. Ultimately, comparing the unzip/matrix blends to a commercially available CAR will be required to confirm that the unzipping polymer is an effective substitute for the catalyst-based CAR design. However, the results from initial attempts to patterning a CAR were suspect due to the unusually high required dose-to-clear (Table 6.2).

The value for the dose to clear shown in Figure 6.18 represents the dose required to generate 1:1 100 nm line/space patterns and fully clear the resist film. The image contrast is different for PMMA/ZEP versus the unzipping blends because the PMMA/ZEP films were patterned on bare silicon versus a BARC layer for the other two. Except for the slightly more rounded features produced by the Novolak matrix, it's difficult to draw any conclusions just by examining these images.

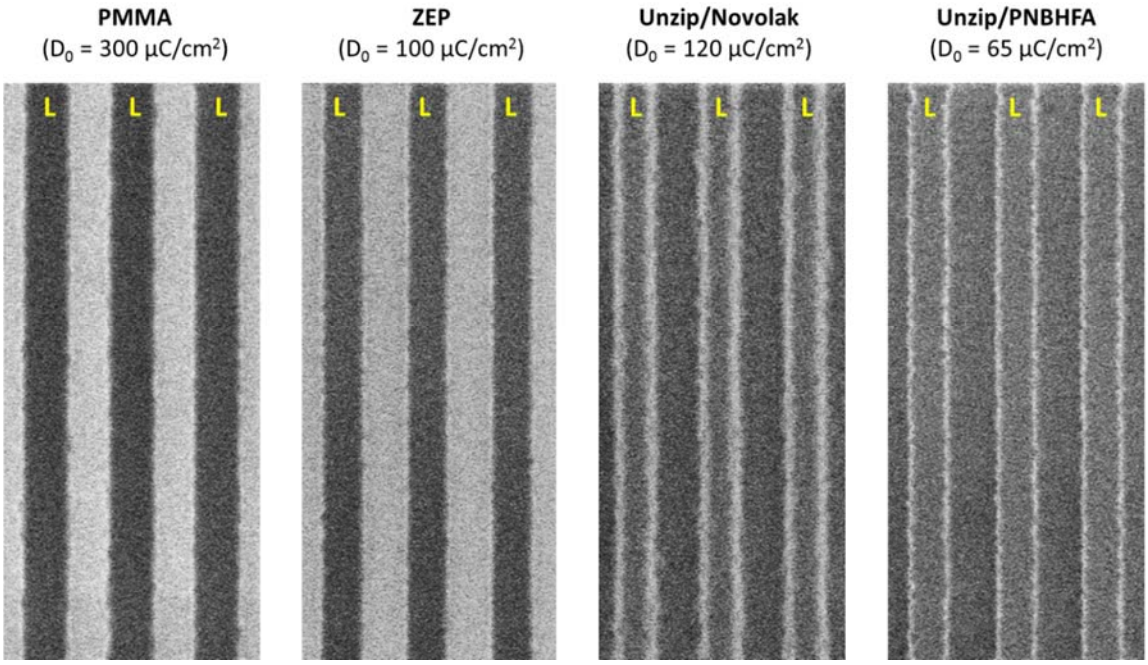

Figure 6.18: CD-SEM images of 1:1, 100 nm (half-pitch) line/space gratings patterned in PMMA, ZEP, 15% unzip/Novolak, and 15% unzip/PNBHFA blends. The D_0 value represents the dose required to completely clear the resist film and achieve symmetric lines and spaces. The image contrast is inverted for the PMMA/ZEP samples because these resists were processed on bare wafer, whereas the unzip blends were processes on a BARC film. For clarity, the "line" feature in each image is marked by a yellow "L".

So, a more quantitative analysis of line roughness was performed by imaging resist features using critical dimension-scanning electron microscopy (CD-SEM) analysis and processing the images using software from Fractilia. The data in Table 6.2 represents an average of 20-30 images, each taken from a single sample of patterned resist.

For each type of resist that was studied, a PSD plot like the one shown in Figure 6.19 was generated. The square of the roughness (line edge, line width, and pattern placement) can be estimated by integrating the area under this curve, and after subtracting

out the apparent roughness from SEM noise, an unbiased estimate of the roughness could be calculated. The results for the commercial CAR are shown in Table 6.2, but as mentioned previously, these data are suspicious due to the unusually high dose required for full development. This is probably the result of working in a cleanroom environment that is not carefully controlled, and future work will include obtaining more reliable data for this resist.

Although the sample size for this initial study was small, one important conclusion seems to present itself by carefully considering the data. If we look at the correlation length for line width roughness and compare it to the dose-to-clear for each resist, the unzipping formulations can be patterned with remarkably low dose-to-clear without causing a large increase in the correlation length. For CARs, the correlation length essentially represents the diffusion length of the acid catalyst. We think that this result is encouraging because it supports the original hypothesis that replacing the catalyst in CAR with unzipping polymers can decouple speed and image blurring, creating gain without significantly worse roughness in the developed feature.

Table 6.2: Roughness data calculated from PSD curves, which were generated by averaging data from 20-30 CD-SEM images for each sample. The ArF resist data is marked due to the unusually high dose required to clear the features. This data should be treated skeptically.

	D_0 (μC/cm^2)	Unbiased LWR (nm)	Correlation Length (nm)
PMMA	300	6.5	20.3
ZEP	100	8.6	13.9
Unzip/Novolak	120	7.8	15.5
Unzip/PNBHFA	65	8.3	16.6
ArF*	240	12.2	25.7

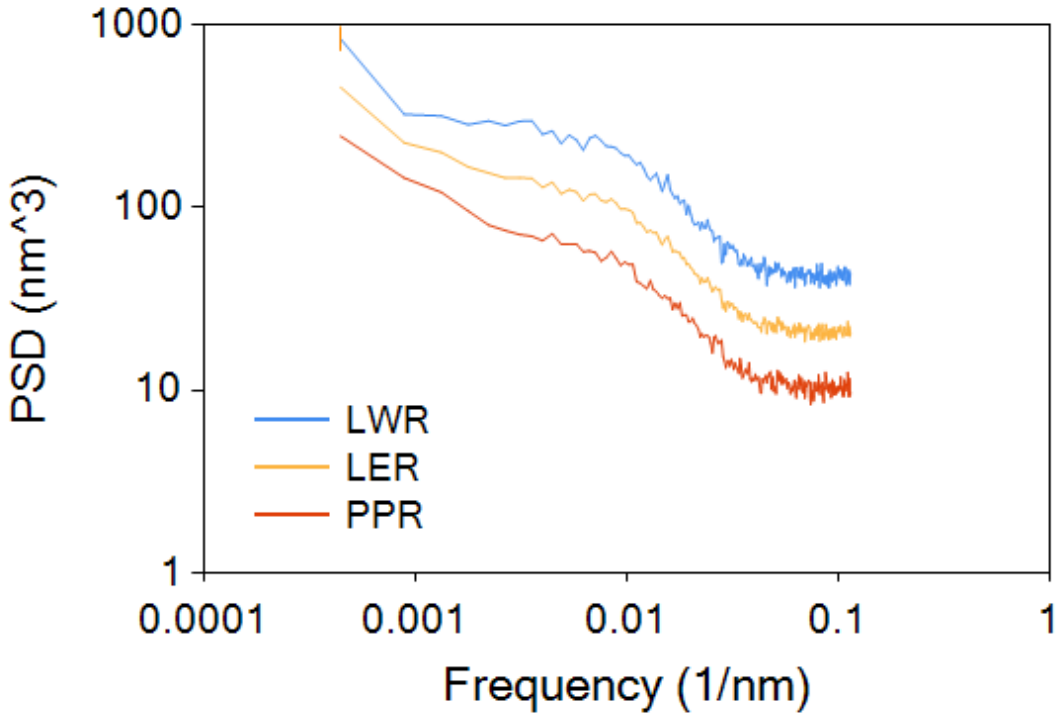

Figure 6.19: A typical plot of PSD curves for line width roughness (LWR), line edge roughness (LER), and pattern placement roughness (PPR). σ^2 can be estimated by integrating the area under the curve. The unbiased roughness can be calculated by subtracting out the roughness corresponding to high frequency noise. The correlation length (ζ) can be estimated by the formula $f = 1/2\pi\zeta$, where f represents the frequency at the "knee" of the curve.

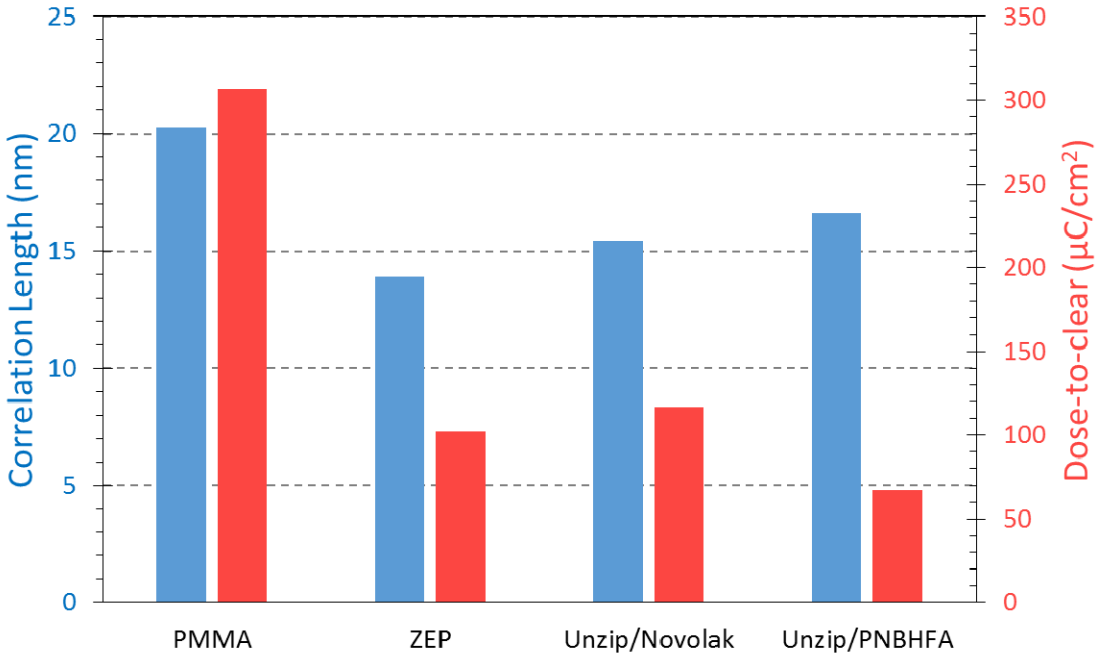

Figure 6.20: Column graph with LWR correlation length and dose-to-clear for each resist tested in the roughness study. Notably, the unzip formulations are approximately as sensitive as (or even more sensitive than) ZEP without having significantly larger correlation length values.

6.7 CONCLUSIONS

The goal of the work described here was to devise a resist system that achieves gain without utilizing photoacid catalysts. The inherent instability of so-called "unzipping" polymers was exploited to facilitate a solubility switch upon exposure to radiation that does not involve diffusion, but provides resist formulations with contrast and sensitivity comparable to that of CARs. In this design, the polymer is a dissolution inhibitor for an etch resistant matrix resin. After exposure, regions of the polymer film where the "unzipping" occurs become soluble in developer. A single exposure event can initiate depolymerization of a polymer chain back to monomer, which involves breaking many bonds and provides the gain.

A carefully designed aromatizing polyester was synthesized by condensation polymerization and then blended with several types of matrix resins. The formulations acted as a positive-tone resist for electron beam lithography. Upon electron irradiation, this catalyst-free CAR demonstrates a lower dose-to-clear than commonly used e-beam resists like PMMA and ZEP while maintaining reasonable pattern quality. In addition, the robust matrix polymer provided etch resistance during reactive ion etching. In the future, we will attempt to image high resolution patterns in unzipping resists, and audition the optimized formulations again for EUV lithography.

6.8 EXPERIMENTAL

6.8.1 Materials

All solvents for casting polymer films were purchased from commercial sources and used as received. The ArF CAR was obtained from JSR Corporation. Poly(norbornene hexafluoroalcohol) matrix resins were provided by Promerus. The synthetic details for synthesizing the aromatizing monomer and polymer will be described in a later publication.

6.8.2 Thin Film Processing

6.8.2.1 Resist Preparation:

<100> wafer coupons were used as the substrate for all EBL experiments. Polymers were dissolved in solvent (5-10 wt%) and filtered using 0.2 μm PTFE filters for spin coating. All films were cast and pre-baked immediately before exposure. For

contrast curve and initial high resolution patterning experiments, 200 nm thick films were targeted. 100 nm films were cast for the line width roughness studies.

PMMA: Commercially-available PMMA with Mn = 960 kDa was dissolved in anisole to make a 4 wt% solution. The solution was stirred overnight to ensure all of the high molecular weight polymer had sufficient time to dissolve. After casting the solution on a wafer coupon, the PMMA film was baked at 180°C for 2 minutes.

ZEP: ZEP 520 was obtained locally at UT. Pre-made ZEP solutions were diluted with anisole to achieve the proper film thicknesses. ZEP films were baked at 165°C for 1 minute following spin coating.

ArF (193 nm) CAR resist: The CAR was dispensed from the original bottle without dilution. Films were subjected to a PAB at 120°C for 1 min.

Unzip blends: All unzipping polymer blends were casted onto films of BARC instead of bare Si/SiO_2. This was to improve the adhesion between the resist blend and the substrate. BARC films were prepared by spin-coating pre-made solutions onto 4" Si wafers. After baking at 180°C for 5 mins, the wafers were rinsed to remove any uncured polymer. The final film thicknesses of the BARC layers were generally around 74 nm. For consistency, unzip/matrix blends were mixed immediately before casting. Previous experiments have shown that the aromatizing polyester has a limited shelf life in solution. All films were baked on hotplates whose temperature had been previously measured using a thermocouple.

6.8.2.2 Exposure:

A JEOL 6000 FSE electron beam lithography tool operating in 5th lens mode at 50 kV was used for all exposures. Direct writing was performed using a beam current of 75 pA and a spot size of approximately 2 nm. A typical exposure pattern can be seen in Figure 6.21. For convenience, the contrast curve features (1 μm half pitch) and 100 nm line/space features were patterned during the same exposure.

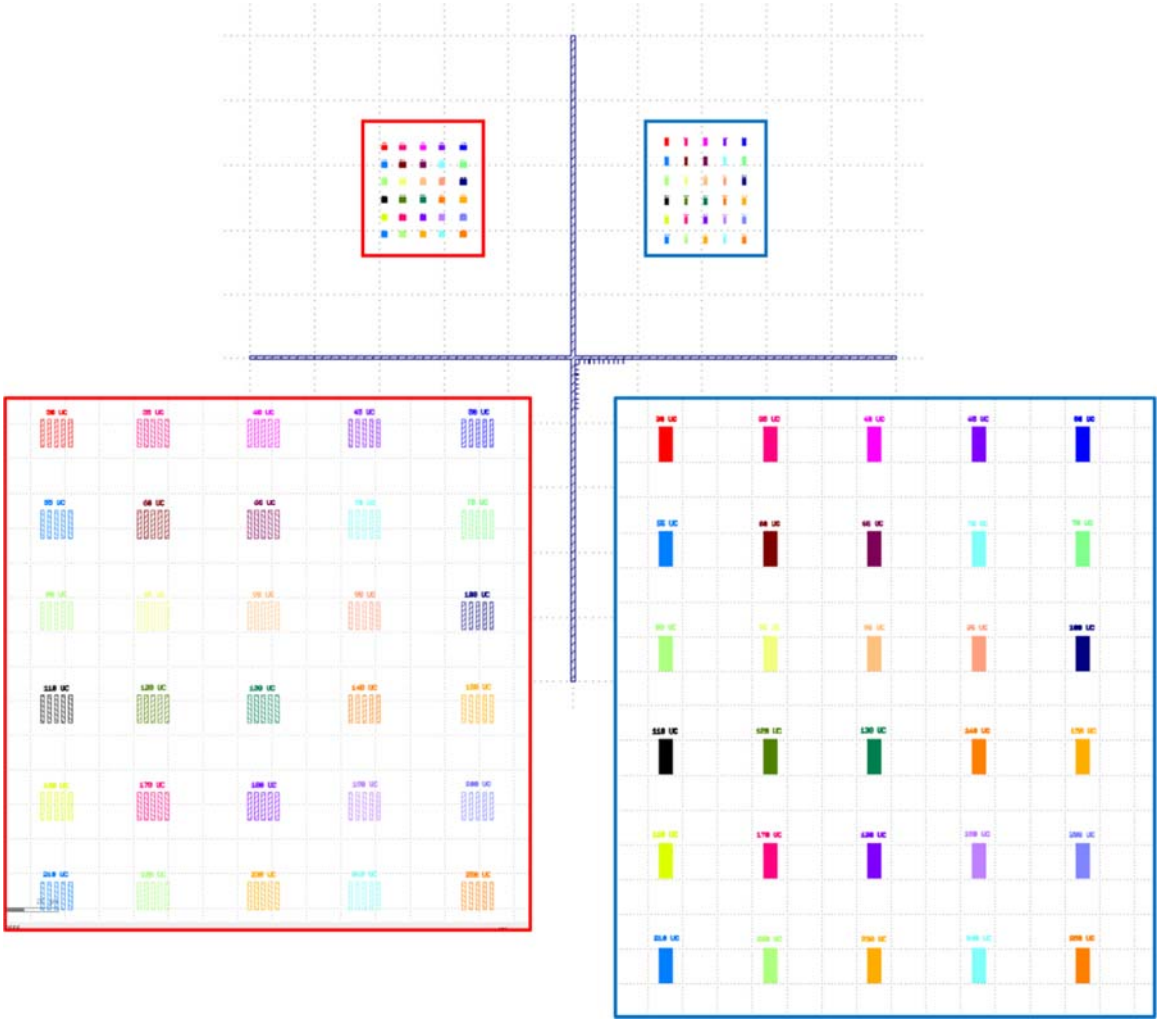

Figure 6.21: Typical pattern design for EBL experiments. The large cross makes the exposure field much easier to find after patterning. The region boxed in red corresponds to the 1 µm line/space dose matrix used to generate contrast curves. The region boxed in blue corresponds to the 100 nm line/space dose matrix used for LWR analysis.

6.8.2.3 Post-Exposure:

No resist required any post-exposure thermal processing except the ArF CAR. This sample was post-exposure baked at 115°C for 1 minute.

6.8.2.4 Development:

PMMA: Films were developed in 1:3 MIBK:IPA for 1 minute, rinsed with IPA for 5 seconds, then blown dry with air.

ZEP: Films were developed in amyl acetate for 1 minute, rinsed with IPA for 5 seconds, then blown dry with aire.

ArF CAR: Films were developed in 2.38% TMAH for 30 seconds, rinsed with water for 5 seconds, then blown dry.

Unzip/matrix blends: Unless otherwise specified, films were developed in 2.38% TMAH for 1 minute, rinsed with water for 5 seconds, then blown dry.

6.8.3 Thin Film Analysis

Ellipsometry was performed with a J.A. Woollam Co, Inc. VB 400 VASE Ellipsometer with wavelengths from 382 to 984 nm and a 65° angle of incidence. AFM scans were obtained using an Asylum MFP-3D Origin operating in tapping mode. A Brewer CEE 100CB Spincoater was used to coat all thin films. A Zeiss Supra 40 VP scanning electron microscope operating at 5 kV with the in-lens detector and a working distance of 2-5 mm was used to collect all initial SEM data. CD-SEM images were collected using a Hitachi 9380 operating at 300V. The images were taken using an asymmetric pixel sizes with an aspect ratio of approximately 2:1. Roughness data was extracted from CD-SEM images using custom software from Fractilia.

6.9 ACKNOWLEDGEMENTS

This project would not have been possible without the combined efforts of Ryan Mesch, Wade Wang, Kensuke Matsuzawa, Benjamin Cassidy, Wontae Joo, and Di Liu to design, synthesize, and scale up the production of the aromatizing polyester. Thank you for supporting the e-beam studies. I would also like to thank Steve Sirard for generating the etch characterization data. Special thanks goes to Chris Mack for processing the CD-SEM images using his custom software, and for teaching us about the importance of carefully measuring LWR.

Bibliography

(1) Hunt, J. C. R. Lewis fry richardson and his contributions to mathematics, meteorology, and models of conflict. *Annu. Rev. Fluid Mech.* **1998**, *30*, xiii–xxxvi.
(2) Howell, E. The Story of NASA's Real "Hidden Figures" https://www.scientificamerican.com/article/the-story-of-nasas-real-ldquo-hidden-figures-rdquo/.
(3) Weik, M. The ENIAC Story http://ftp.arl.mil/mike/comphist/eniac-story.html.
(4) Moye, W. ENIAC: The Army-Sponsored Revolution http://ftp.arl.army.mil/mike/comphist/96summary/.
(5) Farrington, G. ENIAC: The Birth of the Information Age. *Popular Science*. p. 74.
(6) Chodos, A. November 17 - December 23, 1947: Invention of the First Transistor http://www.aps.org/publications/apsnews/200011/history.cfm.
(7) Riordan, M. The Lost History of the Transistor http://spectrum.ieee.org/biomedical/devices/the-lost-history-of-the-transistor.
(8) Engineerguy. How the first transistor worked https://www.youtube.com/watch?v=RdYHljZi7ys.
(9) 1948: Conception of the Junction Transistor http://www.computerhistory.org/siliconengine/conception-of-the-junction-transistor/.
(10) Howlett, J. Computing at Harwell http://www.chilton-computing.org.uk/acl/literature/reports/p009.htm.
(11) Kilby, J. Miniaturized Electronic Circuits, United States Patent Office, US Patent 3,138,743. Filed 1959, Issued 1964.
(12) By Source, Fair use, https://en.wikipedia.org/w/index.php?curid=19287598.
(13) The Apollo guidance computer: Hardware https://history.nasa.gov/computers/Ch2-5.html.
(14) The original uploader was Grabert at German Wikipedia - Transferred from de.wikipedia to Commons by henristosch., Public Domain, https://commons.wikimedia.org/w/index.php?curid=3984085.
(15) Moore, G. E. Cramming More Components onto Integrated Circuits, Reprinted from Electronics, Volume 38, Number 8, April 19, 1965, pp.114 Ff. *IEEE Solid-State Circuits Newsl.* **2006**, *20*, 33–35.
(16) Mack, C. *Fundamental Principles of Optical Lithography: The Science of Microfabrication*; John Wiley & Sons: London, 2007.
(17) Thompson, L.; Willson, C. G.; Bowden, M. *Introduction to Microlithography*; 2nd ed.; American Chemical Society, 1994.
(18) Bruning, J. H. Optical Lithography--Thirty Years and Three Orders of Magnitude: The Evolution of Optical Lithography Tools. In; Tarascon-Auriol, R. G., Ed.; International Society for Optics and Photonics, 1997; p. 14.
(19) Rothschild, M. Projection Optical Lithography. *Mater. Today* **2005**, *8*, 18–24.
(20) Flamholz, A. An Analysis Of Pellicle Parameters For Step-And-Repeat Projection. In; Stover, H. L., Ed.; International Society for Optics and Photonics, 1984; pp.

138–146.
(21) Pummer, H.; Hohla, K.; Diegelmann, M.; Reilly, J. P. Discharge Pumped F_2 Laser at 1580 Å. *Opt. Commun.* **1979**, *28*, 104–106.
(22) Brodsky, C.; Byers, J.; Conley, W.; Hung, R.; Yamada, S.; Patterson, K.; Somervell, M.; Trinque, B.; Tran, H. V.; Cho, S.; *et al.* 157 nm Resist Materials: Progress Report. *J. Vac. Sci. Technol. B Microelectron. Nanom. Struct.* **2000**, *18*, 3396.
(23) Schott ML® – Calcium Fluoride http://www.yuanch.com/pdf/fhg.pdf.
(24) French, R. H.; Wheland, R. C.; Qiu, W. M.; Lemon, M. F.; Blackman, G. S.; Zhang, E.; Gordon, J.; Liberman, V.; Grenville, A.; Kunz, R.; *et al.* 157nm Pellicles: Polymer Design for Transparency and Lifetime. *Proc. SPIE* **2002**, *4691*, 576–583.
(25) Grenville, A.; Liberman, V.; Rothschild, M.; Sedlacek, J. H. C.; French, R. H.; Wheland, R. C.; Zhang, X.; Gordon, J. Behavior of Candidate Organic Pellicle Materials under 157 Nm Laser Irradiation. *Proc. SPIE* **2002**, *4691*, 1644–1653.
(26) Burnett, J.; Levine, Z.; Shirley, E. Intrinsic Birefringence in Calcium Fluoride and Barium Fluoride. *Phys. Rev. B* **2001**, *64*, 241102.
(27) LaPedus, M. Intel revises litho roadmap amid 157nm, EUV delays http://www.eetimes.com/document.asp?doc_id=1174272.
(28) Lammers, D. Big challenges confront EUV commercialization push http://www.eetimes.com/document.asp?doc_id=1216562.
(29) Clarke, P. Intel Orders 15 EUV Lithography Systems http://electronics360.globalspec.com/article/5264/intel-orders-15-euv-lithography-systems.
(30) Archie, C. Performance of the IBM Synchrotron X-Ray Source for Lithography. *IBM J. Res. Dev.* **1993**, *37*, 373–384.
(31) Zoldesi, C.; Bal, K.; Blum, B.; Bock, G.; Brouns, D.; Dhalluin, F.; Diego, J.; Espinoza, A.; Hoogh, J. De; Houweling, S.; *et al.* Progress on EUV Pellicle Development. *Extrem. Ultrav. Lithogr. V* **2014**, *9048*, 904834.
(32) Tchikoulaeva, A.; Miyai, H.; Suzuki, T.; Takehisa, K.; Kusunose, H.; Yamane, T.; Terasawa, T.; Watanabe, H.; Inoue, S.; Mori, I. EUV Actinic Blank Inspection: From Prototype to Production. *Proc. SPIE* **2013**, *8679*, 86790I.
(33) Pfeiffer, H. C. Direct Write Electron Beam Lithography: A Historical Overview. *Proc. SPIE* **2010**, *7823*, 782316.
(34) Ilic, R. CNST Nanolithography Toolbox https://www.nist.gov/services-resources/software/cnst-nanolithography-toolbox.
(35) Anner, G. *Planar Processing Primer*; Van Nostrand Reinhold: New York, 2012.
(36) Mohammad, M. A.; Muhammad, M.; Dew, S. K.; Stepanova, M. Fundamentals of Electron Beam Exposure and Development. In *Nanofabrication*; Springer Vienna: Vienna, 2012; pp. 11–41.
(37) Li, J.; Bernard, D. A.; Rey, J. C.; Boksha, V. V. Model-Based Optical Proximity Correction Including Effects of Photoresist Processes. In; Fuller, G. E., Ed.; International Society for Optics and Photonics, 1997; p. 643.

(38) Granik, Y. Fast Pixel-Based Mask Optimization for Inverse Lithography. *J. Micro/Nanolithography, MEMS, MOEMS* **2006**, *5*, 43002.
(39) Hua, F.; Sun, Y.; Gaur, A.; Meitl, M. A.; Bilhaut, L.; Rotkina, L.; Wang, J.; Geil, P.; Shim, M.; Rogers, J. A.; *et al.* Polymer Imprint Lithography with Molecular-Scale Resolution. *Nano Lett.* **2004**, *4*, 2467–2471.
(40) Sreenivasan, S. V. Nanoscale Manufacturing Enabled by Imprint Lithography. *MRS Bull.* **2008**, *33*, 854–863.
(41) Chou, S. Y.; Krauss, P. R.; Renstrom, P. J. Imprint Lithography with 25-Nanometer Resolution. *Science* **1996**, *272*, (80) 85–87.
(42) Colburn, M.; Johnson, S. C.; Stewart, M. D.; Damle, S.; Bailey, T. C.; Choi, B.; Wedlake, M.; Michaelson, T. B.; Sreenivasan, S. V.; Ekerdt, J. G.; *et al.* Step and Flash Imprint Lithography: A New Approach to High-Resolution Patterning. In *Microlithography '99*; Vladimirsky, Y., Ed.; International Society for Optics and Photonics, 1999; pp. 379–389.
(43) Bates, C. M.; Maher, M. J.; Janes, D. W.; Ellison, C. J.; Willson, C. G. Block Copolymer Lithography. *Macromolecules* **2014**, *47*, 2–12.
(44) Jackson, E. A.; Hillmyer, M. A. Nanoporous Membranes Derived from Block Copolymers: From Drug Delivery to Water Filtration. *ACS Nano* **2010**, *4*, 3548–3553.
(45) Bates, C. M.; Chang, A. B.; Schulze, M. W.; Momčilović, N.; Jones, S. C.; Grubbs, R. H. Brush Polymer Ion Gels. *J. Polym. Sci. Part B Polym. Phys.* **2015**, 292–300.
(46) Bates, F. S.; Fredrickson, G. H. Block Copolymers—Designer Soft Materials. *Phys. Today* **1999**, *52*, 32.
(47) Haryono, A.; Binder, W. H. Controlled Arrangement of Nanoparticle Arrays in Block Copolymer Domains. *Small* **2006**, *2*, 600–611.
(48) Wu, D.; Xu, F.; Sun, B.; Fu, R.; He, H.; Matyjaszewski, K. Design and Preparation of Porous Polymers. *Chem. Rev.* **2012**, *112*, 3959–4015.
(49) Gu, X.; Gunkel, I.; Russell, T. P. Pattern Transfer Using Block Copolymers. *Philos. Trans. A. Math. Phys. Eng. Sci.* **2013**, *371*, 20120306.
(50) Park, M.; Harrison, C.; Chaikin, P.; Register, R.; Adamson, D. Block Copolymer Lithography: Periodic Arrays of 10^{11} Holes in 1 Square Centimeter. *Science* **1997**, *276*, 1401–1404.
(51) Ross, C. A.; Cheng, J. Y. Patterned Magnetic Media Made by Self-Assembled Block-Copolymer Lithography. *MRS Bull.* **2011**, *33*, 838–845.
(52) Tsai, H.; Pitera, J. W.; Miyazoe, H.; Bangsaruntip, S.; Engelmann, S. U.; Liu, C.-C.; Cheng, J. Y.; Bucchignano, J. J.; Klaus, D. P.; Joseph, E. A.; *et al.* Two-Dimensional Pattern Formation Using Graphoepitaxy of PS-*b*-PMMA Block Copolymers for Advanced FinFET Device and Circuit Fabrication. *ACS Nano* **2014**, *8*, 5227–5232.
(53) Doise, J.; Bekaert, J.; Chan, B. T.; Gronheid, R.; Cao, Y.; Hong, S.; Lin, G.; Fishman, D.; Chakk, Y.; Marzook, T. Implementation of Surface Energy Modification in Graphoepitaxy Directed Self-Assembly for Hole Multiplication. *J.*

Vac. Sci. Technol. B, Nanotechnol. Microelectron. Mater. Process. Meas. Phenom. **2015**, *33*, 06F301.
(54) Sirard, S.; Azarnouche, L.; Gurer, E.; Durand, W.; Maher, M.; Mori, K.; Blachut, G.; Janes, D.; Asano, Y.; Someya, Y.; *et al.* Interactions between Plasma and Block Copolymers Used in Directed Self-Assembly Patterning. *Proc. SPIE* **2016**, *9782*, 97820K.
(55) Gu, X.; Liu, Z.; Gunkel, I.; Chourou, S. T.; Hong, S. W.; Olynick, D. L.; Russell, T. P. High Aspect Ratio Sub-15 nm Silicon Trenches From Block Copolymer Templates. *Adv. Mater.* **2012**, *24*, 5688–5694.
(56) Ji, S.; Wan, L.; Liu, C.-C.; Nealey, P. F. Directed Self-Assembly of Block Copolymers on Chemical Patterns: A Platform for Nanofabrication. *Prog. Polym. Sci.* **2016**, *54*, 76–127.
(57) Choi, J.; Carter, K. R.; Russell, T. P. Directed Self-Oriented Self-Assembly of Block Copolymers Using Topographical Surfaces. In *Directed Self-assembly of Block Co-polymers for Nano-manufacturing*; **2015**; pp. 99–127.
(58) Stoykovich, M. P.; Kang, H.; Daoulas, K. C.; Liu, G.; Liu, C.-C.; de Pablo, J. J.; Müller, M.; Nealey, P. F. Directed Self-Assembly of Block Copolymers for Nanolithography: Fabrication of Isolated Features and Essential Integrated Circuit Geometries. *ACS Nano* **2007**, *1*, 168–175.
(59) Stoykovich, M. P.; Müller, M.; Kim, S. O.; Solak, H. H.; Edwards, E. W.; de Pablo, J. J.; Nealey, P. F. Directed Assembly of Block Copolymer Blends into Nonregular Device-Oriented Structures. *Science* **2005**, *308*, 1442–1446.
(60) Xiao, S.; Yang, X.; Steiner, P.; Hsu, Y.; Lee, K.; Wago, K.; Kuo, D. Servo-Integrated Patterned Media by Hybrid Directed Self-Assembly. *ACS Nano* **2014**, *8*, 11854–11859.
(61) Doerk, G. S.; Liu, C.-C.; Cheng, J. Y.; Rettner, C. T.; Pitera, J. W.; Krupp, L. E.; Topuria, T.; Arellano, N.; Sanders, D. P. Pattern Placement Accuracy in Block Copolymer Directed Self-Assembly Based on Chemical Epitaxy. *ACS Nano* **2013**, *7*, 276–285.
(62) Ruiz, R.; Kang, H.; Detcheverry, F. A.; Dobisz, E.; Kercher, D. S.; Albrecht, T. R.; de Pablo, J. J.; Nealey, P. F. Density Multiplication and Improved Lithography by Directed Block Copolymer Assembly. *Science* **2008**, *321*, 936–939.
(63) Yang, X.; Wan, L.; Xiao, S.; Xu, Y.; Weller, D. K. Directed Block Copolymer Assembly versus Electron Beam Lithography for Bit-Patterned Media with Areal Density of 1 Terabit/in^2 and Beyond. *ACS Nano* **2009**, *3*, 1844–1858.
(64) Maher, M. J.; Rettner, C. T.; Bates, C. M.; Blachut, G.; Carlson, M. C.; Durand, W. J.; Ellison, C. J.; Sanders, D. P.; Cheng, J. Y.; Willson, C. G. Directed Self-Assembly of Silicon-Containing Block Copolymer Thin Films. *ACS Appl. Mater. Interfaces* **2015**, *7*, 3323–3328.
(65) Willson, C. G.; Dammel, R. R.; Reiser, A. Photoresist Materials: A Historical Perspective. In *Optical Microlithography X*; Fuller, G. E., Ed.; International Society for Optics and Photonics, 1997; Vol. 48, p. 28.
(66) Gernsheim, H.; Gernsheim, A. *Photogr. J.* **1952**, *Section A*, 118.

(67) W, B. A.; W, M. J. Surface Plate Coatings, **1945**.
(68) Minsk, L. M.; Van Deusen, W. P. Photomechanical Resist, **1954**.
(69) Minsk, L. M. Light Sensitive Unsaturated Esters of Polyvinyl Alcohol, **1955**.
(70) Hepher, M.; Wagner, H. M. Improvements in Diarylazido-Compounds and Photo-Mechanical Processes for Lithographic Printing. GB892811, **1962**.
(71) Willson, C. G.; Ito, H.; Fréchet, J. M. J.; Tessier, T. G.; Houlihan, F. M. Approaches to the Design of Radiation-Sensitive Polymeric Imaging Systems with Improved Sensitivity and Resolution. *J. Electrochem. Soc.* **1986**, *133*, 181.
(72) Meyerhofer, D. Photosolubility of Diazoquinone Resists. *IEEE Trans. Electron Devices* **1980**, *27*, 921–926.
(73) McAdams, C. Structure Function Correlation Studies of Dissolution Inhibitors for Novolac-Based Photoresists (Master's Thesis), 1996.
(74) Willson, C. G.; Robert, D.; Miller, D.; Mckean, D. R.; Lester, A.; Pederson, A.; Jose, S.; Regitz, M. New Diazoketone Dissolution Inhibitors for Deep U.V. Photolithography. *SPIE Vol.771 Adv. Resist Technol. Process. IV* **1987**, 2–10.
(75) Dammel, R. *Diazonaphthoquinone-Based Resists*; SPIE Publications, 1993.
(76) Lin, E. K.; Soles, C. L.; Goldfarb, D. L.; Trinque, B. C.; Burns, S. D.; Jones, R. L.; Lenhart, J. L.; Angelopoulos, M.; Willson, C. G.; Satija, S. K.; *et al.* Direct Measurement of the Reaction Front in Chemically Amplified Photoresists. *Science* **2002**, *297*, 372–375.
(77) Ito, H.; Willson, C. G. Applications of Photoinitiators to the Design of Resists for Semiconductor Manufacturing. In; **1984**; pp. 11–23.
(78) Feely, W. E.; Imhof, J. C.; Stein, C. M. The Role of the Latent Image in a New Dual Image, Aqueous Developable, Thermally Stable Photoresist. *Polym. Eng. Sci.* **1986**, *26*, 1101–1104.
(79) Smith, G.; Bonham, J. Photosolubilizable Compositions and Elements, 1973.
(80) Fréchet, J. M. J.; Eichler, E.; Ito, H.; Willson, C. G. Poly(p-Tert-Butoxycarbonyloxystyrene): A Convenient Precursor to P-Hydroxystyrene Resins. *Polymer* **1983**, *24*, 995–1000.
(81) Maltabcs, J. G.; Steven, J.; Morrow, J. R.; Barr, R. L.; Ilakey, M.; Reynolds, G.; Brunsvold, W. R.; Willson, C. G.; Clecak, N.; MacDonald, S.; *et al.* 1X Deep UV Lithography with Chemical Amplification for 1-Micron DRAM Production. *Proc. SPIE* **1990**, *1262*, 2–7.
(82) Allen, R. D. High Performance Acrylic Polymers for Chemically Amplified Photoresist Applications. *J. Vac. Sci. Technol. B Microelectron. Nanom. Struct.* **1991**, *9*, 3357.
(83) Schmid, G. M.; Smithb, M. D.; Mackb, C. A.; Singh, V. K.; Burns, S. D.; Willson, C. G. Understanding Molecular Level Effects during Post Exposure Processing. *Processing* **2001**, *4345*, 1037–1047.
(84) Postnikov, S. V.; Stewart, M. D.; Tran, H. V.; Nierode, M. A.; Medeiros, D. R.; Cao, T.; Byers, J.; Webber, S. E.; Wilson, C. G. Study of Resolution Limits due to Intrinsic Bias in Chemically Amplified Photoresists. *J. Vac. Sci. Technol. B Microelectron. Nanom. Struct.* **1999**, *17*, 3335.

(85) Mojarad, N.; Gobrecht, J.; Ekinci, Y.; Wang, L.; Mojarad, N. M. Beyond EUV Lithography: A Comparative Study of Efficient Photoresists' Performance. *Sci. Rep.* **2015**, *5*, 9235.
(86) Wallow, T.; Higgins, C.; Brainard, R. L.; Petrillo, K.; Montgomery, W.; Koay, C.-S.; Denbeaux, G.; Wood, O.; Wei, Y. Evaluation of EUV Resist Materials for Use at the 32 nm Half-Pitch Node. In *Proceedings of SPIE*; Schellenberg, F. M., Ed.; International Society for Optics and Photonics, 2008; Vol. 6921, p. 69211F--69211F--11.
(87) Park, S.; Lee, D. H.; Xu, J.; Kim, B.; Hong, S. W.; Jeong, U.; Xu, T.; Russell, T. P. Macroscopic 10-Terabit-per-Square-Inch Arrays from Block Copolymers with Lateral Order. *Science* **2009**, *323*, 1030–1033.
(88) Kennemur, J. G.; Yao, L.; Bates, F. S.; Hillmyer, M. A. Sub-5 nm Domains in Ordered Poly(cyclohexylethylene)-block-poly(methyl methacrylate) Block Polymers for Lithography. *Macromolecules* **2014**, *47*, 1411–1418.
(89) Cushen, J. D.; Otsuka, I.; Bates, C. M.; Halila, S.; Fort, S.; Rochas, C.; Easley, J. A.; Rausch, E. L.; Thio, A.; Borsali, R.; *et al.* Oligosaccharide/silicon-Containing Block Copolymers with 5 nm Features for Lithographic Applications. *ACS Nano* **2012**, *6*, 3424–3433.
(90) Ruiz, R.; Dobisz, E.; Albrecht, T. R. Rectangular Patterns Using Block Copolymer Directed Assembly for High Bit Aspect Ratio Patterned Media. *ACS Nano* **2011**, *5*, 79–84.
(91) Thurn-Albrecht, T.; Schotter, J.; Kästle, G. A.; Emley, N.; Shibauchi, T.; Krusin-Elbaum, L.; Guarini, K.; Black, C. T.; Tuominen, M. T.; Russell, T. P. Ultrahigh-Density Nanowire Arrays Grown in Self-Assembled Diblock Copolymer Templates. *Science* **2000**, *290*, 2126–2129.
(92) Bates, F. S.; Fredrickson, G. H. Block Copolymer Thermodynamics: Theory and Experiment. *Annu. Rev. Phys. Chem.* **1990**, *41*, 525–557.
(93) Cochran, E. W.; Garcia-Cervera, C. J.; Fredrickson, G. H. Stability of the Gyroid Phase in Diblock Copolymers at Strong Segregation. *Macromolecules* **2006**, *39*, 2449–2451.
(94) Yi, H.; Bao, X.-Y.; Zhang, J.; Bencher, C.; Chang, L.-W.; Chen, X.; Tiberio, R.; Conway, J.; Dai, H.; Chen, Y.; *et al.* Flexible Control of Block Copolymer Directed Self-Assembly Using Small, Topographical Templates: Potential Lithography Solution for Integrated Circuit Contact Hole Patterning. *Adv. Mater.* **2012**, *24*, 3107–3114.
(95) Yi, H.; Bao, X.-Y.; Zhang, J.; Tiberio, R.; Conway, J.; Chang, L.-W.; Mitra, S.; Wong, H.-S. P. Contact-Hole Patterning for Random Logic Circuits Using Block Copolymer Directed Self-Assembly. *Proc. SPIE* **2012**, *8323*, 83230W–83230W–6.
(96) Turner, M. S. Equilibrium Properties of a Diblock Copolymer Lamellar Phase Confined between Flat Plates. *Phys. Rev. Lett.* **1992**, *69*, 1788–1791.
(97) Huang, E.; Pruzinsky, S.; Russell, T. P.; Mays, J.; Hawker, C. J. Neutrality Conditions for Block Copolymer Systems on Random Copolymer Brush Surfaces. *Macromolecules* **1999**, *32*, 5299–5303.

(98) Lambooy, P.; Russell, T. P.; Kellogg, G. J.; Mayes, A. M.; Gallagher, P. D.; Satija, S. K. Observed Frustration in Confined Block Copolymers. *Phys. Rev. Lett.* **1994**, *72*, 2899–2902.
(99) Bates, C. M.; Seshimo, T.; Maher, M. J.; Durand, W. J.; Cushen, J. D.; Dean, L. M.; Blachut, G.; Ellison, C. J.; Willson, C. G. Polarity-Switching Top Coats Enable Orientation of Sub-10-nm Block Copolymer Domains. *Science* **2012**, *338*, 775–779.
(100) Sinturel, C.; Vayer, M.; Morris, M.; Hillmyer, M. A. Solvent Vapor Annealing of Block Polymer Thin Films. *Macromolecules* **2013**, *46*, 5399–5415.
(101) Bang, J.; Bae, J.; Löwenhielm, P.; Spiessberger, C.; Given-Beck, S. A.; Russell, T. P.; Hawker, C. J. Facile Routes to Patterned Surface Neutralization Layers for Block Copolymer Lithography. *Adv. Mater.* **2007**, *19*, 4552–4557.
(102) Bates, C. M.; Strahan, J. R.; Santos, L. J.; Mueller, B. K.; Bamgbade, B. O.; Lee, J. A.; Katzenstein, J. M.; Ellison, C. J.; Willson, C. G. Polymeric Cross-Linked Surface Treatments for Controlling Block Copolymer Orientation in Thin Films. *Langmuir* **2011**, *27*, 2000–2006.
(103) Jin, X.; Pang, Y.; Ji, S. From Self-Assembled Monolayers to Chemically Patterned Brushes: Controlling the Orientation of Block Copolymer Domains in Films by Substrate Modification. *Chinese J. Polym. Sci.* **2016**, *34*, 659–678.
(104) Han, E.; Stuen, K. O.; La, Y.-H.; Nealey, P. F.; Gopalan, P. Effect of Composition of Substrate-Modifying Random Copolymers on the Orientation of Symmetric and Asymmetric Diblock Copolymer Domains. *Macromolecules* **2008**, *41*, 9090–9097.
(105) Peters, R. D.; Yang, X. M.; Kim, T. K.; Sohn, B. H.; Nealey, P. F. Using Self-Assembled Monolayers Exposed to X-Rays To Control the Wetting Behavior of Thin Films of Diblock Copolymers. *Langmuir* **2000**, *16*, 4625–4631.
(106) Wan, L.; Ruiz, R.; Gao, H.; Patel, K. C.; Albrecht, T. R.; Yin, J.; Kim, J.; Cao, Y.; Lin, G. The Limits of Lamellae-Forming PS-B-PMMA Block Copolymers for Lithography. *ACS Nano* **2015**, *9*, 7506–7514.
(107) Sinturel, C.; Bates, F. S.; Hillmyer, M. A. High □–Low N Block Polymers: How Far Can We Go? *ACS Macro Lett.* **2015**, *4*, 1044–1050.
(108) Durand, W. J.; Blachut, G.; Maher, M. J.; Sirard, S.; Tein, S.; Carlson, M. C.; Asano, Y.; Zhou, S. X.; Lane, A. P.; Bates, C. M.; *et al.* Design of High-□ Block Copolymers for Lithography. *J. Polym. Sci. Part A Polym. Chem.* **2015**, *53*, 344–352.
(109) Maher, M. J.; Mori, K.; Sirard, S. M.; Dinhobl, A. M.; Bates, C. M.; Gurer, E.; Blachut, G.; Lane, A. P.; Durand, W. J.; Carlson, M. C.; *et al.* Pattern Transfer of Sub-10 Nm Features via Tin-Containing Block Copolymers. *ACS Macro Lett.* **2016**, 391–395.
(110) 2015 ITRS Roadmap https://www.semiconductors.org/main/2015_international_technology_roadmap_for_semiconductors_itrs/.
(111) Chen, Y.; Cheng, Q.; Kang, W. Technological Merits, Process Complexity, and Cost Analysis of Self-Aligned Multiple Patterning. *Proc. SPIE* **2012**, *8326*,

832620.
(112) 2016 ASTC Technology Roadmap http://idema.org/?page_id=5868.
(113) Albrecht, T. R.; Arora, H.; Ayanoor-Vitikkate, V.; Beaujour, J.-M.; Bedau, D.; Berman, D.; Bogdanov, A. L.; Chapuis, Y.-A.; Cushen, J.; Dobisz, E. E.; *et al.* Bit-Patterned Magnetic Recording: Theory, Media Fabrication, and Recording Performance. *IEEE Trans. Magn.* **2015**, *51*, 1–42.
(114) Zhang, J.; Clark, M. B.; Wu, C.; Li, M.; Trefonas, P.; Hustad, P. D. Orientation Control in Thin Films of a High-□ Block Copolymer with a Surface Active Embedded Neutral Layer. *Nano Lett.* **2016**, *16*, 728–735.
(115) Maher, M. J.; Bates, C. M.; Blachut, G.; Sirard, S.; Self, J. L.; Carlson, M. C.; Dean, L. M.; Cushen, J. D.; Durand, W. J.; Hayes, C. O.; *et al.* Interfacial Design for Block Copolymer Thin Films. *Chem. Mater.* **2014**, *26*, 1471–1479.
(116) Azarnouche, L.; Sirard, S. M.; Durand, W. J.; Blachut, G.; Gurer, E.; Hymes, D. J.; Ellison, C. J.; Willson, C. G.; Graves, D. B. Plasma and Photon Interactions with Organosilicon Polymers for Directed Self-Assembly Patterning Applications. *J. Vac. Sci. Technol. B, Nanotechnol. Microelectron. Mater. Process. Meas. Phenom.* **2016**, *34*, 61602.
(117) Griffiths, R. A.; Williams, A.; Oakland, C.; Roberts, J.; Vijayaraghavan, A.; Thomson, T. Directed Self-Assembly of Block Copolymers for Use in Bit Patterned Media Fabrication. *J. Phys. D. Appl. Phys.* **2013**, *46*, 503001.
(118) Ham, S.; Shin, C.; Kim, E.; Ryu, D. Y.; Jeong, U.; Russell, T. P.; Hawker, C. J. Microdomain Orientation of PS- B -PMMA by Controlled Interfacial Interactions. *Macromolecules* **2008**, *41*, 6431–6437.
(119) Vora, A.; Wojtecki, R. J.; Schmidt, K.; Chunder, A.; Cheng, J. Y.; Nelson, A.; Sanders, D. P. Development of Polycarbonate-Containing Block Copolymers for Thin Film Self-Assembly Applications. *Polym. Chem.* **2016**, *7*, 940–950.
(120) Xiong, S.; Wan, L.; Ishida, Y.; Chapuis, Y.-A.; Craig, G. S. W.; Ruiz, R.; Nealey, P. F. Directed Self-Assembly of Triblock Copolymer on Chemical Patterns for Sub-10-Nm Nanofabrication via Solvent Annealing. *ACS Nano* **2016**, *10*, 7855–7865.
(121) Chang, J.-B.; Son, J. G.; Hannon, A. F.; Alexander-Katz, A.; Ross, C. A.; Berggren, K. K. Aligned Sub-10-Nm Block Copolymer Patterns Templated by Post Arrays. *ACS Nano* **2012**, *6*, 2071–2077.
(122) Black, C. T.; Ruiz, R.; Breyta, G.; Cheng, J. Y.; Colburn, M. E.; Guarini, K. W.; Kim, H.-C.; Zhang, Y. Polymer Self Assembly in Semiconductor Microelectronics. *IBM J. Res. Dev.* **2007**, *51*, 605–633.
(123) Blachut, G.; Sirard, S. M.; Maher, M. J.; Asano, Y.; Someya, Y.; Lane, A. P.; Durand, W. J.; Bates, C. M.; Dinhobl, A. M.; Gronheid, R.; *et al.* A Hybrid Chemo-/Grapho-Epitaxial Alignment Strategy for Defect Reduction in Sub-10 nm Directed Self-Assembly of Silicon-Containing Block Copolymers. *Chem. Mater.* **2016**, *28*, 8951–8961.
(124) Ji, S.; Liu, C.-C.; Liu, G.; Nealey, P. F. Molecular Transfer Printing Using Block Copolymers. *ACS Nano* **2010**, *4*, 599–609.

(125) Inoue, T.; Janes, D. W.; Ren, J.; Suh, H. S.; Chen, X.; Ellison, C. J.; Nealey, P. F. Molecular Transfer Printing of Block Copolymer Patterns over Large Areas with Conformal Layers. *Adv. Mater. Interfaces* **2015**, *2*, 1500133.
(126) Janes, D. W.; Kim, C. Bin; Maher, M. J.; Ellison, C. J. Orthogonally Spin-Coated Bilayer Films for Photochemical Immobilization and Patterning of Sub-10-Nanometer Polymer Monolayers. *Langmuir* **2016**, *32*, 6940–6947.
(127) Park, S.-M.; Craig, G. S. W.; Liu, C.-C.; La, Y.-H.; Ferrier, N. J.; Nealey, P. F. Characterization of Cylinder-Forming Block Copolymers Directed to Assemble on Spotted Chemical Patterns. *Macromolecules* **2008**, *41*, 9118–9123.
(128) Kim, S. O.; Solak, H. H.; Stoykovich, M. P.; Ferrier, N. J.; De Pablo, J. J.; Nealey, P. F. Epitaxial Self-Assembly of Block Copolymers on Lithographically Defined Nanopatterned Substrates. *Nature* **2003**, *424*, 411–414.
(129) Kim, J.; Wan, J.; Miyazaki, S.; Yin, J.; Cao, Y.; Her, Y. J.; Wu, H.; Shan, J.; Kurosawa, K.; Lin, G. The SMART Process for Directed Block Co-Polymer Self-Assembly. *J. Photopolym. Sci. Technol.* **2013**, *26*, 573–579.
(130) Pandav, G.; Durand, W. J.; Ellison, C. J.; Willson, C. G.; Ganesan, V.; Herr, D. J. C.; Stoykovich, M. P.; Nealey, P. F.; Darling, S. B.; Bates, C. M.; *et al.* Directed Self Assembly of Block Copolymers Using Chemical Patterns with Sidewall Guiding Lines, Backfilled with Random Copolymer Brushes. *Soft Matter* **2015**, *11*, 9107–9114.
(131) Cushen, J.; Wan, L.; Blachut, G.; Maher, M. J.; Albrecht, T. R.; Ellison, C. J.; Willson, C. G.; Ruiz, R. Double-Patterned Sidewall Directed Self-Assembly and Pattern Transfer of Sub-10 Nm PTMSS-B-PMOST. *ACS Appl. Mater. Interfaces* **2015**, *7*, 13476–13483.
(132) Liu, C.-C.; Ramírez-Hernández, A.; Han, E.; Craig, G. S. W.; Tada, Y.; Yoshida, H.; Kang, H.; Ji, S.; Gopalan, P.; de Pablo, J. J.; *et al.* Chemical Patterns for Directed Self-Assembly of Lamellae-Forming Block Copolymers with Density Multiplication of Features. *Macromolecules* **2013**, *46*, 1415–1424.
(133) Sun, Z.; Chen, Z.; Zhang, W.; Choi, J.; Huang, C.; Jeong, G.; Coughlin, E. B.; Hsu, Y.; Yang, X.; Lee, K. Y.; *et al.* Directed Self-Assembly of Poly(2-Vinylpyridine)-B-Polystyrene-B-poly(2-Vinylpyridine) Triblock Copolymer with Sub-15 Nm Spacing Line Patterns Using a Nanoimprinted Photoresist Template. *Adv. Mater.* **2015**, *27*, 4364–4370.
(134) Park, S.-M.; Stoykovich, M. P.; Ruiz, R.; Zhang, Y.; Black, C. T.; Nealey, P. F. Directed Assembly of Lamellae-Forming Block Copolymers by Using Chemically and Topographically Patterned Substrates. *Adv. Mater.* **2007**, *19*, 607–611.
(135) Han, E.; Kang, H.; Liu, C.-C.; Nealey, P. F.; Gopalan, P. Graphoepitaxial Assembly of Symmetric Block Copolymers on Weakly Preferential Substrates. *Adv. Mater.* **2010**, *22*, 4325–4329.
(136) Guo, R.; Kim, E.; Gong, J.; Choi, S.; Ham, S.; Ryu, D. Y.; Mansky, P.; Harrison, C. K.; Chaikin, P. M.; Register, R. A.; *et al.* Perpendicular Orientation of Microdomains in PS-B-PMMA Thin Films on the PS Brushed Substrates. *Soft Matter* **2011**, *7*, 6920.

(137) Hawker, C. J.; Hedrick, J. L. Accurate Control of Chain Ends by a Novel "Living" Free-Radical Polymerization Process. *Macromolecules* **1995**, *28*, 2993–2995.
(138) Liu, C.-C.; Han, E.; Onses, M. S.; Thode, C. J.; Ji, S.; Gopalan, P.; Nealey, P. F. Fabrication of Lithographically Defined Chemically Patterned Polymer Brushes and Mats. *Macromolecules* **2011**, *44*, 1876–1885.
(139) Milner, S. T. Polymer Brushes. *Science (80-.).* **1991**, *251*, 905 LP-914.
(140) Zhao, B.; Brittain, W. . Polymer Brushes: Surface-Immobilized Macromolecules. *Prog. Polym. Sci.* **2000**, *25*, 677–710.
(141) van der Waarden, M. Stabilization of Carbon-Black Dispersions in Hydrocarbons. *J. Colloid Sci.* **1950**, *5*, 317–325.
(142) Kruszewski, K. M.; Gawalt, E. S. Perfluorocarbon Thin Films and Polymer Brushes on Stainless Steel 316 L for the Control of Interfacial Properties. *Langmuir* **2011**, *27*, 8120–8125.
(143) Halperin, A.; Tirrell, M.; Lodge, T. P. Tethered Chains in Polymer Microstructures. In *Macromolecules: Synthesis, Order and Advanced Properties*; Springer-Verlag: Berlin/Heidelberg, 1992; pp. 31–71.
(144) Minko, S. Grafting on Solid Surfaces: "Grafting To" and "Grafting From" Methods. In *Polymer Surfaces and Interfaces*; Springer Berlin Heidelberg: Berlin, Heidelberg, 2008; pp. 215–234.
(145) Bojko, A.; Andreatta, G.; Montagne, F.; Renaud, P.; Pugin, R. Fabrication of Thermo-Responsive Nano-Valve by Grafting-to in Melt of poly(N-Isopropylacrylamide) onto Nanoporous Silicon Nitride Membranes. *J. Memb. Sci.* **2014**, *468*, 118–125.
(146) Jones, R. A. L.; Lehnert, R. J.; Schonherr, H.; Vancso, J. Factors Affecting the Preparation of Permanently End-Grafted Polystyrene Layers. *Polymer (Guildf).* **1999**, *40*, 525–530.
(147) Harrison, C.; Chaikin, P. M.; Huse, D. A.; Register, R. A.; Adamson, D. H.; Daniel, A.; Huang, E.; Mansky, P.; Russell, T. P.; Hawker, C. J.; *et al.* Reducing Substrate Pinning of Block Copolymer Microdomains with a Buffer Layer of Polymer Brushes. *Macromolecules* **2000**, *33*, 857–865.
(148) Tairy, O.; Kampf, N.; Driver, M. J.; Armes, S. P.; Klein, J. Dense, Highly Hydrated Polymer Brushes via Modified Atom-Transfer-Radical-Polymerization: Structure, Surface Interactions, and Frictional Dissipation. *Macromolecules* **2015**, *48*, 140–151.
(149) Shah, R. R.; Merreceyes, D.; Husemann, M.; Rees, I.; Abbott, N. L.; Hawker, C. J.; Hedrick, J. L. Using Atom Transfer Radical Polymerization To Amplify Monolayers of Initiators Patterned by Microcontact Printing into Polymer Brushes for Pattern Transfer. *Macromolecules* **2000**, *33*, 597–605.
(150) Roling, O.; De Bruycker, K.; Vonhören, B.; Stricker, L.; Körsgen, M.; Arlinghaus, H. F.; Ravoo, B. J.; Du Prez, F. E. Rewritable Polymer Brush Micropatterns Grafted by Triazolinedione Click Chemistry. *Angew. Chemie Int. Ed.* **2015**, *54*, 13126–13129.
(151) Liu, C.-C.; Thode, C. J.; Rincon Delgadillo, P. A.; Craig, G. S. W.; Nealey, P. F.;

Gronheid, R. Towards an All-Track 300 Mm Process for Directed Self-Assembly. *J. Vac. Sci. Technol. B Microelectron. Nanom. Struct.* **2011**, *29*, 06F203.
(152) Krzysztof Matyjaszewski, *, †; Peter J. Miller, †; Nisha Shukla, ‡; Boonchuan Immaraporn, ‡; Andrew Gelman, ‡; Barry B. Luokala, §; Tiberiu M. Siclovan, ◘; Guido Kickelbick, ⊥; Thomas Vallant, ⊥; Helmuth Hoffmann, ⊥ and; *et al.* Polymers at Interfaces: Using Atom Transfer Radical Polymerization in the Controlled Growth of Homopolymers and Block Copolymers from Silicon Surfaces in the Absence of Untethered Sacrificial Initiator. **1999**.
(153) Park, Y. S.; Ito, Y.; Imanishi, Y. Photocontrolled Gating by Polymer Brushes Grafted on Porous Glass Filter. *Macromolecules* **1998**, *31*, 2606–2610.
(154) Mansky, P.; Liu, Y.; Huang, E.; Russell, T. P.; Hawker, C. Controlling Polymer-Surface Interactions with Random Copolymer Brushes. *Science* **1997**, *275*.
(155) Pujari, S. P.; Scheres, L.; Marcelis, A. T. M.; Zuilhof, H. Covalent Surface Modification of Oxide Surfaces. *Angew. Chemie Int. Ed.* **2014**, *53*, 6322–6356.
(156) Williamson, L. D.; Seidel, R. N.; Chen, X.; Suh, H. S.; Rincon Delgadillo, P.; Gronheid, R.; Nealey, P. F. Three-Tone Chemical Patterns for Block Copolymer Directed Self-Assembly. *ACS Appl. Mater. Interfaces* **2016**, *8*, 2704–2712.
(157) Pujari, S. P.; Li, Y.; Regeling, R.; Zuilhof, H. Tribology and Stability of Organic Monolayers on CrN: A Comparison among Silane, Phosphonate, Alkene, and Alkyne Chemistries. *Langmuir* **2013**, *29*, 10405–10415.
(158) Bhairamadgi, N. S.; Pujari, S. P.; Trovela, F. G.; Debrassi, A.; Khamis, A. A.; Alonso, J. M.; Al Zahrani, A. A.; Wennekes, T.; Al-Turaif, H. A.; van Rijn, C.; *et al.* Hydrolytic and Thermal Stability of Organic Monolayers on Various Inorganic Substrates. *Langmuir* **2014**, *30*, 5829–5839.
(159) Pujari, S. P.; Scheres, L.; van Lagen, B.; Zuilhof, H. Organic Monolayers from 1-Alkynes Covalently Attached to Chromium Nitride: Alkyl and Fluoroalkyl Termination. *Langmuir* **2013**, *29*, 10393–10404.
(160) Noda, H.; Motokura, K.; Miyaji, A.; Baba, T. Efficient Allylation of Nucleophiles Catalyzed by a Bifunctional Heterogeneous Palladium Complex-Tertiary Amine System. *Adv. Synth. Catal.* **2013**, *355*, 973–980.
(161) Hemelaere, R.; Carreaux, F.; Carboni, B. A Diastereoselective Route to Trans -2-Aryl-2,3-Dihydrobenzofurans through Sequential Cross-Metathesis/Isomerization/Allylboration Reactions: Synthesis of Bioactive Neolignans. *European J. Org. Chem.* **2015**, *2015*, 2470–2481.
(162) Li, T.; Wang, Z.; Schulte, L.; Hansen, O.; Ndoni, S. Fast & Scalable Pattern Transfer via Block Copolymer Nanolithography. *RSC Adv.* **2015**, *5*, 102619–102624.
(163) Olson, D. A.; Chen, L.; Hillmyer, M. A. Templating Nanoporous Polymers with Ordered Block Copolymers †. *Chem. Mater.* **2008**, *20*, 869–890.
(164) Liu, C.-C.; Nealey, P. F.; Ting, Y.-H.; Wendt, A. E. Pattern Transfer Using Poly(styrene-Block-Methyl Methacrylate) Copolymer Films and Reactive Ion Etching. *J. Vac. Sci. Technol. B Microelectron. Nanom. Struct.* **2007**, *25*, 1963.
(165) Thurn-Albrecht, T.; Steiner, R.; DeRouchey, J.; Stafford, C. M.; Huang, E.; Bal,

M.; Tuominen, M.; Hawker, C. J.; Russell, T. P. Nanoscopic Templates from Oriented Block Copolymer Films. *Adv. Mater.* **2000**, *12*, 787–791.
(166) Schumers, J.-M.; Vlad, A.; Huynen, I.; Gohy, J.-F.; Fustin, C.-A. Functionalized Nanoporous Thin Films from Photocleavable Block Copolymers. *Macromol. Rapid Commun.* **2012**, *33*, 199–205.
(167) Zhao, H.; Gu, W.; Sterner, E.; Russell, T. P.; Coughlin, E. B.; Theato, P. Highly Ordered Nanoporous Thin Films from Photocleavable Block Copolymers. *Macromolecules* **2011**, *44*, 6433–6440.
(168) Ito, H. Thermally Developable, Positive Resist Systems with High Sensitivity. *J. Electrochem. Soc.* **1989**, *136*, 241.
(169) Houlihan, F. M.; Bouchard, F.; Fréchet, J. M. J.; Willson, C. G. Thermally Depolymerizable Polycarbonates. 2. Synthesis of Novel Linear Tertiary Copolycarbonates by Phase-Transfer Catalysis. *Macromolecules* **1986**, *19*, 13–19.
(170) Fréchet, J. M. J.; Houlihan, F. M.; Bouchard, F.; Kryczka, B.; Wilson, C. G. Design, Synthesis, and Study of Novel, Thermally Depolymerizable Polycarbonates. *J. Chem. Soc. Chem. Commun.* **1985**, 1514.
(171) Jayachandran, J. P.; Reed, H. A.; Zhen, H.; Rhodes, L. F.; Henderson, C. L.; Bidstrup Allen, S. A.; Kohl, P. A. Air-Channel Fabrication for Microelectromechanical Systems via Sacrificial Photosensitive Polycarbonates. *J. Microelectromechanical Syst.* **2003**, *12*, 147–159.
(172) Fréchet, J. M. J.; Bouchard, F.; Eichler, E.; Houlihan, F. M.; Iizawa, T.; Kryczka, B.; Willson, C. G. Thermally Depolymerizable Polycarbonates V. Acid Catalyzed Thermolysis of Allylic and Benzylic Polycarbonates: A New Route to Resist Imaging. *Polym. J.* **1987**, *19*, 31–49.
(173) Jean M. J. Fréchet; C. Grant Willson; T. Iizawa; T. Nishikubo; K. Igarashi; J. Fahey. New Design for Self-Developing Imaging Systems Based on Thermally Labile Polyformals. In *Polymers in Microlithography*; Reichmanis, E.; MacDonald, S. A.; Iwayanagi, T., Eds.; ACS Symposium Series; American Chemical Society: Washington, DC, 1989; Vol. 412, pp. 100–112.
(174) Fréchet, J. M. J.; Fahey, J.; Willson, C. G.; Iizawa, T.; Igarashi, K.; Nishikubo, T. Synthesis of Polyformals and Their Use as Dry-Developing Imaging Systems. *Polym.Mat.Sci.& Eng.* **1989**, 174–178.
(175) Tsuda, M.; Hata, M.; Nishida, R.; Oikawa, S. Acid-Catalyzed Degradation Mechanism of Poly(phthalaldehyde): Unzipping Reaction of Chemical Amplification Resist. *J. Polym. Sci. Part A Polym. Chem.* **1997**, *35*, 77–89.
(176) Hernandez, H. L.; Kang, S.-K.; Lee, O. P.; Hwang, S.-W.; Kaitz, J. A.; Inci, B.; Park, C. W.; Chung, S.; Sottos, N. R.; Moore, J. S.; *et al.* Triggered Transience of Metastable Poly(phthalaldehyde) for Transient Electronics. *Adv. Mater.* **2014**, *26*, 7637–7642.
(177) Geis, M. W. Self-Developing Resist with Submicrometer Resolution and Processing Stability. *Appl. Phys. Lett.* **1983**, *43*, 74.
(178) Kaitz, J. A.; Diesendruck, C. E.; Moore, J. S. End Group Characterization of Poly(phthalaldehyde): Surprising Discovery of a Reversible, Cationic

Macrocyclization Mechanism. *J. Am. Chem. Soc.* **2013**, *135*, 12755–12761.
(179) Dilauro, A. M.; Abbaspourrad, A.; Weitz, D. A.; Phillips, S. T. Stimuli-Responsive Core-Shell Microcapsules with Tunable Rates of Release by Using a Depolymerizable Poly(phthalaldehyde) Membrane. *Macromolecules* **2013**, *46*, 3309–3313.
(180) DiLauro, A. M.; Robbins, J. S.; Phillips, S. T. Reproducible and Scalable Synthesis of End-Cap-Functionalized Depolymerizable Poly(phthalaldehydes). *Macromolecules* **2013**, *46*, 2963–2968.
(181) Seo, W.; Phillips, S. T. Patterned Plastics That Change Physical Structure in Response to Applied Chemical Signals. *J. Am. Chem. Soc.* **2010**, *132*, 9234–9235.
(182) Ito, H.; Jose, S. Preparation of Lithographic Resist Polymers by Anionic Polymerization. In *In Applications of Anionic Polymerization Research*; 1998; pp. 218–234.
(183) DiLauro, A. M.; Zhang, H.; Baker, M. S.; Wong, F.; Sen, A.; Phillips, S. T. Accessibility of Responsive End-Caps in Films Composed of Stimuli-Responsive, Depolymerizable Poly(phthalaldehydes). *Macromolecules* **2013**, *46*, 7257–7265.
(184) Ito, H. Chemical Amplification Resists: Inception, Implementation in Device Manufacture, and New Developments. *J. Polym. Sci. Part A Polym. Chem.* **2003**, *41*, 3863–3870.
(185) Vogl, O.; Bryant, W. M. D. Polymerization of Higher Aldehydes. VI. Mechanism of Aldehyde Polymerization. *J. Polym. Sci. Part A Gen. Pap.* **1964**, *2*, 4633–4645.
(186) Hirao, A.; Loykulnant, S.; Ishizone, T. Recent Advance in Living Anionic Polymerization of Functionalized Styrene Derivatives. *Prog. Polym. Sci.* **2002**, *27*, 1399–1471.
(187) DiLauro, A. M.; Phillips, S. T. End-Capped poly(4,5-Dichlorophthalaldehyde): A Stable Self-Immolative Poly(aldehyde) for Translating Specific Inputs into Amplified Outputs, Both in Solution and the Solid State. *Polym. Chem.* **2015**, *6*, 3252–3258.
(188) DiLauro, A. M.; Lewis, G. G.; Phillips, S. T. Self-Immolative Poly(4,5-Dichlorophthalaldehyde) and Its Applications in Multi-Stimuli-Responsive Macroscopic Plastics. *Angew. Chem. Int. Ed. Engl.* **2015**, *54*, 6200–6205.
(189) Fournier, D.; Hoogenboom, R.; Schubert, U. S. Clicking Polymers: A Straightforward Approach to Novel Macromolecular Architectures. *Chem. Soc. Rev.* **2007**, *36*, 1369.
(190) Inglis, A. J.; Barner-Kowollik, C. Ultra Rapid Approaches to Mild Macromolecular Conjugation. *Macromol. Rapid Commun.* **2010**, *31*, 1247–1266.
(191) Meldal, M.; Tornøe, C. W. Cu-Catalyzed Azide−Alkyne Cycloaddition. *Chem. Rev.* **2008**, *108*, 2952–3015.
(192) Vogt, A. P.; De Winter, J.; Krolla-Sidenstein, P.; Geckle, U.; Coulembier, O.; Barner-Kowollik, C. Polyphthalaldehyde-Block-Polystyrene as a Nanochannel Template. *J. Mater. Chem. B* **2014**, *2*, 3578.
(193) Pessoni, L.; De Winter, J.; Surin, M.; Hergué, N.; Delbosc, N.; Lazzaroni, R.; Dubois, P.; Gerbaux, P.; Coulembier, O. Synthesis of Polyphthalaldehyde-Based

Block Copolymers: Utilization of a Thermo-Sacrificial Segment for an Easy Access to Fine-Tuned Poly(3-Hexylthiophene) Nanostructured Films. *Macromolecules* **2016**, *49*, 3001–3008.
(194) Köstler, S.; Zechner, B.; Trathnigg, B.; Fasl, H.; Kern, W.; Ribitsch, V. Amphiphilic Block Copolymers Containing Thermally Degradable Poly(phthalaldehyde) Blocks. *J. Polym. Sci. Part A Polym. Chem.* **2009**, *47*, 1499–1509.
(195) Douglas, P. S.; Patellis, A. P.; Vredenburgh, W. A. Copolymers of Alpha-Methylstyrene and Styrene and Uses Thereof, 1976.
(196) Nishida, T.; Notomi, M.; Iga, R.; Tamamura, T. Quantum Wire Fabrication by E-Beam Elithography Using High-Resolution and High-Sensitivity E-Beam Resist ZEP-520. *Jpn. J. Appl. Phys.* **1992**, *31*, 4508–4514.
(197) McCormick, H. W. Ceiling Temperature of □-Methylstyrene. *J. Polym. Sci.* **1957**, *25*, 488–490.
(198) Roestamsjah; Wall, L.; Florin, R. E.; Aldridge, M.; Fetters, L. Pyrolysis of Monodisperse Poly-a-Methylstyrene. *J. Res. Natl. Bur. Stand. (1934).* **1978**, *83*, 848.
(199) Brown, D. W.; Wall, L. A. The Pyrolysis of Poly-□-Methylstyrene. *J. Phys. Chem.* **1958**, *62*, 848–852.
(200) Hedrick, J. L.; DiPietro, R.; Plummer, C. J. G.; Hilborn, J.; Jerome, R. Polyimide Foams Derived from a High Tg Polyimide with Grafted Poly(□-Methylstyrene). *Polymer (Guildf).* **1996**, *37*, 5229–5236.
(201) Charlier, Y.; Hedrick, J. L.; Russell, T. P.; Swanson, S.; Sanchez, M.; Jérôme, R. Crosslinked Polyimide Foams Derived from Pyromellitic Dianhydride and 1,1-bis(4-Aminophenyl)-1-Phenyl-2,2,3-Trifluoroethane with Poly(□-Methylstyrene). *Polymer (Guildf).* **1995**, *36*, 1315–1320.
(202) Ito, H.; England, W. Acid-Catalyzed Depolymerization of Poly(□-Methylstyrene) Derivatives. *Polym. Prepr.* **1990**, *31*, 427.
(203) Bosworth, J. K.; Black, C. T.; Ober, C. K. Selective Area Control of Self-Assembled Pattern Architecture Using a Lithographically Patternable Block Copolymer. *ACS Nano* **2009**, *3*, 1761–1766.
(204) Li, M.; Douki, K.; Goto, K.; Li, X.; Coenjarts, C.; Smilgies, D. M.; Ober, C. K. Spatially Controlled Fabrication of Nanoporous Block Copolymers. *Chem. Mater.* **2004**, *16*, 3800–3808.
(205) Bosworth, J. K.; Paik, M. Y.; Ruiz, R.; Schwartz, E. L.; Huang, J. Q.; Ko, A. W.; Smilgies, D.-M.; Black, C. T.; Ober, C. K. Control of Self-Assembly of Lithographically Patternable Block Copolymer Films. *ACS Nano* **2008**, *2*, 1396–1402.
(206) Nagasaki, Y.; Yamazaki, N.; Kato, M. Polymers Degradable under Environmental Conditions through End□modification of Poly(□□methylstyrene) Derivatives. *Angew. Makromol. Chemie* **1997**, *247*, 163–178.
(207) Nagasaki, Y.; Yamazaki, N.; Kato, M. Polymers with Controlled Degradability through End-Modification of Poly(□-Methylstyrene) Derivatives. *Polymer*

(Guildf). **1996**, *37*, 4321–4326.
(208) Hirao, A.; Goseki, R.; Ishizone, T. Advances in Living Anionic Polymerization: From Functional Monomers, Polymerization Systems, to Macromolecular Architectures. *Macromolecules* **2014**, *47*, 1883–1905.
(209) Coulon, G.; Collin, B.; Chatenay, D.; Gallot, Y. Kinetics of Growth of Islands and Holes on the Free Surface of Thin Diblock Copolymer Films. *J. Phys. II* **1993**, *3*, 697–717.
(210) Coulon, G.; Collin, B.; Ausserre, D.; Chatenay, D.; Russell, T. P.; Russell, T. P. Islands and Holes on the Free Surface of Thin Diblock Copolymer Films. I. Characteristics of Formation and Growth. *J. Phys.* **1990**, *51*, 2801–2811.
(211) Kim, S.; Bates, C. M.; Thio, A.; Cushen, J. D.; Ellison, C. J.; Willson, C. G.; Bates, F. S. Consequences of Surface Neutralization in Diblock Copolymer Thin Films. *ACS Nano* **2013**, *7*, 9905–9919.
(212) Bruning, J. H. Optical Lithography: 40 Years and Holding. *Proc. SPIE* **2007**, *6520*, 652004-652004–652013.
(213) Endert, H.; Pa¨tzel, R.; Powell, M.; Rebhan, U.; Basting, D. New KrF and ArF Excimer Laser for Advanced DUV Lithography. *Microelectron. Eng.* **1995**, *27*, 221–224.
(214) MacDonald, S. A.; Willson, C. G.; Frechet, J. M. J. Chemical Amplification in High-Resolution Imaging Systems. *Acc. Chem. Res.* **1994**, *27*, 151–158.
(215) Adam R. Pawloski; Christian, A.; Nealey*, P. F. The Multifunctional Role of Base Quenchers in Chemically Amplified Photoresists. **2002**.
(216) Michaelson, T. B.; Jamieson, A. T.; Pawloski, A. R.; Byers, J.; Acheta, A.; Willson, C. G. Understanding the Role of Base Quenchers in Photoresists. In *Proceedings of SPIE*; Sturtevant, J. L., Ed.; International Society for Optics and Photonics, 2004; Vol. 5376, pp. 1282–1293.
(217) Gronheid, R.; Vaglio Pret, A.; Rathsack, B.; Hooge, J.; Scheer, S.; Nafus, K.; Shite, H.; Kitano, J. EUV RLS Performance Tradeoffs for a Polymer Bound PAG Resist. In; Allen, R. D., Ed.; International Society for Optics and Photonics, **2010**; p. 76390M.
(218) Gronheid, R.; Roey, F. Van; Steenwinckel, D. Van. Using KLUP for Understanding Trends in EUV Resist Performance. *J. Photopolym. Sci. Technol.* **2008**, *21*, 429–434.
(219) Hatzakis, M. Electron Resists for Microcircuit and Mask Production. *J. Electrochem. Soc.* **1969**, *116*, 1033.
(220) Peterson, G. I.; Larsen, M. B.; Boydston, A. J. Controlled Depolymerization: Stimuli-Responsive Self-Immolative Polymers. *Macromolecules* **2012**, *45*, 7317–7328.
(221) Sagi, A.; Weinstain, R.; Karton, N.; Shabat, D. Self-Immolative Polymers. *J. Am. Chem. Soc.* **2008**, *130*, 5434–5435.
(222) Phillips, S. T.; Robbins, J. S.; DiLauro, A. M.; Olah, M. G. Amplified Responses in Materials Using Linear Polymers That Depolymerize from End-to-End When Exposed to Specific Stimuli. *J. Appl. Polym. Sci.* **2014**, *131*, n/a-n/a.

(223) Phillips, S. T.; DiLauro, A. M. Continuous Head-to-Tail Depolymerization: An Emerging Concept for Imparting Amplified Responses to Stimuli-Responsive Materials. *ACS Macro Lett.* **2014**, *3*, 298–304.
(224) Frechet, J. M. J.; Stanciulescu, M.; Iizawa, T.; Willson, C. G. Self-Developing Imaging Systems Based on Polyesters and Polyethers. In *Proc. Polym. Mat. Sci. Eng.*; 1989; pp. 170–173.
(225) Sawada, H. Thermodynamics of Polymerization. I. *J. Macromol. Sci. Part C Polym. Rev.* **1969**, *3*, 313–338.
(226) HEIKENS, D.; GEELEN, H. Ceiling Temperature and Low Temperature Polymerization. *Polymer (Guildf).* **1962**, *3*, 591–594.
(227) Hanabata, M. Novolac-Based Resists. *Adv. Mater. Opt. Electron.* **1994**, *4*, 75–82.
(228) Schlegel, L.; Ueno, T.; Shiraishi, H.; Hayashi, N.; Hesp, S.; Iwayanagi, T. Dissolution Behavior of Novolak/Dissolution Inhibitor Resist Systems in an Aqueous Base Developer. *Jpn. J. Appl. Phys.* **1989**, *28*, 2114–2119.
(229) Ito, H.; Pederson, L. A.; MacDonald, S. A.; Cheng, Y. Y.; Lyerla, J. R.; Willson, C. G. A Sensitive, Etch Resistant, Positive Tone E-Beam Resist System. *J. Electrochem. Soc.* **1988**, *135*, 1504.
(230) Agrawal, A.; Henderson, C. L. A Polysulfone-Novolac Resist for Electron Beam Lithography - Part II: Effects of Resist Formulation and Processing. *Adv. Resist Technol. Process. Xix, Pts 1 2* **2002**, *4690*, 453–464.
(231) Agrawal, A.; Henderson, C. L. Polysulfone-Novolac Resist for Electron Beam Lithography: Part I. Fundamental Studies of Resist Properties. **2002**, *4690*, 1138–1149.
(232) Olah, M. G.; Robbins, J. S.; Baker, M. S.; Phillips, S. T. End-Capped Poly(benzyl Ethers): Acid and Base Stable Polymers That Depolymerize Rapidly from Head-to-Tail in Response to Specific Applied Signals. *Macromolecules* **2013**, *46*, 5924–5928.
(233) Mesch, R. Catalysis and Materials Development for Photolithography, (Dissertation) 2014.